CRANFIELD UNIVERSITY

School of Aerospace, Transport and Manufacturing
Dynamics, Simulation and Control Group

Doctoral thesis

High aspect ratio wings on commercial aircraft: a numerical and experimental approach

Alessandro Pontillo

Supervisors: Dr M. M. Lone and Dr J. F. Whidborne

Cranfield University
School of Aerospace, Transport and Manufacturing
Dynamics, Simulation and Control Group

Alessandro Pontillo

High aspect ratio wings on commercial aircraft: a numerical and experimental approach
Supervisors: Dr M. M. Lone and Dr J. F. Whidborne

Cranfield University
Dynamics, Simulation and Control Group
School of Aerospace, Transport and Manufacturing
College Road
Cranfield, Bedfordshire, UK
MK43 0AL

CRANFIELD UNIVERSITY

Dynamics, Simulation and Control Group
School of Aerospace, Transport and Manufacturing

Doctoral Thesis
Academic year: 2019-2020

HIGH ASPECT RATIO WINGS ON COMMERCIAL AIRCRAFT: A NUMERICAL AND EXPERIMENTAL APPROACH

Alessandro Pontillo

Supervisors: Dr. M. M. Lone and Dr. J. F. Whidborne

Submitted: 20 December 2019

This Thesis is submitted in fulfilment of the requirements for the degree of Doctor of Philosophy at Cranfield University School of Aerospace , Transport and Manufacturing.

To Laura and Aurelio,
you are my whole world.

Abstract

The aim of this work is to assess the aeroelastic response to gust of a flexible high aspect ratio wing (HARW) single-aisle commercial aircraft and to design a viable open-loop Gust Load Alleviation (GLA) system. Aeroservoelastic assessment was carried out by adopting the low-fidelity Cranfield Accelerated Aircraft Load Model (CA^{2}LM) aeroelastic framework. Wind tunnel testing of two flexible wing models was carried out to assess the limitations of low-fidelity numerical frameworks in modelling highly flexible structures.

The numerical work firstly focused on upgrading the CA^{2}LM framework by including the non-linear aerodynamic effects of spoiler deflection into the low-fidelity model. The novel method was able to locally change the wing lift distribution evaluated with strip theory by combining ESDU 14004 experimental data with the numerical estimation. Finally, the aeroelastic response of the High Aspect Ratio Technology ENabler (HARTEN) concept aircraft to gust input was carried out for a single flight condition (h=26000 ft and v=200 m/s) and for two different structural configurations: rigid wing and flexible wing structure. Tuned discrete gust analysis, as specified in CS-25, was adopted in this analysis. Results showed that tuned gust is able to excite flexible wing dynamics along with the rigid-body dynamics, having a detrimental impact on aircraft performance. Finally, an open-loop GLA system was designed to alleviate Wing Root Bending Moment (WRBM) increment due to gust load. The GLA deflected spoilers and ailerons for a fixed amount of time (hold time) once a specific vertical load factor was crossed. An optimization algorithm was used to optimize parameters such as control surfaces deflection, hold time and load factor threshold. Several configurations of the GLA were evaluated. The optimal GLA configuration was able to alleviate WRBM from a minimum of 2.4% to a maximum of 8.1% with respect to the non-alleviated scenario.

Two wind tunnel models were built with the common spar and skin configuration, while a novel approach for the skin manufacturing was introduced: the skin was 3D printed with PolyJet technology which allowed to provide a continuous aerodynamic shape removing the typical gaps necessary for flexible models to allow wing bending, limiting the impact of the skin to less than 12.5% of the overall model stiffness. The first model was tested in the Cranfield Weybridge wind tunnel at 27 m/s (Re = 3.5e5) and $\alpha = 6°$. The model span was 0.840 m and Aspect Ratio AR = 12. The model was successfully tested to prove the ability of the skin to retain the aerodynamic shape and sustain the load under large deformation, reaching a max wingtip displacement of 32% of the model span. The second model was tested in the Cranfield 8x6 ft wind tunnel in the speed range of 20 m/s to 40 m/s (3.1e5 < Re < 6.2e5) at $-2° < \alpha < 8°$. The model span was 1.5 m and AR = 18.8. The main result showed that in the most severe aerodynamic load scenario ($v = 40$ m/s and $\alpha = 8°$), the spanwise force coefficient accounted for 10% of the wing overall C_L and was 2.5 times higher than C_D. The overall damping was also estimated for different velocities at $\alpha = 6°$, reaching a maximum of 26.9% at 35 m/s and a minimum of 17.8% at 20 m/s, with aerodynamic damping accounting for a minimum of 61% to a maximum of 74% of the overall damping. Maximum displacement of the wing tip was 13.7% of the model span (0.21 m). In both tests a low-cost acquisition system built with off-the-shelf components was used. The system was based on Raspberry Pi board able to acquire accelerations and rotations from four MPU6050 IMU boards, with the main benefit being the small size of the sensors, which were able to fit within tiny volumes typical of HARW wind tunnel models.

Keywords: *flight dynamics, wind tunnel test, flexible wings, high aspect ratio, gust load alleviation, optimization.*

Acknowledgements

I would like to express my gratitude to my supervisors, Dr Mudassir Lone and Dr James Whidborne, for guiding me through this long journey, to my fellows for making this time so enjoyable, even in the hardest moments, to my colleagues at Airbus UK, especially Dr. Etienne Coetzee, who helped to shape the meaning of this work, to SATM lab technicians for their invaluable work, to my family for supporting me in every choice of my life and finally to my wife and son, light of my days, without whom I would have not been here writing these words today.

This work was founded by Airbus UK, Innovate UK and ATI within the scope of the Agile Wing Integration (AWI) project.

Contents

List of Figures

List of Tables

Nomenclature

A_n	Prandtl coefficients
b	Wingspan [b]
$[C]$	Damping matrix
C_{D_i}	Induced drag coefficient
C_{D_0}	Zero-lift drag coefficient
C_L	Lift coefficient
C_{L_α}	Lift coefficient slope
D	Drag [N]
D_i	Induced drag [N]
e	Oswald efficiency factor
E	Young's modulus [Pa]
f	Frequency [Hz]
$[F]$	Force matrix
Fr	Froude number
n_z	Vertical Load factor
p	Roll rate [deg/s]
q	Pitch rate [deg/s]
$\bar{q}$	Generalised coordinates
H	Gust gradient [m]
I	Second moment of area $[m^4]$
J	Cost function
$[K]$	Stiffness matrix
L	Lift [N]
Ma	Mach number
$[M]$	Mass matrix
Q	Generalised force [N]
r	Yaw rate [deg/s]
Re	Reynolds number
S	Wing area [m^2]
T	Kinetic energy [J]
V	Speed [m/s]
u, v, w	Longitudinal, lateral and vertical speed [m/s]

W	Weight [kg]
x, y, z	Displacement coordinates
X, Y, Z	Longitudinal, lateral and vertical force [N]

Greek alphabet

α	Angle of attack [deg]
β	Sideslip angle [deg]
$\bar{\beta}$	Compressibility factor
δ_s	Spoiler deflection angle [deg]
η	Elevator deflection angle [deg]
$\bar{\eta}$	Vibration modes component
Γ	Circulation
ι	Rudder deflection angle [deg]
ω	Natural frequency [rad/s]
$\bar{\omega}$	Angular velocity [deg/s]
$\boldsymbol{\Omega}$	Mode shape matrix
ϕ	Roll angle [deg]
ϕ_w	Wagner function
π	Scaling coefficients
ψ	Yaw angle [deg]
ρ	Density [kg/m^3]
σ	Standard Deviation
σ_x	Standard Error of the mean
τ	Hold time [s]
θ	Pitch angle [deg]
$\ddot{\theta}$	Angular acceleration [deg/s^2]
ξ	Aileron deflection angle [deg]
ζ	Damping

Subscript

$_A$	Aircraft
$_d$	Demand
$_D$	Drag
$_f$	Flexible
$_{ff}$	Full wing (model)
$_g$	Gust
$_L$	Lift
$_{ss}$	Scaled wing (model)
$_T$	Tail
$_W$	Wing
$_z$	z-axis direction

Superscript

^{B}	Body-axis system
^{c}	Circulatory
^{nc}	Non-circulatory
^{w}	Wing-axis system
$\dot{}$	Time derivative

Abbreviations

AFS	Active Flutter Suppression
AoA	Angle of Attack
AR	Aspect Ratio
BEaRDS	Beam Reduction and Dynamic Scaling
BEaRDS^{TM}	Beam Reduction and Dynamic Scaling Theoretical Model
BWB	Blended Wing Body
CA^{2}**LM**	Cranfield Accelerated Aircraft Loads Model
CoG	Centre of Gravity
CFD	Computational Fluid Dynamics
DOF	Degrees of Freedom
EAS	Equivalent Air Speed [m/s or kts]
EOM	Equations of Motion
FCS	Flight Control System
GLA	Gust Load Alleviation
GTM	Generic Transport Model
GVT	Ground Vibration Test
EoMs	Equations of Motion
EAS	Equivalent Air Speed
FCS	Flight Control System
FEM	Finite Element Model
FRF	Frequency Response Function
FSW	Forward Swept Wing
HALE	High Altitude Long Endurance
HARTEN	High Aspect Ratio Technology ENabler
HARW	High Aspect Ratio Wing
LE	Leading Edge
MLA	Manoeuvre Load Alleviation
MTOW	Maximum Take Off Weight
OEW	Operating Empty Weight
PID	Proportional Integral Derivative controller
RoR	Random on Random
SNR	Signal to Noise Ratio
TE	Trailing Edge
TAS	True Air Speed
UVLM	Unsteady Vortex Lattice Method
WRBM	Wing Root Bending Moment
XB-1	eXperimental Beards 1
XB-2	eXperimental Beards 2

1

Introduction

The aviation industry is driven towards novel configurations and innovative technologies by the need for more efficient aircraft capable of addressing current and future societal challenges. The International Air Transport Association (IATA) commission estimated 8.2 billion air travellers in 2037 [11]. Such an increase in the aviation traffic inevitably leads to a higher demand for new efficient aircraft [114]. This requires a series of technical challenges to be solved, such as the increase in pollution due to aircraft emission in the high atmosphere, the management of air traffic around busier airports and the increase in noise in the area surrounding the airports. The European Commission published two documents [18, 10], setting the requirements for the aviation industry to be met by 2050. A short summary of the requirements is as follows:

- improving the passengers experience aiming to 99% of on-time flights and a constant drop in travel charges,
- drastically reduce the impact of human error,
- to invest in technologies able to reduce by 75% the CO_2 emissions per passenger kilometre, [1]
- to target a 90% reduction of NOx emissions,[1]
- to design and manufacture recyclable aircraft, able to be emission-free while taxiing.

A broad range of possible solutions exist enabled by new technologies both at the subsystem and overall aircraft levels. In the latter category, several potential options are available, such as Blended Wing Bodies (BWB) [103, 90] or High Aspect Ratio Wings (HARW) [1]. When considering which option to adopt, a risk benefit analysis must be carried out where solutions such as BWB configurations impose a significant amount of risk for the aviation stakeholders. In this context, HARW can be adopted for current aircraft configurations while introducing considerable benefits to performance. HARW are long and slender structures that focus on reducing induced drag. Induced drag, C_{D_i}, is proportional to the lift and is classically defined as [4]:

$$C_{D_i} = \frac{C_L^2}{\pi ARe} \tag{1.1}$$

---

[1] Relative to typical aircraft performance in 2000

where C_L is the lift coefficient, e the Oswald efficiency factor and AR is the wing aspect ratio defined as

$$AR = \frac{b^2}{S} \tag{1.2}$$

Here b is the aircraft wingspan and S is the wing reference area. C_{D_i} is responsible for more than 40% of the overall drag in cruise flight [1]. The trend in the aviation industry has been to increase the aspect ratio, but today's commercial aircraft are limited to $AR \approx 10$, which is far from the AR of highly efficient aircraft such as sailplanes, with AR up to 40 [55]. Hence, there is a need for investigating HARW configurations as a possible means of creating a step improvement in aircraft efficiency. Extensive studies have been done on HARW aircraft, but the focus has been mostly on High Altitude Long Endurance (HALE) aircraft [126, 125]. Today, the application of HARW technology on commercial aircraft is limited to the NASA/Boeing SUGAR concept [25, 3].

Along with the main aerodynamic benefit of reducing induced drag, HARW introduce a set of new problems in the aeroelastic domain related to the increased flexibility of the slender wing structure [43, 22]. Such structures have the tendency to undergo large deformations even when flying within the standard flight envelope which impacts the flight dynamic stability as well as structural response to aerodynamic loads. This brings a new variable in the equation since AR cannot be increased exponentially. The highest AR achievable is in fact a compromise between the aerodynamic benefit and the penalty introduced by increases in the Wing Root Bending Moment (WRBM) and wing structure weight. In fact, a critical point in the design process exists when the weight penalty incurred for strengthening the wing box exceeds the aerodynamic benefit of the extended wing span.

Besides the fact that such a compromise has to be made, it is possible to develop methods that reduce WRBM in the most critical flight phases. These mechanisms usually rely on the deployment of control surfaces when needed and can be divided in two categories: Manoeuvre Load Alleviation (MLA) and Gust Load Alleviation (GLA). While the use of MLA helps to manage and reduce the load in normal manoeuvring conditions, the GLA is activated when the aircraft is subject to atmospheric disturbances such as turbulence. Such disturbances are characterised by the increment in the local wing angle of attack, that suddenly varies the load distribution over the wing in a gust encounter scenario. This phenomenon is exacerbated on HARW due to the increased span. A focus of this work is on the design of an industrially viable GLA system for HARW commercial aircraft.

GLA systems are controllers specifically designed to mitigate the effect of gust and turbulence [80]. Numerous designs and methods can be found in the available literature; some achieving reductions of WRBM up to 50% with respect to the non alleviated case. Example strategies utilise methods like Model Predictive Control (MPC) [68], PID [142] and Linear Quadratic Regulator (LQR) controllers which belong to *feedback control systems* category. This family of controllers rely on the knowledge of *state* of the system in order to develop the appropriate action to mitigate loads in the event of a gust. While some use data from

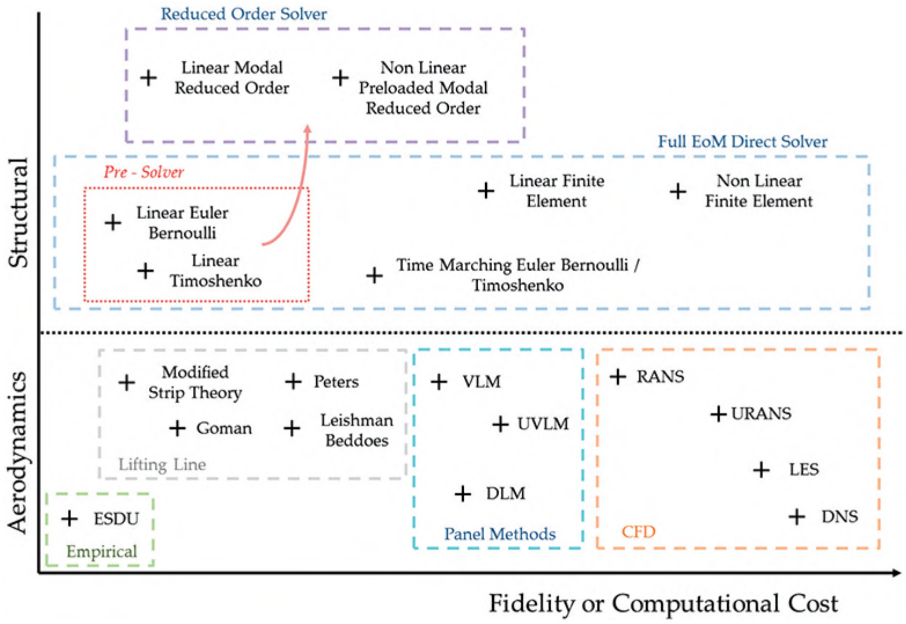

Fig. 1.1.: Summary of the possible modelling methods ranked by complexity and fidelity.

accelerometers or angle of attack sensors to reconstruct the state, others use more novel sensors such as LIDAR [76, 140]. However, while feedback control systems can limit the error introduced by the uncertainty of the model, this tends to be difficult to certify for industrial use. Certification of feedback systems can be difficult, time and budget consuming due to safety criticality. Hence, the need for a more industrially viable GLA system. Open-loop controllers are an alternative due to the more simple architecture.

A numerical aeroelastic framework is needed to design and test such GLA systems. Requirements and strategies of aeroelastic modelling mostly depend on the model fidelity and the computational power available. Figure 1.1 provides an overview of some of the available modelling techniques for both structures and aerodynamics. All possible methods for modelling can be divided in two main subsets: linear and non-linear. HARW are characterised by large structural deformations, where contributions from the non-linear structural dynamics to the overall aeroelastic behaviour may not be negligible. Yet, when modelling such phenomena, assumptions are made and models are subject to the resulting limitations. Therefore, an estimation of the error introduced by the model is also needed. Experimental testing allows the validation of numerical models and an assessment of these limitations.

Aeroelastic testing is mainly performed in wind tunnels at different scales. The validation of the dynamic aeroelasticity plays an important role in the context of predicting the response of HARW commercial aircraft. Hence, there is a need to develop a dynamic scaling methodology to reproduce (in the wind tunnel) the dynamic response of the full scale design. Designing, manufacturing and testing flexible wind tunnel models is not trivial and it is effectively a multidisciplinary design problem. Different methods and technologies can be used to build flexible wing models [165, 163, 143]. Surveying the different manufacturing techniques however, shows that each technique has its own limitations. Hence, a new manufacturing and design approach is needed for building scaled aeroelastic wind tunnel models.

1.1 Aim and objectives

The aim of this work is to assess the aeroelastic response to gust of a flexible high aspect ratio wing medium-range commercial aircraft and to develop a suitable open-loop gust load alleviation system. The study will focus on the interaction of flexible wings and the rigid-body dynamics of the High Aspect Ratio Technology ENabler (HARTEN) concept aircraft specifically designed and developed for the scope of this study with the contribution of project partners. The following objectives are therefore defined:

- To be able to model the dynamic interaction between rigid body and flexible wing structures and to understand how structure dynamics affects the overall aircraft flight qualities.
- To design and carry out wind tunnel tests to assess scaled flexible wing models and to use experimental observations to find limitations of aeroservoelastic frameworks. The use of experimental data for the evaluation of aeroservoelastic frameworks should include considerations on the suitability of such models to represent the dynamic response of HARW structures and their elastic properties which characterise such configurations.
- To design and manufacture low-cost flexible dynamically scaled wind tunnel models. The low-cost aspect should be made crucial in this study due to the impact of costs on wind tunnel models specifications. Furthermore, a low-cost solution mitigates the costs of any necessary fixes of damaged parts.
- To be able to design and assemble a low-cost acquisition system using off-the-shelf components. The acquisition system must be able to fit in limited volumes dictated by the HARW slender configuration and to provide performance comparable with commercial and more expensive equipment.
- To develop a numerical aeroelastic framework able to simulate flexible wing models response in order to assist the design and testing of dynamically scaled model in the wind tunnel.
- To augment the Cranfield Accelerated Aircraft Load Model (CA^{2}LM) aeroservoelastic framework with a spoiler model able to replicate the non-linear spoiler effects subject to modelling constraints dictated by the low-fidelity nature of the framework.
- To design an open-loop GLA system and assess its effectiveness on the HARTEN HARW concept aircraft. Therefore use results of the analysis to compare performance of the open-loop GLA system with close-loop GLA systems.

1.2 Contribution to knowledge

The contributions to knowledge of the overall work can be summarised as follows:

- The development of a coupled model manufacturing and wind tunnel test methodology that provides the designer with tools and guidelines for experimentally assessing the aeroelastic response of dynamically scaled high aspect ratio wings. The methodology provides a numerical framework to dynamically scale and assess the aeroelastic response of a highly flexible wing while establishing a novel manufacturing process to build and assemble the flexible wind tunnel model.

- The definition of a novel manufacturing process for highly flexible wind tunnel models. The process aims to decouple the mass and stiffness design of dynamically scaled models limiting to less than 12.5% the impact of the skin on the overall model stiffness. Furthermore, the skin manufacture process is designed to overcome aerodynamic interference in the gaps between pods commonly used to allow the model to deform.

- The modelling of non-linear spoiler effects in a numerical aeroservoelastic framework. The local loss of lift due to the spoiler action influences the overall aerodynamic load distribution over the wingspan. Due to the fully non-linear behaviour of the flow behind the spoiler, there are not many theoretical models able to describe the spoiler function. Common practice is therefore to use Computational Fluid Dynamics (CFD) to reproduce the turbulent flow downstream of the spoiler. However, this does not allow the use of spoilers in real-time simulations. The method proposed in this work overcomes these limitations by modifying the local lift distribution estimated by strip theory by using experimental data provided by the ESDU 14004 datasheet. The method proposed is effectively able to impact the lift distribution along the span without affecting real-time capabilities of the framework.

- The design of an open-loop GLA system for HARW configurations. Although close-loop systems can be effective and are able to reduce considerably the wing root bending moment (WRBM), their application for the aviation industry is difficult due to certification requirements. The adoption of open-loop GLA does not impact aircraft stability and therefore overcomes such critical issues. The open-loop system developed within this work was able to reduce the WRBM by up to 8.1% with respect to the non-alleviated case. The open-loop GLA is designed for an A320-like HARW commercial aircraft, which denotes a novelty in the research itself as most of the work done on flexible HARW aircraft is applied to UAVs or High Altitude Long Endurance (HALE) vehicles.

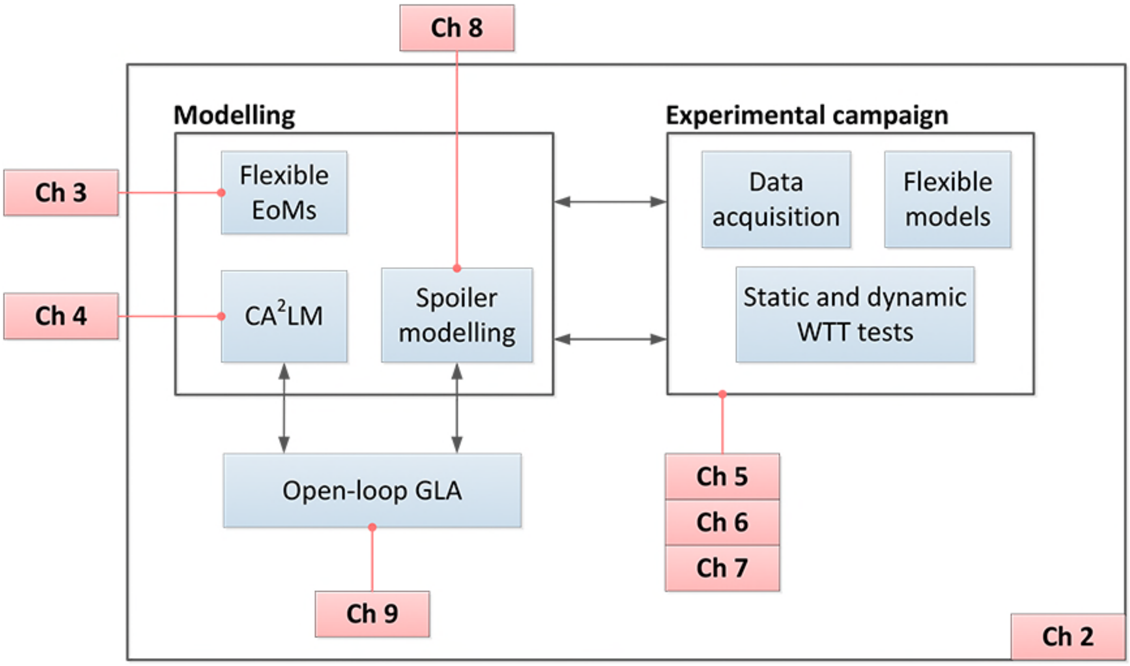

Fig. 1.2.: Thesis layout

1.3 Thesis structure

The thesis is structured to guide the reader through the numerical and experimental analysis of the impact of highly flexible HARW on commercial aircraft. A schematic of the thesis structure is shown in Figure 1.2.

Firstly, an extensive review on the effects of flexible structures on aircraft static and dynamic response is presented in Chapter 2. The literature available highlights the impact of flexible structures when the lower natural frequency of the wing, usually the first bending frequency, overlaps the highest rigid-body dynamics frequency of the aircraft, usually the short period mode. As well, the literature focuses on the experimental techniques (and their limitations) adopted to test flexible models. Finally, an overview of GLA systems designed for flexible aircraft is provided.

Following the literature review, Chapter 3 provides a further investigation on the impact of structural flexibility on the aircraft dynamics. In order to fully understand the nature of such interaction, a rigid-body model of a GTM aircraft is enhanced adding a layer of complexity able to evaluate the structural dynamics of the vehicle. A parametric study is then performed varying damping and natural frequencies of the structure in order to investigate the degree of interaction between the rigid-body and structural dynamics.

Chapter 4 introduces the CA^{2}LM framework along with the BEaRDS programme. The first one is the aeroelastic framework adopted to perform the numerical evaluation of the HARW aircraft gust response and the design of the open-loop GLA system. BEaRDS instead is an experimental programme developed within the scope of this work with the purpose of experimentally assessing the response of a flexible wind tunnel model and to determine the limitations of the CA^{2}LM framework.

Chapter 5 describes the development of a new manufacturing process for flexible wind tunnel models. The tested model (eXperimental BEaRDS 1, XB-1) is able to reduce the impact of the model skin on the overall stiffness by 3D printing the skin with Polyjet technology. Along with the model design and manufacturing, a new acquisition system assembled with off-the-shelf components is introduced and its performance compared against a commercial system through data acquired from Ground Vibration Tests (GVT).

Chapter 6 and 7 describe the design, manufacturing and testing of a 1.5 m wingspan flexible wing model tested in the Cranfield 8x6 ft (the eXperimental BEaRDS 2, XB-2). Chapter 6 details the design and manufacturing steps of the process. The model is dynamically scaled from a full scale HARW A320-like aircraft. Part of the model development process is the tailoring of its dynamic response to match the one of the full scale wing. In Chapter 7 testing of the XB-2 is described and its dynamic and static response evaluated. Wind tunnel data are then used to validate the CA^{2}LM framework.

Following the experimental part, Chapter 8 introduces the HARTEN aircraft, the HARW medium-haul aircraft object of the numerical analysis of this work. In the same chapter, the novel spoiler modelling technique and its integration in the CA^{2}LM framework is presented along with an assessment of the impact of the spoiler action on the aircraft wing aerodynamics.

Chapter 9 assesses the dynamic response of the HARTEN aircraft to a range of discrete gust inputs. The response analysis focuses on flight dynamics characteristics along with the evaluation of structural nature estimating parameters such as the WRBM. Following the gust analysis, an open-loop GLA system is designed for the HARTEN aircraft exploring different combinations of critical parameters such as spoilers and ailerons deflection and the deployment time.

Finally, Chapter 10 provides a summary of the results obtained within this work, providing further insights into the work needed to improve both the numerical and experimental procedures proposed above.

Literature review

2

Benefits and associated challenges of adopting High Aspect Ratio Wings (HARW) for commercial aircraft can be analysed from multiple perspectives due to the multidisciplinary nature of the problem. From a structural point of view, the design of longer and slender wings leads to more flexible structures which affects internal loads of the wing. From a flight dynamics perspective, more flexible structures result in lower structural natural frequencies that can couple with the rigid body dynamics, affecting the aircraft response. From an aerodynamic point of view, the introduction of HARW reduces the induced drag component generating a different flow pattern with respect to a wing with lower aspect ratio.

These fields represent just a limited subset of the design areas affected by the introduction of HARW. Although each one of these plays a crucial role in the design process, this work focuses on the flight dynamics aspect and the design of a suitable Gust Load Alleviation (GLA) system to lower the Wing Root Bending Moment (WRBM) induced by gust loads.

Therefore, the following review firstly focuses on motivations behind the possible adoption of HARW. Secondly, the impact of HARW on structures and flight dynamics is discussed. Thirdly, suitable adopted strategies for GLA on HARW are shown highlighting benefits and drawbacks. Finally, the state of the art of flexible wind tunnel models is detailed.

2.1 Different approaches

To drastically improve the aircraft performance, a breakthrough in the development of new technologies is required and different approaches can be considered [1]:

- a non-conventional design able to increase aerodynamic efficiency,
- the reduction of cruise drag, mainly focusing on flow control and reduction of induced drag and
- new propulsion options with more efficient and more silent engines.

Figure 2.1 shows some of the possible solutions and their impact on aircraft performance: while some of the technologies shown can improve more than one aspect of the design, none of them can provide a comprehensive solution to the problem. Therefore, a compromise in the design must be made focusing on the specific aspect that the designer wants to improve.

	High aspect ratio wing	Adaptive sections	More highly loaded sections	Direct shock control	Laminar flow promotion	Turbulent skin friction drag reduction	More effective gust and maneuver load alleviation control	Unsteady flow separation and turbulent noise source	Unsteady loads control (i.e. flutter LCO and buffet onset delay)	More effective (smaller) control surfaces for given aircraft control requirement	More effective (smaller) high lift devices for given low speed requirement	Management/elimination of unsteady flow separations + turbulent source noise	Engine noise shielding	Engine exhaust control & trust vector control	Reduced wake vortex signature for given low speed requirement	Simplified high lift system for given low speed requirement
Reduce vortex drag	X															
Reduce wave drag		X		X												
Reduce friction drag					X	X										
Reduce pressure drag								X								
Reduce critical loads		X					X	X	X							
Increase structural efficiency			X							X	X			X		
Reduce airframe source noise								X				X				
Reduce engine noise	X	X											X	X		
Reduce separation distances	X														X	
Reduce complexity																X

Fig. 2.1.: New design concepts and their impact on aerodynamic performance (reproduced from [1]).

Blended Wing Body (BWB) was a new configuration of aircraft characterized by removing the common cylindrical fuselage, and blending it into the wing structure. One of the first BWB designs was attempted by NASA in 1994. Such a configuration represented a revolution as it aimed to design a vehicle able to transport 800 passengers, almost three times the maximum aircraft capacity at the time of the project [102, 103]. Due to its innovative design, the BWB was the object of several studies. Liebecks' analysis showed that the BWB configuration was able to save up to 27% in fuel burn, 15% of MTOW with respect a generic widebody aircraft [103] and to increase the aerodynamic efficiency by up to 20%. The most evident feature of the aircraft is the large wing wetted area compared to a conventional aircraft. Furthermore, different versions of the original BWB were designed: in one of them boundary layer

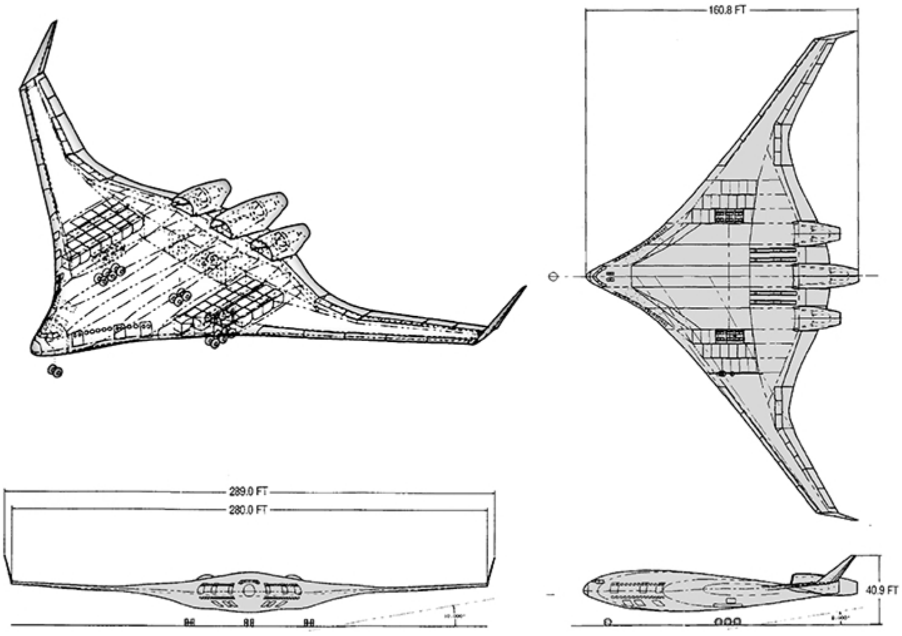

Fig. 2.2.: NASA Wing-Blended-Body aircraft (reproduced from [103]).

ingestion technology [90] was added, drastically reducing ram drag, engine wetted area and structural weight [1]. Although the benefits of such configuration are significant, introducing a brand new concept aircraft on the market requires a large investment and great risk from the company and its stakeholders. Problems like the structural integration, the presence of a non-circular fuselage, the absence of vertical empennage, or the rigid coupling between aerodynamics and stability are all factors that must be addressed from an entirely new point of view. However, the research on this type of vehicle continued throughout the years exploiting its aerodynamic benefit and addressing the drawbacks. The evaluation of the aerodynamic performance of BWB can be found in Reference [139, 112], while details on the BWB stability analysis can be found in the work carried out by Su et al. [161].

Fig. 2.3.: NASA X-29 forward-swept wing demonstrator (source NASA/Larry Sammons, reproduced from commons.wikimedia.org).

Moving to more a conventional approach, one solution is to adopt Forward Swept Wing (FSW) technology. The adoption of the FSW allows a more conservative approach into the design of the aircraft. FSW configuration benefits the aerodynamics of the wing extending the angle of attack range and reducing the transonic and induced drag. As well, the flow separation pattern of the FSW starts from the root propagating outboards towards the tip, improving the aileron effectiveness for high angles of attack with respect to a conventional configuration [1]. However, the gust response of the FSW aircraft is degraded due to possible separation effects at the wing inboard section, along with the worsening of the lateral-direction control characteristics. Benefit of FSW configuration in achieving laminar flow over the wingspan [141] were shown by Seitz's work [157], which assessed the application of FSW on a A320-size commercial aircraft focusing on preventing structural divergence due to additional nose-up wing twist. Because of its aerodynamic benefit, the adoption of FSW has been investigated in the past. First example ever produced was the German bomber Junker JU 287, developed during World War II. However, further development of this study along with several others in the following years, was limited by the early onset of static aeroelastic divergence at low speed [183, 148]. Such a problem could have been solved by stiffening the wing structure significantly. However, until the 80s, the wing structure would have been made only of metal, and the impact of the additional weight on performance would have cancelled out the aerodyanmic benefit of the FSW configuration. With the development of composite materials, the FSW concept had been resumed and developed further [183].

A third proposed option is the adoption of High Aspect Ratio Wings (HARW). High values of *AR* indicate long and slender wings. A common value of *AR* for commercial aircraft is 10, while sailplanes can reach *AR* of up to 40. Increasing the aspect ratio is a viable and efficient way to decrease drag. The overall drag can be broken-down in skin-friction drag, due to shear stress acting on the wing surface, and pressure drag caused by the flow separation. Both of them strongly depend on *Re* number [4]. Once it comes to the engineering process of drag minimization, a relevant portion of the drag can be modelled as the one linked to lift generation, known as induced drag, D_i, and ideally caused by the backward tilting of the lift vector. In fact such rotation is responsible for reducing the wing angle of attack and generating the wing downwash [4]. Other ways to model drag includes wave drag, due to the formation of supersonic shock waves[1] and drag caused by the interaction of aircraft components, such as wing-fuselage, tail-fuselage, antennas or external devices. It is estimated that in cruise flight drag is mainly associated with friction phenomena (47%) and lift generation (43%) [1]. HARW can address and improve three key factors of the aircraft performance (Figure 2.1): i) reduction in the vortex drag, linked to lift production, ii) the engine noise and iii) the separation point of the flow along the chord.

A short summary of other possible solutions to improve aerodynamic performance is as follows:

- the adoption of laminar flow technologies to delay the boundary layer separation [40, 157, 154],
- the use of passive control devices able to energize the boundary layer [188, 92],
- the implementation of wing-tip devices (also known as winglets) able to decrease the intensity of the wingtip trailing vortices [4], reducing the induced drag[2].

The solutions shown above are a subset of an extensive group of new technologies and configurations proposed to boost aircraft performance. For brevity, only the most advanced and developed options were shown here. While all of them were at least numerically proven to be effective in one or more aspects of the aircraft performance, not all of them represent a real industrial option in terms of design, manufacturing and certification. In fact, the manufacturer must compromise between new technologies and the risk their introduction represents in terms of profit margin. In this context, an entirely newly designed aircraft would not be a *safe* marketing choice. Adopting HARW instead would allow companies to redesign

---

[1] This phenomena is relevant in transonic flight as well because of local supersonic bubbles that generate on the wing surface.

[2] The use of winglets does not exclude the implementation of other solutions, especially HARW. Some examples of winglets application can be found in the work of Mattos et al. [115], Kravchenko [94] or Spillman [160]. The latter work actually investigated the process of the drag reduction implementing wing-tip sails rather than winglets. The device was tested in flight on a Paris aircraft, showing a drag reduction of 30% and an increase of lift-to-drag ratio of 25%.

only partially the aircraft and benefit from the aerodynamic improvements introduced by the adoption of such a new wing configuration. For this reason, this work focuses on HARW configurations as representative of a viable and realistic option for aircraft manufacturers.

2.2 HARW configurations

Kroo [95] defines the aircraft as *"a zero-efficient system as it moves mass from one rest point to another rest point so that it spends energy for not varying the state of the system".* This is obviously a paradox that however underlines the need of an energetic approach in the design of the aircraft systems in the effort of reducing the drag due to lift, also known as induced drag. Kroo estimated that 1% reduction of induced drag may increases the MTOW by 1%, leading to an important advantage in terms of range. Furthermore, the increase in the efficiency results in reduction of the noise as well.

The importance of the aspect ratio in relation to vortex drag finds its root at the beginning of the century when studies on inviscid flow were done by Lanchester [96] and Prandtl [137]. Prandtl defined the optimal lift distribution [136] that minimizes the induced drag for a given total lift value and wingspan to be elliptical[3]. The deviation from the nonoptimal Prandtl lift loading is evaluated through the Oswald efficiency factor, e, which is equal to 1 when the lift distribution matches the optimal one. This aspect is particularly important when analysing wind tunnel and flight tests data. It was found by Brown[84] that sailplanes, whose wing design aim to achieve the *ideal* lift distribution, achieve values of e from 0.7 to 0.8. The source of this difference lies in the fact that the vortex drag is not the only source of lift-dependant drag, differently from what was theorized by Prandtl. Other sources of induced drag are linked to friction and viscosity effects [84]. However, while it is possible to minimize the induced drag, it is not possible to zero it, as it would correspond to a zero lift state [95].

While the elliptical optimal solution derived by Prandtl is obtained imposing a constrained wingspan, a different numerical solution again proposed by Prandtl showed that when the wingspan is unconstrained, the minimum of the induced drag is achieved for longer value of the span [79]. Prandtl as well then proved the benefit of HARW in reducing the induced drag. Applications of this configuration are shown by gliders or human-powered aircraft, such as

---

[3] Greene [73], while still accepting that the Prandtl formulation is the mathematical optimum distribution, argued that the Prandtl solution is physically impossible to create. In fact, Greene showed that the gradient of the circulation is proportional to the local entropy. Therefore, the Prandtl elliptical distribution of the circulation, Γ, defined as:

$$\Gamma(y) = \Gamma_0 \left[1 - \left(\frac{y}{2}\right)^2\right]^{\frac{1}{2}} \tag{2.1}$$

would provide an infinite value of the entropy at the wing-tip, violating the 2^{nd} law of thermodynamics. Greene then proposes a parabolic distribution defined as:

$$\Gamma(y) = \Gamma_0 \left[1 - \left(\frac{y}{2}\right)^2\right] \tag{2.2}$$

which still minimizes the induced drag while being physically achievable. For more details the reader is referred to Hayes et al. [79].

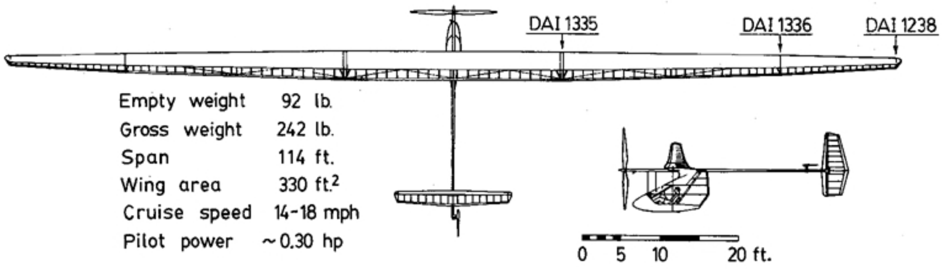

Fig. 2.4.: The Eagle human-powered aircraft (reproduced from [55]).

the Eagle, shown in Figure 2.4. The Eagle is an ultra high aspect ratio wing ($AR = 39.4$) built by the MIT with the purpose of beating the world distance record for human powered aircraft. Drela and the MIT team were able to design the wing such as to reach a lift-to-drag ratio of 40 [55, 193], achieving the world record for the longest flight scoring a distance of 71.53 miles in 1988.

However, this cannot always be a viable solution due to design requirements and practical restrictions [2]. A common argument is that an increase in span is related to an increase in structural weight. There is a point where the HARW benefit on the induced drag is overcome by the penalties of the extra weight. Considering the same area, the higher the wingspan the higher is the wing structure weight due to the need to compensate for the higher bending moment. This threshold was calculated by Kroo as the wing weight to be 30% of the aircraft structure. As we are currently far from this value (a typical value on modern aircraft is 10%), the weight penalty does not represent a strong reason to not pursue this option. More challenges are linked to the increased flexibility of the wing structure, which leads to lower structural natural frequencies. This aspect implies that the frequency gap between rigid-body dynamics and structural dynamics is reduced and the two dynamics can now overlap interacting (Figure 2.5). Su et al. [161], while investigating the non-linear aeroelastic response of flexible aircraft, stressed the need to consider this interaction. In fact, a finding of the study has shown that the flutter boundary estimated for rigid-body aircraft configuration might be different from the one that considered the interaction between rigid-body and flexible dynamics. Benefits of increasing AR are shown in Figure 2.6 where the tendency of manufacturers of increasing AR over the past 70 years is clear. When not possible to re-design the whole wing, companies and manufacturers opted for equipping aircraft wings with new devices, able to increase the aspect ratio of the wing. Examples of this strategy are the A320-200 and B737-NG which increased their wing aspect ratio by 10.2% and 8.7% respectively [2]. The literature on the stability, aeroelasticity and gust response of HARW however, focuses mainly on High Altitude Long Endurance (HALE) aircraft and very few studies focus on the application of HARW to commercial aircraft. Calderon et al. [28] carried out a work on the non-linear sizing of a generic medium haul size aircraft. Industrial applications are found in the NASA-Boeing Subsonic Ultra Green Aircraft Research (SUGAR) aircraft [25, 3] (see Figure 2.7), a truss braced wing HARW aircraft [24]. It is worth to stress the adopted struts [21] to limit the flexibility of the wing while retaining the aerodynamic benefit of HARW configuration.

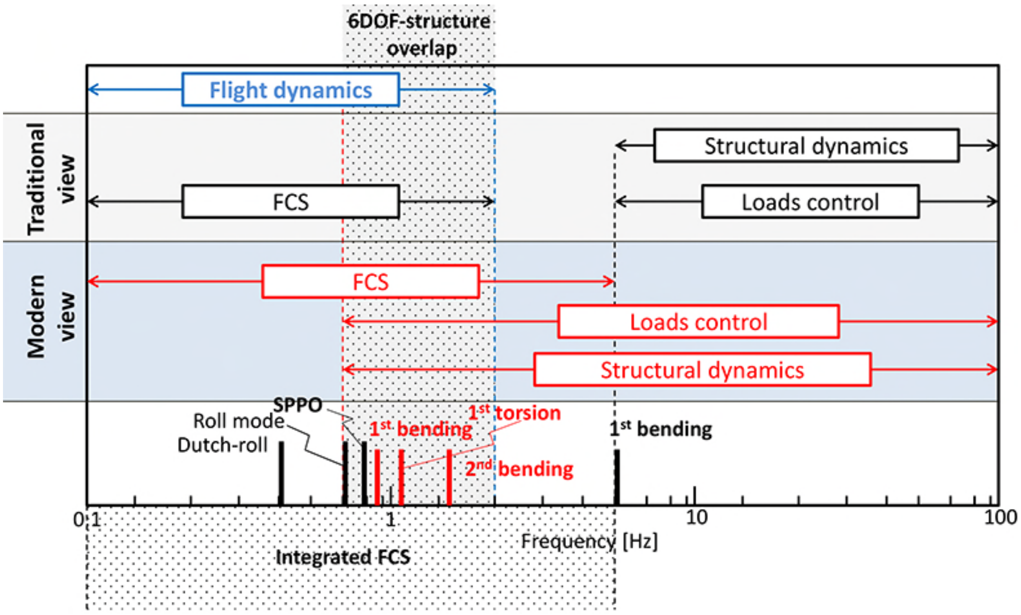

Fig. 2.5.: Structural flexibility impact on aircraft flying qualities and control systems.

The literature presented in this section showed that the main challenge associated with adopting HARW is the reduction of structural natural frequencies due to the increased flexibility of the wing structure. In fact, whenever this happens, the structural dynamics couples with the rigid-body dynamics impacting the dynamic response of the aircraft (Figure 2.5). In such a case, in order to model the flexible aircraft dynamic response, the Equation of Motions (EoMs) must consider the contribution of the structural dynamics and the response of the aircraft may differ from the one of the same vehicle assumed with a rigid structure.

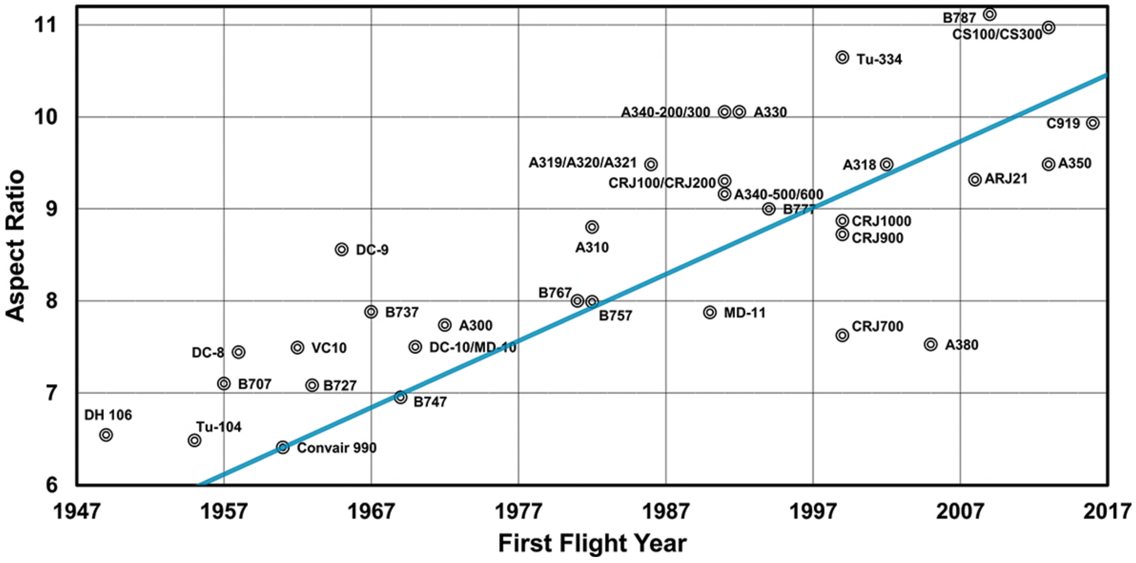

Fig. 2.6.: Aspect ratio wing trends over the years [79].

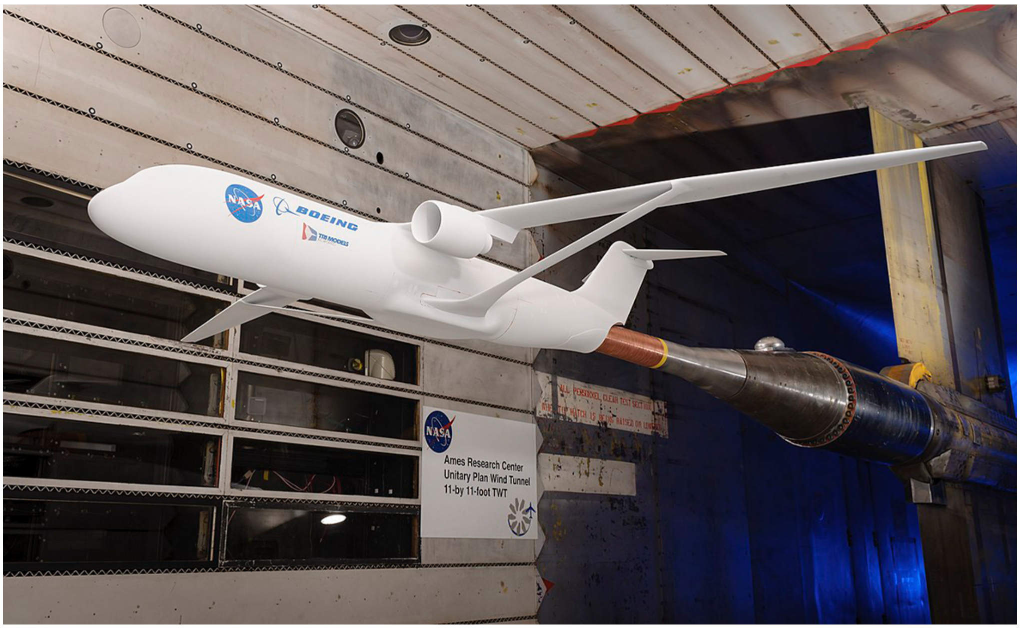

Fig. 2.7.: NASA-Boeing SUGAR aircraft in its wind tunnel configuration (source nasa.gov, reproduced from commons.wikimedia.org)

2.3 Rigid-body and flexible structure dynamics interaction

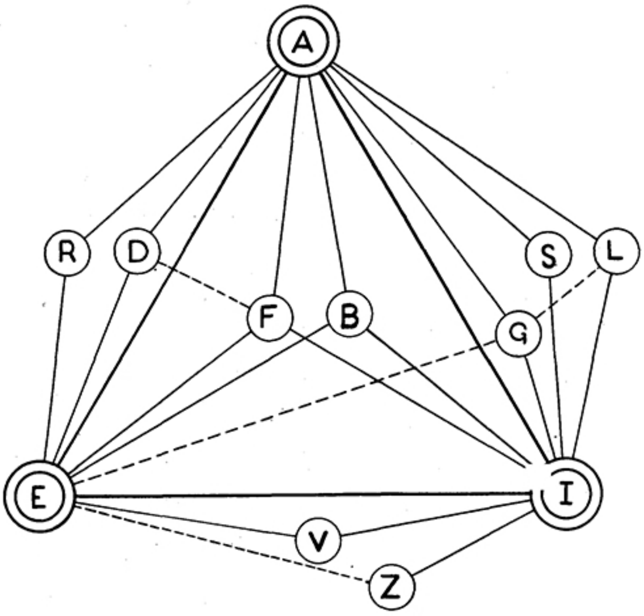

Fig. 2.8.: The Collar's triangle. A: aerodynamic forces, E: elastic forces, I: inertia forces, F: flutter, S: stability and control, G: gust, D: divergence, B: buffeting, R: control reversal, L: loading problems, V: mechanical vibration, Z: impacts (Reproduced from [43]).

The effect of the interaction between elastic, inertia and aerodynamic forces is a problem that has been known since the birth of aviation. However, it was in 1946 when Collar defined clearly the aeroelastic boundaries and the instabilities that derive from the possible interaction of the these three forces [43]. Referring to Figure 2.8, phenomena like flutter or buffeting are defined as the interaction of all three components, while divergence or gust for example lies outside the triangle as result of the interaction of only two of the forces. When looking at flexible structures like HARW, the interaction between the aeroelastic components is even stronger and the results of their interaction might lead to worsening of the aircraft performance. The adoption of HARW, as said, increases the flexibility of the structure, reducing the structural natural frequencies. When the structure is not rigid *enough* the separation of the rigid and flexible dynamics might not be evident and their interaction possible [134].

A typical example of interaction between inertial, aerodynamic and elastic forces is represented by flutter. Flutter can be considered as the most important aeroelastic phenomenon [187]. It is defined as an unstable self-excited vibration where the aerodynamic loads associated with two (or more) natural modes couple together often resulting in catastrophic structural failure [187]. Due to its critical impact on the wing design, flutter is already part of the standard wing design loop [22, 153, 187]. In fact, flutter instability and the development of Active Flutter Suppression (AFS) systems have been investigated since the end of World War II. Studies on flutter suppression have been done throughout the years. A non-exhaustive list of investigated aircraft includes the B-2 [26], B-52 [171, 149] and DC-10 [186].

However, when considering very flexible structures, such phenomena become even more severe. Mykes et al. [189] investigated the implementation and the impact of an active control system to damp structural motion of the flexible structure on the B-1 aircraft. Figure 2.9 shows that the control system implemented control vanes placed on the nose of the aircraft

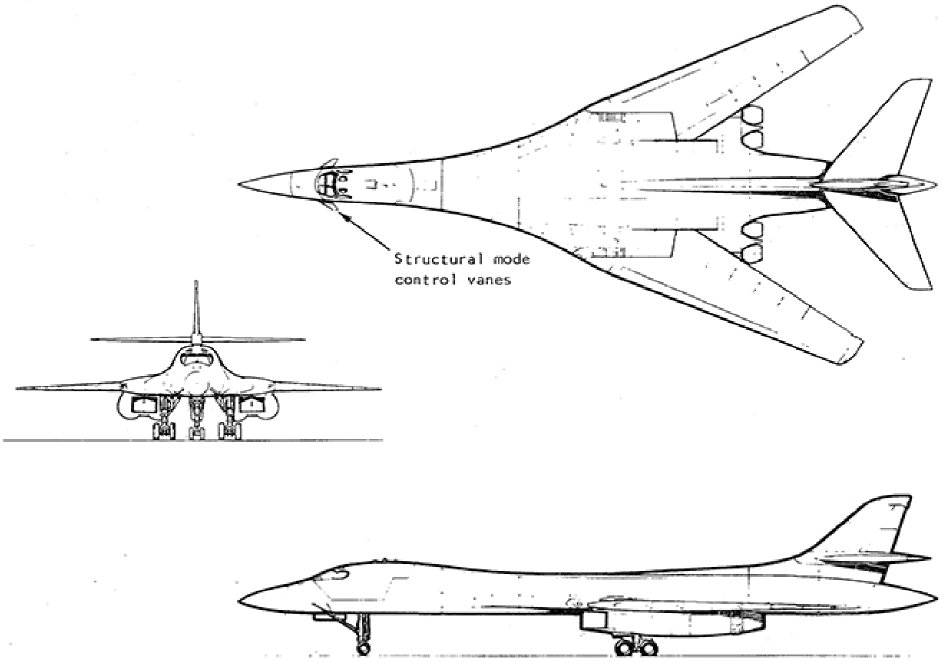

Fig. 2.9.: Development of the structural mode control system on the B-1 aircraft (reproduced from [189])

able to rotate around the vane-axis. The system proved to be effective and able to damp the fuselage bending mode both in subsonic and supersonic design speeds. Mykes investigated as well the design of a Stability Augmentation System (SAS) and GLA system for the flexible XB-70 aircraft [190]. The system successfully reduced the structural load and fatigue. In more recent days, the focus of flexible structural dynamics shifted to High Altitude Long Endurance (HALE) vehicles [158, 126]. The purpose of these aircraft is to fly as long as possible to meet requirements for environmental sensing, military and civil reconnaissance [161]. The solution adopted for the long endurance flight has been to look for the highest aerodynamic efficiency possible, which leads to an ultra HARW vehicle [178]. Such wing configuration was responsible as well for large structural deformations and rigid body and flexible dynamics interaction. In the Unmanned Aerial Vehicle (UAV) field the X-56 programme represents as well an important source of study for rigid-body dynamics and structural dynamics interaction. The X-56 aircraft is a flight research vehicle developed by Lockheed Martin Skunkworks as testbed for elastic aircraft control research (Figure 2.10). The X-56 particularly focused on vehicles with low pitch inertia and highly flexible wings (such as flying wings). This might lead the specific aircraft to have high short-period frequencies that can couple with the lowest wing-bending frequencies producing instabilities [105]. An example is the work done by Jones et al. [85] who developed a linear mathematical model of the X-56 to investigate aeroelastic instabilities such as flutter or elastic-rigid-body coupling. More work on the investigation of flutter onset of the X-56 aircraft can be found in Reference [27].

Fig. 2.10.: The Lockheed Martin X-56 (reproduced from [105]).

It is clear then the rigid EoMs are not able to represent the aeroelastic coupling of the rigid-body and flexible dynamics due to the lack of a model of the flexible dynamics. Van Schoor et al. [176] pioneered the field when they recognized the need to couple structural dynamics with rigid body dynamics. Van Schoor modelled the augmented flexible EoMs of a human-powered ultra flexible vehicle following a modal approach for structural dynamics. The coupling between the structural dynamics and the rigid body dynamics was made possible through the right-end term of the rigid equation of motions, i.e the force term. The following stability analysis showed the deterioration of the longitudinal dynamics due the impact of the flexible structure dynamics.

Waszak and Schmidt [179, 181, 180] investigated the development of flexible EoMs for the Rockwell B-1 bomber. The coupling of the two dynamics was made by introducing a new vector of generalised coordinates, $\bar{q}$ (where rigid and flexible dynamics were merged together) to use into the Lagrangian equations for evaluating the flexible EoMs. The vector was given as:

$$\bar{q} = \left[x, y, z, \phi, \theta, \psi, \eta_1, ..., \eta_N\right] \tag{2.3}$$

where the vector $[x, y, z, \phi, \theta, \psi]$ represents the rigid body displacements and rotations, while η_i is the generalised displacement, calculated as:

$$\ddot{\eta}_i + \omega^2 \eta_i = \frac{Q_{\eta_i}}{M_i} \quad \textit{for i =1,...,N} \tag{2.4}$$

where Q_{η_i} and M_i are the generalised forces and masses respectively. The new set of flexible EoMs then included the standard 6 rigid EoM and N new flexible equations able to represent the dynamics of the structure. The coupling between the two sets was again made through the aerodynamic forces and moments.

A similar approach was derived by Wright and Cooper [187] who extended the EoMs to a flexible structure. The work assumed small structural displacements and flexible contribution only in z direction, defined as:

$$z_f(x, y, t) = \Omega_f(x, y)\bar{q}_f(t) \tag{2.5}$$

where Ω_f is the mode shape defining the modal displacement in z, $\bar{q}_f$ is the corresponding generalised coordinate and the subscript f indicates the flexible term. After some manipulations, Wright and Cooper defined the acceleration in x and z direction including the flexible contribution as [187]:

$$a_x = \dot{u} + wq - x_r q^2 + (z_r + z_f) + 2\dot{z}_f q \tag{2.6}$$

$$a_z = \dot{w} - uq - (z_r + z_f)q^2 - x_r \dot{q} + \ddot{z}_f \tag{2.7}$$

where the subscript r indicates the rigid term. The overall EoMs including the flexible terms can therefore be described as [187]:

$$\left[\begin{array}{cc|c} m & 0 & 0 \\ 0 & I_y & 0 \\ \hline 0 & 0 & m_f \end{array}\right] \left\{\begin{array}{c} \dot{w} \\ \dot{q} \\ \hline \ddot{q}_f \end{array}\right\} + \left[\begin{array}{cc|c} 0 & -m u_f & 0 \\ 0 & 0 & 0 \\ \hline 0 & 0 & c_e \end{array}\right] \left\{\begin{array}{c} w \\ q \\ \hline \dot{q}_f \end{array}\right\} + \left[\begin{array}{cc|c} 0 & 0 & 0 \\ 0 & 0 & 0 \\ \hline 0 & 0 & k_f \end{array}\right] \left\{\begin{array}{c} \int w \\ \int q \\ \hline q_f \end{array}\right\} = \left\{\begin{array}{c} Z \\ M \\ \hline Q_{ext} \end{array}\right\} \tag{2.8}$$

where the effect of the flexible structure is reflected in the addition of a new set of equations dedicated to solve the dynamics of the flexible generalised coordinate.

Cook's derivation of the aircraft's EoMs [45] took account of the flexibility of the aircraft while defining the speed of a generic point *p(x,y,z)* of the body as:

$$u = \dot{x} - r y + q z \tag{2.9}$$

$$v = \dot{y} - pz + rx \tag{2.10}$$

$$w = \dot{z} - qx + py \tag{2.11}$$

where the flexible contribution lies in the acceleration term *d/dt [x,y,z]*. Such term is then developed in the EoMs derivation in the Newtonian form:

$$\sum \vec{F} = \sum (m\vec{a}) \tag{2.12}$$

$$\sum \vec{M} = \sum \left(I\dot{\vec{\omega}} \right) \tag{2.13}$$

where $\vec{F}$ is the force vector, $\vec{M}$ is the moment vector and $\dot{\vec{\omega}}$ the angular acceleration vector. Portapas [134, 135] derived the full set of EoMs developing further Cook's EoMs following the same approach and investigated the impact of the flexible terms on the aircraft overall dynamic and static response. The extended formulation of EoMs derived by Portapas was given as [134]:

$$\begin{aligned} \vec{F} = {} & \overbrace{\dot{\vec{v}}_0 \sum_{i=1}^{N} \delta m_i + \vec{\bar{\omega}}_0 \times \vec{v}_0 \sum_{i=1}^{N} \delta m_i}^{rigid} + \overbrace{\vec{\bar{\omega}}_0 \times \left(\vec{\bar{\omega}}_0 \times \sum_{i=1}^{N} \delta m_i \vec{r}_i \right) + \dot{\vec{\bar{\omega}}}_0 \times \sum_{i=1}^{N} \delta m_i \vec{r}_i +}^{flexible} \\ & + \overbrace{\sum_{i=1}^{N} \delta m_i \ddot{\vec{r}}_i + 2\vec{\bar{\omega}}_0 \times \sum_{i=1}^{N} \delta m_i \dot{\vec{r}}_i}^{flexible} \end{aligned} \tag{2.14}$$

$$\begin{aligned} \vec{M} = {} & \overbrace{\vec{\bar{\omega}}_0 \times \left(I\vec{\bar{\omega}}_0 \right) + I\dot{\vec{\bar{\omega}}}_0}^{rigid} + \overbrace{\sum_{i=1}^{N} \delta m_i \vec{r}_i \times \dot{\vec{v}}_0 + \sum_{i=1}^{N} \delta m_i \vec{r}_i \times \left(\vec{\bar{\omega}}_0 \times \vec{v}_0 \right) + \sum_{i=1}^{N} \delta m_i \vec{r}_i \times \ddot{\vec{r}}_i +}^{flexible} \\ & + \overbrace{\dot{I}\vec{\bar{\omega}}_0 + \vec{\bar{\omega}}_0 \times \delta m_i \left(\vec{r}_i \times \dot{\vec{r}}_i \right)}^{flexible} \end{aligned} \tag{2.15}$$

where $\dot{\vec{v}}_0$ is the velocity vector, $\vec{\bar{\omega}}_0$ is the angular velocity, $\vec{r}$ is the generic point p distance from the aircraft CoG and m is its associated mass. Coupling between structural dynamics and aerodynamics is modelled through the left-hand side term of the Equations 2.14-2.15, where aerodynamic forces and moments are evaluated. Comparison between the rigid and flexible-extended EoMs showed that while for trimming the aircraft the impact of the flexible terms was negligible, the dynamic response of the flexible structure requires the use of the flexible terms in the equations to evaluate correctly the magnitude of the response. In fact Portapas found that when flexible terms are neglected, the response of the structure is underestimated [134].

Another approach to account for flexibility is to use the same linear EoMs that model the rigid body aircraft dynamics while applying corrections to the aerodynamic stability derivatives [105]. The corrections account for fuselage flexibility as well as control surfaces effectiveness, dihedral and neutral point position. Correction coefficients are usually evaluated through wind tunnel tests. Examples can be found in References [83],[132], [150].

From the literature presented in this chapter it is clear that the modelling of flexibility is essential for evaluating the dynamic and static response of the HARW aircraft. Therefore, within the work done in this study, the HARW EoMs will be modelled including the flexible component of structural dynamics. Limitations of the modelling will be assessed as well through a wind tunnel test campaign on flexible wind tunnel models.

2.3.1 Computational aeroelastic frameworks

Once the set of flexible EoMs is derived, they are usually included in an aeroelastic framework to simulate and evaluate the coupled response of the flexible aircraft. Frameworks can be linear or non-linear in both structures and aerodynamics. A system response is generally characterised as linear when an increase in the input causes a response linearly proportional to the magnitude of the input [52]. Source of structural non-linearities for the HARW are [2]: i) geometric, where the change in the initial geometry of the structure affects the system response, ii) damping, when the relating damping forces alter the system response and iii) material, when the the material undergoes into plastic deformation and produces an unpredictable non-linear response of the system. Considering non-linear effects induced by the flexible structure implies to reconsider the load distribution in the context of the new wing deformed shape [28]. Structural deformation of the wing leads to some of the aerodynamic non-linear effect such as: [2] the flow separation due to the local increase of angle of attack or structure-wake coupling due to the large deformation of the aircraft. An application of non-liner modelling is shown by Calderon et al. [28]. The study included geometric non linearities for the wing sizing of HARW commercial aircraft. Results show the impact of non-linear modelling affects the wing mass, leading to a 5% mass saving on the wing structure.

Several publications are available in the literature describing computation frameworks able to reproduce the aeroelastic response of flexible aircraft. The fidelity of these tools however depends on their case application. Commercial and industrial framework are high fidelity system that include Computational Fluid Dynamics (CFD) to model aerodynamics and Computational Structural Modelling (CSM) to model structures [61]. To reproduce the rigid-flexible coupling typical of aeroelastic systems, CFD and CSM can be coupled together. Results though are obtained at a high computational cost.

Low/medium fidelity tools are available as well to approach aeroservoelastic analysis of HARW. Advantage of such tools lies mainly in their limited requirement of computational power. Example of such models are:

- ASWING framework [54, 53] proposed by Drela and used for preliminary flexible aircraft design. The framework incorporates non-linear beam model for structures and Unsteady Vortex Lattice Method (UVLM) for aerodynamics with compressibility corrections. Gust modelling is also provided. The framework was successfully used by

Love et. al [110] to assess the aeroelastic response of the high aspect ratio flying wing SensorCraft.

- The UN/NAST was developed by Cesnik et al. [38, 162]. The structure is modelled as strain based non-linear beam formulation and the aerodynamics is defined by the finite-state unsteady subsonic model. The model was used by Su et al. [162] to validate the numerical prediction of the aeroelastic response of a slender wing against wind tunnel test data.
- The Cranfield Accelerated Aircraft Load (CA^2LM) which incorporates reduced order modal solver to compute structural deformations and state-space unsteady aerodynamic modelling coupled with strip theory [6, 5, 135].

Every of the listed framework, as well as the ones not mentioned in this short description, presents benefits and drawbacks. Some of them include and focus on the modelling of structural non-linearities [54, 53], while others focus more on other aspects such as aerodynamic non-linearities. Therefore, the right choice for the adoption of the aeroelastic framework strictly depends on the aim of the study. The CA^2LM framework focuses on the flight dynamics aspect of the aircraft performance, while still providing data on structural dynamics and aerodynamics. This nicely fit with the aim of this work, as discussed in Chapter 1.1, which focuses on the flight dynamic response of HARW aircraft. As well, the CA^2LM framework was chosen as the core of the flight simulator activity of the project within which this study develops. For all these reasons, the CA^2LM framework was chosen as the reference aeroelastic framework for this work.

However, CA^2LM is a low fidelity model and the implementation of highly non-linear devices like spoilers was not included. In order to be able to design GLA systems, as the aim of this work, spoilers must be modelled, as one of the control surfaces adopted for load alleviation purposes. However, their use is minimal due to the use of inboard and outboard ailerons. When considering highly flexible wings however, effectiveness of ailerons could be jeopardised by the vertical displacement of the outboard portion of the wing. Spoilers are instead distributed along the wing and therefore less sensible to the tip deformation. Hence, spoilers may be good candidates for GLA in highly flexible wings. In order to explore the impact of spoilers for load alleviation, they were modelled in CA^2LM as part of the development of the framework. In the next section, an overview of the experimental data collected for describing spoiler aerodynamics and modelling techniques adopted to simulate the spoiler effect is provided.

2.3.2 Spoiler modelling

Spoilers are secondary control surfaces that impact the lateral-directional dynamics of the aircraft, and used for roll control, load alleviation and as airbrakes. They are usually located on the top surface of the wing and their deflection results in a local controlled [113] loss in lift and an increment in drag. Spoilers can be divided by deployment mechanism (flat-

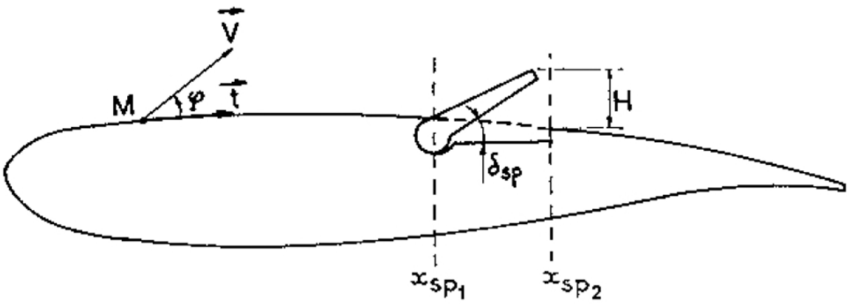

Fig. 2.11.: Sketch of a wing profile section with spoiler (reproduced from [113]).

plate, circular-arc or lower-surface) or by geometry (perforated, segmented, hinge-line gap and notched). Most of the work on the spoilers aerodynamics and modelling was done over the 1970s and 1980s, as spoilers were thought able to be included in aircraft flight control systems along with ailerons [113] to improve lateral-directional controllability of the aircraft as spoilers can as well be used at any speed. On the flight dynamic aspect, spoilers eliminate the adverse yaw, and prevent the excessive excitation of the Dutch roll mode [151].

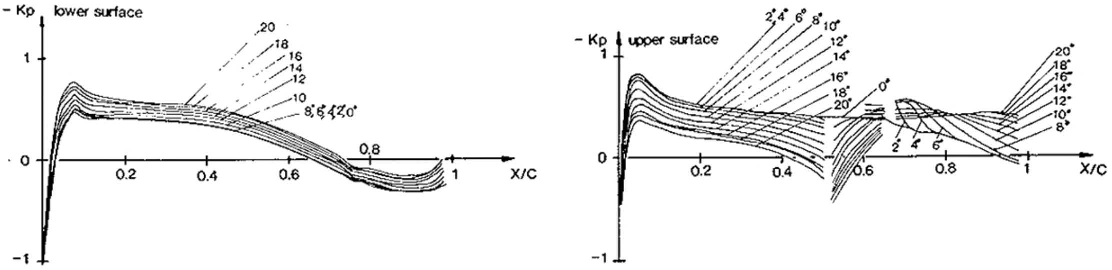

Fig. 2.12.: Profile pressure distribution for different spoiler deflection angles (reproduced from [113]

Due to their highly non-linear nature, spoilers are commonly characterised by experimental wind tunnel tests. An example of the impact of the spoiler on the wing flow dynamics is shown in Figure 2.12. In this case the spoiler is placed at $0.51c$, where c is the chord, for $\mathrm{Ma} = 0.3$. For small angles of deflection the interference of the spoiler is limited to the area strictly behind the spoiler itself. From deflection greater than 8 deg instead, the flow is fully separated downstream the spoiler and results in a reduction of the lower surface pressure as well through the LE. Consigny et al. [44] tested experimentally spoilers for multiple configurations and chord position and deflection angle in order to estimate aerodynamic coefficients. Results showed that spoilers have a large impact on the aerofoil unsteady pressure distribution and that the local lift depends on the spoiler deployment. Effectiveness of the device depends on the deployment angle: the higher is the angle, the higher is the lift reduction. However, it was found that below a certain angle (functions of the test conditions), the impact of the spoiler is negligible.

Work in the effort of modelling spoilers within a numerical framework was done by ONERA [47]. The aerodynamic characteristics of a two-dimensional aerofoil equipped with spoilers were estimated by using non-linear codes. Results proved the difficulties in modelling such non-linear devices. In fact, while the trend of lift and drag is the same showed by experimental results for spoilers placed far from the leading edge, quantitative data comparison provided a large error between the numerical and the experimental datasets. However, for small deflections, numerical results are in agreement with experimental ones. Mack et al. [113] proposed a method for spoiler modelling where lifting-surface theory is used to model the spoiler and two-dimensional experimental data are used to correct the result. Experimental data are collected and provided by ESDU [167, 168] or by Wentz et al. [185] in the form of aerodynamic coefficients.

The approach pursued in this work in order to overcome limitations in the spoiler modelling is to merge theoretical and empirical models. The idea is to *correct* the aerodynamic load evaluation done by using strip theory at spoiler location through the empirical data provided by the ESDU datasheet when spoilers are deflected. In this way, the benefit of using strip theory can be retained while the local non-linear impact of spoilers can be modelled within the same framework. The spoiler modelling is discussed in detail in Chapter 8.

2.4 HARW flight dynamics

Flight dynamics instabilities can be associated with the occurrence of large deformations coupled with aerodynamic non-linear effects. For HARW structures though, large deformations are not only expected in specific load scenarios like manoeuvring or gust encounter, but under normal trim conditions as well. An example of this behaviour is the crash of the HALE Helios aircraft (Figure 2.13). Investigation showed that after the aircraft encountered a turbulence, the vehicle morphed in an unexpected high dihedral configuration, which led to an unstable pitch motion. The new attitude though caused the aircraft to fly exceeding the maximum airspeed resulting in the crash of the aircraft [123], showing a strong interaction of structural and rigid body dynamics.

Fig. 2.13.: HALE Helios aircraft (source nasa.gov, reproduced from commons.wikimedia.org).

Therefore, flight dynamics modes are as well affected by structural flexibility. Longitudinal and lateral-directional modes can be excited by external inputs, such as pilot or environmental inputs, which can causes changes in the airframe configuration [45]. Subject to these inputs, when the wing structure is highly flexible, it may undergo large deformation, coupling with the rigid body dynamics and leading to unstable attitude of the aircraft. Patil [126] investigated the impact of such large deformations on the HALE aircraft suggesting that deflections could change the aerodynamic load distribution and the overall dynamic behaviour of the aircraft. In particular, the flutter speed of the HALE was reduced because of the non-linear coupling and the flight dynamics characteristics (such as phugoid mode and trim point) were as well affected.

The analysis on HALE vehicles showed that flight dynamics instabilities could occur when also considering the trim shape of the aircraft. For very flexible aircraft, the airframe of the vehicle can assume an U-shape configuration, impacting the aeroelastics [125]. In fact, when the reduced order model is based on a modal approach, the set of the structural mode shapes used for the numerical evaluation of the response cannot be extracted by the unloaded, straight shape as they would not consider the material or geometrical non-linearities introduced by the deformed structure. U-shape configuration are not actually related to general aviation. In fact, for commercial aircraft, the current *most flexible* wing structure on the market is the Boeing 787 Dreamliner [51]. For this aircraft, the 1 g deflection corresponds to 12% of the wing semispan, while the ultimate load deflection is 25% of the wing semispan.

The impact of higher *AR* is reflected in the values of aerodynamic stability derivative as well. The stability derivatives are coefficients that describe the influence of motion, control and power variable on the aerodynamic terms within the linearised EoMs framework. Stability derivatives are derived by expanding the aerodynamic term as a sum of Taylor series [45]. Assuming the generic aerodynamic term X_a to be function of the motion variable *(p,q,r)* and *(u,v,w)*, X_a can be expressed as [45]:

$$\begin{aligned} X_a = X_{a_e} &+ \left(\frac{\partial X}{\partial u} u + \frac{\partial^2 X}{\partial^2 u} \frac{u^2}{2!} + \frac{\partial^3 X}{\partial^3 u} \frac{u^3}{3!} + \dots \right) \\ &+ \left(\frac{\partial X}{\partial v} v + \frac{\partial^2 X}{\partial^2 v} \frac{v^2}{2!} + \frac{\partial^3 X}{\partial^3 v} \frac{v^3}{3!} + \dots \right) \\ &+ \left(\frac{\partial X}{\partial w} w + \frac{\partial^2 X}{\partial^2 w} \frac{w^2}{2!} + \frac{\partial^3 X}{\partial^3 w} \frac{w^3}{3!} + \dots \right) \\ &+ \left(\frac{\partial X}{\partial p} u + \frac{\partial^2 X}{\partial^2 p} \frac{p^2}{2!} + \frac{\partial^3 X}{\partial^3 p} \frac{p^3}{3!} + \dots \right) \\ &+ \textit{series in } q, r, \dot{u}, \dot{v}, \dot{w}, \dot{p}, \dot{q}, \dot{r} \end{aligned} \tag{2.16}$$

Since the perturbations are assumed to be small, the first order term is the most significant and all the other terms can be ignored. Therefore, Equation 2.16 can be written as:

$$X_a = X_{a_e} + \frac{\partial X}{\partial u} u + \frac{\partial X}{\partial v} v + \frac{\partial X}{\partial w} w + \frac{\partial X}{\partial p} p + \frac{\partial X}{\partial q} q + \frac{\partial X}{\partial r} r + \frac{\partial X}{\partial \dot{w}} \dot{w} \tag{2.17}$$

where X_{a_e} is the equilibrium value and the term $\frac{\partial X}{\partial \cdot} = \mathring{X}_{\cdot}$ is called a stability derivative. The impact on HARW is mostly on the lateral stability derivatives as longer wings increase the roll inertia of the aircraft moving more mass away from the CoG. For example, the rolling moment due to roll rate $\mathring{L}_p$ can be written as [45]:

$$\mathring{L}_p = -\frac{1}{Sb}\int_0^s (a_y + C_{D_y}) c_y y^2 dy \tag{2.18}$$

where a_y is the local lift coefficient slope. Focusing on the constant term only, it is clear that if the wingspan b increases, the roll damping increases as well and the impact on the rolling moment is greater.

Furthermore, a higher *AR* affects the longitudinal dynamics as well. In fact, the damping associated with the phugoid mode can be written as:

$$\zeta_p \cong \frac{1}{\sqrt{2}} \frac{C_D}{C_L} \tag{2.19}$$

Thus the phugoid damping is inversely proportional to the aerodynamic efficiency. Recalling that increasing *AR* leads to a reduction in drag, hence higher L/D, HARW are characterised by higher phugoid damping values.

2.5 HARW gust load alleviation

Gust loads are among the flight conditions needed for further investigations as they are able to increase considerably the aerodynamic load on the structure. Any gust condition, either discrete gust or continuous (also known as turbulence), results in a change of angle of attack, as shown in Figure 2.14 for upwards gust. The variation in lift due to the change in angle of attack is given as [80]:

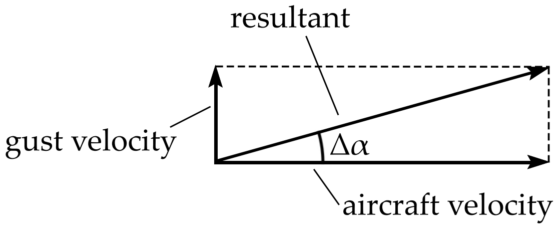

Fig. 2.14.: Gust velocity triangle and $\Delta\alpha$.

$$\Delta L = \frac{\rho}{2} V^2 S C_{L_\alpha} \Delta\alpha = \frac{\rho}{2} V^2 S C_{L_\alpha} \frac{w_g}{V} \tag{2.20}$$

where w_g is the gust velocity, S is the wing surface, ρ is the density and V the aircraft speed.. The extra lift results in a change of the vertical load factor n_z as:

$$\Delta n_z = \frac{\Delta L}{W} = \frac{\frac{\rho}{2} w_g V C_{L_\alpha} S}{W} \tag{2.21}$$

Once the aircraft is hit by the gust, it reacts in two different steps: 1) the aircraft translates vertically in the direction of the gust velocity due to the sudden change of angle of attack. The motion adds another component to $\Delta\alpha$ as[187]:

$$\Delta\alpha \approx \frac{w_g + \dot{z}_c}{V} \tag{2.22}$$

where $\dot{z}_c$ represents the vertical acceleration of the aircraft. Following the plunge, the aircraft sees a brief pitch increment in the gust direction. Due to its natural pitch stability 2) the aircraft pitches opposite to the gust as to counterbalance the $\Delta\alpha$.
A typical gust profile can be represented as a Gaussian random process with a normal Gaussian distribution as follows [80]:

$$p(y) = \frac{1}{\sqrt{2\pi}\sigma_y} e^{-\frac{1}{2}\left(\frac{y}{\sigma_y}\right)^2} \tag{2.23}$$

where y represents the gust intensity and σ_y is its root-mean-square. Figure 2.15 shows a typical velocity profile for a continuous gust represented by Equation 2.23. The same figure as well shows the idealization of the gust structure made using the discrete gust model *1-cosine*. For the purpose of this study, only the response under *1-cosine* gust load is assessed. The *1-cosine* gust definition is provided by the aviation regulator. The European Aviation Safety Agency (EASA) provides specifications in the Certification Specification CS-25 for Large Aircraft documentation. To define the gust profiles for the presented study, definition of the gust is taken as defined by CS-25 datasheet[9]. The discrete gust design criteria for sizing the structure under gust loads defines the shape of the gust as:

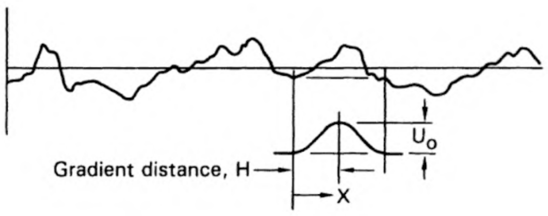

Fig. 2.15.: Continuous and discrete gust profiles[80].

$$U = \begin{cases} \frac{U_{ds}}{2}\left[1 - \cos\left(\frac{\pi s}{H}\right)\right] & for \quad 0 \leq s \leq 2H \\ 0 & for \quad s > 2H \end{cases} \tag{2.24}$$

where s is the distance penetrated into the gust and H is known as the gust gradient and it is the distance parallel to the aircraft's flight path where the gust reaches the maximum velocity. The term U_{ds} is the design gust velocity and it is given as follows:

$$U_{ds} = U_{ref} F_g \left(\frac{H}{107}\right)^{\frac{1}{6}} \tag{2.25}$$

where U_{ref} is the reference gust velocity defined as 17.07 m/s (56 ft/s) at sea level reduced linearly to 13.41 m/s (44 ft/s) at 4572 m (15000 ft). The reference gust velocity is further reduced linearly from 13.41 m/s (44 ft/s) at 4572 m (15000 ft) to 6.36 m/s (20.86 ft/s) at 18288 m (60000 ft). The term F_g is the profile alleviation factor, defined as follows:

$$F_g = 0.5\left(F_{gz} + F_{gm}\right) \tag{2.26}$$

where

$$F_{gz} = 1 - \frac{Z_{mo}}{25000}[ft] \tag{2.27}$$

$$F_{gm} = \sqrt{R_2 \tan\left(\frac{\pi R_1}{4}\right)} \tag{2.28}$$

$$R_1 = \frac{MLW}{MTOW} \tag{2.29}$$

$$R_2 = \frac{MZFW}{MTOW} \tag{2.30}$$

and Z_{mo} as the maximum operative altitude.

The gust model proposed by the CS-25 specification assumes the gust profile uniformly distributed over the wingspan. When considering high aspect ratio wings instead, the distribution of the gust velocity profile might impact the evaluation of the maximum load. Lone et al. [108] found that when considering a non-uniform spanwise distribution of the gust on flexible aircraft, the derivation of the gust load envelope might differ from the one calculated by following CS-25 requirements. Cook et al. [46] investigated the worst case gust scenario for flexible wings aircraft modelling the gust velocity profile combining vertical and lateral gust velocities through a round-the-clock approach. Results in this case showed that the new approach do not generally lead to a worsening of the aeroelastic load induced by the gust. Results from these two works are in contradiction and suggest that the need or not to consider a non-uniform gust might depends on the aircraft configuration and structure. For the purpose of this work the gust profile is assumed to be constant along the span.

The increase of the angle of attack will induce an extra load on the structure, mostly on the the wing. Hence the need of a system able to alleviate the induced load on the wing. The design of GLA for flexible wing structure is object of a variety of different approaches. The simplest one is to design the GLA as a PID controller [142]. Such system usually read the state by relying on accelerometers placed on the wing surface. Ricci et al. [142] designed a simple PI controller to alleviate the WRBM of a HARW wind tunnel model. The feedback controller was based on the reading of accelerometers [67] on the wing and the use of aileron only. The system was able to reduce the WRBM by 9% in the tested case. The limited reduction of the WRBM is linked to the fact that the controller cannot *anticipate* the gust. In fact, reading the acceleration at the wing station implies to activate the controller when the gust already hit the wing. Therefore, due to the time lag between the accelerometer reading and the control surfaces full deployment, the controller is unable to fully capture the gust dynamics. To overcame this problem, the use more complex controllers was evaluated.

The key feature to include to overcome the time-lag problem is the possibility to predict the gust profile before the gust hit the wing. In general, the challenge of using a feedback controller is that rigid-body motion and structural dynamics are tracked separately and separated by the use of notch filter. However, the flexibility of HARW structures makes the design of a controller more difficult to implement [76]. One solution might be to use the Light Detecting and Ranging (LIDAR) sensor. Such system can measure the airflow dynamics and be used to detect gust up to 100 m ahead of the aircraft nose [140]. Rabadan [140] provided flight test data of Airbus A340-300 featuring LIDAR technology proving that the system is able to scan effectively 50 m ahead of the aircraft nose, sensing the gust 300 ms ahead of when it hit the wing. As well a possible use of the LIDAR is using the Model Predictive Control (MPC) [68]. MPC uses a model of the plant in the effort of predicting its behaviour in n step ahead in the future. MPC can handles MIMO systems and deal with constraints. The use of MPC for gust load alleviation might be advantageous when considering non-linear plants and when inputs must be constrained [75]. Application of GLA with use of LIDAR can be found in Reference [72, 65, 75, 76, 159]. Giesseler et al. [72] successfully applied LIDAR technology to predict the gust income 50 m ahead of the nose in a MPC controller based GLA system. Results showed that the MPC was able to alleviate the WRBM considerably (up to 50%) as able to deploy control surfaces ahead of the wing hitting the gust. Problems with the use of MPC are the high computational power required to estimate the missing states and to predict the plant behaviour [72, 75].

Other controllers for GLA are Linear Quadratic Regulator (LQR) [119] or Static Output Feedback [67]. For a more futuristic approach, devices like folding wing-tip can be used to alleviate the load [34, 33].

Common choice for control surfaces in GLA systems are ailerons [142] and spoilers to alleviate the gust, and elevator to account for the aircraft attitude [67]. The benefit of using ailerons is clear. In fact, by deflecting symmetrically ailerons upwards, the GLA system can shift the extra load induced by the gust towards the root of the aircraft. Spoilers instead are distributed along the wing, usually from 15% to 75% of the wingspan [153] and their benefit is less evident as closer to the wing root. A second aspect to consider is that spoilers can only deflect on the up surface of the wing, so that the effect on downwards gust speed would be null. For GLA purposes then, only outer spoilers are used [71] while inboard spoilers are maintained for their function as air brakes.

All the control strategies described in this section are based on closed-loop control systems that may be harder to certify and expensive for the manufacturer to test. In fact, several aspects of closed-loop control systems are considered critical for a system such as an aircraft: the sensitivity of the system to the parameter change, the stability of the closed-loop system

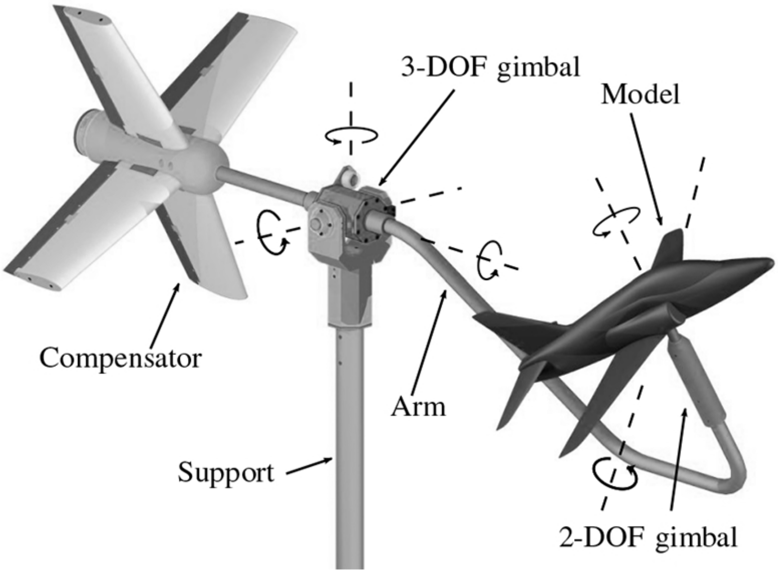

Fig. 2.16.: Bristol 5-DOF dynamic rig (reproduced from [130]).

or the ability of disturbance rejection. For this reason, this study focuses on an open-loop control system that may be more effective for the aviation use.

2.6 Flexible wind tunnel models and testing

Flexible wing models of high aspect ratio wing are usually tested in the wind tunnel mainly to validate codes in the non-linear region of structures and aerodynamic modelling. Focus is on the need of aeroelastic validation of the model [104, 163] due to the large displacements induced by the structural flexibility. The aim of this section is to focus on the manufacturing techniques and acquisition systems adopted to assess the response of high aspect ratio flexible wing models. To build the model in order to capture the potentially non-linear response of the wing, different manufacturing processes are applied to this new category of problems. However, the overlap of the rigid body dynamics and the flexible dynamics might impact the results when the model is constrained to the wind tunnel [161]. In fact, rigging the model on the wall, some of the model rigid degrees of freedom are suppressed. This aspect, when considering flexible structures, could interfere with the analysis of aeroelastic modes such as flutter as prevents the rigid-body/flexible interaction. In order to overcome this issue, dynamic rigs were developed to allow models to move freely in some of the degrees of freedom during the wind tunnel test. Gatto [70] developed a 3-DOF dynamic test rig that allows the aircraft model the roll, pitch and yaw degrees of freedom. The same author developed a second rig to perform heave manoeuvres while testing the model [69]. More complicated rigs were built, such as the 6-DOF rig designed and tested by Pattinson at Bristol University [129, 130, 128] (Figure 2.16), and later improved by Araujo-Estrada [17, 16], or the Cranfield 4-DOF dynamic rig [30, 29]. This aspect of the investigation however is beyond the scope of this work as the experimental test focused on the isolated wing structure.

Although the whole free-body dynamics of the aircraft cannot be reproduced, testing flexible models still plays a crucial role for investigating aerodynamic and structural properties of the wing. When building a model, in order to reproduce the aerodynamic, static and dynamic response of the full scale wing, the model must be able to reproduce one or more of these characteristics compared with the original wing [22]: the external aerodynamic shape, the stiffness distribution and the mass distribution. To account for these requirements, different methods can be applied to manufacture the model.

The wing structure can be reproduced in the same configuration of the full scale aircraft [15], made of a wing boxes covered by a shell [22]. This methodology introduces many difficulties both in the modelling and in the manufacturing of the wing and do not adapt well to the flexibility requirements for HARW flexible models. A second possible solution is to reduce the stiffness properties of the model to a ladder structure made of two spars, which provide the bending stiffness, connected by torque rods, responsible for the torsional stiffness [22]. Such configuration is still a valid experimental option [144, 145], but presents difficulties in aligning the elastic centres of the sections and it is not well suited to fit limited volumes such as the one available in a slender aerofoil typical of HARW configurations.

The most common solution is to reproduce the model structure as spar covered by a shell (or skin) to reproduce the aerodynamic shape. This configuration simplifies the process of overlapping the spar axis with the desired elastic axis of the model. In order to reproduce the external skin of the model, different solutions can be adopted: i) distribute ribs along the spar and cover the volume with shrinking plastic film [104, 74], fill the gap with wood [165, 163], to manufacture the external volume as one filled piece (usually foam) [144] or simply using composite materials [177, 143, 66].

When considering HARW models, one of the most important characteristics is the to reproduce the model as flexible in order to evaluate the structural response of the wing and its interaction with the aircraft dynamics in the bandwidth of interest. The literature provides some examples of flexible wing testing. Yi et al. [104] investigated the gust response of slender, flexible 1.5 m long wing to validate the modelling of geometric non-linearities. The aspect ratio of the wing is $AR = 25$. The model was built using an aluminium spar to provide bending and twist stiffness, while wooden ribs covered with plastic film were used to maintain the aerodynamic shape. However, Yi had to cut the film shell at several point to avoid additional stiffness effects introduced by the shell. During the test, the model went on high deformations (wing tip vertical displacement $>$ 25% of model span). While results of the test were in agreement with the numerical prediction, the use of film obliged the authors to cut the skin, interfering with the aerodynamics.

Tang et al. [163, 164] investigated the flutter boundaries and aerodynamic response of HARW models. Although the model accounts as HARW model ($AR = 17.7$), its chord length was 0.06 m circa, tested for a maximum speed of 35 m/s. The estimated Reynolds number was $1.3e5$. However, the manufacturing of the model consisted in an aluminium spar with multiple NACA 0012 flanges used to maintain the aerodynamic shape and increase the torsional stiffness. The gap in between flanges was filled with light wood. Authors recognized that flanges impacted on the mass and bending stiffness of the model. The same model was successfully used to investigate the gust response for HARW flexible models [165].

Within the context of the Air Force Research Lab project called SensorCraft, a 3.35 m long flexible model was tested in the NASA Langley Transonic Wind Tunnel [74, 177]. Again the model was built as a metal spar covered with an aerodynamic metal shell and equipped with accelerometers, gyroscopes, and a gust vane sensor placed in the front of the model. A force balance was placed at the root of the model to measure forces. The mass distribution of the wing was defined to reflect the dynamic response of the full scale aircraft. More examples on the spar and skin configuration can be found in the work done by Cecrdle [37], Ricci et al. [143] or Fonte et al. [66].

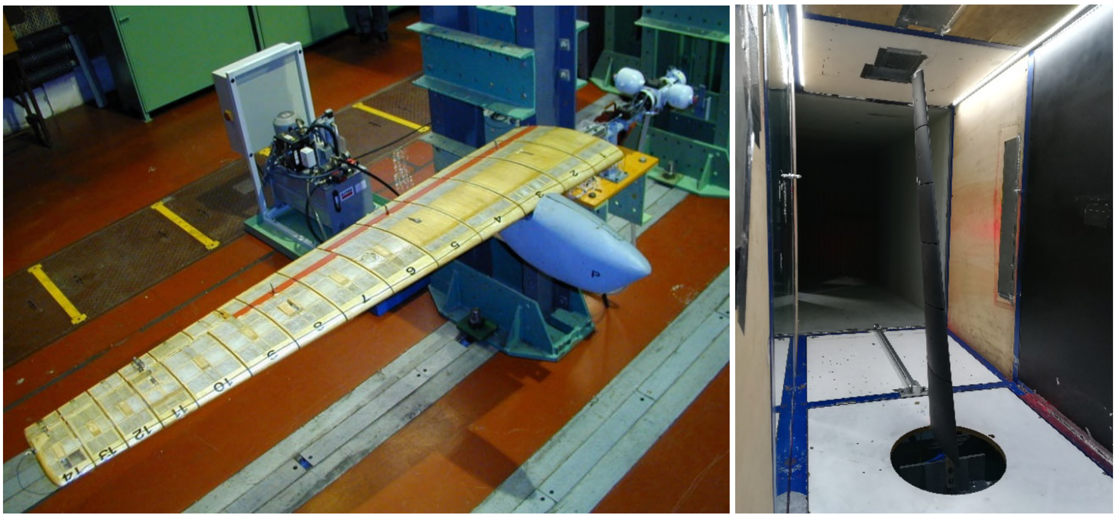

(a) Reproduced from [37] **(b)** Reproduced from [66]

Fig. 2.17.: Flexible wing models characterized by the gaps in between the pods.

There are however examples of the structural spar made of composite materials rather than aluminium [117, 118]. These structures are still able to undergo large deformation although the modelling of their properties is more complicated than a metallic spar. However, models are not always built as spar and shell configuration. De Gaspari et al. [49] designed, manufactured and built a 930 mm long wind tunnel test for the purposes of testing material for morphing application. As the model had to host mechanisms to shape the skin of the wing, De Gaspari opted for using two aluminium spars connected by 6 ribs. The flexibility of the model was obviously compromised. However, the studies did not consider flexibility effect.

The structural characteristics of the model can be assessed using accelerometers [104, 143, 66] for accelerations, velocities and displacements, strain gauges [163, 164] for strain and shape reconstruction or force balance [165] for the overall forces and moments, among the most common sensors. Yi et al. [104] implemented a 3D camera measurement system to measure the wing displacement throughout the gust response. Most of these systems are connected to National Instrument hardware [163, 164] or dSpace boards [111, 69].

Figure 2.17 shows one of the limitations of the spar and skin configuration when considering flexible scaled models: in order to allow the bending of the model, cuts in the skin are usually made [41]. These separation in the skin material allows the spar to bend without increase the stiffness of the wing due to the tension or compression of the shell material. However, such gaps might interfere with local aerodynamics of the model and change the aerodynamic properties, or induce unwanted vibrations due to vortex shedding.

A solution to the problem may have been presented in the work done by Pankonien [124], where a novel way to manufacture flutter models for wind tunnel test was proposed. The wing model was built in four parts, each of them 3D printed. One of the requirements was to have full control on the material properties to define flutter characteristics. Hence the Polyjet 3D printing technology was used to manufacture pieces, as able to print each component with different materials. Rapid prototyping in general was not new as previously used for 3D printed models [23, 120] or additive manufacturing resin made parts [196, 195]

2.7 Discussion and next step

This chapter provided the reader with an overview of the benefits associated with the application of HARW technology on commercial aircraft. Along with these, main problems associated with the flexibility of HARW structures were introduced. Linear and non-linear aeroelastic frameworks were described, along with a description of spoiler modelling. The need of wind tunnel tests were justified by the uncertainty of predicting the response of HARW which undergo large deformations. Considering the aim of this research, the following key points can be made:

- There is little knowledge on HARW applied on commercial aircraft. Most of the literature refers to UAV or HALE vehicle and the real impact of highly flexible structures on medium-haul aircraft must be fully investigated. While know-how and experience acquired by designing and operating UAV and HALE vehicles is valuable when applied on HARW commercial aircraft, differences between these types of aircraft is crucial. Firstly the size of the vehicle has an impact on wing load and therefore on the structure design. Secondly, in commercial-type aircraft, it is likely to have elements on the wing that are not present on UAV or HALE, such as turbojet engines. Finally, the payload of these aircraft differs significantly. Therefore, further investigation is needed to understand the aeroelastic response of HARW commercial aircraft.

- Spoiler models heavily rely on the use of experimental data and high fidelity modelling such as CFD. In order to include spoiler effects on the aircraft aerodynamics into low fidelity aeroelastic frameworks, a novel modelling technique is needed. A possible solution is to adapt empirical modellings, such as the the one provided by ESDU data sheet, to the numerical estimation of lift and drag variations due to the deployment of spoilers.

- Commonly, to allow flexible wind tunnel models to undergo large deformations, the shell must be manufactured in several, separated pods. Gaps in between these pods generate vortices that alter the local aerodynamics of the model. A new manufacturing process to overcame the aerodynamic interference while retaining the ability of the skin to deform will be addressed in the scope of this work.

3

Further investigation into the flight-dynamics/flexible-structure interaction

A further step towards investigating the interaction between rigid and flexible body dynamics is carried out in this chapter from a more practical and generic point of view. In the following analysis, the flexible structural dynamics are added to an existing rigid body dynamics model, such that the two are able to interact with each other. Once the model is built, a parametric study is carried out where the aircraft's flight dynamic response is considered as the airframe structural frequencies and damping are varied.

The numerical model is built such that the flexible Equations of Motion (EoMs) of the Rockwell B-1 Lancer are merged to the existing 5.5% dynamically scaled Generic Transport Model rigid EoMs. The size (and therefore properties) of the two aircraft clearly differs and their response might not be comparable. However, this study aims to show that any numerical dynamic model simulating rigid aircraft can be extended to account for the effects of structure flexibility by expanding the EoMs and including a new set of equations for the flexible dynamics. Since in this specific case mass distribution and modal properties of the GTM are not known, the goal is to evaluate the *qualitative* impact of structural flexibility on flight dynamics, while if the exact response of the GTM is required, the same set of equations can be applied by replacing inertia and stiffness properties into the model.

3.1 Generic Transport Model (GTM)

The work presented here is based on the NASA's GTM Simulink framework, which simulates the rigid body motion of the 5.5% dynamically scaled Generic Transport Model (GTM)[81]. The GTM is a conceptual twin-engine short-to-medium range commercial aircraft developed by NASA Langley Research Center based on the Boeing 757[87]. The scaled aircraft was extensively tested in the wind tunnel to validate computational models providing a comprehensive database on aerodynamics and flight dynamics characteristics of the vehicle. The full scale model is obtained by scaling up the wind tunnel model[174].

The GTM model was developed to provide a common configuration for designing and comparing new technologies for commercial aircraft. The development of the numerical model was part of a wider program called AirSTAR, developed by NASA Langley Research Center, in order to investigate and prevent aircraft loss of control [86].

Nguyen used the GTM aircraft as test case in one of the studies where the impact of the Variable Camber Continuous Trailing Edge Flap, a novel control surface configuration, was assessed [121]. Other examples of the use of the GTM as common research platform can be found in Cunningham et al. [48] and Tuzcu and Nguyen [175] work. In the first example, the authors showed handling qualities study results based on Cooper-Harper Rating to assess flight control technologies to satisfy stability and control when control characteristics were degraded. The impact of several flight control laws were studied through a series of tests. In the second example, the GTM was used to model unsteady aeroelasticity. This was extended to the non-linear case in the following work carried on by Nguyen et al. [122] [1]. These are only few examples of the possible applications of the model as a development platform.

The scaled aircraft model was built to validate the mathematical framework developed in the AirSTAR programme through a series of wind tunnel tests. Table 3.1 provides details of the full scale and 5.5% scaled GMT aircraft. The dynamically scaled model was designed for a specific flight condition in order to meet the non-dimensional dynamic scaling requirements. The scaled model is built using fiberglass and honeycomb for fuselage and carbon fibre for wings and empennage to make it as light as possible. According to dynamic scaling laws [39], the dynamics of the scaled model is $\sqrt{K} = 4.3$ faster than the full scale model, where $K = 0.055$ is the scaling factor.

	Full Scale	**5.5% scaled**
Length [m]	44.4	2.5
Wingspan [m]	37.8	2
Weight [kg]	90720	22.5
Airspeed [m/s]	135	33.5
Altitude [m]	400	305

Tab. 3.1.: Full size Generic Transport Model compared with the 5.5% dynamically scaled model[87].

The GTM framework used for the study was built in a Simulink environment and provided by NASA Langley Research Center in order to support pilot training. In fact, the numerical model reproduces the dynamics of the scaled aircraft. The simulation environment consists of a non-linear 6-DOF model which includes aerodynamics, engine dynamics, mass and geometry properties [87, 89, 88]. Representation of the outer layer of the Simulink model is shown in Figure 3.1, where inputs and outputs are detailed. The model is fed with control surfaces position (*cdms*) and external inputs, such as gusts and turbulence (*winds*) while the output includes positions of the control surfaces, the engines status, the equation of motion states and derivatives along with the aerodynamic coefficients. Each of these outputs can be singularly selected to be used into the feedback loop to design specific control system for the

---

[1] The model used by Nguyen for the study is the scaled-up version of the GTM adopted in this thesis. The scaled-up model weighs 190,000 lbs and cruises at Mach 0.8 at 30,000 ft [122]. Furthermore, scaled-up GTM aeroelastic properties are partially available as natural frequencies and damping in reference [122], while structural properties such as mass and inertia distribution as well as aerodynamic properties are not publicly available. Therefore while the original rigid-body sub-scale GTM model is validated by NASA, his enhanced flexible version developed in this chapter cannot be validated against available test data or literature. Hence the choice to adopt for this analysis the sub-scale model rather than the full-scale one.

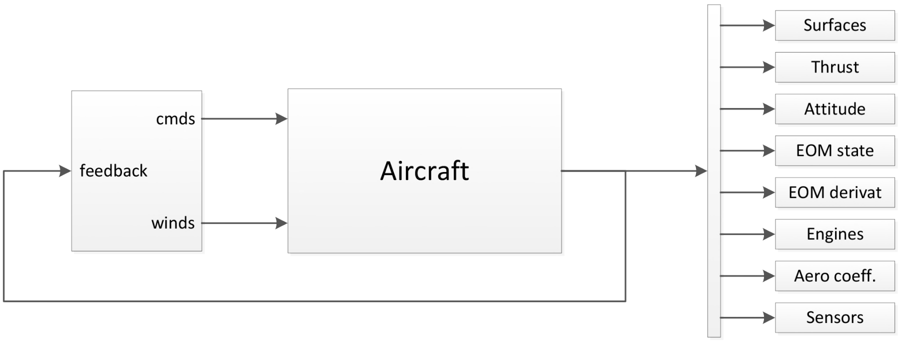

Fig. 3.1.: Generic Transport Model Simulink architecture.

aircraft, such as FCS or GLA. The aerodynamic model is based on wind tunnel tests carried out in the NASA Langley Research Center 14x22 wind tunnel facility. The tests were run using a model identical to the scaled GTM aircraft for a range of angle of attack, α, from $-10°$ to $+80°$ and sideslip angle β from $-45°$ to $45°$. Throughout this range, data was collected for different control surfaces deflection and angular rates. This data was used to build aerodynamic look-up tables in Simulink.

Details of the GTM subsystems are shown in Figure A.1 in Appendix A. The two main blocks that calculate the model response are the aerodynamic block, which simulates the the aircraft aerodynamics interpolating data points in look-up tables, and the EoMs block, which models the non-linear dynamics of the point-mass GTM vehicle.

Key aspect of this chapter lies in the enhancement of the EoMs block: in the original EoMs block, no structural dynamics is represented, i.e. the model is considered to be rigid. Therefore, the aircraft is simply identified with the rigid motion of its Centre of Gravity (CoG). When extending the dynamic response of the aircraft by adding an additional layer of flexible EoMs, the model is still represented by the motion of its CoG, but the response is now affected by the forces and moments produced by the interaction between aerodynamics and structural dynamics.

3.2 Model enhancement

The model was augmented by merging flexible EoMs with the existing rigid body dynamics, following the approach developed by Waszak and Schmidt [180, 156, 155, 182, 181]. Waszak and Schmidt investigated the impact of flexible structures on the Rockwell B-1 Lancer dynamic response. The work derives the full set of flexible EoMs and solves them based on the modal approach, accounting for the first 4 symmetric modes and the first asymmetric mode. Here a parameter variation study is carried out, varying the natural frequencies of the modes from fully rigid ($\omega_n = 0$), going through different levels of flexibility. The baseline of the study is the rigid structure case.

The flexible EoMs were derived assuming the structural deformations sufficiently small to consider the linear assumptions valid and a set of free vibration modes along with their natural frequencies is assumed to be available. The equations are obtained through the Lagrangian approach where the generalized coordinates, $\bar{q}$, can be defined as:

$$\bar{q} = [\underbrace{x, y, z, \phi, \theta, \psi}_{rigid}, \underbrace{\eta_1, \eta_2, ..., \eta_N}_{flexible}] \tag{3.1}$$

where (x, y, z) are the linear displacements, (ϕ, θ, ψ) the rotations along the body axis and $\eta_1, \eta_2, ..., \eta_N$ are the first N vibration modes. Making these assumptions, Waszak and Schimdt derived the flexible EOMs as:

$$M[\dot{U} - rV + qW + g\sin\theta] = Q_x \tag{3.2}$$

$$M[\dot{V} - pW + rU - g\sin\phi\cos\theta] = Q_y \tag{3.3}$$

$$M[\dot{W} - qU + pV - g\cos\phi\cos\theta] = Q_z \tag{3.4}$$

$$I_{xx}\dot{p} - (I_{xy}\dot{q} + I_{xz}\dot{r}) + (I_{zz} - I_{yy})qr + (I_{xy}r - I_{xz}q)p + (r^2 - q^2)I_{yz} = Q_{\phi_B} \tag{3.5}$$

$$I_{yy}\dot{q} - (I_{xy}\dot{p} + I_{yz}\dot{r}) + (I_{xx} - I_{zz})pr + (I_{yz}p - I_{xy}r)q + (p^2 - r^2)I_{xz} = Q_{\theta_B} \tag{3.6}$$

$$I_{zz}\dot{r} - (I_{xz}\dot{p} + I_{yz}\dot{q}) + (I_{yy} - I_{xx})pq + (I_{xz}q - I_{yz}p)r + (q^2 - p^2)I_{xy} = Q_{\psi_B} \tag{3.7}$$

$$\ddot{\eta}_i + \omega^2\eta_i = \frac{Q_{\eta_i}}{M_i} \qquad \textit{for i=1..N} \tag{3.8}$$

where Q_x, Q_y, Q_z are the aerodynamic forces along body-reference axis and Q_{ϕ_B}, Q_{θ_B}, Q_{ψ_B} are the equivalent of the total aerodynamic and propulsive moments (L,M,N) about the body-reference axis. The coupling between the structural dynamics and rigid body dynamics is possible through the generalized forces and moments. An example of the calculation of the generalized forces and moments, Q, is as follows:

$$Q_x = \frac{\rho V_0^2 S}{2}\left(C_{x_0} + C_{x_\alpha}\alpha + C_{x_\delta}\delta + \sum_{i=1}^{\infty} C_{x_\eta}\eta_i\right) + \frac{\rho V_0^2 S\bar{c}}{4}\left(C_{x_\alpha}\dot{\alpha} + C_{x_q}q + \sum_{i=1}^{\infty} C_{x_{\dot{\eta}}}\dot{\eta}_i\right) + T_x \tag{3.9}$$

$$Q_{\phi_B} = \frac{\rho V_0^2 Sb}{2}\left(C_{L_0} + C_{L_\beta}\beta + C_{L_\delta}\delta + \sum_{i=1}^{\infty} C_{L_\eta}\eta_i\right) + \frac{\rho V_0^2 Sb^2}{4}\left(C_{L_p}p + C_{L_r} + \sum_{i=1}^{\infty} C_{L_{\dot{\eta}}}\dot{\eta}_i\right) + L_T \tag{3.10}$$

$$\begin{aligned} Q_{\eta_j} = \frac{\rho V_0^2 S\bar{c}}{2}&\left(C_0^{\eta_j} + C_\alpha^{\eta_j}\alpha + C_\beta^{\eta_j}\beta + C_\delta^{\eta_j}\delta + \sum_{i=1}^{\infty} C_{\eta_i}^{\eta_j}\eta_i\right) + \\ &+ \frac{\rho V_0^2 S\bar{c}^2}{4}\left(C_\alpha^{\eta_j}\dot{\alpha} + C_p^{\eta_j}p + C_q^{\eta_j}q + C_r^{\eta_j}r + \sum_{i=1}^{\infty} C_{\eta_i}^{\eta_j}\dot{\eta}_i\right) \end{aligned} \tag{3.11}$$

where both rigid and flexible contributions are evident.

While the number of modes N to use in the mathematical model is a user choice depending on the bandwidth of interest, it was decided for this case study to share the same modes of the study carried out by Waszak and Schimdt. Thus, the modes used for the study were the first *five* structural modes of the B-1 aircraft, shown in Figure 3.2. The first *four* modes represent the first full-aircraft symmetric bending modes while the fifth mode is the first anti-symmetric one. Details of the modes are given in Table 3.2[2]. It is important to stress the assumptions behind the case study presented in this chapter. As most of the properties needed for the GTM model were not publicly available, it was decided to assume the following:

		Modal mass [kg]	**Frequency** [rad/s]	**Frequency** [Hz]	**Damping**
Symmetric	**1^{st} mode**	248.93	12.57	2.01	2%
	2^{nd} mode	12997.66	14.07	2.23	2%
	3^{rd} mode	1809.2	21.17	3.37	2%
	4^{th} mode	59109.98	22.05	3.51	2%
Anti-sym	**5^{th} mode**	39306.87	9.425	1.50	2%

Tab. 3.2.: Modal mass, frequency and damping of the B-1 Lancer structural modes.

- *All the modal characteristics used in the simulation are the same of the B-1 Lancer aircraft.* This is a significant assumption implying that the GTM vibrates with same mode shapes as those of the B-1 Lancer. This is clearly incorrect, especially considering the different size and the mass, stiffness and inertia distribution of the two aircraft. However, as this study aims to assess the impact of flexible structure on the flight dynamics rather than providing a flexible framework of the GTM model, it was decided to scale down the available B-1 mode shapes by using a scaling vector, k, to ensure compatibility with the GTM framework.

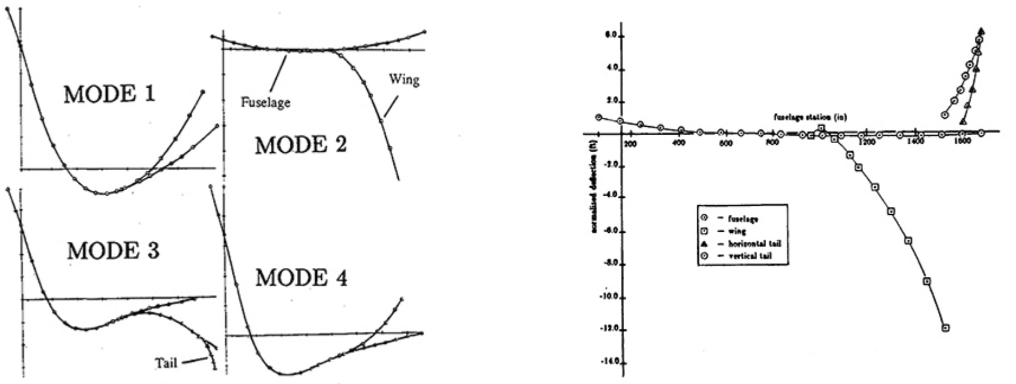

(a) B1 modes shapes [Reproduced from [179]]

(b) B1 fifth mode, anti-symmetric [Reproduced from [181]]

Fig. 3.2.: First five structural modes of B-1 Lancer.

---

[2] Although damping is not included in the original flexible dynamics model as given in Equation 3.8, these were extended in this work to include structural damping as shown in Equation 3.29.

- *All inertia and mass properties adopted for the flexible EoMs, such as modal mass, inertia and damping belongs to the B-1 Lancer aircraft.* In this case as well, the aforementioned assumption is adopted for the augmented GTM model.
- The contribution of the *rigid* dynamics, forces and moments in the Equations 3.2-3.8 is removed as such a contribution is already evaluated by the original GTM framework. In fact, rigid body dynamics are generated by the original GTM model before being fed into the flexible EoMs. Therefore, the only contribution retained from the flexible EoMs is the one related to the modal variables η_i.

Flexible modes act differently on the aircraft dynamics: in fact, the symmetric modes impact the longitudinal dynamics of the aircraft while the anti-symmetric modes affect the lateral-directional dynamics. Table 3.3 shows how this is applied to this specific work.

	Mode 1	**Mode 2**	**Mode 3**	**Mode 4**	**Mode 5**
Q_x					
Q_y					x
Q_z	x	x	x	x	
Q_{ϕ_B}					x
Q_{θ_B}	x	x	x	x	
Q_{ψ_B}					x

Tab. 3.3.: Impact of the first five modes on the flexible forces and moments as modelled in the GTM framework.

The right hand side of the *flexible* EoMs given in Equations 3.2-3.8 can be adapted to the scope of the work before being included in the model, as follows:

$$Q_x = 0 \tag{3.12}$$

$$Q_y = \frac{\rho V_0^2 S}{2}(C_{y_{\eta_5}}\eta_5) + \frac{\rho V_0^2 S\bar{c}}{4}(C_{y_{\dot\eta_5}}\dot\eta_5) \tag{3.13}$$

$$Q_z = \frac{\rho V_0^2 S}{2}(C_{z_{\eta_1}}\eta_1 + C_{z_{\eta_2}}\eta_2 + C_{z_{\eta_3}}\eta_3 + C_{z_{\eta_4}}\eta_4) + \frac{\rho V_0^2 S\bar{c}}{4}(C_{z_{\dot\eta_1}}\dot\eta_1 + C_{z_{\dot\eta_2}}\dot\eta_2 + C_{z_{\dot\eta_3}}\dot\eta_3 + C_{z_{\dot\eta_4}}\dot\eta_4) \tag{3.14}$$

$$Q_{\phi_B} = \frac{\rho V_0^2 S}{2}(C_{\phi_{\eta_5}}\eta_5) + \frac{\rho V_0^2 S\bar{c}}{4}(C_{\phi_{\dot\eta_5}}\dot\eta_5) \tag{3.15}$$

$$Q_{\theta_B} = \frac{\rho V_0^2 S}{2}(C_{\theta_{\eta_1}}\eta_1 + C_{\theta_{\eta_2}}\eta_2 + C_{\theta_{\eta_3}}\eta_3 + C_{\theta_{\eta_4}}\eta_4) + \frac{\rho V_0^2 S\bar{c}}{4}(C_{\theta_{\dot\eta_1}}\dot\eta_1 + C_{\theta_{\dot\eta_2}}\dot\eta_2 + C_{\theta_{\dot\eta_3}}\dot\eta_3 + C_{\theta_{\dot\eta_4}}\dot\eta_4) \tag{3.16}$$

$$Q_{\psi_B} = \frac{\rho V_0^2 S}{2}(C_{\psi_{\eta_5}}\eta_5) + \frac{\rho V_0^2 S\bar{c}}{4}(C_{\psi_{\dot\eta_5}}\dot\eta_5) \tag{3.17}$$

$$\begin{aligned} Q_{\eta_1} = \frac{\rho V_0^2 S\bar{c}}{2}&\left(C_0^{\eta_1} + C_\alpha^{\eta_1}\alpha + C_{\eta_1}^{\eta_1}\eta_1 + C_{\eta_1}^{\eta_2}\eta_2 + C_{\eta_1}^{\eta_3}\eta_3 + C_{\eta_1}^{\eta_4}\eta_4\right) + \\ &+ \frac{\rho V_0^2 S\bar{c}^2}{4}\left(C_\alpha^{\eta_1}\dot\alpha + C_q^{\eta_1}q + C_{\eta_1}^{\eta_1}\dot\eta_1 + C_{\eta_1}^{\eta_2}\dot\eta_2 + C_{\eta_1}^{\eta_3}\dot\eta_3 + C_{\eta_1}^{\eta_4}\dot\eta_4\right) \end{aligned} \tag{3.18}$$

$$\begin{aligned} Q_{\eta_2} = \frac{\rho V_0^2 S\bar{c}}{2}&\left(C_0^{\eta_2} + C_\alpha^{\eta_2}\alpha + C_{\eta_2}^{\eta_1}\eta_1 + C_{\eta_2}^{\eta_2}\eta_2 + C_{\eta_2}^{\eta_3}\eta_3 + C_{\eta_2}^{\eta_4}\eta_4\right) + \\ &+ \frac{\rho V_0^2 S\bar{c}^2}{4}\left(C_\alpha^{\eta_2}\dot\alpha + C_q^{\eta_2}q + C_{\eta_2}^{\eta_1}\dot\eta_1 + C_{\eta_2}^{\eta_2}\dot\eta_2 + C_{\eta_2}^{\eta_3}\dot\eta_3 + C_{\eta_2}^{\eta_4}\dot\eta_4\right) \end{aligned} \tag{3.19}$$

$$\begin{aligned} Q_{\eta_3} = \frac{\rho V_0^2 S\bar{c}}{2}&\left(C_0^{\eta_3} + C_\alpha^{\eta_3}\alpha + C_{\eta_3}^{\eta_1}\eta_1 + C_{\eta_3}^{\eta_2}\eta_2 + C_{\eta_3}^{\eta_3}\eta_3 + C_{\eta_3}^{\eta_4}\eta_4\right) + \\ &+ \frac{\rho V_0^2 S\bar{c}^2}{4}\left(C_\alpha^{\eta_3}\dot\alpha + C_q^{\eta_3}q + C_{\eta_3}^{\eta_1}\dot\eta_1 + C_{\eta_3}^{\eta_2}\dot\eta_2 + C_{\eta_3}^{\eta_3}\dot\eta_3 + C_{\eta_3}^{\eta_4}\dot\eta_4\right) \end{aligned} \tag{3.20}$$

$$Q_{\eta_4} = \frac{\rho V_0^2 S \bar{c}}{2}\Big(C_0^{\eta_4} + C_\alpha^{\eta_4}\alpha + C_{\eta_4}^{\eta_1}\eta_1 + C_{\eta_4}^{\eta_2}\eta_2 + C_{\eta_4}^{\eta_3}\eta_3 + C_{\eta_4}^{\eta_4}\eta_4\Big) + \\ + \frac{\rho V_0^2 S \bar{c}^2}{4}\Big(C_\alpha^{\eta_4}\dot{\alpha} + C_q^{\eta_4} q + C_{\eta_4}^{\eta_1}\dot{\eta}_1 + C_{\eta_4}^{\eta_2}\dot{\eta}_2 + C_{\eta_4}^{\eta_3}\dot{\eta}_3 + C_{\eta_4}^{\eta_4}\dot{\eta}_4\Big) \tag{3.21}$$

$$Q_{\eta_5} = \frac{\rho V_0^2 S \bar{c}}{2}\Big(C_0^{\eta_5} + C_\beta^{\eta_5}\beta + C_\delta^{\eta_5}\delta + C_{\eta_5}^{\eta_5}\eta_5\Big) + \frac{\rho V_0^2 S \bar{c}^2}{4}\Big(C_p^{\eta_5} p + C_r^{\eta_5} r + C_{\eta_5}^{\eta_5}\dot{\eta}_5\Big) \tag{3.22}$$

Note that the meaning of $Q_x = 0$ (Equation 3.12), is that the structural dynamics does not influence forces along the longitudinal body axis, as already shown in Table 3.3. While EoMs are linearised around the trim point, all aerodynamic coefficients necessary for the solution of the equations are referred to the B-1 Lancer aircraft and taken from Baghdadi et al. [19].

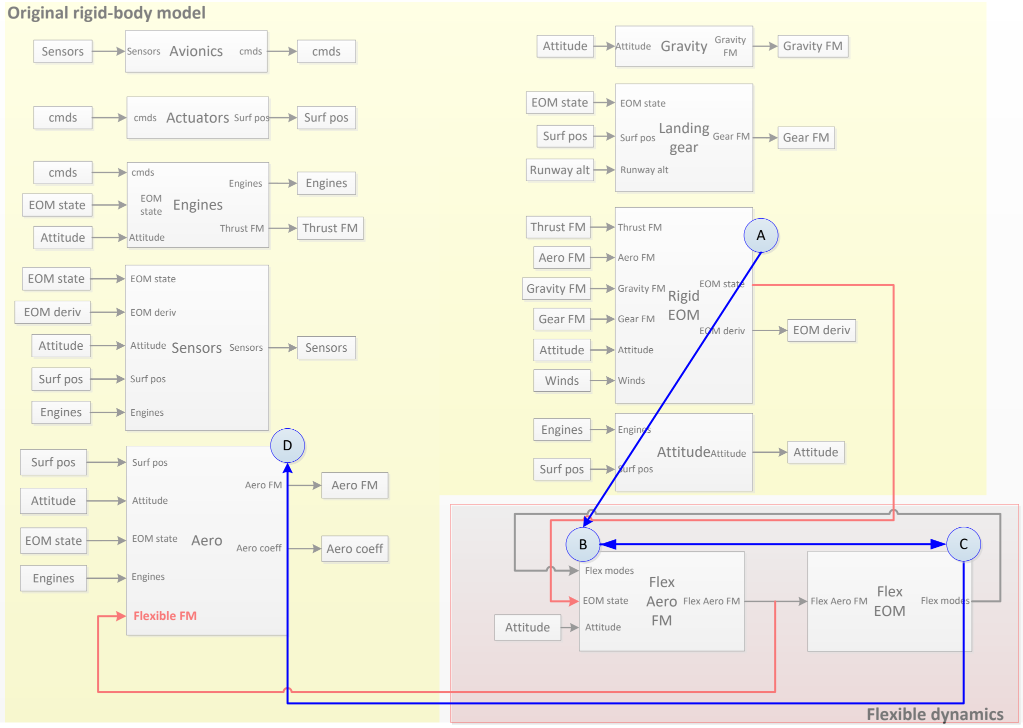

Fig. 3.3.: Generic Transport Model Simulink inner flexible loop architecture. The flexible augmentation is highlighted in red.

To add the effect of flexibility into the GTM model, the flexible EoMs were included into the Simulink model as shown in Figure 3.3. The EoMs model was adapted from the Baghdadi model [19] to fit the GTM architecture and then merge the original rigid EoMs. Once these new blocks are included, the new model workflow is given as:

1. The set of the rigid EoMs defined as [45]:

$$m\big(\dot{u} - rv + qw\big) = X \tag{3.23}$$

$$m\big(\dot{v} - pw + ru\big) = Y \tag{3.24}$$

$$m\big(\dot{w} - qu + pv\big) = Z \tag{3.25}$$

$$I_x \dot{p} - \left(I_y - I_z\right) q r - I_{xz}\left(p q + \dot{r}\right) = L \tag{3.26}$$

$$I_y \dot{q} + \left(I_x - I_z\right) p r + I_{xz}\left(p^2 - r^2\right) = M \tag{3.27}$$

$$I_z \dot{r} - \left(I_x - I_y\right) p q - I_{xz}\left(q r + \dot{p}\right) = N \tag{3.28}$$

is solved by the original model Ⓐ, where (X, Y, Z) are the rigid forces along the body axis and (L, M, N) are the rigid moments along the same axis. The output of Ⓐ is the rigid state vector x^R, defined as:

$$x^R = \left[u, v, w, \dot{p}, \dot{q}, \dot{r}, \dot{\phi}, \dot{\theta}, \dot{\psi}\right]$$

2. The rigid state vector x^R is fed into the flexible aerodynamic forces and moments estimation algorithm Ⓑ, along with the flexible state vector $\left[\eta_1, ..., \eta_N, \dot{\eta}_1, ..., \dot{\eta}_N\right]$ and the vector of aerodynamic coefficient $\left[C_1^\eta, ..., C_N^\eta\right]$. Equations 3.12-3.22 are solved in Ⓑ, which provides as output the vector of forces $\left[Q_x, Q_y, Q_z\right]^F$, moments $\left[Q_{\phi_B}, Q_{\theta_B}, Q_{\psi_B}\right]^F$ and generalised forces $\left[Q_{\eta_1}, ..., Q_{\eta_N}\right]^F$ associated with the flexible dynamics. Aerodynamic coefficients are provided in form of look-up tables and extracted from [182].

   Flexible forces and moments are fed into the flexible EoMs block Ⓒ in order to evaluate the flexible dynamics and estimate the flexible state vector. As the aim of the work showed in this chapter is to assess the impact of structure flexibility on the aircraft flight dynamics, the flexible dynamics equations

   $$\ddot{\eta}_i + 2\zeta_i \omega_i \dot{\eta}_i + \omega^2 \eta_i = \frac{Q_{\eta_i}}{M_i} \tag{3.29}$$

   are solved for different values of damping ζ and natural frequencies ω, as detailed in Section 3.3.

3. Flexible forces and moments vector is finally fed into the aerodynamic forces and moments evaluation algorithm Ⓓ. Here, the flexible contribution is added to the rigid forces and moments to provide the overall load acting of the aircraft structure. However, in this study, prior the addition, the flexible contribution is multiplied by a scaling vector k in order to scale down the B-1 Lancer dynamics and make it compatible with the GTM model (Figure 3.4). The vector was manually tuned in order to provide a same order of magnitude of the flexible forces and moments with respect the rigid one, as follows:

   $$k = \left[K_{Q_x}, K_{Q_y}, K_{Q_z}, K_L, K_M, K_N\right] = \left[10^{-5}, 10^{-5}, 10^{-4}, 10^{-5}, 10^{-5}, 10^{-7}\right] \tag{3.30}$$

The choice of the vector k highly impacts the flexible forces and moments contribution. In fact, by scaling down the B1 aircraft forces and moments, their impact on the overall dynamics can be tailored by adjusting the coefficients k_i. This can be clearly seen in the lateral-

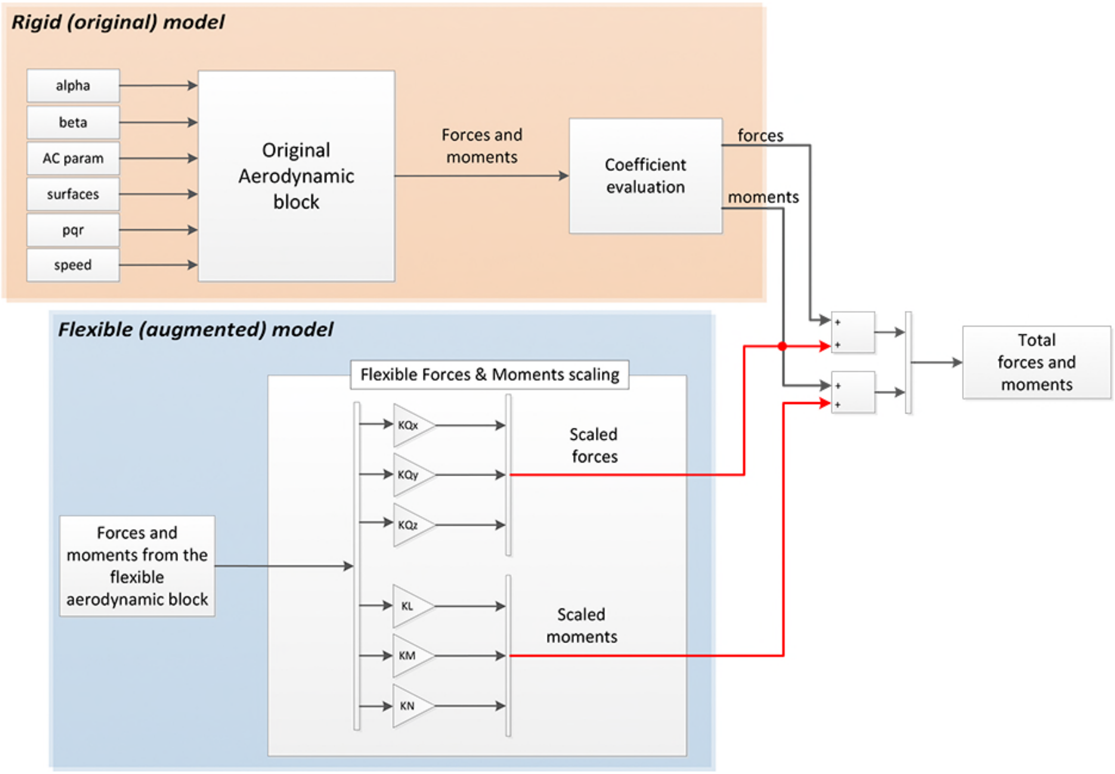

Fig. 3.4.: Augmented GTM aerodynamic block. Along with the forces and moments calculated by the rigid model, the flexible contribution is added to enhance the model.

directional response where the asymmetric modes has a minimal impact on the GTM dynamics probably because a too low choice of magnitude of K_N. While the vector k was manually chosen for this study, a more rigorous approach may be used to define the scaling vector through an optimization process aiming to meet specific requirements.

3.3 Simulation setup

A bandwidth of interest of the aircraft dynamics must be chosen before initialising the simulation environment. For the purpose of this study, the target frequency is the one associated with the short period mode for the longitudinal analysis and the Dutch roll frequency for the lateral-directional response analysis. The exact frequency of the short period mode for the scaled GTM aircraft, however, is unknown. Hence the target[3] frequency is estimated from literature, which provides both the short period and Dutch roll range as typically between 0.16 Hz and 1.6 Hz[45]. The target frequency for both longitudinal and lateral-directional dynamics was chosen to be 0.5 Hz. The flexible model was structured to allow parametric variation of the natural frequencies and damping of the structure. While the damping value

---

[3] Defined as the frequency to excite.

is fed directly into the flexible EoMs block, the scaling coefficient, c, defines the natural frequencies of the first five structural modes as:

$$f_i^{modes} = \frac{f_i}{c} \tag{3.31}$$

where f_i is the set of original B-1 aircraft natural frequencies. This is an important aspect to stress as it defines the fact that for each iteration, the *entire* set of natural frequencies is scaled by the same constant. The overall analysis explores the domain made of the all possible combinations of (ζ, c), for a total of 66 simulations for each test cases. The simulation matrix is given in Table 3.4, where the value of the first modal frequency is provided for clarity. Structural damping range was chosen from 2% to 100%, dividing the range in 10 equal increments. The flight condition simulated was altitude $\mathrm{h} = 305$ m (1000 ft), angle of attack $\alpha = 4°$ and $\mathrm{v} = 38.5$ m/s (75 kt). The length of the simulation was 10 s and the input was fed into the system at $\mathrm{t} = 2$ s.

	f_1^{modes}	**2.01 Hz**	**1.34 Hz**	**1.01 Hz**	**0.81 Hz**	**0.67 Hz**	**0.57 Hz**
ζ	**c**	**1**	**1.5**	**2**	**2.5**	**3**	**3.5**
2%		x	x	x	x	x	x
11.8%		x	x	x	x	x	x
21.6%		x	x	x	x	x	x
31.4%		x	x	x	x	x	x
41.2%		x	x	x	x	x	x
51%		x	x	x	x	x	x
60.8%		x	x	x	x	x	x
70.6%		x	x	x	x	x	x
80.4%		x	x	x	x	x	x
90.2%		x	x	x	x	x	x
100%		x	x	x	x	x	x

Tab. 3.4.: Augmented GTM simulation matrix.

Both the longitudinal and lateral-directional dynamics were assessed in the presented work. The longitudinal response was excited by the elevator input, while the lateral-directional response was assessed for both spoilers and ailerons input separately. The control surfaces of the GTM are shown in Figure 3.5 and the input is tailored to excite the target frequency of 0.5 Hz. For the purpose of this study, the model was trimmed as rigid (assuming $\eta_i = \dot{\eta}_i = 0$) and the time histories are initiated with the model already trimmed.

3.4 Longitudinal response

The longitudinal dynamics are excited with a symmetric positive deflection of the elevator. The magnitude of the deflection is 5°. The input is fed into the system at $\mathrm{t} = 2$ s, lasts for 1 second, and aims to excites the aircraft response at $f_{long} = 0.5$ Hz. The time history of the input is shown in Figure 3.6 where, at $t = 0$, the elevator is already deflected to about 1° for

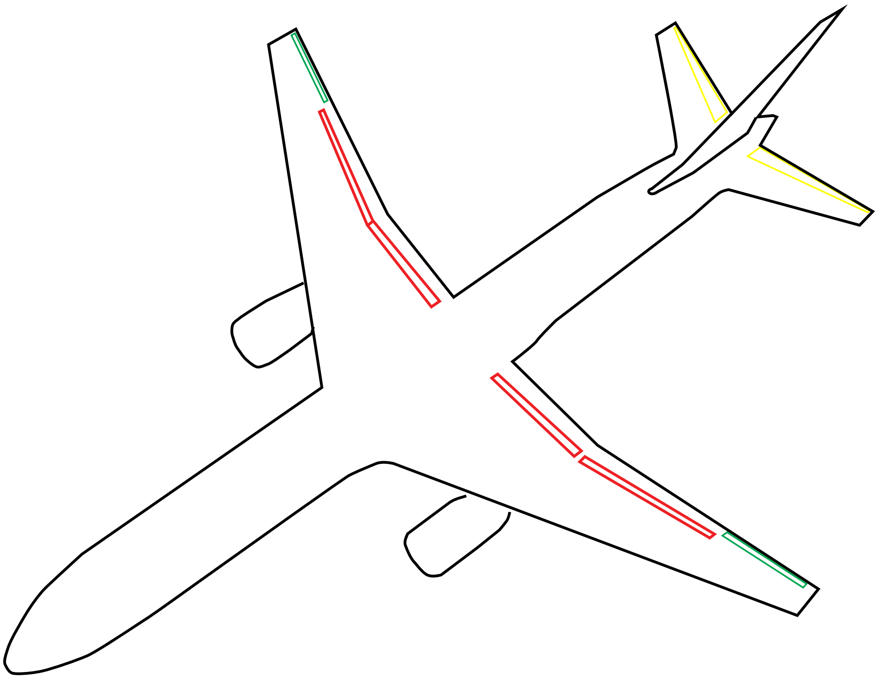

Fig. 3.5.: GTM control surfaces: spoilers (red), ailerons (green) and elevator (yellow)

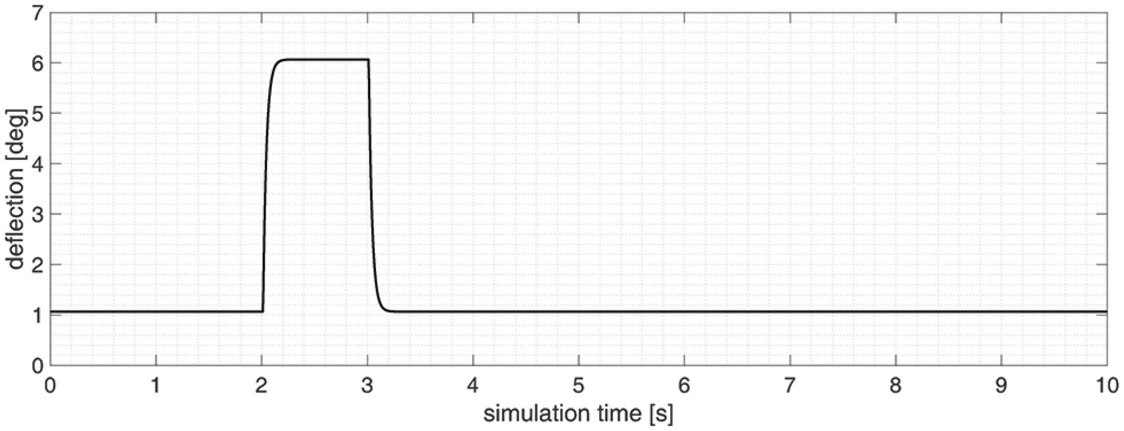

Fig. 3.6.: Time history of elevator input for the longitudinal analysis.

trim. The output vector of the longitudinal analysis includes pitch rate, q, pitch angle, θ, angle of attack, α and equivalent airspeed EAS. The vector is thus defined as follows:

$$y_{long} = [q, \theta, \alpha, EAS] \tag{3.32}$$

Figures 3.7 and 3.8 show an example of the aircraft longitudinal response for different values of structural frequencies and damping values. The response is compared with the rigid response. Figure 3.7 shows the response of the GTM for the lowest simulated value of the first symmetric mode (corresponding to the scaling factor $c = 3.5$), where the impact of the overlapping is predicted to be the most severe, and different values of damping. The comparison aims to show the impact of the damping on the aeroelastic response of the aircraft.

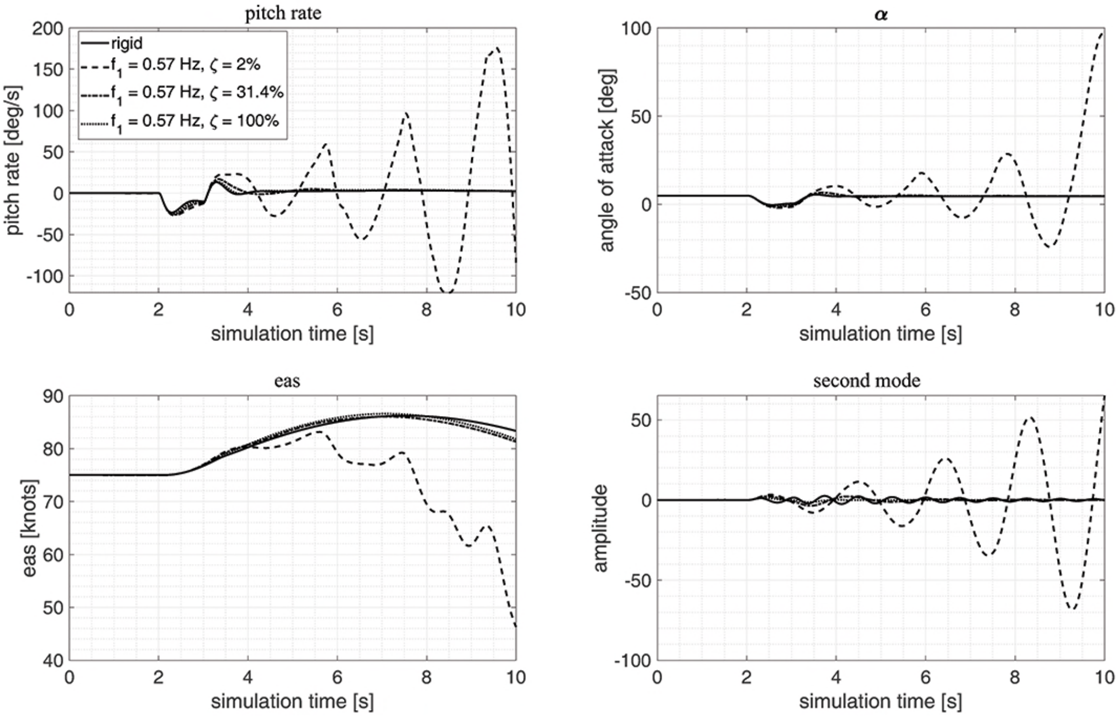

Fig. 3.7.: GTM longitudinal response to elevator input for $f_1 = 0.57$ Hz and different values of damping.

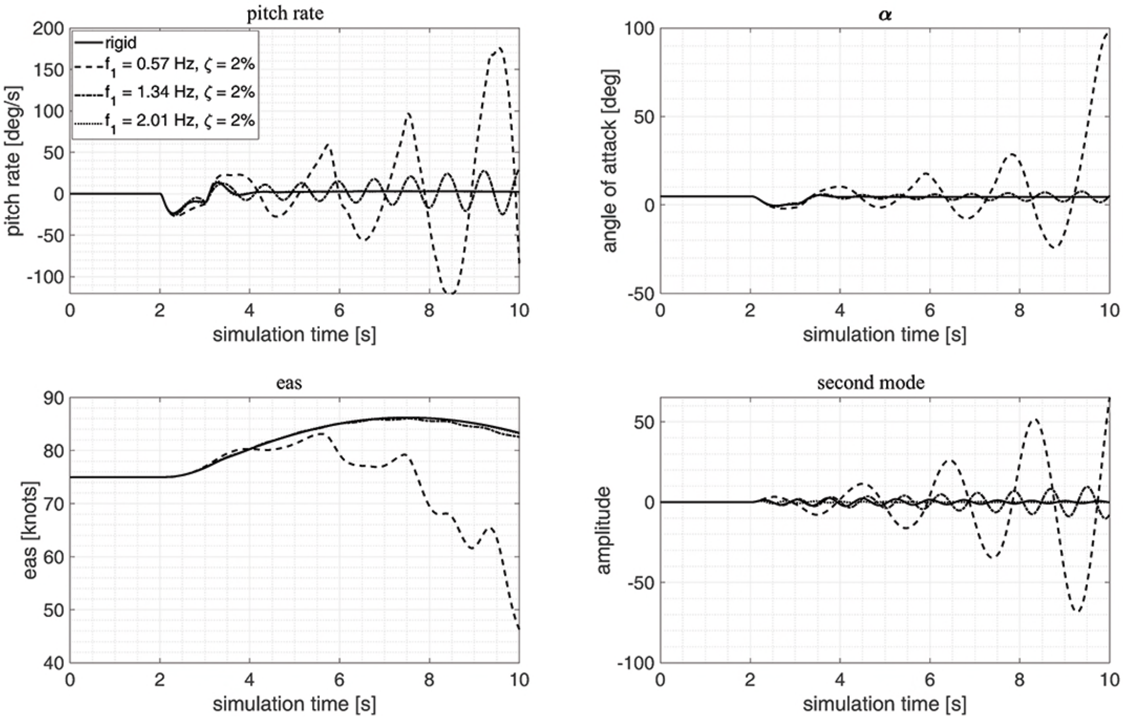

Fig. 3.8.: GTM longitudinal response to elevator input for $\zeta = 2\%$ and different values of frequency.

Results show that although the rigid and flexible dynamics are strongly coupled, when the the structural damping is sufficiently high, the response is well damped. In fact, for $\zeta = 100\%$, the response is exactly the same as the rigid case, while when $\zeta = 31.4\%$ the response oscillates, although still converging for $t \gg 3s$. However, for a lower value of structural damping such as $\zeta = 2\%$ (more realistic for aircraft structures), the response diverges quickly. This only happens if the structure excites the rigid modes of the aircraft, i.e. the rigid and flexible dynamics overlap. This aspect is clear when considering Figure 3.8, which shows the same response just discussed above, but with constant damping $\zeta = 2\%$ and examining different values of modal frequency. When the structural dynamics do not overlap the short period mode ($f_1 = 2.01$ Hz), the flexible system response converges rapidly to the rigid one although the damping is low. For lower values of f, the system response is oscillatory unstable. For $f_1 = 1.34$ Hz the system slowly diverges. The bottom right plot shows the second structural mode amplitude. For brevity, only the second mode was plotted because it was found to be one with the largest response. The trend of the mode reflects the behaviour of the structural response. In fact, the most critical case is the case with $f_1 = 0.57$ Hz and $\zeta = 2\%$.

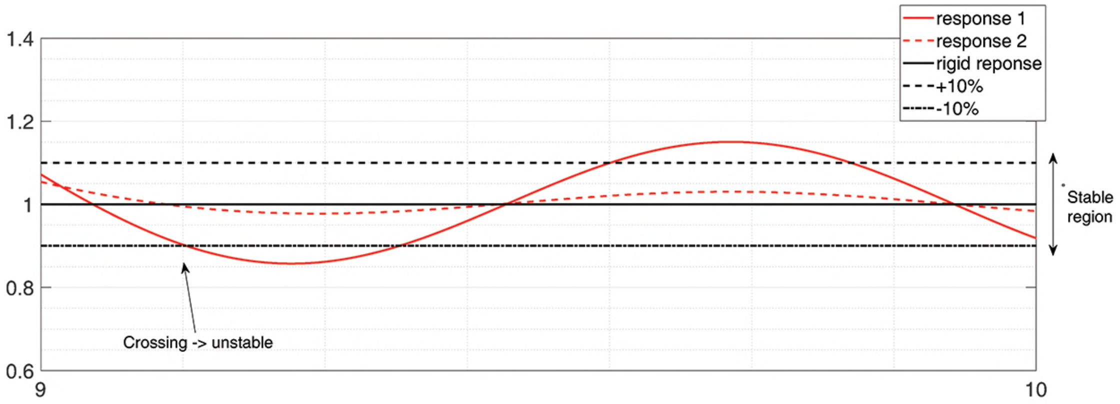

Fig. 3.9.: Definition of convergence region and stable response.

To summarise the dynamic response of the GTM in the whole simulation domain, the so-called *steady-state grid plots* were generated. Such plots are shown in Figure 3.10. These plots allow the comparison of the rigid and flexible response for $t \gg 3s$, where the transient response does not play a primary role and the steady-state response is far more relevant. The flexible response is expected either to converge to the rigid body response or to diverge from it. The time considered for this analysis is the last second of the simulation, corresponding to 10% of the overall simulation time. Each point displayed in the steady-state grid plot represents a possible combination of the structural natural frequencies and damping. The aim of the steady-state grid plots is to represent graphically results from the application of a convergence criterion specifically designed for the purpose of this study. In fact, while the aircraft attitude does not necessary go back to its initial condition due to the excitation of the longitudinal and lateral-directional modes, the convergence criterion aims to provide a metric to compare the steady state response of the rigid and flexible configurations, rather than providing an assessment of their absolute response.

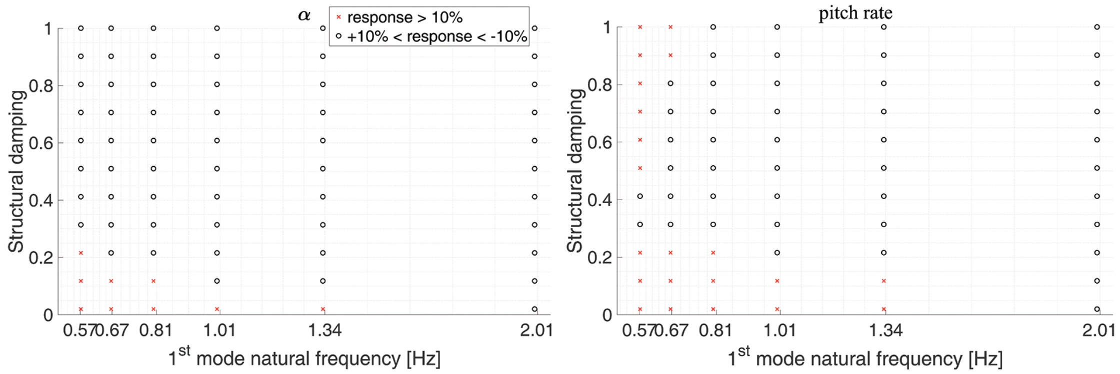

(a) Angle of attack α *steady-state* grid. **(b)** Pitch rate q *steady-state* grid.

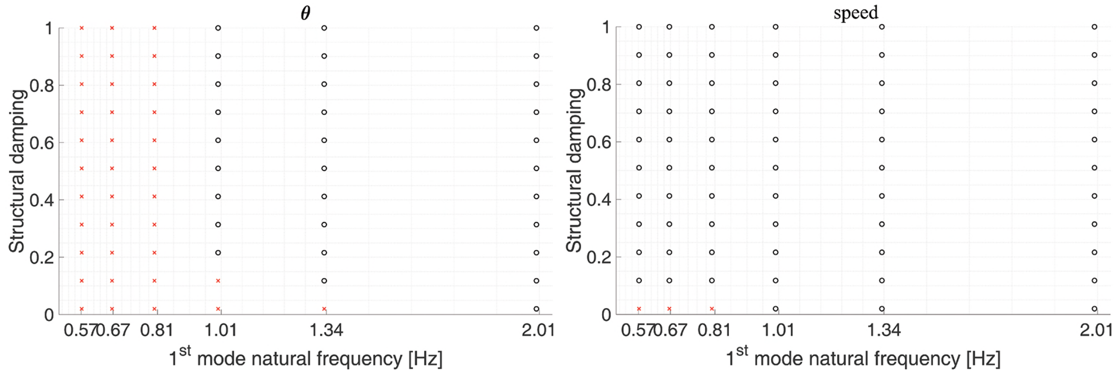

(c) Pitch angle θ *steady-state* grid. **(d)** Estimated airspeed *eas steady-state* grid.

Fig. 3.10.: *Steady-state* grid plots for longitudinal dynamics.

Before comparing the rigid and flexible response, a *convergence* region is defined: this region is defined as the area between the +10% and −10% of the rigid response (Figure 3.9). The mathematical definition of the boundaries of the convergence region, $y^+(t)$ and $y^-(t)$, is given as follows:

$$\forall \quad 90\% < t < 100\%, \quad y^+(t) = y_{ss}^R(t) + 0.1 y_{ss}^R(t) \quad and \quad y^-(t) = y_{ss}^R(t) - 0.1 y_{ss}^R(t). \tag{3.33}$$

where the superscript R shows the rigid response. Therefore, to identify the nature of the flexible response, each point of the last second of simulation is compared with the rigid response. If even just one point of the flexible response in such time range falls outside the convergence region, i.e. the flexible response exceeds ±10% of the rigid response, the flexible response is considered to be not converging (either stable or unstable) and thus the aircraft dynamics is considered to violate the criterion, although the response it is not necessary unstable as it may settle on a different steady state value with respect of the rigid response. Instead, if every point of the last second of the flexible response is included in the convergence region, then the response is considered to meet the convergence criterion. The mathematical relationship applied to define this concept is given as follows:

$$\forall \quad 90\% < t < 100\%, \quad if \quad y_{flex}(t) > y^+(t) \quad or \quad y_{flex}(t) < y^-(t) \rightarrow diverges \tag{3.34}$$

$$\forall \quad 90\% < t < 100\%, \quad if \quad y^+(t) < y_{flex}(t) < y^-(t) \quad \rightarrow converges \tag{3.35}$$

It is important to stress that the condition where $y_{flex} > \pm 10\%$ does not necessary imply that the flexible response is unstable and diverging, but it may mean that the flexible steady state response is stable and settles on different values other than the rigid one. Figure 3.9 shows an example of the two signals response: while the *second response* is considered to meet the convergence criterion as it always lies within the stable region, the *first response*, although it does not diverge, does not satisfy the convergence criterion as it crosses the stable region boundaries twice.

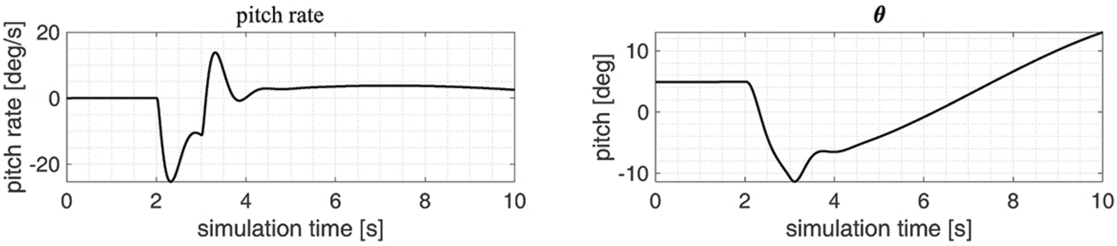

Fig. 3.11.: Flexible response of the pitch rate and pitch angle for $f_1 = 0.57$ Hz and $\zeta = 100\%$.

Figure 3.10a shows the steady-state response of angle of attack, α. The flexible response of α converges to the rigid response either when the two dynamics do not overlap ($f_1 > 1.34$ Hz), or when the structural damping is sufficiently high ($\zeta > 20\%$). In general, the flexible response of α converges across the simulation domain. The pitch rate and the pitch attitude response instead (Figure 3.10b and c respectively) do not converge for most of the combinations. This is a clear example for proving that the response is not neither oscillating nor unstable when it does not fall in the convergence region. In fact, Figure 3.11 shows that the reason why the pitch rate is classified as not converging for low frequencies value although values of damping are fairly high, is because it settles on a different value with respect to the rigid case. Even for a fully damped response, pitch rate does not return to the initial value[4] of 0 deg/s, but settles on 3.8 deg/s. This leads to the *divergence* in pitch attitude. Such phenomena can easily be addressed by implementing a flight control system, able to correct the aircraft attitude ensuring convergence to a desired value. Therefore, the impact of flexibility is not just limited to the transient response, but affects the steady state response as well.

The final steady-state plot is related to the EAS (Figure 3.10c). The trend of the dynamic response for this parameter is mostly converging. Aircraft speed diverges only for $0.57\text{Hz} < f_1 < 0.81\text{Hz}$ and damping $\zeta = 2\%$. Such a smooth behaviour was predicted because the flexible EoMs do not explicitly affect the longitudinal axis dynamics (as previously said, $Q_x = 0$). The only contribution to the change in speed is given by the change in the angle of attack and dynamic pressure.

---

[4] Numerically the rigid steady-state value is not zero to prevent the case where it is impossible to determine the $\pm 10\%$ boundaries of the convergence region.

3.5 Lateral-directional response

To investigate the impact of flexibility on lateral-directional dynamics, response to deflections of either spoilers or ailerons was investigated individually. Both the inputs are designed to target the Dutch roll unstable mode at a frequency of $f_{lat} = 0.5$ Hz. The output of the lateral-directional dynamics assessment is defined as follows:

$$y_{lat} = [\phi, \beta, p, r] \tag{3.36}$$

where ϕ is the roll angle, β the sideslip angle and (p, r) are the roll and yaw rate respectively. The simulation time is 10 s and the control surfaces are deflected again at t = 2 s. The GTM flight conditions are the same as those of the longitudinal case. Results are presented separately in the following two sections.

3.5.1 Ailerons deflection

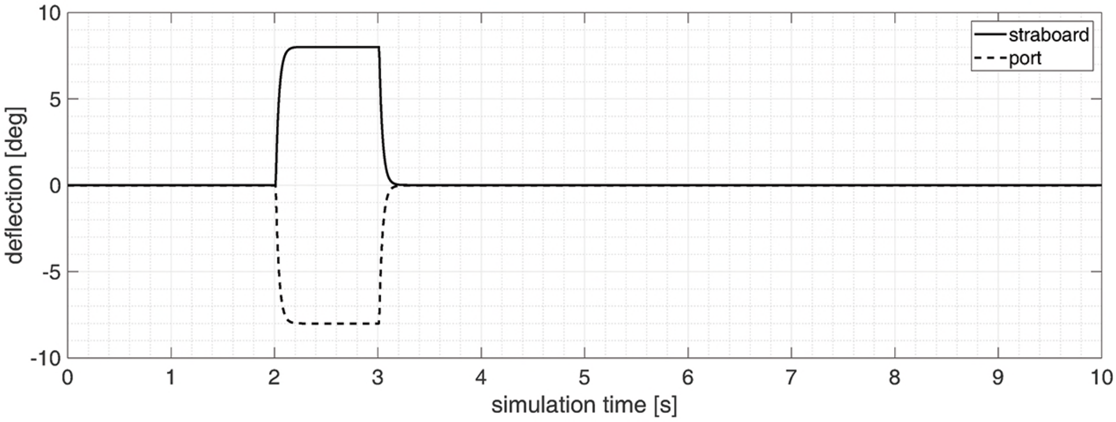

Fig. 3.12.: Aileron deflection for lateral-directional flight dynamics assessment.

The time history of the ailerons deflection is shown in Figure 3.12. Ailerons were deflected asymmetrically by 8 degrees in order to produce a right turn. Figures 3.13 and 3.14 show the lateral-directional response of the the aircraft to the prescribed input.

Figures 3.13 shows the response of the GTM for the scaling factor c = 3.5, which corresponds to the first mode natural frequency of $f_1 = 0.57$ Hz, and different values of damping. The lateral-directional response still diverges for $\zeta = 2\%$, but when compared to the longitudinal case is less severe. Although it was expected the lateral-directional response to be mainly affected by the asymmetric mode, i.e. the 5^{th} mode, it was decided to focus on the 2^{nd} mode. In fact, the modes impact on the aircraft response depends on the values of the scaling vector, k, defined in Equation 3.30. The impact of k on the lateral-directional response is further discussed later in the chapter. For values of the damping different from 2%, the response is non-oscillatory although steadily diverging from the rigid body one, except for p, which converges to the rigid response. The impact of the frequency is shown in Figure 3.14. It is evident that when the structural natural frequency overlaps the Dutch roll ($f_1 = 0.57$ Hz

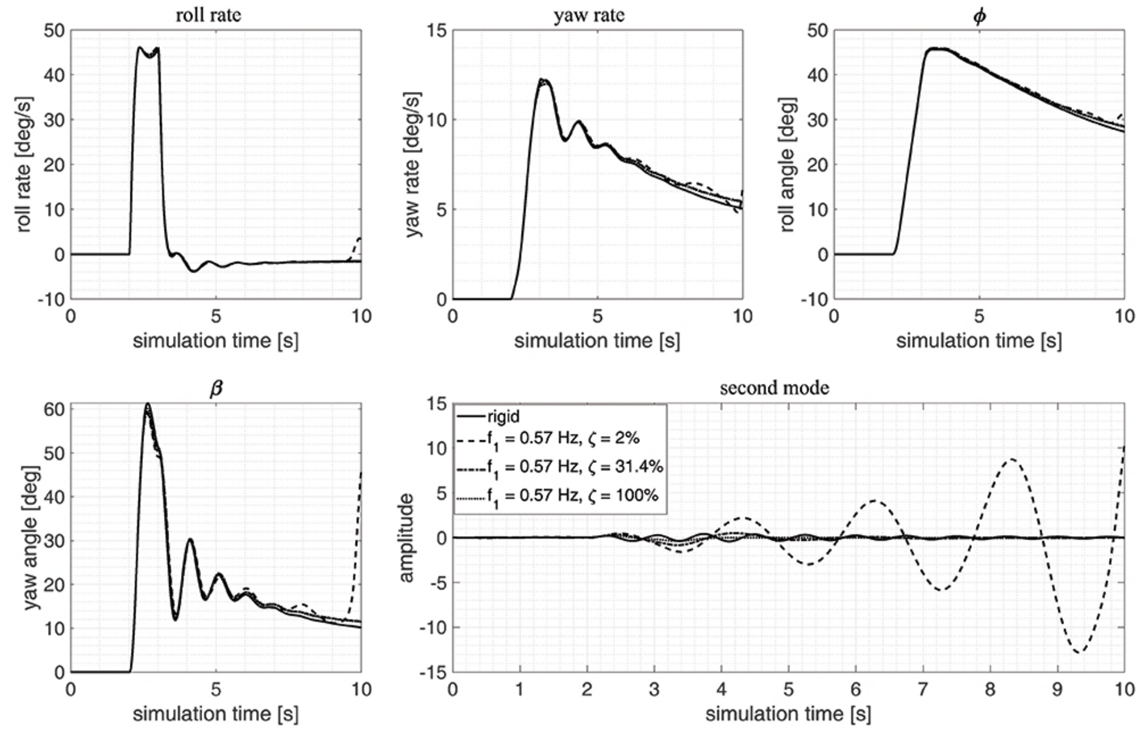

Fig. 3.13.: GTM lateral-directional response to ailerons input for $f_1 = 0.57$ Hz and different values of damping.

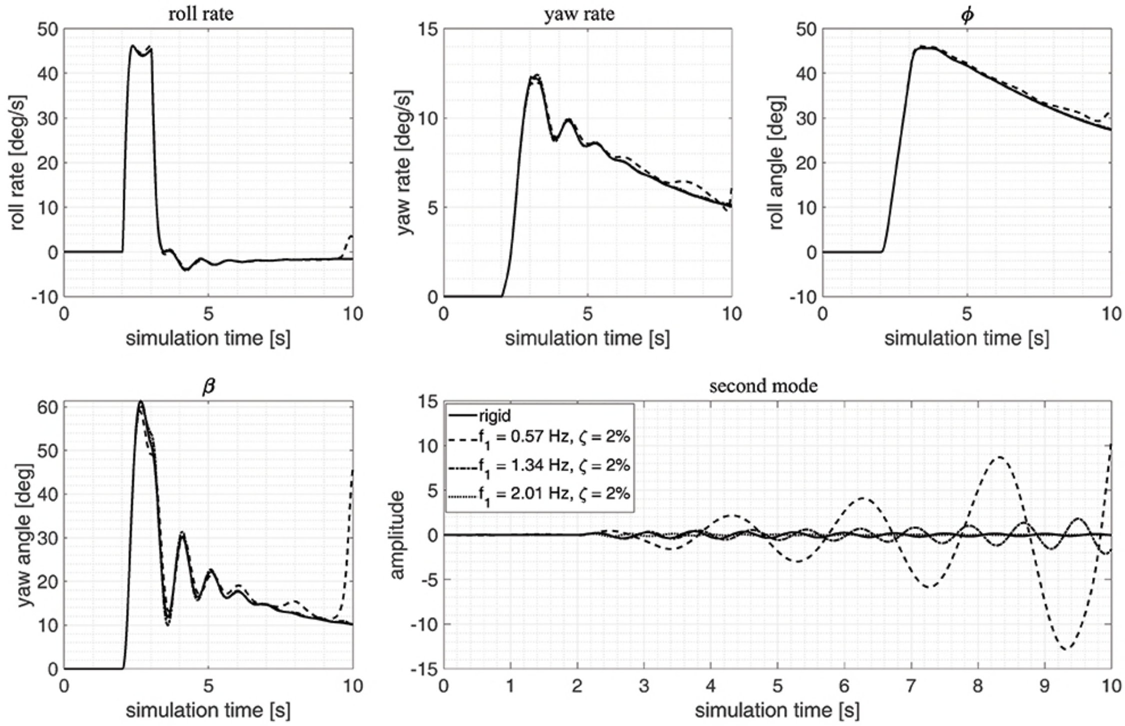

Fig. 3.14.: GTM lateral-directional response to ailerons input for $\zeta = 2\%$ and different values of frequencies.

and $f_1 = 1.34$ Hz), if the damping is not high enough to attenuate the coupling, the response diverges. In fact, mode plot shows that the second mode diverges oscillating for $f_1 = 1.34$ Hz, producing an unstable response of the aircraft for $t \gg 10s$.

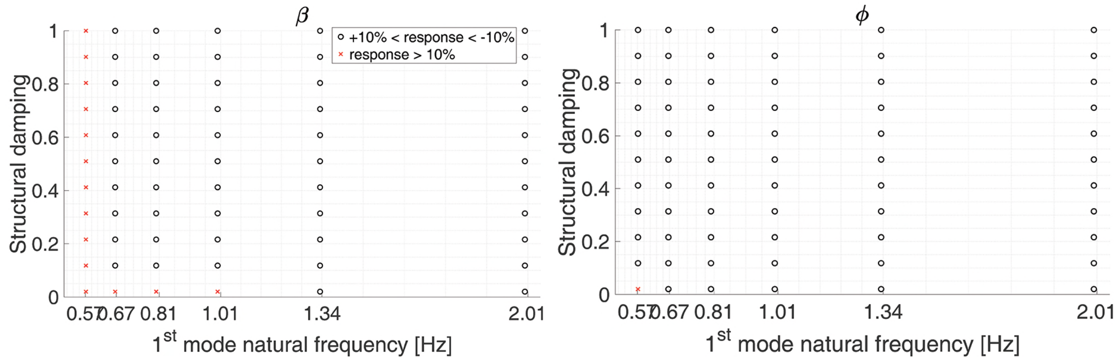

(a) Sideslip angle β *steady-state* grid. **(b)** Roll angle ϕ *steady-state* grid.

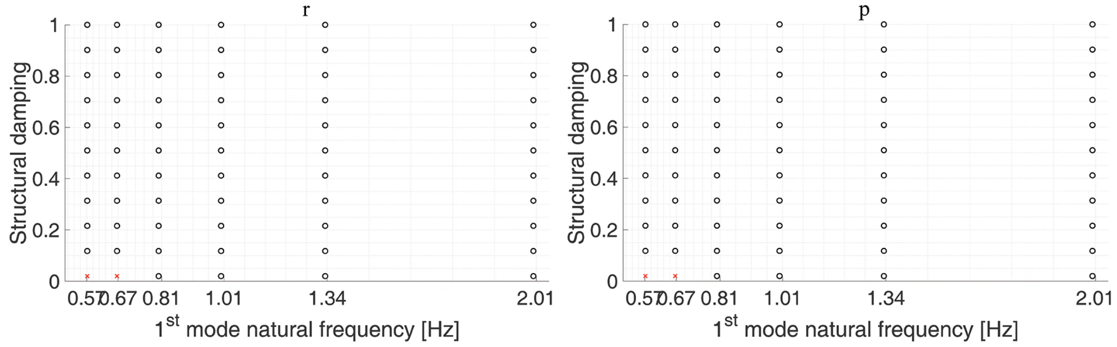

(c) Yaw rate r *steady-state* grid. **(d)** Roll rate p *steady-state* grid.

Fig. 3.15.: *Steady-state* grid plots for lateral-directional dynamics due to aileron input.

Equations 3.33-3.35 were applied again to derive the *steady-state* grid plots for the lateral-directional response to aileron input. The plots general outcome is that the lateral-directional response is not heavily affected by the flexible/rigid coupling. In fact, the roll angle, the roll rate and the yaw rate diverge from the rigid body response only for a combination of low frequency and damping. The sideslip angle, instead, shows more non-converging points (Figure 3.15a). The angle β is non-converging for all combinations of damping at $f_1 = 0.57$ Hz. However, as shown in Figure 3.13, for $f_1 = 0.57$ Hz and $\zeta = 100\%$ the response does not oscillate, although it settles on a steady state value grater than 10% with respect to the rigid case. The comparison of results in Figure 3.10 with results in Figure 3.15 shows that in the context of this work, the impact of flexibility is more limited on the lateral-directional response than the longitudinal case.

3.5.2 Spoilers deflection

The final case to be considered is the aircraft lateral-directional response to spoilers input. The spoilers deflection is shown in Figure 3.16. Both the inboard and outboard port spoilers were deflected by 15° at t = 2 s, aiming to excite the rigid dynamics frequency of $f_{sp} = 0.5$ Hz. Only port spoilers were deflected, while starboard spoilers were not used during the simula-

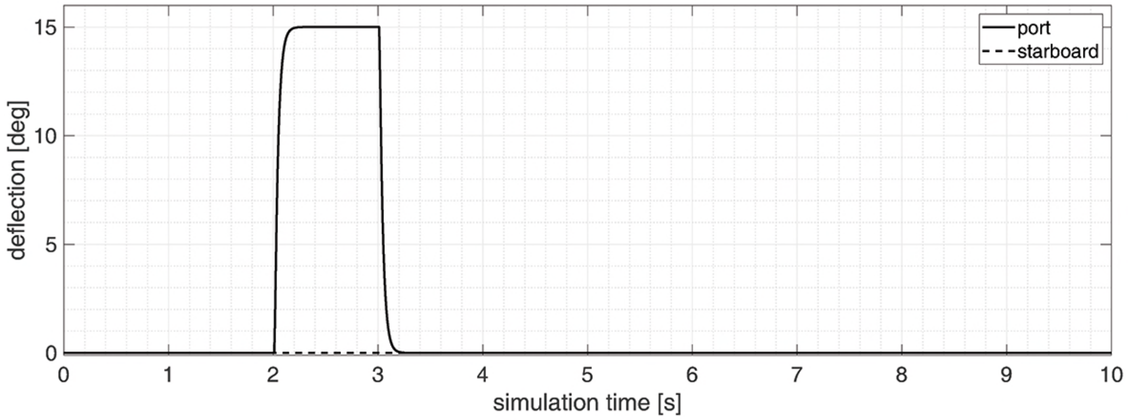

Fig. 3.16.: Spoilers deflection for lateral-directional dynamics assessment.

tion in order to generate a negative rolling moment. The output of the simulations is the one defined for the lateral-directional dynamics analysis, stated in Equation 3.36.

The response of the aircraft is shown in Figures 3.17 and 3.18. As seen earlier for the response to aileron input, the impact of flexibility is not as significant as in the longitudinal case. Figure 3.17 shows the response of the GTM for $f_1 = 0.57$ Hz and different values of damping. The response oscillates when the value of the damping is as small as $\zeta = 2\%$. Mainly the impact of structural flexibility is to make the response to steadily diverge from the rigid body one. The magnitude of the mode oscillation is now even lower than the aileron input case. Figure 3.18 instead shows the impact of the structural natural frequency, plotting the response for $\zeta = 2\%$ and different values of frequencies. The outcome from the plot analysis is that when the two dynamics overlap ($f_1 = 0.57$ Hz and $f_1 = 1.34$ Hz), the response of the aircraft becomes unstable and diverges oscillating from the rigid body response. Such behaviour can be predicted from the natural mode behaviour (Figure 3.18, bottom right) that is unstable for ($f_1 = 0.57$ Hz and $f_1 = 1.34$ Hz).

The *steady-state* grid plots analysis was performed for spoilers input and plotted in Figure 3.19. The impact of the spoilers on the lateral-directional dynamics is relatively modest. In fact, yaw rate and roll angle flexible response always converge to the rigid body response, for all combinations of structural frequencies and damping. The flexible roll rate response instead diverges from the rigid body response only for combinations of low modal frequencies and damping. The sideslip angle however, presents the worst behaviour among the considered parameters. It was seen that for low values of frequency and damping, the response of β is not converging, while for higher values of damping, although the steady-state plot shows that the response does not satisfy the convergence criterion, the flexible β response simply settles to a steady state located outside the convergence region.

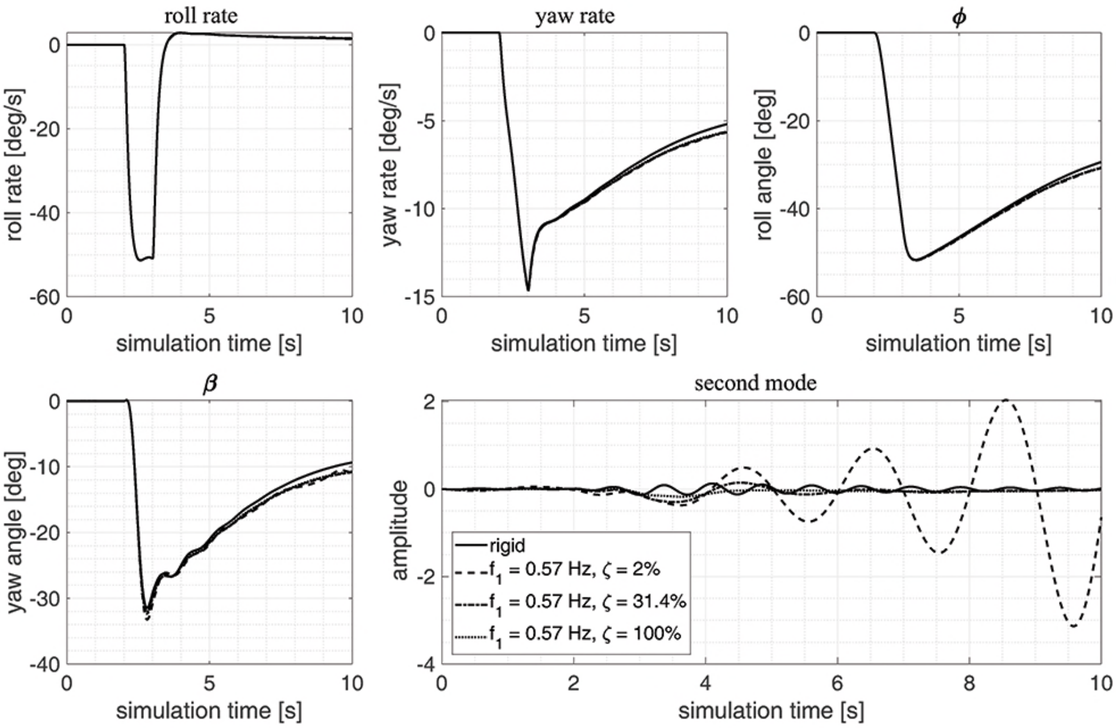

Fig. 3.17.: GTM lateral-directional response to spoiler input for $f_1 = 0.57$ Hz and different values of damping. It is important to stress that the frequency in the legend refers to the first bending frequency.

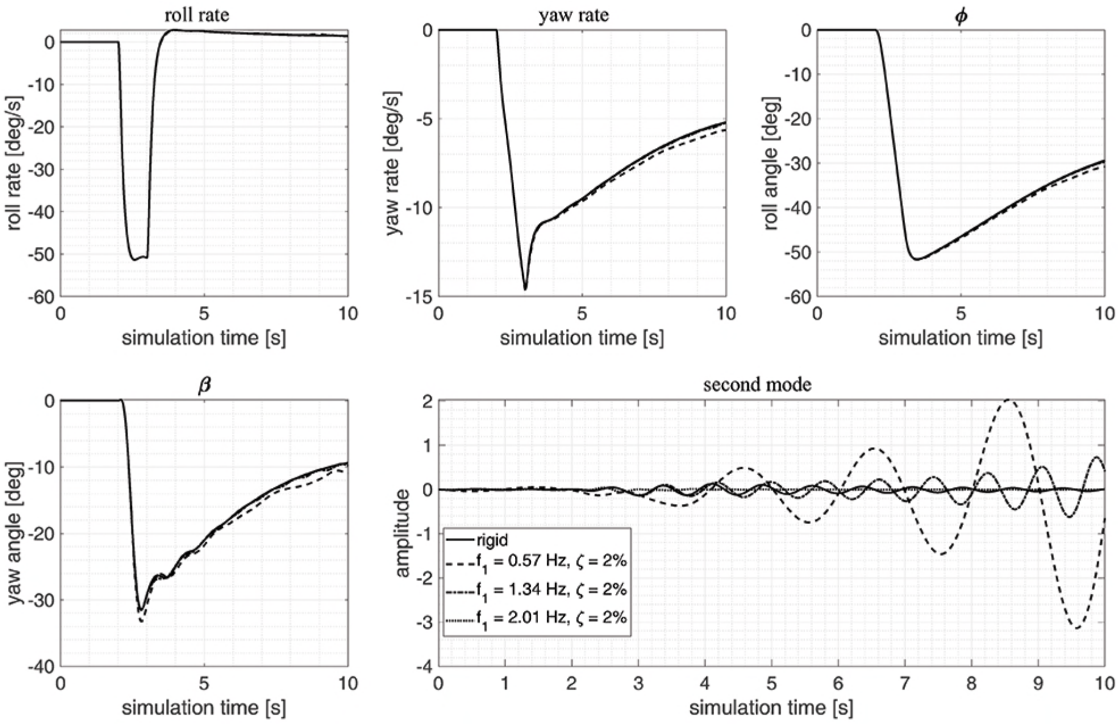

Fig. 3.18.: GTM lateral-directional response to spoiler input for $\zeta = 2\%$ and different values of frequencies.

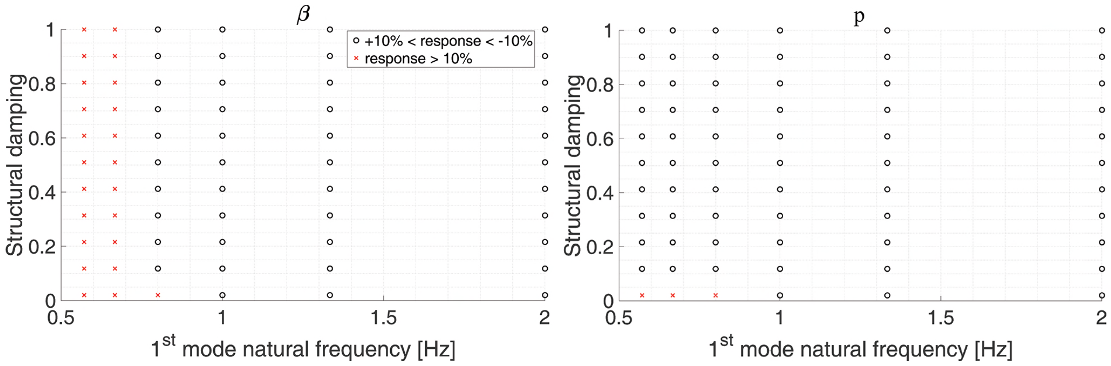

(a) Sideslip angle β *steady-state* grid. **(b)** Roll rate p *steady-state* grid.

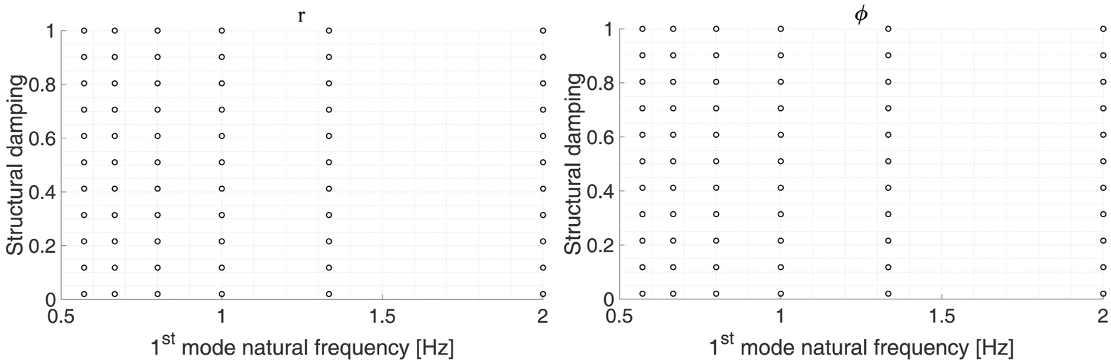

(c) Yaw rate r *steady-state* grid. **(d)** Roll angle ϕ *steady-state* grid.

Fig. 3.19.: Steady-state grid plot for lateral-directional dynamics analysis due to spoiler input.

3.6 Discussion and next step

The chapter has proposed a method to augment rigid flight dynamic models with structural dynamics to consider the effects of aeroelasticity on flight dynamics. The model used to demonstrate the methodology was the NASA Generic Transport Model. This model provides rigid EoM of a 5.5% scaled model derived from the Boeing 757. Flexible Equations of Motion derived from the work done by Waszak and Schmidt[180] were merged and adapted to the GTM model in order to account for structural flexibility. A flight dynamics assessment was carried out for the longitudinal dynamics (elevator input), and the lateral-directional dynamics, (spoilers and ailerons inputs), following a parametric investigation where combinations of structural natural frequencies and damping were simulated.

The study has shown that flight qualities generally degrades with the aircraft being more flexible as structural dynamics overlaps rigid body dynamics. In particular, it has been highlighted that when the structural modes are triggered and the structure is not stiff *enough*, some form of modal control is necessary to damp the response and avoid divergence. The impact of structural dynamics has been seen to be more severe in the longitudinal case than the lateral-directional cases. However, this aspect of the problem cannot considered properly investigated. In fact, while the qualitative impact of flexible structure on the aircraft dynamics is well represented, its magnitude of response is not representative of the considered aircraft as it depends on the scaling coefficient given in Equation 3.27. However, these coefficients were manually tuned within the scope of this investigation and therefore not descriptive of the GTM aircraft. In general three types of responses were observed:

- unstable, when the structural damping is not able to attenuate the flexible response and it diverges exponentially;
- converging, when the flexible response converges to the rigid response for $t \gg 1s$, and
- stable, when the flexible response does not oscillates for $t \gg 1s$ but still converges towards a steady state value different from the rigid body one.

In order to summarise the response of the aircraft across the simulation domain, the steady-state grid plots were introduced. Such approach allows to have an overview of the flexible response of the aircraft in the steady state case compared with the rigid body response. These plots re-emphasize the more severe response for longitudinal cases. Although the idea behind the convergence criterion for comparing the steady state is to provide a global overview of the flexible response, some improvements are definitely required:

- the definition of the convergence region must be updated. In fact, when the magnitude of the rigid steady state response is too small, i.e. close to zero, the margin to get a converging flexible response is so limited that the response, almost certainly, results in being outside the convergence region.
- A definition to capture the nature of the non-converging flexible response, either oscillatory divergent of non-oscillatory divergent, must be considered as it makes an important difference knowing if the response strictly diverges or simply settles steadily outside the 10% boundary of the rigid response.

This chapter provided a deeper insight into the types of interactions that should be expected when flight dynamics are coupled with structural dynamics. This is applied in the following chapter to improve and understand the limitations of aeroelastic frameworks adopted to assess the response of the flexible high aspect ratio wing aircraft.

4

Aeroelastic frameworks and BeaRDS programme

The Cranfield Accelerated Aircraft Loads Model (CA^{2}LM) framework was used to investigate the effects of the airframe flexibility on aircraft gust response. CA^{2}LM was originally known as the AX-1 framework and developed in partnership with Airbus UK by Andrews [5, 6]. The original framework was implemented within a MATLAB® /Simulink environment with an aim to enable research of aeroservoelastic phenomena. The model was used successfully through the years to investigate the coupling of flight and structural dynamics. Examples of the framework's application are the work carried out by Lone[107, 109, 106] to investigate the pilot-in-the-loop impact on the handling qualities of the flexible aircraft, the work done by Dussart [59, 60, 62] who investigated pilot-in-the-loop effects on flight dynamics and the use of folding wingtips as GLA and finally, the work carried out by Portapas [134, 135] on flexible aircraft handling qualities.

The CA^{2}LM framework's ability to run in real time is made possible by the low-fidelity approach adopted for modelling structures and aerodynamics. CA^{2}LM was partially validated with flight test data [5] and CFD analysis [32]. While these studies gave an initial insight into the framework limitations, an experimental programme was developed for an in-depth assessment of these limitations and to evaluate resulting impact on the design of Gust Load Alleviation (GLA) systems. The consequent wind tunnel test campaign (discussed in Chapters 5 and 6) is part of the Beam Reduction and Dynamic Scaling (BEaRDS) programme. The aim and the scope of the BEaRDS programme is to develop a design loop covering the design of flexible models, the respective dynamic scaling of properties, manufacturing techniques and testing of such scaled models in the wind tunnel to reproduce the dynamics of the full scale model. As part of the BEaRDS project, an aeroelastic framework was derived from CA^{2}LM to assist the designer in its design process. The software, BEaRDS Theoretical Model (BEaRDS^{TM}), was developed by several people, but primary by Yusuf [191]. The main differences between the two frameworks are i) the absence of the rigid body equations of motion in BEaRDS^{TM} due to the fact the model is assumed to be constrained in the wind tunnel and ii) BEaRDS^{TM} simulates only one wing.

This chapter aims to provide the reader with a concise overview of both CA^{2}LM and BEaRDS^{TM} simulation frameworks together with key assumptions. Moreover, the method for modelling control surface aerodynamics will be presented. CA^{2}LM and BEaRDS^{TM} effectively constitute the core modelling and simulation engines that were used to obtain the results presented in Chapters 5, 6 and 9.

4.1 CA^{2}LM aeroelastic framework

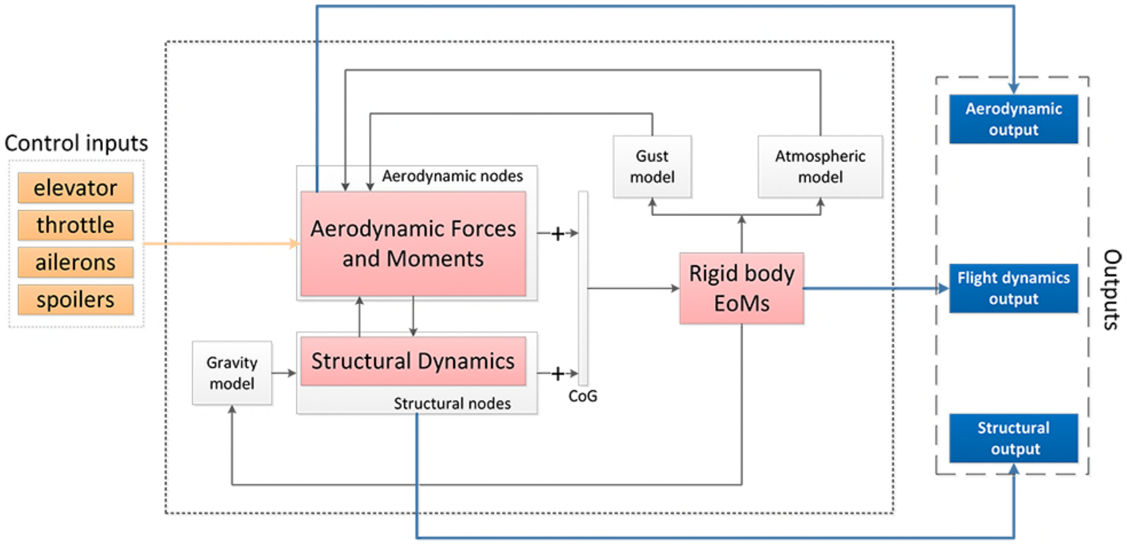

Fig. 4.1.: CA^{2}LM framework architecture.

Aerodynamic and structural dynamics models within of CA^{2}LM were designed as low-fidelity models to meet the requirement for real time simulations of any aircraft configuration[1] on flight simulators. To achieve that, computationally expensive methods such as CFD or complex FE structural analysis were discarded in favour of more simplified modelling techniques. The framework uses state-space models for time-domain simulations of both structures and aerodynamics. Although the development of CA^{2}LM is not part of this study, an overview of the framework is introduced here for two main reasons:

- the CA^{2}LM simulation environment was used to design an industrially viable GLA system for flexible aircraft and,
- the author designed and implemented a methodology to simulate the non-linear effects of spoilers for real time simulations within CA^{2}LM .

The general architecture of CA^{2}LM is shown in Figure 4.1. Central to the framework is the coupling of the aerodynamic block (responsible for computing the aerodynamic load at the aerodynamic stations) and the structural block (which computes the internal load to provide nodal displacement, velocity and acceleration). Aerodynamic and structural calculations are referred to different nodes in order to decouple the density of the grid for the calculation of the aerodynamic and internal loads. Two grids are defined in the initialisation routine. A function that transfers the load from the aerodynamic nodes to the structural nodes is also implemented within the framework.

---

[1] The model can be loaded in CA^{2}LM either by providing structural and aerodynamic grids along with M,K and modal properties separately or by including the NASTRAN .bdf file of the aircraft structure. In the latter case, CA^{2}LM is able to derive mass and stiffness distribution as well as modal properties by coupling MATLAB with NASTRAN. It is however required that the FE aircraft model is already reduced to beam model.

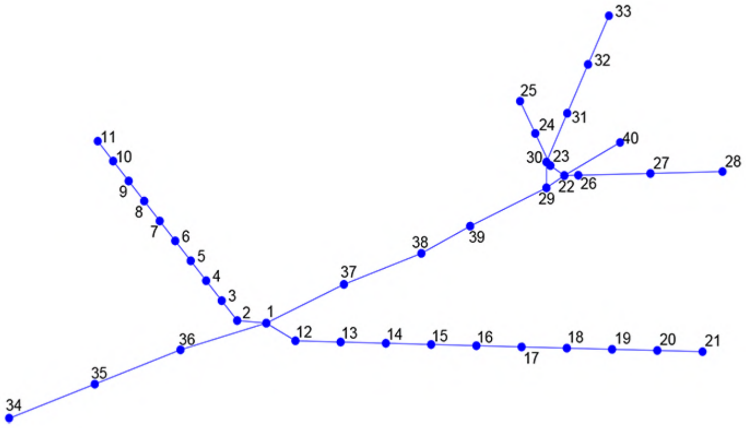

Fig. 4.2.: Example of the beam reduction of the aircraft structure. Numbered are the nodes of the structural grid [5].

The inputs of the model are the control surface deflections and throttle. The main outputs are aerodynamic forces and moments, structural loading and displacements and flight dynamic parameters, such as Euler angles, angular rates and accelerations. The word *main* was used to stress the concept of modularity behind the CA^{2}LM design. In fact, new features can be easily added as a new block with its own inputs/outputs, interacting with the other blocks but still functioning independently. The simulation environment is completed with

- the Equations of Motion block which produces translations and rotations of the centre of gravity,
- the Gravity block, to include gravitational effects,
- the Atmospheric model to extract air characteristic at a specific altitude and
- the Gust block, to simulate *1-cosine* and turbulence environment.

For the purposes of this work, only the aerodynamic and structural blocks are discussed in more detail.

4.1.1 Structural modelling

The Structural Dynamics block is responsible for computing the internal structural loads, displacements, velocities and accelerations at each structural node. The airframe is modelled using a set of beam and node elements (refer to Figure 4.2). Each node can translate and rotate in six degrees of freedom. The global mass [M] and stiffness [K] matrices are built to reflect the properties of the structure at each node. The stiffness matrix defines characteristics of each beam element as bending, axial extension and torsion properties, while the mass matrix contains characteristics of each node in terms of mass and inertia derived by the properties of the surrounding beams.

The overall flexible equations of motion of the structure are derived through the Lagrangian approach. The kinetic energy of the system is defined as:

$$T = \frac{1}{2}\sum_{i=1}^{n} m_i \dot{U}_i^2 \tag{4.1}$$

where U is the node displacement, n is the number of nodes and m the mass of the node. Considering the coordinate transformation given by:

$$U_i = \sum_{k=1}^{n} \frac{\partial U_k}{\partial \upsilon_k} \upsilon_k \tag{4.2}$$

where υ_k is the generalised coordinate. Applying the Langrange formulation, the equation of motion can be written as:

$$\frac{d}{dt}\left(\frac{\partial T}{\partial \dot{\upsilon}_i}\right) - \frac{\partial T}{\partial \upsilon_i} + Q_{E_i} - Q_{D_i} = Q_{A_i} \quad i{=}1{,}...N \tag{4.3}$$

where Q_{E_i} are the elastic force, Q_{D_i} the damping force and Q_{A_i} the applied force. A general approach however, is to express the equations of motion in terms of the generalised coordinate $\bar{\Gamma}$. Given the coordinate transformation:

$$\boldsymbol{U} = [\Omega]\bar{\boldsymbol{\Gamma}} \tag{4.4}$$

where Ω represents the normal mode shape matrix. After some manipulation, Equations 4.3 can be formulated as:

$$\ddot{\bar{\boldsymbol{\Gamma}}} + 2\zeta\omega\dot{\bar{\boldsymbol{\Gamma}}} + \omega^2\bar{\boldsymbol{\Gamma}} = \frac{[F]}{[M]} \tag{4.5}$$

where ω is the natural frequency vector, ζ is the structural damping vector and *[F]* and *[M]* are the generalised force and mass matrix respectively, defined as:

$$[F] = [\Omega][F][\Omega]^{-1} \tag{4.6}$$

$$[M] = [\Omega][M][\Omega]^{-1} \tag{4.7}$$

representing the generalized forces and masses respectively. Structural damping is considered constant and equal to 3%. Equations 4.5 is made of r equations, where r is chosen so that Equation 4.5 is representative of the model dynamics in the bandwidth of interest. Therefore, the first r natural frequencies and mode shapes are calculated solving the eigenproblem associated with the solution of the characteristic equation defined as:

$$\det\big([K] - \omega^2[M]\big)\Omega = 0 \tag{4.8}$$

CA^{2}LM is coupled with MSC NASTRAN to extract the first r undamped modal frequencies and mode shapes of the selected structure to be used in the structural solver.

Finally, the elastic equations of motion in state-space form are expressed as:

$$\dot{\boldsymbol{x}} = \begin{bmatrix} \mathbf{0} & [I] \\ \omega^2 & 2\zeta\omega \end{bmatrix} \boldsymbol{x} + \begin{bmatrix} \mathbf{0} \\ [M]^{-1} \end{bmatrix} [F] \tag{4.9}$$

$$\bar{\boldsymbol{\Gamma}} = \begin{bmatrix} [0] & [I] \end{bmatrix} \boldsymbol{x} \tag{4.10}$$

where $\boldsymbol{x}$ represents the state vector. For more details on the derivation of the equations of motion the reader is referred to Andrews [5].

The rigid body equations of motion are derived applying the mean-axis assumption[2], which allows the decoupling of rigid-body motion and elastic deformation. The derivation of the rigid equations of motion is done through a Newtonian approach and implemented in CA^{2}LM as follows:

$$\frac{\mathrm{d}\boldsymbol{\omega}_B}{\mathrm{d}t} = [I]_B^{-1} \left(\boldsymbol{m} - \boldsymbol{\omega}_B \times I_B \boldsymbol{\omega}_B \right) \tag{4.11}$$

$$\frac{\mathrm{d}\boldsymbol{v}_B}{\mathrm{d}t} = \frac{\boldsymbol{f}_B}{\bar{M}} - \boldsymbol{\omega}_B \times \boldsymbol{v}_B \tag{4.12}$$

where *[I]* is the inertia matrix in body axis, $\boldsymbol{f}_B$ is the force vector in body axis and $\bar{M}$ is the total mass.

4.1.2 Aerodynamic modelling

CA^{2}LM aerodynamics is a combination of theoretical models, namely strip theory, with empirical data extracted from ESDU data sheets. Empirical data are used to adjust aerodynamic load estimation, especially where linear theoretical models cannot be applied for drag prediction, aerodynamic 3D effects or fuselage/wing interaction. Aerodynamic loads are calculated locally at each aerodynamic station, and a modified version of the strip theory is used to extend the 2D results to the overall wing. The architecture of the Aerodynamic block

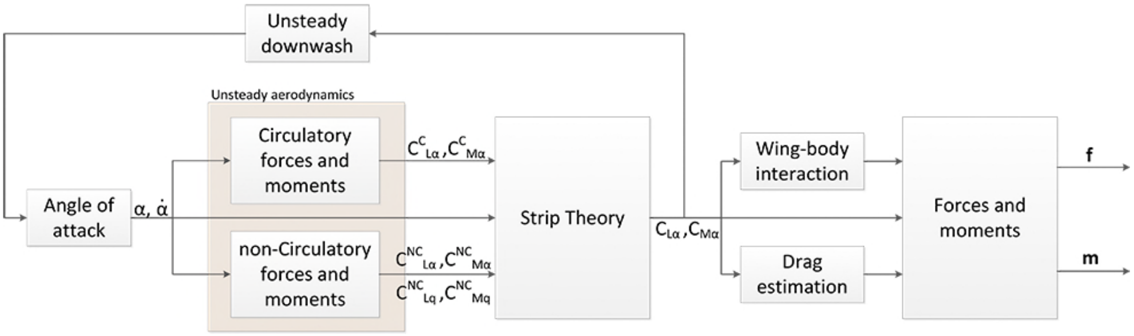

Fig. 4.3.: CA^{2}LM aerodynamics estimation.

---

[2] The mean-axes system is defined as a frame of reference which does not remain fixed during the motion but it is free to float relative to the body. It is chosen such that the angular and linear momentum are zero at every time step with respect to the body axis. Such an assumption allows the decoupling of the rigid body motion from elastic deformations.

is shown in Figure 4.3. The same approach is used to evaluate aerodynamic forces and moments for wings, and the empennage. Inputs are the angle of attack α for the wing and the horizontal tail plane (HTP) and the side-slip angle β for the vertical tail plane (VTP). Angles are *local* and calculated at each aerodynamic node depending on local twist, bending and flow characteristics. The effective angle of attack of the tailplane also considers the unsteady downwash generated by the wing.

The unsteady aerodynamics is implemented as a two-dimensional indicial model [5, 133]. To model the unsteady build-up of lift due to changes in angle of attack and airspeed, a state-space representation of the unsteady aerodynamics of the aerofoil was implemented following the work done by Leishman et al. [101]. This method calculates the unsteady aerodynamic forces change due to an arbitrary motion of the aerofoil as the superposition of the indicial lift response applying the principle of the Duhamel's integral [22][3]. The Wagner function, $\phi_W(\tau)$, linked to the unsteady change of the angle of attack, is defined as:

$$\phi_W(\tau) \approx 1 - 0.918 e^{-0.366\tau\bar{\beta}^2} - 0.082 e^{-0.102\tau\bar{\beta}^2} \tag{4.13}$$

which accounts for compressibility effects through the coefficient $\bar{\beta} = \sqrt{1 - Ma^2}$ introduced by Beddoes [98]. Coefficients of Equations 4.13 were derived by Leishman in order to obtain the indicial response approximation for a two dimensional subsonic flow [100].

The overall unsteady aerodynamic response can be considered as the contribution of two terms: First, the non-circulatory term, which is proportional to the vertical acceleration, is related to the motion of the body and it is also known as apparent mass. It decays rapidly from its initial value and it is important at relatively high values of reduced frequency[4]. Second, the circulatory term, which represents the effect of lift generation and vortex shedding and it is relevant at low values of reduced frequency. Leishman and Nguyen[101] have shown that the circulatory response due to a change in angle of attack can be formulated in state-space form as:

$$\begin{bmatrix} \dot{x}_1 \\ \dot{x}_2 \end{bmatrix} = \left(\frac{2V}{c}\right)\bar{\beta}^2 \begin{bmatrix} -b_1 & 0 \\ 0 & -b_2 \end{bmatrix} \begin{bmatrix} x_1 \\ x_2 \end{bmatrix} + \begin{bmatrix} 1 \\ 1 \end{bmatrix} \alpha_{3/4}(t, \phi_W) \tag{4.14}$$

$$\alpha_{3/4} = \alpha(\phi_W) + \frac{q_\alpha}{2} \tag{4.15}$$

$$q_\alpha = \frac{\dot{\alpha} c}{V}. \tag{4.16}$$

---

[3] The Duhamel's principle is a method of obtaining the response of linear systems to time-variant inputs, where the response of the system can be decomposed in a series of impulse responses.

[4] The reduced frequency is defined as

$$k = \frac{\omega L}{V}$$

where ω is the oscillation frequency of the phenomenon, L is a characteristic length and V is the velocity. The parameter is crucial for unsteady aerodynamics and provides the number of times the aerofoil oscillates by the time a particle of flow travels across the chord.

where $\boldsymbol{x}$ is the state vector defined by Leishman et al. in [101], $\alpha_{3/4}$ is the angle of attack defined at the aerofoil 3/4-chord position and q_α is the dimensionless pitching moment due to the change in angle of attack.

Furthermore, the circulatory term is given as:

$$C_N^C(t) = 2\pi\left(\frac{2V}{c}\right)\beta^2\begin{bmatrix} A_1 b_1 & A_2 b_2 \end{bmatrix}\begin{bmatrix} x_1 \\ x_2 \end{bmatrix} \tag{4.17}$$

where $\boldsymbol{A}$ and $\boldsymbol{b}$ are derived by Leishman [99] from experimental oscillatory measurements.

The overall unsteady lift acting on the aerofoil is the sum of the circulatory and the non-circulatory components and functions of the angle of attack and pitch rate, as follows:

$$C_N(t) = C_N^c(t) + C_{N_\alpha}^{nc}(t) + C_{N_q}^{nc}(t). \tag{4.18}$$

where $C_{N_\alpha}^{nc}(t)$ and $C_{N_q}^{nc}(t)$ are the non-circulatory terms due to change in angle of attack and pitch rate respectively. The unsteady aerodynamics coefficients are fed into the linear aerodynamic block which evaluates lift and moment coefficients, where the local angle of attack at each aerodynamic station is obtained from the local unsteady angle of attack as:

$$\alpha_n = \frac{W_n}{V_n}\phi_W(\tau) \tag{4.19}$$

where W_n and V_n are respectively the vertical and axial components of the local air velocity.

The spanwise lift distribution is found by applying the Modified Strip Theory (MST). MST was developed by Weissinger [184] who showed that the aerodynamic loading of a finite wing can be represented by a series of horseshoe vortices. The downwash in a generic point P (x, y) due to the effect of the horseshoe vortices is given as [184, 5]:

$$w = \frac{\mathrm{d}\Gamma}{4\pi h}\left(\cos\theta_1 + \cos\theta_2\right) + \frac{\Gamma h\,\mathrm{d}s}{4\pi r^3} \tag{4.20}$$

where $\mathrm{d}\Gamma$ is the vortex strength of vortex line element $\mathrm{d}s$, r is the distance of the point (x, y) from the vortex line, h is the perpendicular distance of P from the vortex line and θ_1, θ_2 are geometric parameters dictated by the position (x, y). By finding the integral solution of Equation 4.20, the aerodynamic loading at any point can be found.

De Young and Harper [50] discretized Equation 4.20 into m control points and showed that the solution can be expressed as [6, 50]:

$$c\,C_{l_v} = \sum_{n=1}^{m} A_{vn} G_n \alpha_n, \quad n = 1, 2, \ldots, m \tag{4.21}$$

where A_{vn} is the influence matrix which defines the effect of circulation of node v on the downwash at node n. The load coefficient G is the dimensionless circulation which describes the strength of the circulation at any node n. In CA^{2}LM the control points are assumed to be at the aerodynamic nodes. Look-up tables are used to compute values for C_{L_0} and C_{L_α} as functions of Reynolds and Mach numbers[5]. The coefficients are evaluated by adopting codes such as XFoil or AVL for example. These are needed to compute steady aerodynamics at aerodynamic nodes. The use of these software for the evaluation of the coefficients introduces limitations in the stall region modelling as XFoil and AVL are linear aerodynamic solvers. Once the aerodynamic forces and moments at each node are obtained, the load is transferred from nodal-axis to body-axis to provide an estimation of lift, drag and moment acting on the aircraft structure.

The drag force coefficient at each aerodynamic station is given as the sum of the profile drag, C_{D_0}, and the induced drag, C_{D_i}. C_{D_i} is evaluated as the sum of two contributions: the trailing vortices $C_{in_{iv}}$ and the lift-dependant viscous phenomena $C_{in_{vc}}$. The expression of drag is thus:

$$C_D = C_{D_0} + C_{in_{iv}} + C_{in_{vc}} \tag{4.22}$$

Lift-dependant drag is given as:

$$C_{in_{vc}} = K_{D_i} C_{L_i}^2 \tag{4.23}$$

where the coefficient K_{D_i} is estimated from empirical data extracted from ESDU 07003[166] and expressed as:

$$K_{D_i} = \frac{1.15}{a_{1_w}} \left(1 - \left(\frac{a_0}{a_{0_T}} \right)_\eta \right) \tag{4.24}$$

where a_{1_w} is the lift slope of the wing, a_0 is the lift slope of the aerofoil section and a_{0_T} is the inviscid lift slope of the aerofoil section.

A validation study of the CA^{2}LM aerodynamics was carried out and discussed in Carrizales et al.[32]. The study performed a CFD simulation based on Reynolds-Average Navier Stokes equations (RANS) of the original AX-1 aircraft in different configurations. Results show that while there is agreement in the lift prediction, the drag values are far off from the ones estimated by CA^{2}LM . The limitation on the drag estimation however is considered to not impact the outcome of this work as for GLA applications the lift force has the most important role in driving the transient structural response of the wing due to gust encounter.

4.1.3 Control surface modelling

The original control surfaces modelled in CA^{2}LM were ailerons, elevators and rudder. Contribution of control deflections is effectively modelled as a change to the wing camber line that allows local contributions to be evaluated through strip theory. The associated transient dynamics leads to an unsteady value of local lift, which is calculated again as the sum of both

---

[5] Limits of the framework are linked to the conditions used to evaluate C_{L_0} and C_{L_α}. Specifically, the flight envelope is limited to a Mach number range of 0.05 to 0.8 and an angle of attack range of $-10°$ to $+15°$.

circulatory and non-circulatory component. Using the aileron as example, the lift force due to the trailing-edge control surface deflection is given as[5]:

$$C_{L_{\xi_i}} = C^{C}_{L_{\xi_i}} + C^{nc}_{L_{\xi_i}} + C^{nc}_{L_{\dot{\xi}_i}} \tag{4.25}$$

where ξ is the aileron deflection angle. The expressions of $C^{C}_{L_{\xi_i}}$, $C^{nc}_{L_{\xi_i}}$ and $C^{nc}_{L_{\dot{\xi}_i}}$ are beyond the scope of this chapter and the reader can find the definition of the coefficients in Leishman [100] and Andrews [5]. The contribution of the control surface deflection is defined as a ΔC_L and added to the local aerofoil lift coefficient at each time step. This impacts the calculation of the drag at the local aerofoil section as defined in Equation 4.23.

An extra ΔC_D is provided by the ESDU 87024[170] method. The datasheet provides an empirical estimation of the drag increase due to the deflection of trailing edge flaps. The increase in drag is given as:

$$\Delta C_D = k(\gamma)F(\delta_f, \gamma, c_f/c) - F(0, \gamma, c_f/c) \tag{4.26}$$

where δ_f is the flap deflection, γ is the trailing edge camber line, and c_f/c is the flap to section chord ratio. The function F and coefficient k are defined as:

$$F(\delta_f, \gamma, c_f/c) = \frac{c_f}{c}\sin^2(\delta_f + \gamma)\cos(\delta_f + \gamma) \tag{4.27}$$

$$k(\gamma) = 1.0 - 0.005\gamma^2 \tag{4.28}$$

Control surface actuator dynamics are modelled using transfer functions. For example, the aileron actuator dynamics of the HARTEN aircraft was modelled as a second order transfer function as follows [64]:

$$\frac{\xi}{\xi_d} = \frac{-1.77s + 399}{s^2 + 48.2s + 399} \tag{4.29}$$

Similarly, elevator and rudder actuators were modelled as the following second and third-order transfer functions respectively, as follows:

$$\frac{\eta}{\eta_d} = \frac{-8.42s + 2046}{s^2 + 102.87s + 2046} \tag{4.30}$$

$$\frac{\iota}{\iota_d} = \frac{-12.6s^2 - 1185s + 27350}{s^3 + 77.7s^2 + 3331s + 27350} \tag{4.31}$$

Saturation and rate limits for the control surfaces can also be implemented. Table 4.1 contains the data used for the HARTEN example.

	Saturation	**Rate limit**
Aileron	±25 deg	±60 deg/s
Elevator	±30 deg	±60 deg/s
Rudder	±30 deg	±60 deg/s

Tab. 4.1.: CA^{2}LM control surfaces saturation and rate limits.

4.2 The BeaRDS programme

Each numerical model by definition approximates some aspects of the physical problem (the CA^{2}LM framework is not an exception). The BEaRDS programme aims to carry out an assessment of the limitations of the model and modelling methods rather than attempt its validation. Most of these limitations are likely to emerge when structural deformations become *non negligible*, inducing non-linearities. The definition of a *non-linear* system is not strictly defined as susceptible to the definition of the system itself and its parameters[6]. Within the aerospace community, it is generally accepted that linear models are valid for vertical tip deflections below 10% of the wingspan. Hence there is a need to develop a procedure to validate non-linear models of flexible aircraft, for which wing-tip deformations are expected to be large.

The BEAM Reduction and Dynamic Scaling programme (BEaRDS) therefore aims to provide a tool to design, dynamically scale, manufacture and test flexible structures in wind tunnel facilities in order to validate aeroelastic non-linear models used to evaluate the response of very flexible structures. The importance of wind tunnel tests lies in predicting possible problems linked with interactions between aerodynamic loads and resulting structural response, that can be too expensive to fix at the flight test stages. However, the BEaRDS programme aims to extend this work by providing a new manufacturing technique that allows to decouple mass and stiffness design of dynamically scaled flexible wind tunnel models. Along with that, BEaRDS provides an aeroelastic framework, called BEaRDS Theoretical Model (BEaRDS^{TM}), that helps the designer to predict loads and deflections and to tailor the model design for a specific test.

Figure 4.4 presents the BEaRDS work flow. The programme is run in two different phases in order to develop the technology and the skills needed to proceed in the testing of dynamically scaled models. The two phases are described as follows:

(I) *Phase I* aimed to develop a novel manufacturing methodology to overcome limitations of previous models, as broadly described in the literature [104, 163, 164]. A common way to manufacture flexible models is to use rigid pods to define the aerodynamic shape of the wing and to transfer the load from the surface to main structure, usually

---

[6] Mathematically speaking, linear operators are well defined. Instead, when considering more complex problems and their approximations, these boundaries are looser and the definition of linearity is not always shared in the academic community. Cambridge dictionary defines linearity as something that *involves a series of events or thoughts in which one follows another one directly*. However, the main problem is to define the meaning of *directly*, which in the modelling language translates as *proportionally*. When considering the response of a system, H, if the system is *assumed* linear, it is expected that the system obeys the principle of superposition: given two inputs, $u_1(t)$ and $u_2(t)$, the system response should be the linear combination of the two:

$$H(k_1 u_1(t) + k_2 u_2(t)) = k_1 y_1(t) + k_2 y_2(t)$$

Most of the time, however, a system cannot be defined as linear in the whole domain of interest. It is more common to define regions where the linear assumption is valid. An example is the lift slope curve, C_{L_α}, which is commonly linear in specific ranges of angles of attack and becomes non linear when 3D effects are not negligible. When considering the deformation of the wing structure, the system is usually considered linear below a specific threshold defined in functions of the wing-tip displacement.

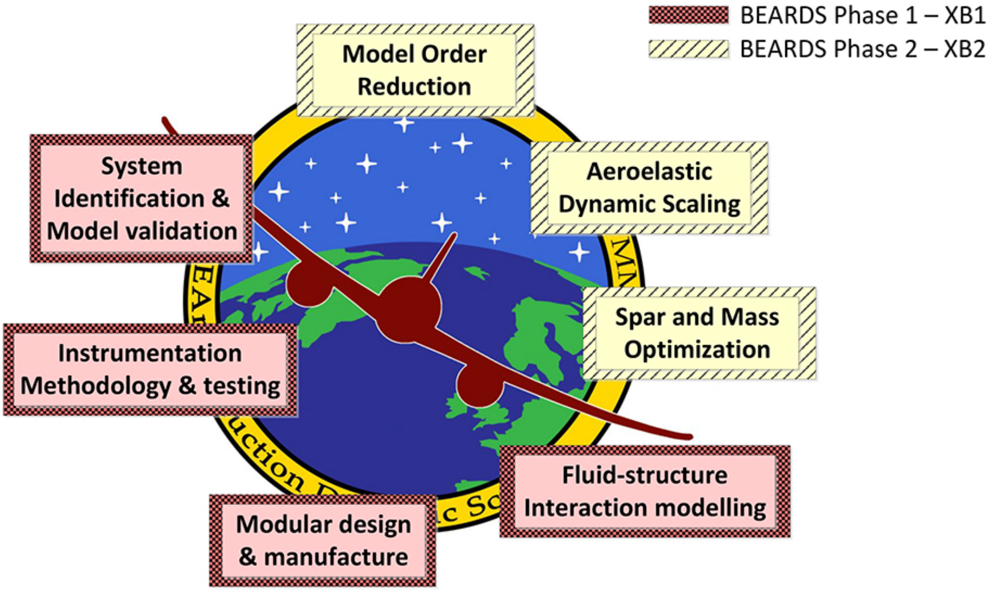

Fig. 4.4.: BEaRDS steps. The programme was divided in two different phases: Phase-1 aimed to build the first BEaRDS flexible model (XB-1), which worked as proof-of-concept for the new manufacturing technology and material. Phase-2 instead focused on the design, manufacturing and testing of a 1.5 m long dynamically scaled model (XB-2), by applying skills gained through the first phase of the programme.

a metal spar. Pods are built with different techniques, from being 3D printed to using carbon fibre or more commonly using foam. Benefits and drawbacks are associated with each of these approaches. During the first phase of BEaRDS these aspects are evaluated and a novel manufacturing process is developed in order to improve testing of flexible models. Result of Phase I is the manufacturing and testing of the eXperimental BEaRDS 1 (XB-1), a proof-of-concept flexible model tested in the Cranfield Weybridge wind tunnel.

(II) *Phase II* transfers the skills acquired from Phase I to the development of a 1.5 m wingspan flexible wind tunnel model, the eXperimental BEaRDS 2 (XB-2). The manufacturing process of the XB-2 model required a detailed design which adopted new solutions to distribute correctly the structural and inertial characteristics of the model along the spar. Ground Vibration Tests (GVT) were carried out to assess the structural properties of the model and to validate the numerical model used to predict structural loading and deformation. Eventually, the model was tested in the Cranfield 8x6 ft subsonic wind tunnel. The acquisition system used was an improved version of the one designed for the XB-1 test. More details on the XB-2 test campaign are discussed in Chapter 6.

In general, the whole programme is divided into several steps. Referring to Figure 4.4, a short description of BEaRDS objectives are provided here:

(i) **Fluid-Structure Interaction Modelling**. To assist the user with the design and testing of the flexible wing model, the BEaRDS programme provides a numerical aeroelastic framework able to predict aerodynamic and structural loads, nodal displacements, velocities and accelerations. The BEaRDS Theoretical Model (BEaRDS^{TM}) is derived from CA^{2}LM and simulates a cantilever half-wing model. The simulation environment provides two different approaches of solving the structures: a Reduced Order Model (ROM) approach using modal states and a newly modelled FE solver which sees the structure modelled in a state-space form, where mass and stiffness matrices are built following the Przemieniecki theory [138]. The latter approach was a new feature introduced in the framework which is not included in CA^{2}LM .

(ii) **Modular Design & Manufacture**. The BEaRDS models were built and designed following the modularity philosophy, which is essential for design management and risk mitigation. In fact, the programme aims to provide a low-cost but reliable manufacturing and experimental methodology. Building the wing as an assembly of few parts allows to replace a single section rather than the entire wing when needed. This approach extends the capabilities of the models and mitigates the risk in case of damage.

(iii) **Instrumentation Methodology**. The core of the BEaRDS acquisition system is the RaspberryPi board, responsible for acquiring and displaying data. The communications between the board and the control computer is wireless over the WiFi local network. The RaspberryPi samples data from four different sensor boards, each one featuring the MPU6050 sensor. The software running on the RaspberryPi was coded in-house using Python language.

(iv) **System Identification & Model Validation**. This is undertaken on the scaled model to identify aeroelastic parameters of the flexible wing. Modal properties were identified using ground vibration testing, while the aerodynamic coefficients were extracted from the wind tunnel data. System identification studies were also carried out to assess the impact of the skin on the overall wing stiffness [191].

(v) **Model Order Reduction**. Providing a full FE model of the aircraft means that its properties must be condensed into a simpler model such as beam element model in order to run into the BEaRDS flow. Hence, the need of a tool that could provide a reduced order model of any aircraft geometry. At this stage, this step has not been developed as a specific BEaRDS tool. Instead, the model used in this work was already provided as a beam element model. A possible alternative is to use available software, such as the NeoCASS suite[36, 35].

(vi) **Aeroelastic Dynamic Scaling**. As part of the full scale model response validation, the BEaRDS programme provides a numerical method able to dynamically scale characteristics of the flexible wing. The scaling optimization algorithm is based on the work done by Ricciardi [147, 146] and it is adapted to be integrated into the BEaRDS design loop.

(vii) **Spar and mass optimization**. One of the novelties introduced by BEaRDS is the simplification of the model design assuming the decoupling of mass and stiffness distributions. Behind this approach, there is the assumption that the novel manufacturing process adopted for the skin allows to limit the impact of the skin on the overall stiffness below a maximum of 15%.

Although for the purpose of this work the BEaRDS workflow considered as well the design of an optimized wing tailored for an A320-type concept aircraft, generally the BEaRDS algorithms can be applied to any given aircraft geometry. In fact, the aim of the BEaRDS programme is to develop a tool to assist the researcher to design and test aeroelastic behaviour on any dynamically scaled flexible wing tunnel model with the use of numerical tools for the prediction of the wing response.

4.3 BeaRDS^{TM}

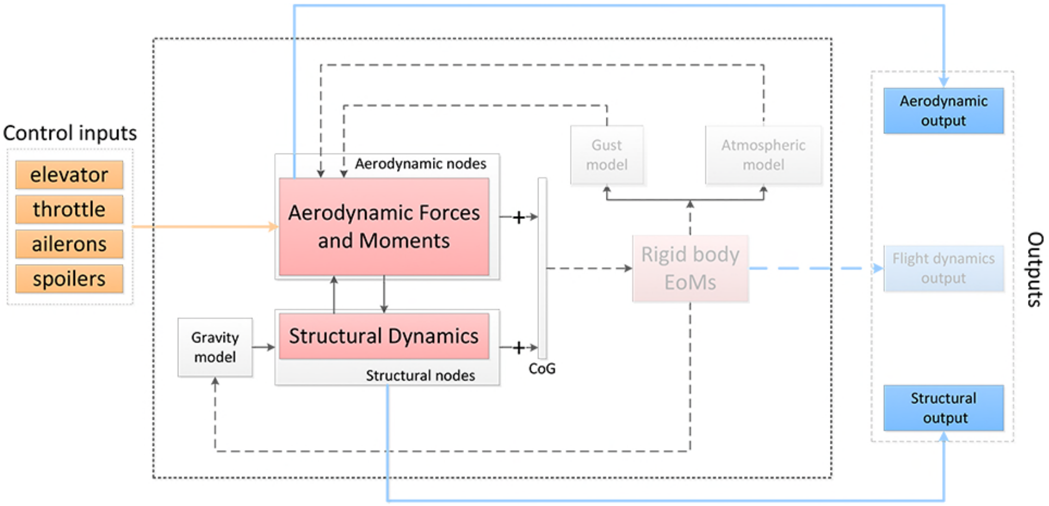

Fig. 4.5.: BEaRDS Theoretical Model Architecture

As previously mentioned, BEaRDS^{TM} is derived from the CA^{2}LM framework. The main difference is that BEaRDS^{TM} simulates a constrained half-wing rather than the full aircraft. To implement that, the aircraft rigid equations of motion block was removed, along with the aircraft dynamics output (Figure 4.5). Scaled equations of motion are implemented in order to scale both structural and aerodynamic response of the model. The framework is also able to simulate the full-scale model. In this case rigid EoMs are retained and BEaRDS^{TM} does not differ much from CA^{2}LM . In BEaRDS^{TM} as well as in CA^{2}LM , follower forces are not modelled and the aerodynamic force is always considered to lie in the plane which contains the local aerofoil. While this assumption is always true for rigid models, it may introduce errors in the force estimation in flexible structures. Discussion on the impact of follower forces can be found in Chapter 7.

Differently from CA^{2}LM , the wing structural model is simply fed into the initialization routine through the NASTRAN .o4 file, which contains model mass and stiffness matrices. The extracted *[M]* and *[K]* matrices are then processed to be used either for the FE state-space approach or for the reduced-order modal approach. In case the latter method is used, the first n natural frequencies and mode shapes are extracted and fed into the structural solver.

The state-space structural dynamics solves the full structural differential equations of motion derived by Timoshenko [173] beam theory approach. The root nodes of the wing model are fully constrained in order to replicate the wing-fuselage structural constraint. For the XB-1 and XB-2 wing, first 3 nodes of the model were constrained. Unlike CA^{2}LM structural damping was modelled as proportional to the stiffness matrix as follows [138, 77]:

$$[C] = \lambda[K]. \tag{4.32}$$

The value of the constant λ was set to be 0.013 [77] for the full scale model and scaled accordingly for the scaled model [191].

The aerodynamic model is the same as in CA^{2}LM . The main modification was carried out by Yusuf [191] into the indicial evaluation for the scaled model. The assumption made was to consider the flow in the wind tunnel as incompressible (the Cranfield 8x6 ft wind tunnel has a maximum Mach number of $Ma = 0.15$). The indicial angle of attack can be considered instantaneous, therefore the non-circulatory terms can be considered negligible. All other aerodynamic parameters included in look-up tables were estimated by Carrizales et al. [31] for the scaled model using the Athena Vortex Lattice (AVL) [7] software along with XFoil [57, 56].

4.4 Discussion and next step

This chapter provides the reader with an overview of the simulation environments used in this work to assess the dynamic response of flexible aircraft. In particular, the CA^{2}LM framework was described with a focus on the aerodynamic and structural modelling approaches. The aeroelastic framework was described as built with low-fidelity models for both aerodynamics and structures to allow real time performance on flight simulators. From here, the need to set up an experimental programme able to assess limitations of the framework through wind tunnel testing was discussed. The BEaRDS programme was then introduced as an experimental work which aims to develop a methodology to design, manufacture and test dynamically scaled flexible wind tunnel models. The BEaRDS^{TM} aeroelastic framework was derived from CA^{2}LM to simulate the wind tunnel test environment of a cantilevered half-wing. Data from BEaRDS can therefore be used to compare the experimental result against the BEaRDS^{TM} prediction.

In the following chapters, the experimental procedure is discussed in detail. In particular, the next chapter shows the novel manufacturing process developed, adopted to overcome previous experimental issues encountered during past tests described in literature and applied to the XB-1 model.

5

eXperimental BeaRDS 1 (XB-1)

eXperimental Beards 1 (XB-1) is the first flexible wing model to be designed and manufactured for wind tunnel testing as part of the BEaRDS programme. The goal of XB-1 is to develop the manufacturing method to overcome common problems in the testing of flexible wings. A discussion of the limitations linked to flexible wind tunnel models was provided in Chapter 2. Mainly this work aims to address the aerodynamic local field perturbation introduced by the gaps in between pods. The model consists of a metal spar designed to take the aerodynamic load covered with an external shell (or skin) with the dual purposes of transferring the load to the spar and maintaining the aerodynamic shape. The XB-1 model was manufactured following a design process[1] where the external shell was 3D printed as a continuum, made of a succession of different materials to allow the wing to deform while preserving the required aerodynamic shape. The need for a new manufacturing approach arises for two reasons:

1. to reduce the impact of the gaps in between shell pods on the aerodynamic performance, while allowing the model to exhibit the desired structural dynamics and
2. to retain the aerodynamic shape when the model bends.

Along with model design, a new low-cost data acquisition system was developed specifically for the BEaRDS programme. The main feature of the system consists of using off-the-shelf low cost components.

In this chapter, the challenges of building a flexible wing model are considered and a possible solution to the problem is provided. It follows the design, manufacturing and structural characterisation of the 3D printed skin along with the development of the acquisition system. The chapter concludes with a brief discussion of the wind tunnel test setup and collected results.

5.1 Problem definition

A common way to build flexible wing models for wind tunnel testing is to reduce the structural properties of the wing on a metal spar and to *wrap* the structure with a shell in order to retain the desired aerodynamic shape [22, 104]. An advantage of this approach is that the impact of the shell on the overall stiffness is minimal [22]. The XB-1 wing design adopts the same approach. These problems are mostly related with the manufacturing of the shell. A

---

[1] As shown in Chapter 2, a common solution to maintain the aerodynamic shape of the flexible model, while allowing the wing to undergo large deformations, is to cut gaps into the skin.

typical way of manufacturing the shell is either to shape it with foam, or to make it as hollow pods connected to the spar or simply using wooden ribs as the main structure covered with some sort of plastic film. Some previous projects have already investigated the impact of different shell types on the model stiffness and Figure 5.1 shows one of the models tested in the aforementioned studies. In this particular test it was seen that the use of plastic film to cover the ribs presents several critical issues:

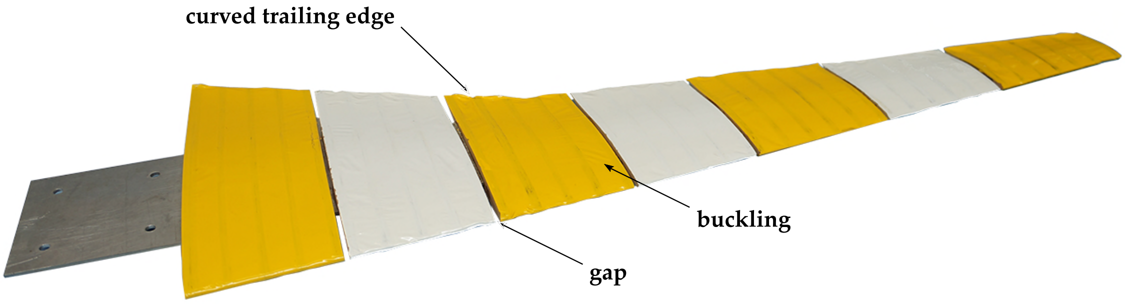

Fig. 5.1.: Previous Cranfield scaled A-13 programme wing buckling of aerodynamic surface

i) the skin is not able to maintain the shape of the leading and trailing edges. When the film is applied it tends to fill the volume in between the ribs.

ii) The top surface buckles when the wing bends. Therefore, the impossibility to maintain the shape of the model makes the wing unsuitable for the purposes of this work.

iii) There is an increase in stiffness when the skin is in tension. While such a configuration might be suitable for an aeroelastic assessment of a generic wing model, it is not applicable for testing dynamically scaled models as the exact knowledge of the stiffness distribution is crucial.

As the aim of the XB-1 is not to scale the full model wing, the spar was not designed within the context of this work. Instead it was inherited from previous designs, specifically from the Cranfield A-13 programme. The focus then was on developing a new manufacturing process for the skin. A first attempt consisted in simply 3D printing skin pods and assembling the wing leaving gaps in between the pods.

A potential problem was identified in the possibility of those gaps to generate aerodynamic interference, changing either locally or globally the aerodynamic load distribution. In order to assess the magnitude of this interference, a CFD[2] study was carried out comparing XB-1

---

[2] Details of the CFD simulation setup are given as follows:

Mesh settings	Values	
	No gaps	Gaps
Edge size (m)	2.5e-3	
Surface size (m)	2.5e-3	
Nodes	884136	800795
Elements	3732206	3531141
Average Skewness	0.2316	0.25368
Average Element quality	0.68866	0.70825

CFD settings	Values
Turbulence Model	K-omega (SST)
Air Density (kg/m^3)	1.225
Air Dynamic Viscosity (kg/ms)	1.7894e-5
Velocity (m/s)	27
Spatial Discretization	Least Squares

aerodynamics of the wing shell in two configurations: with and without gaps in between pods. The numerical evaluation of the aerodynamic coefficients is given in Table 5.1. The presence of gaps leads to a reduction in lift of 22.1% and an increase in drag of 106.5%. The pitching moment instead changes sign, from positive to a negative value. To prevent the interference between the gaps on the aerodynamic properties of the model, electrical tape was applied to the A-13 wing (Figure 5.2). The latter model shared the same spar of the wing model previously described and shown in Figure 5.1, but the skin manufacturing was different as in this case was 3D printed. As expected, the tape was not able to help maintain the aerodynamic shape of the profile. The tape behaved just as the plastic film, buckling in compression and unable to maintain the leading and trailing edge geometry.

	No gaps	**Gaps**	**Diff Δ**
C_L	0.603	0.470	-22.1%
C_D	0.028	0.058	+106.5%
C_M	0.012	-0.108	-194.9%

Tab. 5.1.: Lift, drag and moment coefficient calculated for XB-1 wing flying at $\alpha = 6°$ @ 27 m/s.

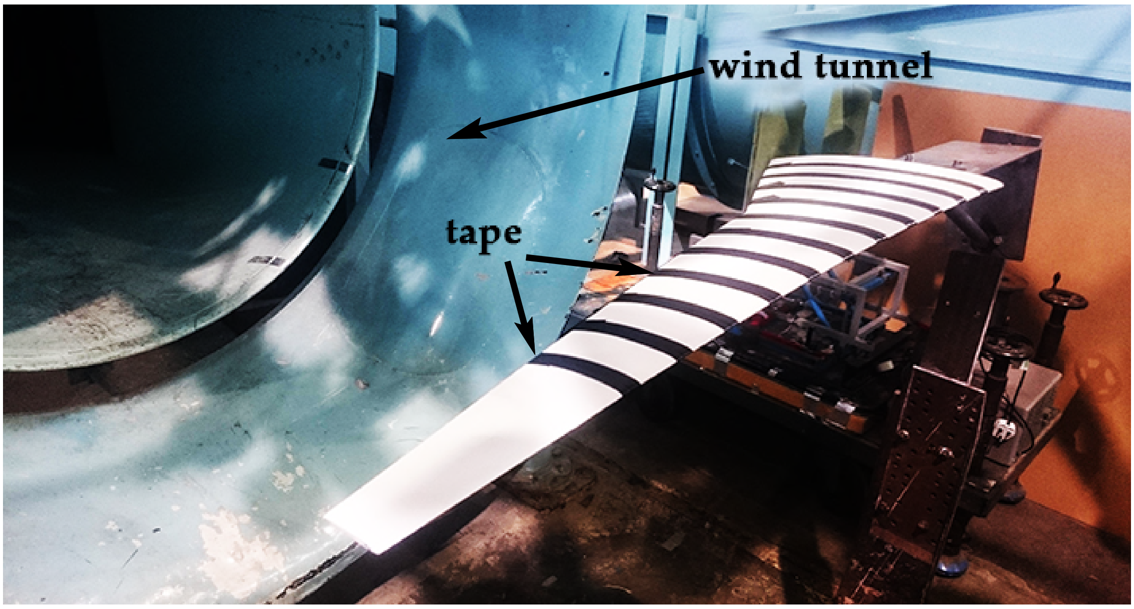

Fig. 5.2.: A-13 wing placed in the wind tunnel and ready for test.

The novel approach adopted in this work to retain the rigid/flexible configuration benefit while removing gaps, involved using the Polyjet 3D printing technology to print the skin. The main advantage of printing parts with the Polyjet is the possibility of using different materials without discontinuity. The gaps were hence covered by flexible pods which are connected to preceding and following rigid pods.

The XB-1 wing is only statically scaled as it was designed to be a proof-of-concept both for manufacturing the skin and developing the acquisition system. The main characteristics of the A-13 are provided in Table 5.2, while the general configuration is presented in Figure 5.3.

In the process of designing the XB-1 model, the wing of the A-13 was statically scaled. The stiffness distribution of the wing was provided by the A-13 design group, so that the XB-1 wing could be designed to match the static deflection for a set of flight conditions. Although the aspect ratio of the A-13 is not higher than current commercial aircraft, the wing was chosen as highly flexible.

Max payload	37000 Kg	**Cruise altitude**	35000 ft
Cruise speed	M 0.78	**Passengers**	209
Wing area	123 m^2	**Root chord**	6.5 m
AR	12	**Wing span**	38.3 m

Tab. 5.2.: Cranfield A-13 Voyager main characteristics

Fig. 5.3.: Cranfield A-13 Voyager

5.2 Skin design

The XB-1 is a 1:22 scaled model which aims to reproduce the static and geometric characteristics of the A-13 Voyager. Details of the XB-1 wing are provided in Table 5.3. It is important to underline that the root section of the model is defined at 0.100 m from the ideal scaled model center line (Figure 5.4c). In fact, the area between the center line and the root of the wing was used to rig the model on the wind tunnel support. As previously said, the spar was not designed within the context of this work. The spar is cranked at 0.357 m from the center line to reproduce the discontinuity provided in the original stiffness distribution. A top view of the spar is shown in Figure 5.4c.

	Value
Model span	0.840 m
Tip chord	0.053 m
Root chord	0.220 m
AR	12
Airfoil	NACA 23015

Tab. 5.3.: XB-1 geometric characteristics

The skin was designed to reflect three main characteristics:

1. To have a minimal impact on the overall stiffness.
2. To cover the gaps while maintaining the aerodynamic shape of the wing.
3. To allow access to the inner volume of the model. This is a requirement set to be able to access the instrumentation system and to fix the skin on the spar.

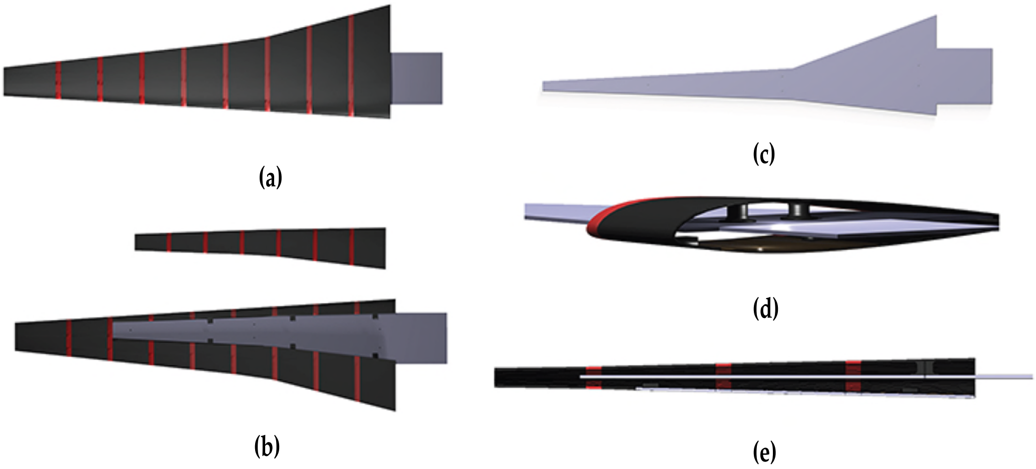

Fig. 5.4.: XB-1 geometry. Figure a) the top-view of the skin as series of rigid (black) and elastic (white) pods. Figure b) bottom view. Figure c) top-view of the aluminium spar. Figure d) and Figure e) details of the rigid pillars used to anchor the skin to spar.

It was necessary to minimize the contact surface between the skin and the spar to achieve the first requirement. However, the contact surface had to be designed such that it could not be too extended to avoid adding stiffness due to friction with the spar and it could not be too small to avoid cracks in the material while transferring the load from the skin to the spar. The adopted solution involved *load pillars* to connect the skin to the spar. These pillars are simply cylinders extruded from the skin. The cylinder's base is in contact with the spar and connected to it through an M3 screw. Seven load cylinders in total were used to connect the spar to the skin and to transfer the aerodynamic load from the shell to the metal structure. This design feature is shown in Figure 5.4d-e.

3D printing is a natural candidate for manufacturing the skin when recognising the complexity of the geometry. In fact, using 3D printing gives the advantage of being able to design as complex geometry as needed. However, the material used for printing can be fragile and may be unsuitable for wind tunnel tests. In order to retain the benefits of the 3D printing and to overcome some of its common drawbacks, the Polyjet technology was opted for. Unlike common 3D printers, where the material is first melted and then extruded through a nozzle before being laid down on the print bed, the Polyjet process effectively sprays the material. In fact, materials are loaded into the printing machine in liquid form and up to 6 different materials at the same time can be used. Once the material is deposited on the bed it is cured and solidified with UV light. The advantages associated with this technology are as follows:

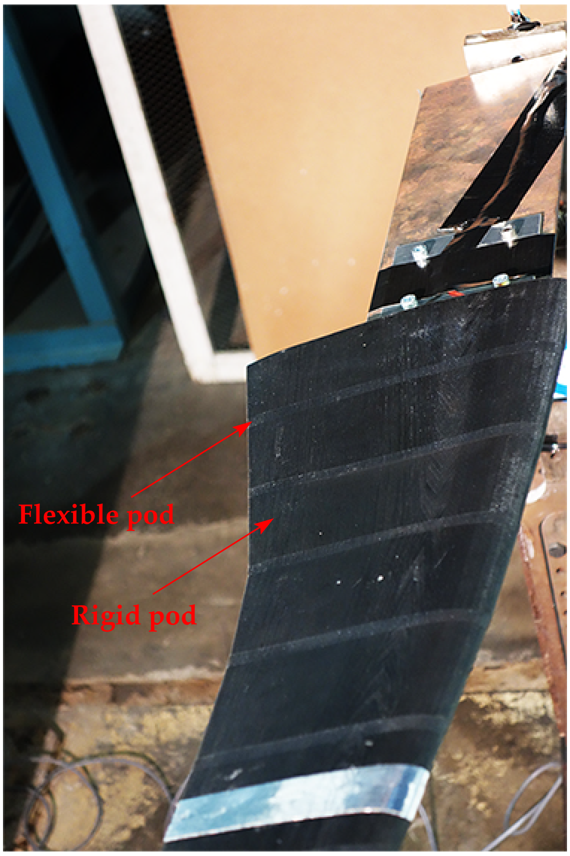

Fig. 5.5.: XB-1 wing rigged in the Weybridge wind tunnel.

i) more than one material can be used to print a piece. Therefore it is possible to print rigid and flexible pods as a continuum, transitioning from one to the other simply mixing the materials. The process allows to control the hardness of the flexible materials as well.

ii) Since the material is sprayed on the printing bed, the finishing of the layers is finer than other technologies that apply the extrusion process.

iii) Resolution of Polyjet is 0.014 mm per layer.

iv) The support material can be printed as soluble so that it can be simply removed submerging the part in the solvent at the end of the process.

The material used for printing the rigid pods was the digital-ABS and the flexible parts used the Agilus30. Details of these two materials are given in Table 5.4 and Figure 5.5 shows the

	Agilus30	**digital-ABS**
Tensile strength [MPa]	2.4-3.1	55-60
Modulus of elasticity [MPa]	-	2600-3000
Density [g/cm^3]	1.14	1.17

Tab. 5.4.: Properties of the materials used for printing XB-1 sections.

skin of the model with its succession of rigid and flexible pods. Rigid pods were printed 100 mm wide and the flexible pods extension was 10 mm. No stress analysis was carried out for the skin sections because failure was not expected based on confidence gained from past experience with the materials used.

In order to address the last requirement of access to the inner volume of the wing, a window was cut in the wing's lower skin which spanned 3/4 of the model span and was fixed to the bottom of the wing with screws. The heads of the screws were flush with the surface to minimise aerodynamic interference. It was observed that due to its length, the window could not follow the deformed wing shape. To account for this problem, more screws were needed to constrain the window to the main skin body in more points and avoid the cover to deform inappropriately[3].

5.3 Experimental setup

An objective of the BEaRDS programme was to develop an affordable low-cost acquisition system. The common choice for professional acquisition systems are either the dSpace board [111, 69] or National Instrument equipment [163, 164] which are extremely reliable and precise but also expensive. The BEaRDS acquisition system instead relies on the Raspberry Pi as the core of the system. The board is in continuous development and for the XB-1 test the Raspberry Pi 2 model B[4] was used. Figure 5.6 shows the architecture of the acquisition system used for both XB-1 and XB-2 tests. The Raspberry Pi is responsible for acquiring data from sensors and to command actions, such as start recording, stop recording, change sample frequencies and shutting down the system. The communication between the user desktop computer and the acquisition board is wireless and the data is transmitted from the Raspberry Pi to the computer for display only. In order to avoid data loss or packages corruption [127, 130] over wireless transmission, data is saved locally on the SD card of the board and

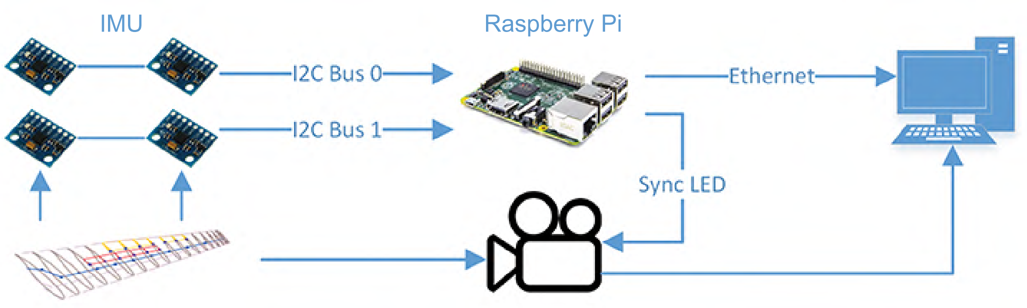

Fig. 5.6.: Instrumentation architecture.

---

[3] Being the XB-1 a proof of concept, no more screws were added for the test and the cover was kept in place with aluminium tape applied in the most critical spots. For a more permanent solution, the XB-2 wing adopts multiple windows rather than a long one.

[4] The Raspberry Pi 2 model B is powered by a Broadcom BCM2837Arm7 Quad Core processor running at 900 MHz. It has 1GB RAM, 4 USB-2 ports and one 10/100 Ethernet port. It has 40 I/O pins which provide serial, I^{2}C and SPI connection interface with external devices.

later downloaded to be processed. Python code specifically written for the test was responsible for the data acquisition, data saving and data wireless transmission.

Wing deformation data is acquired from four different Inertial Measurement Units (IMUs), through two I^{2}C buses. IMUs feature the MPU6050 chip[5] which combines a 3-axis accelerometer and a 3-axis gyroscope. The 4 sensors were distributed over the spar as shown in Figure 5.7. The chip includes a 16-bit Analogue to Digital Converter (ADC), which provides a digital value of acceleration and angular velocity to the board. The sensitivity of the chip is configurable.

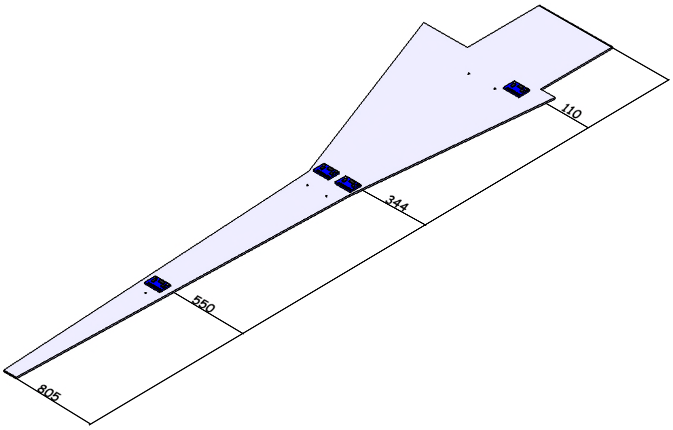

Fig. 5.7.: XB-1 IMUs configuration for wind tunnel test.

In order to assess the error that a low-cost off-the-shelf component could introduce on the measurement due to the hardware limitations, structural tests were carried out on the spar and accelerations recorded both with the MPU6050 sensors and professional laser vibrometer, the Polytec OFV-505 Sensor Head for comparison. Sampling frequency of the MPU6050 was set to 100 Hz and the vibrometer sampled at 1.6 kHz. The input of the test was a sine sweep signal in the frequency 0-60 Hz. Sensors were placed at 20 mm from the tip of the spar to ensure first bending mode was captured. The response of the XB-1 spar to the sine sweep input and the comparison between the acquisition setups are shown in Figure 5.8. The overall response of the tip is shown in Figure 5.8a for both the MPU6050 and the vibrometer. As well Figure 5.8 shows the response in two specific conditions:

- When the response is attenuated (SNR < -4dB), performance of the MPU6050 is not as precise as the one provided by the vibrometer as the Signal to Noise Ratio (SNR)[6] is too low for such low-cost sensor to detect any acceleration. In fact, comparison with

---

[5] The MPU-6050 is a 6-axis device which integrates a 3-axis accelerometer and a 3-axis gyroscope. Communications between the MPU-6050 device and the acquisition board are possible through a dedicated I^{2}C bus. Range of the gyroscope and accelerometer is user-programmable. Gyroscope full-range is ±250, ±500, ±1000, ±2000°/s. Accelerometer full-range is ±2g, ±4g, ±8g, ±16g. Range for the test is set to be ±250°/s for the gyroscope and ±4g for the accelerometer. The maximum communication rate from the device is 400 kHz over I^{2}C.

[6] For this test, the threshold for low SNR was set to -2dB. SNR was calculated as SNR=$20\log(S/N)$

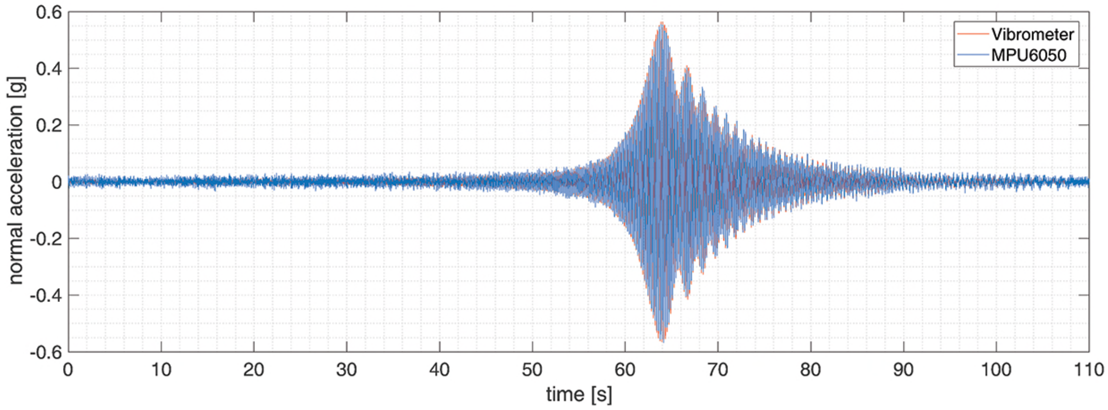

(a) Sine sweep response of XB-1 spar.

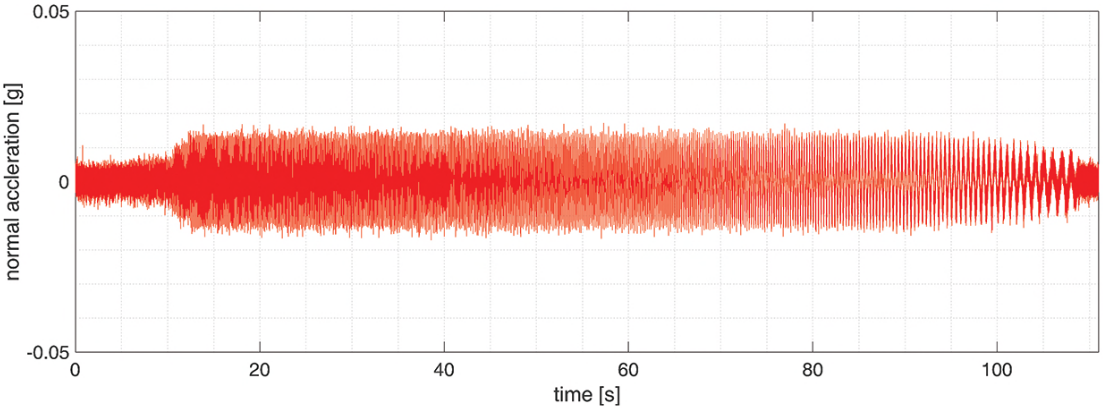

(b) Sine sweep 0-60 Hz input.

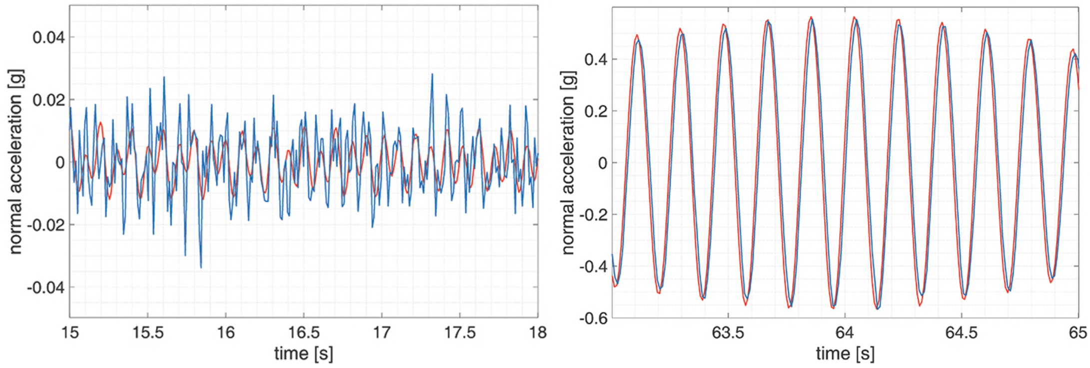

(c) Zoom of the response for low signal to noise ratio.

(d) Zoom of the response for high signal to noise ratio

Fig. 5.8.: XB-1 response to sine sweep signal recorded with MPU6050 sensor (blue) and with Polytec vibrometer (red).

the vibrometer shows an average error of 100% between the two and the inability of the MPU6050 signal to follow tip acceleration due to the high levels of measurement noise.

- For higher accelerations and SNR values (SNR > 10dB) the response from the two systems is practically identical.

System	Pros	Cons
Professional	high performance at low SNR	expensive
	higher sampling frequency	bulky
	less noise	not customisable
	higher resolution	
MPU6050	low-cost	higher noise
	customisable	lower performance at low SNR
	small volume	lower sampling frequency
	light	

Tab. 5.5.: Summary of advantages and disadvantages of professional systems compared with the MPU6050 and Raspberry Pi system.

A summary of the advantages and disadvantages of the two system is given in Table 5.5. In general, for the purpose of this work, disadvantages of the low-cost system are negligible. In fact, although the max sampling frequency achievable is only about 100 Hz, the bandwidth of interest for flight dynamics studies is not wider than 0-50 Hz. As well, the aerofoil chosen, the NACA 23015, is particularly slender and does not leave much volume to host instrumentation and other devices. Professional accelerometers are usually bigger than the small chip featured by the MPU6050 board and might not fit inside the model. For all these reasons, the low-cost acquisition system was considered suitable to be used for the BEaRDS programme.

To complete the experimental setup, an Olympus i-Speed 2[7] high speed camera was used to track the displacement of the wingtip using two markers. Data from the high speed camera was used to validate the shape estimation of the wing, evaluated with IMU data. The acquisition rate of the camera was set to 100 fps. A blinking LED was used to synchronize data acquired by the IMUs and the video recorded by the camera.

5.4 Structural characterisation

The structural assessment of the wing was carried out to satisfy two requirements:

- to validate the modal response prediction from BEaRDS^{TM} and,
- to assess the impact of the skin on the overall model stiffness.

Figure 5.9 shows the Ground Vibration Tests (GVT) setup used to run the structural test. The wing was rigged on the shaker in both configurations, spar-only and full-wing, with the latter including the contribution of the external shell. Attachment of the model on the rig was the same of the one later used in the wind tunnel. The acceleration at the tip was measured both with the MPU6050 sensors and the vibrometer, while the input of the shaker on the root of the wing was recorded with a PCB356B18 accelerometer. Although the low-cost system was in place fully recording, the Frequency Response Function (FRF) was calculated using

---

[7] The camera has an internal memory of 4GB and it is able to acquire up to 200 000 frames per second. The maximum resolution of the frame is 800x600 pixels.

the the vibrometer output as the FRF was directly provided by the lab equipment without any need of post-processing. The FRF in the frequency range 0-100 Hz for the spar-only configuration is shown in Figure 5.10, while the white noise input in the bandwidth 0-625 Hz used for the FRF characterisation is shown in Figure 5.11. The detected frequencies are linked only to the bending modes due to the nature of the uni-directional measurement. The plot shows two different FRF because the test was done twice with the vibrometer placed first at 200 mm and then at 300 mm from the tip to avoid cases where measuring a node of the structure, where displacement might be zero for some mode shapes. Test results provide the first three bending natural frequencies at 5.12 Hz, 22.02 Hz and 55.3 Hz respectively.

	1^{st} mode [Hz]	2^{nd} mode [Hz]	3^{rd} mode [Hz]
BEaRDS^{TM}	6	22.7	58
GVT	5.12	22.02	55.3
Δ	15%	3%	4.7%

Tab. 5.6.: Modal frequencies comparison between BEaRDS^{TM} solver and GVT experimental data.

Meanwhile, a beam model of the spar was modelled in Nastran, the mass and stiffness matrices extracted and the mode shapes and frequencies evaluated from BEaRDS^{TM}. The first three numerical mode shapes are shown in Figure 5.12 they are associated with the following frequencies: 6.0 Hz, 22.7 Hz and 58.0 Hz. A summary of the natural frequencies and the error between numerical and experimental estimation is given in Table 5.6. The comparison of the two sets of results shows numerical and experimental results are in agreement. The maximum error, associated with the first bending mode is 15%, which is still considered acceptable given the scope of the work. The discrepancy might be due to either the sudden change in spar chord at the crank position, or to the numerical inaccuracy of reproducing the physical clamp constraint in the BEaRDS^{TM} framework. All these uncertainties are considered acceptable in the context of the BEaRDS programme due to the nature of the model approximation and the experimental uncertainty.

To assess the impact of the skin on the overall stiffness, the same GVT setup was used to test the full-wing configuration as well. The mathematical assumption for the evaluation of the change in stiffness was done by adopting the simplest relationship to define the natural frequency ω:

$$\omega = \sqrt{\frac{k}{m}} \tag{5.1}$$

where k is the stiffness and m is the mass. Now, let us assume, as defined in the premise of the BEaRDS work, that the stiffness of the two configurations, spar-only (subscript $_{ss}$) and full-wing (subscript $_{ff}$), is the same:

$$k = k_{ss} = k_{ff} \tag{5.2}$$

Therefore, the ratio of the natural frequencies, R, between the two configurations, is defined as follows:

$$R = \frac{\omega_{ss}}{\omega_{ff}} = \sqrt{\frac{k}{m_{ss}}}\sqrt{\frac{m_{ff}}{k}} = \sqrt{\frac{m_{ff}}{m_{ss}}}. \tag{5.3}$$

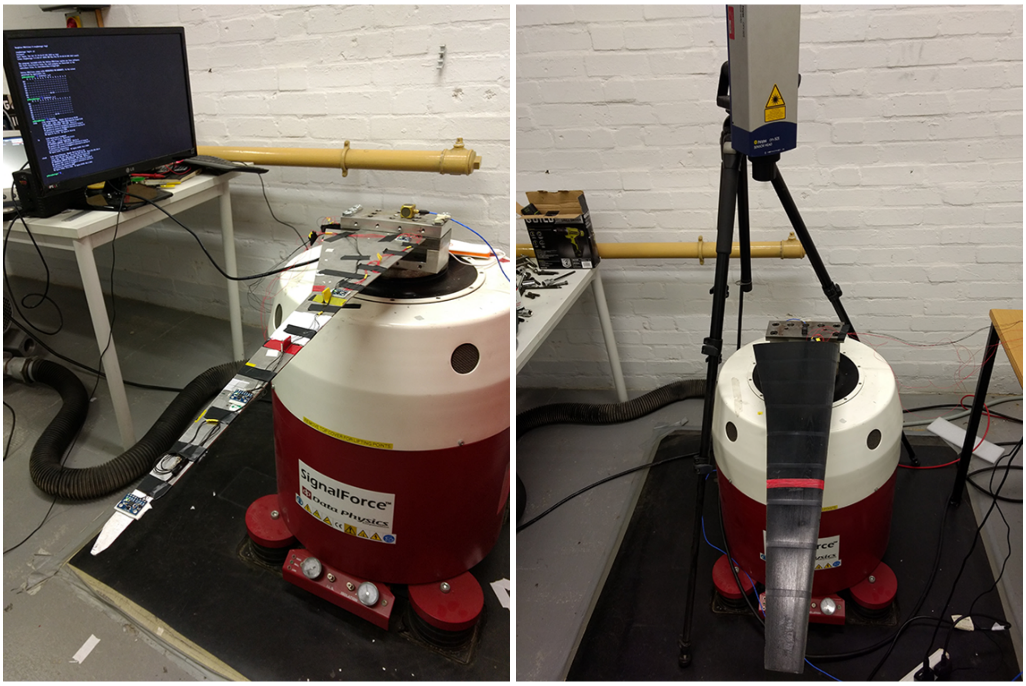

(a) GVT setup for the spar-only model.

(b) GVT setup for the full-wing configuration.

Fig. 5.9.: XB-1 wing model being tested during Ground Vibration Test. Spar only (a) and full wing (b).

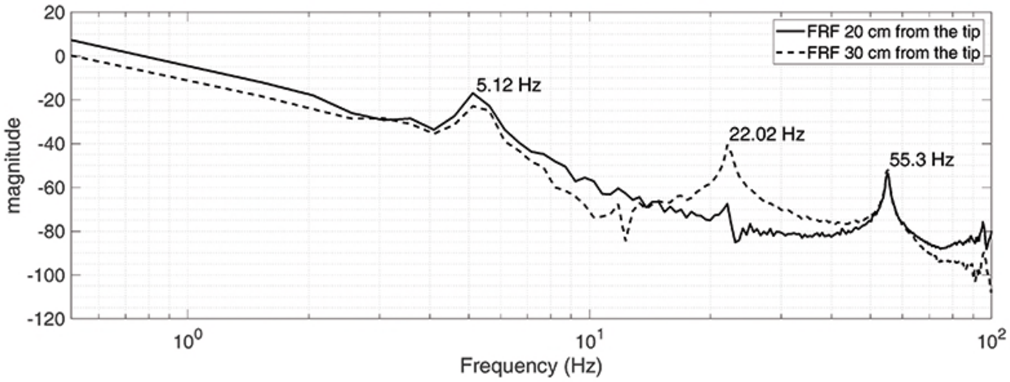

Fig. 5.10.: BEaRDS XB-1 modal response from Ground Vibration Test.

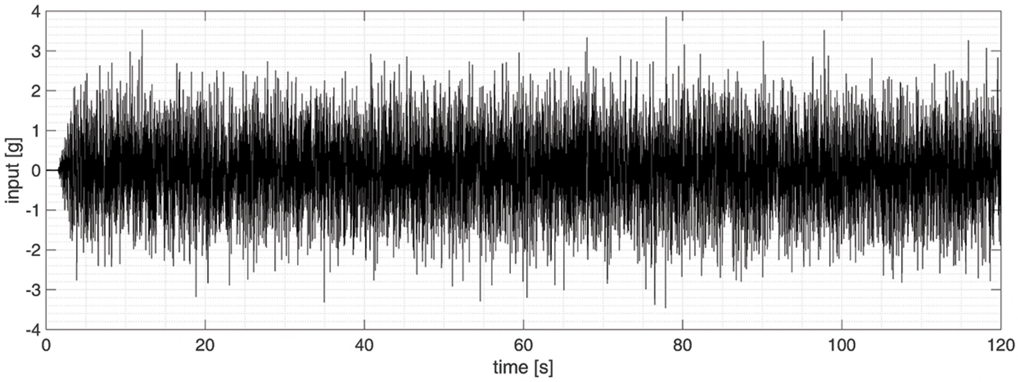

Fig. 5.11.: BEaRDS XB-1 White Noise Input used for FRF characterisation.

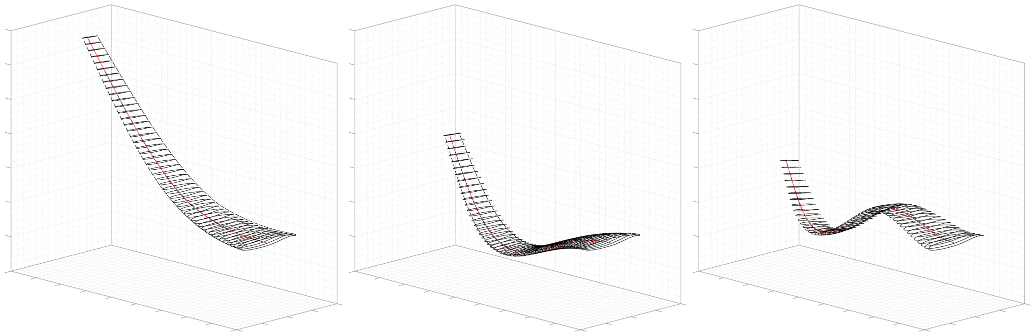

(a) Mode 1 ($6.0Hz$) **(b)** Mode 2 ($22.7Hz$) **(c)** Mode 3 ($58.0Hz$)

Fig. 5.12.: BEaRDS XB-1 dynamic response prediction using BEaRDS^{TM} solver

The total mass of the two configurations was measured providing 0.316 kg for the spar-only configuration and 0.687 kg for the full-wing one. Substituting the value of the masses in Equation 5.3, assuming the same k the ratio between the two frequencies is $R = 1.47$. Difference between the numerical prediction and experimental results is shown in Table 5.7, where Δ quantifies the change in stiffness due to the addition of the skin. The second column of the table shows the natural frequency of the full-wing obtained with the same sine sweep signal used to characterise the wing spar. The natural frequencies of the spar-only configuration are omitted as already provided in Table 5.6. The third column shows the value of the ratio of the natural frequencies calculated as in Equation 5.3, assuming ideally the same value of the stiffness. The fourth column provides the ratio of the natural frequencies as derived from the GVT data, i.e. the value ω_{ss}/ω_{ff}. Last column shows the difference between the ideally predicted stiffness and the one derived from experimental data. Data presented in Table 5.7 shows that the adopted approach to the skin manufacturing process limits the impact of the skin on the overall stiffness. In fact, the difference in frequency associated with the first mode is 12.5% while the one associated with the second is 3%.

A comparison of the frequency response of the spar-only and full-wing model is shown in Figure 5.13. The presented frequency response was processed from the response of the MPU6050 accelerometer distributed over the wing. Placement of the sensors is shown in Figure 5.14 for both configurations. In the spar+skin configuration the tip IMU was placed closer to the root due to volume constraints. The response of just three sensors rather than four is plotted because one of the sensors was placed on the root to be used as the input channel in the FRF evaluation. The frequency response of the three sensors shows the shift in frequency from the higher value of the spar-only configuration to the lower value of full-wing skin. Peaks associated with the full-wing configuration are generally wider and of smaller magnitude than the ones related to the spar-only case due to the structural damping intro-

	ω_{ff} [Hz]	ω_{ss}/ω_{ff} from Eq. 5.3	ω_{ss}/ω_{ff} from GVT	Δ
1^{st} mode	3.04	1.47	1.68	12.5%
2^{nd} mode	14.32	1.47	1.53	3%

Tab. 5.7.: Impact of the skin on the overall model stiffness.

duced by the shell. Damping associated with the first mode was estimated to be 0.86% for the spar-only configuration and 4.30% for the full-wing configuration [191].

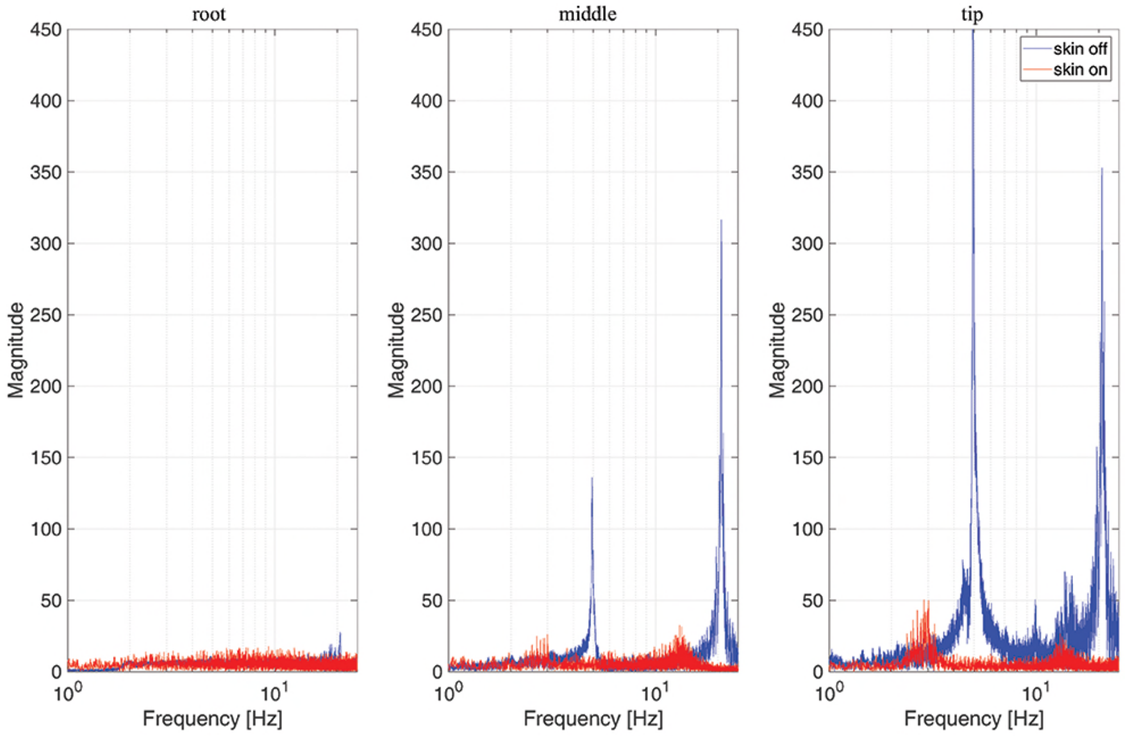

Fig. 5.13.: Frequency response function for sine-sweep input comparing skin-on and skin-off configurations.

5.5 Wind tunnel test

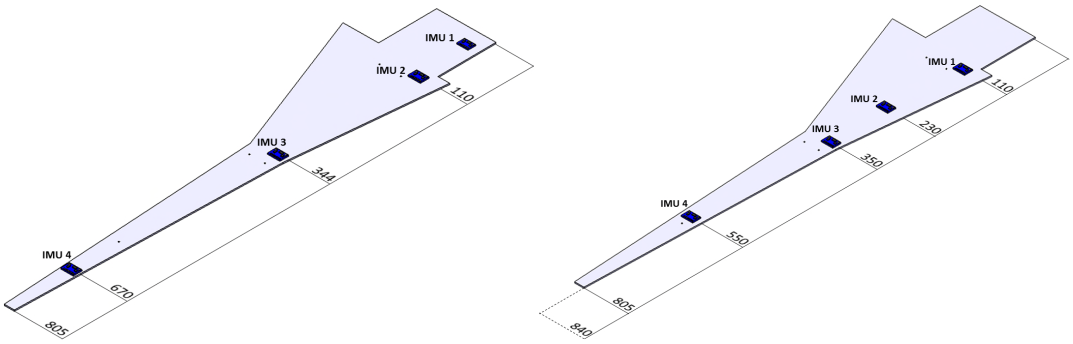

(a) IMU position for spar only configuration. **(b)** IMU position for spar and skin configuration.

Fig. 5.14.: IMU position for GVT.

The XB-1 model was tested in the Cranfield Weybridge wind tunnel which is an open section closed return facility. Specifications of the wind tunnel are given in Table 5.8.

The experiment was set up and run to achieve four objectives:

Designation	Open section closed return circuit	**Max speed**	38 m/s
Max Reynolds No	2.7 x 10^6/m	**Section diameter**	1.067 m
Pressure	ambient		

Tab. 5.8.: Cranfield Weybridge wind tunnel specifications.

1. To prove the safety and reliability of the manufacturing process for highly flexible wind tunnel models.
2. To test the performance of the newly designed data acquisition system.
3. To compare static aeroelastic deformations with BEaRDS^{TM} prediction.
4. To find and correct any possible problems related to model manufacturing.

The wing was tested at only one flight point, for the angle of attack $\alpha = 6°$ and velocity 27 m/s. The option of testing only one value of α was dictated by the available rig. Repeatability was checked testing the wing multiple times, showing agreement (Figure 5.15).

The test was characterised by three phases (refer to Figure 5.15):

- the ramp-up, where the flow goes to steady velocity, from 0 m/s to the target speed,
- the steady state, where the target velocity is kept constant for at least 10 seconds and,
- the ramp-down, when the flow goes back to 0 m/s and the model is aerodynamically unloaded.

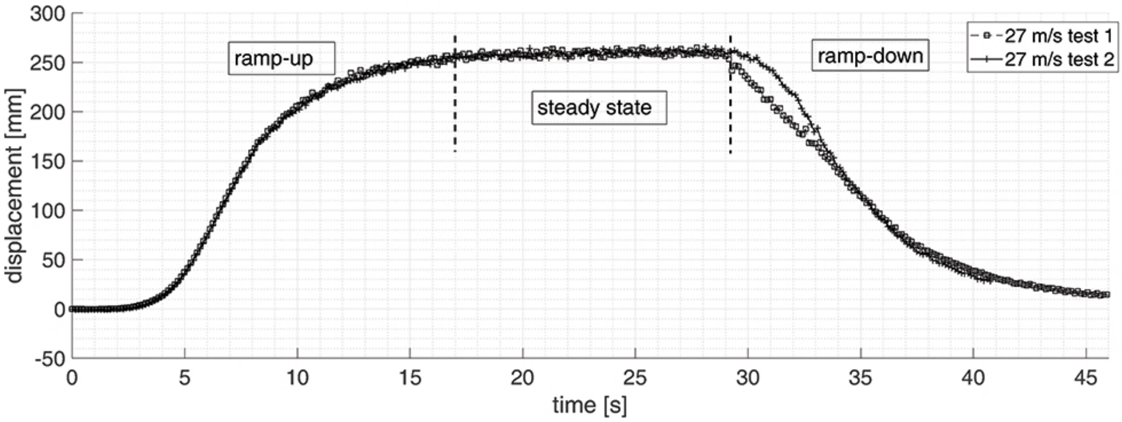

Fig. 5.15.: Estimated time history of the displacement of the wing-tip for $\alpha = 6°$ and $v = 27$ m/s.

The maximum tip displacement occurs in the steady-state phase. To measure such displacement, two different approaches were used:

- acquiring accelerations and angular velocities from IMUs placed at different locations (as shown in Figure 5.7) and
- to record the wing-tip position with the Olympus high speed camera.

The benefit of using the first method is that it provides an estimation of the deformed shape of the whole wing. In fact, it is possible to reconstruct an approximation of the wing shape knowing the rotation at each of the four IMU locations.

Figure 5.15 shows the tip displacement evaluated processing data from the IMU sensors. Data are representative of the time history of the deformation, where the initial (reference) point is the tip of the wing deformed under the gravity load. In order to evaluate the approximated shape of the wing, and eventually the tip deflection, the rotation of the section, θ, at the IMU locations, is required.

The measured quantities are:

$$\ddot{\theta}_i \quad i = 1, ..., 4 \tag{5.4}$$

$$\ddot{x}_i \quad i = 1, ..., 4 \tag{5.5}$$

where $\ddot{\theta}$ is the angular acceleration at the IMU location and $\ddot{x}$ is the vertical acceleration at the IMU location. Both of these variables have measured noise and offset. While the offset can be corrected with calibration, the noise always affects the reading. The problem is that determining θ simply integrating $\ddot{\theta}$ twice will give an unbounded solution due to the presence of noise. The use of the complementary filter is then proposed to estimate the angle θ.

This filter processes data from the accelerometers and the gyroscopes simultaneously. In fact, the rotation of the IMU can be estimated from the accelerometer data as well. Decomposing the acceleration vector into the body axis system, provides an estimation of the rotation of the sensor (Equations 5.8-5.10). Angles derived from the accelerometer output are reliable in the long term as no integration is needed, thus the estimation does not drift. However the estimation is not precise in the short term because the measurement from the accelerometer contains mechanical noise since the sensor is affected by any force acting on the structure, vibrations included. The gyroscope reading instead is less affected by the structural vibrations and thus more reliable in the short term. The complementary filter therefore combines the benefits of the two measurements, correcting the drift of θ adjusting the gyroscope integration with the accelerometer estimation, through a weight κ. The rotation of each section at each time step, θ_z, is therefore given as:

$$\theta_z = \kappa \left(\theta_{z-1} + \dot{\theta}_z^{\,gyro} \Delta t \right) + (1 - \kappa) \theta_z^{acc} \tag{5.6}$$

where Δt is the sampling period and θ_z^{acc} is the estimation of the angle from the accelerometer reading defined as:

$$\theta_z^{\mathrm{acc}} = \sqrt{\left(\theta_z^x\right)^2 + \left(\theta_z^y\right)^2 + \left(\theta_z^z\right)^2} \tag{5.7}$$

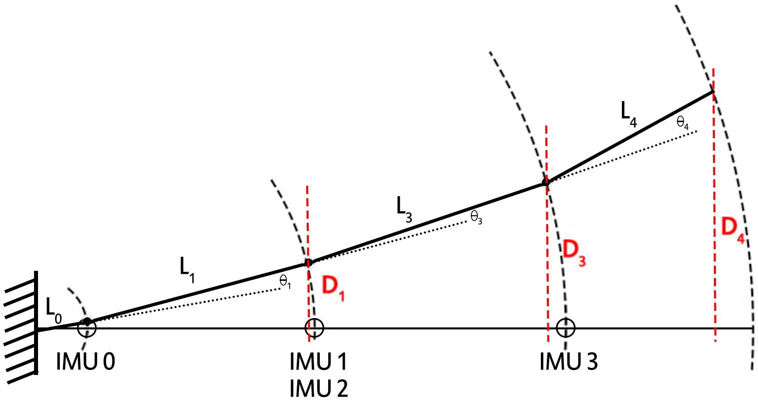

Fig. 5.16.: Geometric parameters for the shape estimation.

where [93]:

$$\theta_z^x = \tan^{-1}\left(\frac{a_x}{\sqrt{a_y^2+a_z^2}}\right) \tag{5.8}$$

$$\theta_z^y = \tan^{-1}\left(\frac{a_y}{\sqrt{a_x^2+a_z^2}}\right) \tag{5.9}$$

$$\theta_z^z = \tan^{-1}\left(\frac{\sqrt{a_x^2+a_y^2}}{a_z}\right). \tag{5.10}$$

A common value for the weight κ is 0.98, although it can be tuned to correct drift behaviours. Data that are fed into the complementary filter are firstly processed with a low-pass filter to remove high frequency noise and vibrations effects.

Once the rotation of each IMU is known and assuming the spar section to be rigid in between two IMUs, the x and y displacements (respectively vertical and spanwise displacements, refer to Figure 5.16) can be estimated as follows:

$$x_i = x_{i-1} + L_i \cos\left(\sum_{n=1}^{i} \theta_n\right) \tag{5.11}$$

$$y_i = y_{i-1} - L_i \sin\left(\sum_{n=1}^{i} \theta_n\right) \tag{5.12}$$

where n is the number of sensors and i identifies the IMU location.

The sampling frequency of the XB-1 sensors was 100 Hz. Estimating the shape of the deformed wing results in the following limitations:

- considering the spar section in between sensors as rigid, just rotating around an ideal hinge, introduces an error especially when considering flexible structures,

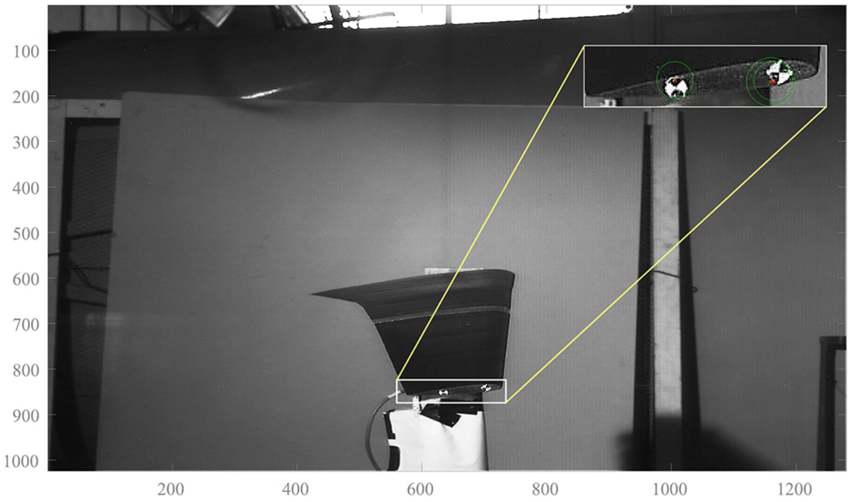

Fig. 5.17.: High speed camera frame used in the tracking script to identify the target.

- The noise of the sensor must be taken in account.

The tip deflection estimated through the MPU6050 data was compared with a second method which consisted of recording and tracking the tip displacement with the high speed camera. Photos of the tip featuring two markers were recorded at 100 Hz. Figure 5.17 shows markers on the side of the wing-tip along with the identified features from the tracking software. Once the features linked to the markers are recognized the software identifies the marker in each frame providing spacial coordinates for each frame. Figure 5.18 shows four frames representing four different instants of the overall test time line. The tracking software was developed in-house for the purpose of this study in MATLAB® and it follows a linear sequence of actions. It initially recognises the markers by comparing the features in the whole frame with a provided example of the marker shape (Figure 5.17). Once the marker's features are recognised, they are stored and compared with each pixel of the frame at each time step. When the marker is detected within the frame, an (x,y) coordinate vector is provided. The distance of (x,y) from the initial point (zero velocity, wing bent due to the gravity load) is then evaluated and provided as output.

A comparison of the displacements calculated with the two methods is shown in Figure 5.19 for $\alpha = 6°$ and $v = 27$ m/s. The steady-state displacement calculated applying the complementary filter to IMU data overestimates the one provided by the high speed camera by 8.5%. The explanation might be found in two aspects of the shape estimation process:

- the spar sections in between two IMUs are considered rigid while they are flexible and,
- it is assumed that the IMUs move on a circular trajectory while for high deformation each point of the beam moves on a parabola.

Figure 5.20 shows some tests carried out on the XB-1 spar by Civera [42] where it was proven that the assumption of circular trajectory cannot be made when considering large deformations. To account for the first problem, higher density of sensors would lower the error of

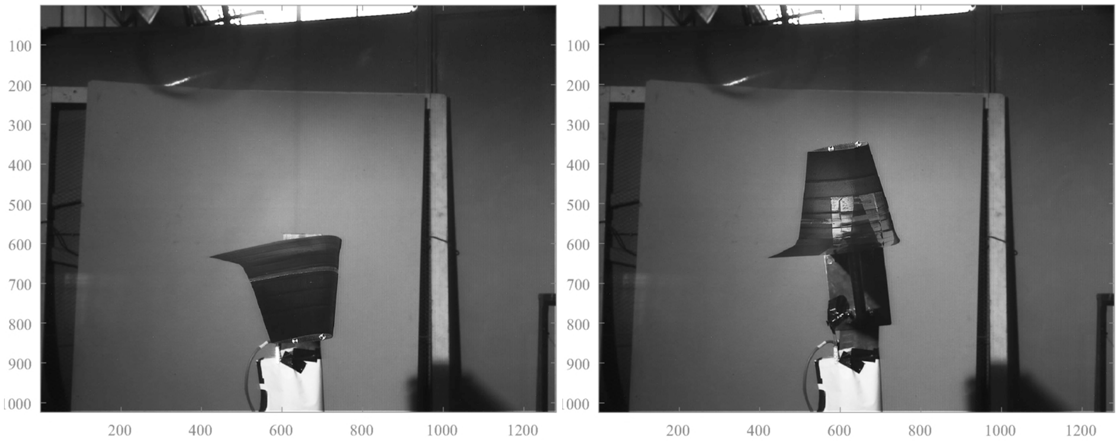

(a) t=3 s **(b)** t = 10 s

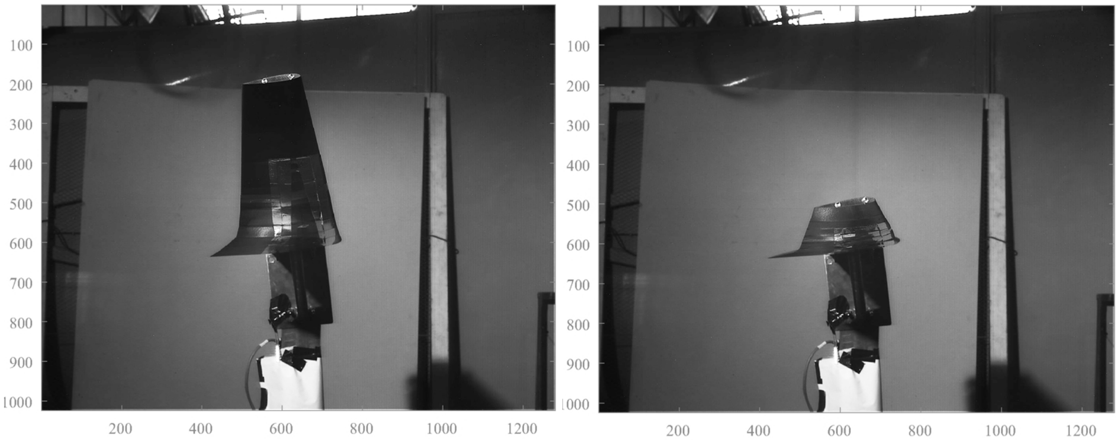

(c) t= 25s **(d)** t= 35 s

Fig. 5.18.: Frame of XB-1 test recording acquired with the high speed camera.

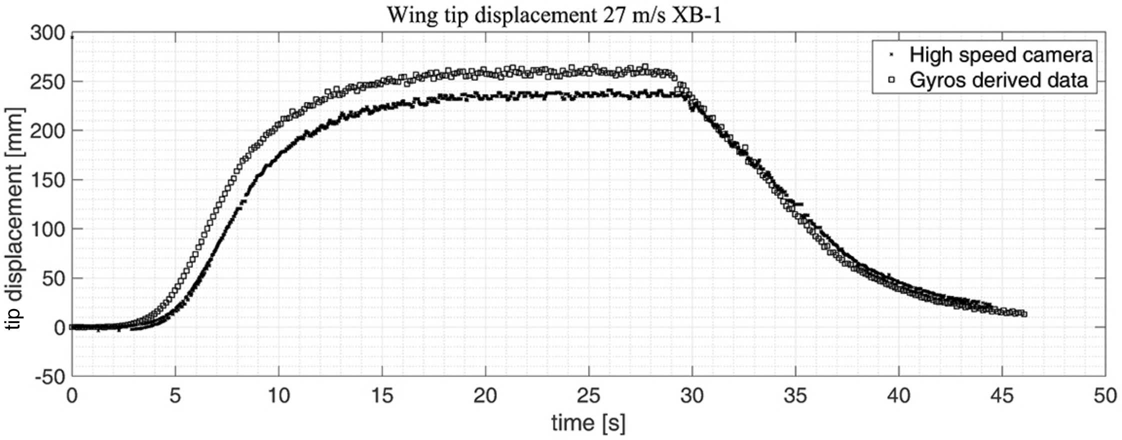

Fig. 5.19.: BEaRDS XB1 Weybridge wind tunnel test results for $\alpha = 6$ deg end v= 27 m/s.

approximating the section as rigid. Instead, to compensate for the second error, a different numerical model is needed (refer to Equation 5.12), where points move on parabolas rather than circles. .

The overall estimated displacement[8] is compared with the prediction of BEaRDS^{TM} . Representation of the predicted numerical displacement is shown in Figure 5.21. Data from high speed camera are then chosen as reference to compare with BEaRDS^{TM} prediction. A summary of the results is given in Table 5.9, showing two interesting aspects:

	Experimental	**BEaRDS^{TM} prediction**	**Δ**
Displacement	238 ±3.9 mm	210 mm	-12%
% of wingspan	32%	28%	

Tab. 5.9.: Experimental tip deflection compared with the BEaRDS^{TM} prediction [77].

- The wing-tip deflection is well above the 10% deflection threshold, proving the ability of the XB-1 model to safely reproduce the response of highly flexible wings in the wind tunnel.
- BEaRDS^{TM} underestimates the deflections. The error is introduced by the simplifications introduced in the modelling of the wing. The modelling of the skin properties especially and their distribution along the spar cannot be accurately calculated due to the uncertainty in the material properties and the complex geometry. However, an error of 12% on the static deflection is considerable acceptable for the purpose of this work.

5.6 Discussion and next step

In this chapter the manufacturing and testing of the XB-1 flexible model was introduced and the results of the static wing tunnel test were discussed. The test has shown that the novel manufacturing approach is able to correct the effects of the gaps on the aerodynamic performance of the model without excessively affecting the overall stiffness of the model. Therefore, the key findings of the test can be summarised as follows:

- The skin of the model was successfully designed and then printed applying the 3D Polyjet technology. The approach allowed to cover the gaps in between rigid pods retaining the aerodynamic shape of the section while limiting the impact of the skin on the overall stiffness. Such contribution is 12.5% for the first mode and 3% for the second one. In general the result is considered acceptable considering the assumptions made in the

---

[8] The error on the displacement is calculated as standard error of the mean, σ_x, defined as:

$$\sigma_x = \frac{\sigma}{\sqrt{n}} \tag{5.13}$$

where σ is the standard deviation of the sample vector and n is the number of samples used to evaluate the average value of the displacement.

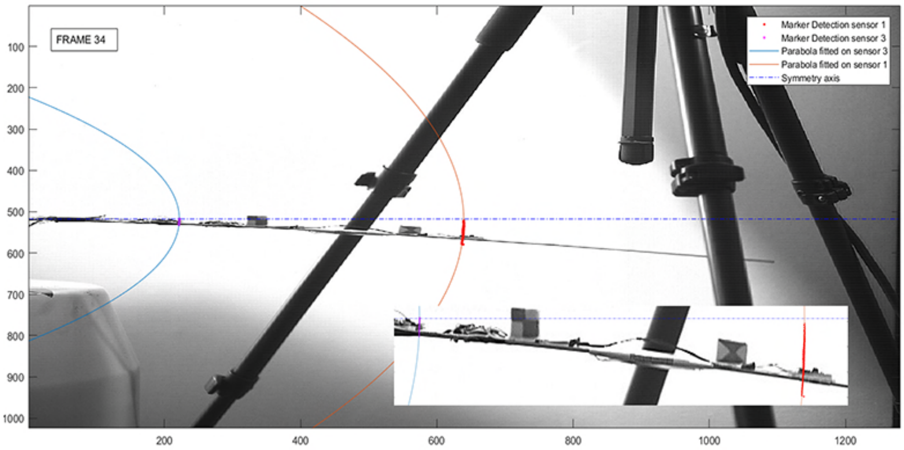

Fig. 5.20.: Frame taken from GVT test on spar-only configuration. [42] (*image courtesy of M. Civera, L. Zanotti Fragonara and C. Surace*).

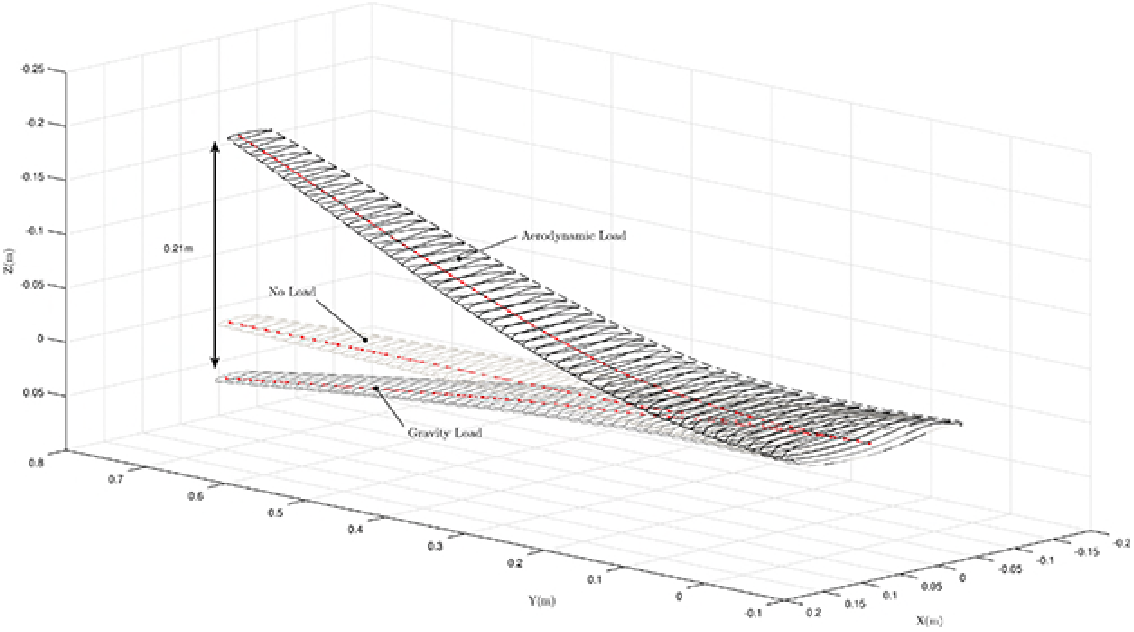

Fig. 5.21.: BEaRDS XB-1 static deflection prediction using BEaRDS^{TM} solver [77].

calculation of such contribution. Therefore the same method is applied to the second phase of the BEaRDS programme.

- The use of load pillars are a viable way to transfer aerodynamic load from the skin to the structure. By reducing the contact surface between the skin and the spar, the impact of friction on the model stiffness is limited.
- The acquisition system was designed and assembled as a low cost alternative to commercial and more expensive systems. The RaspberryPi board was able to acquire data from four 6-DOF sensors placed on the wing. Data were successfully saved on the inboard SD card and later processed. The analysis of the results has shown that the system has the required accuracy for the scope of this work. Furthermore, the use of off-the-shelf MPU6050 sensors to measure linear and rotational acceleration made sensors mounting possible within very limited volumes which characterise slender wing tunnel models. In fact, while most of the commercial 3-axial professional accelerometers would have not fit in such small space, the use of these IMU proved to be a valid alternative for tests were model's inner volume is heavily limited.
- Torsional measurement was planned for the XB-1 test in order to understand the impact of the torsional effects on the wing deformations and flutter properties. Two markers were applied on the tip of the model in order to read the tip rotation along with the vertical displacement. However, when processing the images, the software was not able to discriminate between the two markers because too similar in the printed pattern. Therefore, the torsional analysis turned out not to be possible.

Aspects of the design identified for improvements are as follows:

- The bottom window used to allow access to the inner volume of the model must be designed as multiple windows rather than a long piece spanning the entire length of the model.
- The trailing edge of the model must be reinforced with filling material. This step is necessary in order to prevent cracks in the skin due the sharp change in angle imposed by the TE shape.
- The rigid pods were too fragile and must be reinforced. A different material for printing the part is also considered. Each threaded hole needs to be reinforced with metal inserts. When screwing and unscrewing repeatedly into plastic, the thread gets deteriorated and the screw is no longer secure in place.

Such upgrades are taken in account and implemented in the design and manufacturing of the XB-2 model.

The next step was to design and build the 1.5 m long XB-2 flexible wing. As previously said, XB-2 was not only a manufacturing exercise. It was more to develop a tool to test and validate high aspect ratio wing models. Thus, an extra layer is added on top of the experimental stage, which is the design and the matching of the dynamic response of a full scale flexible aircraft wing. Details of the eXperimental Beards 2 stage of the BEaRDS programme are detailed in the next chapter.

6

eXperimental BeaRDS 2: design and manufacturing (XB-2)

The final phase of the BEaRDS programme involved the design, manufacturing and testing of the flexible eXperimental BEaRDS 2 (XB-2) model. The knowledge acquired from the XB-1 test was applied to the XB-2 model, improving the process of manufacturing and testing where needed as learnt from the XB-1 experience. The aim of the XB-2 is to carry out a series of static and dynamic aeroelastic tests on a flexible wing model in order to assess the limitations of CA^{2}LM (and its scaled version BEaRDS^{TM}) before designing the gust load alleviation system for the HARTEN aircraft.

The XB-2 work flow differs significantly from the XB-1 work flow. Figures 6.1 and 6.2 show the design process of the XB-2. An important aspect to stress is that the XB-2 design and testing was itself a broad project. Therefore, the author developed some of the aspects of it, while contributed marginally to others. Details of contributions from other researchers can be found in the figures. Steps of the design process are briefly discussed here:

1. The key requirement was to have a scaled high aspect ratio wing capable of exhibiting aeroelastic phenomena. Threfore, the first step of the design process focused on designing a full scale aircraft based on an AIRBUS A320. The wing design was based on the principle of minimum exergy destruction[1]. Eventually, the aircraft structure was reduced to a beam model and the mass and stiffness matrices of the full scale aircraft were provided as output.

2. The full scale mass and stiffness matrices were fed into the dynamic scaling algorithm developed by Yusuf [191]. The non-dimensional equations of motion were derived along with the dimensionless coefficients. To derive the scaled mass and stiffness matrices, the scaling algorithm matched the coefficients for the full-scale and the scaled model, providing the criteria for the dynamic scaling. The outputs of this phase were the scaled mass and stiffness matrices.

3. The inertia and stiffness parameters are extracted from the scaled stiffness matrix in order to design the shape of the metal spar. The assumption is that the impact of the skin on the overall stiffness is minimal (as proved by the XB-1 test).

---

[1] Exergy is a metric used to quantify the useful energy that can be extracted out of any system. For more details the reader is referred to Hayes [77, 78].

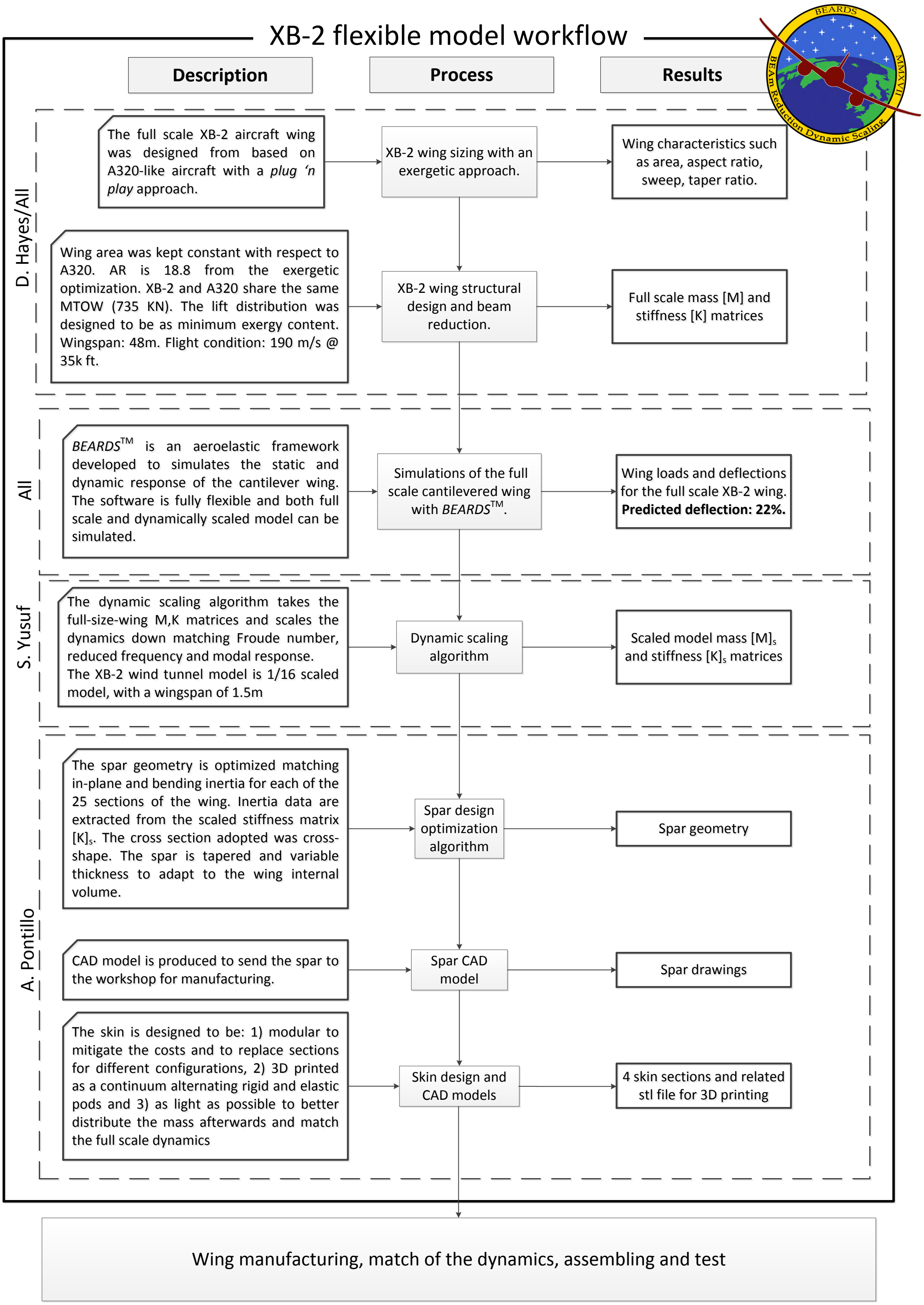

The full scale XB-2 aircraft wing was designed from based on A320-like aircraft with a *plug 'n play* approach.

Wing area was kept constant with respect to A320. AR is 18.8 from the exergetic optimization. XB-2 and A320 share the same MTOW (735 KN). The lift distribution was designed to be as minimum exergy content. Wingspan: 48m. Flight condition: 190 m/s @ 35k ft.

BEARDS^{TM} is an aeroelastic framework developed to simulates the static and dynamic response of the cantilever wing. The software is fully flexible and both full scale and dynamically scaled model can be simulated.

Wing loads and deflections for the full scale XB-2 wing. **Predicted deflection: 22%.**

The dynamic scaling algorithm takes the full-size-wing M,K matrices and scales the dynamics down matching Froude number, reduced frequency and modal response. The XB-2 wind tunnel model is 1/16 scaled model, with a wingspan of 1.5m

The spar geometry is optimized matching in-plane and bending inertia for each of the 25 sections of the wing. Inertia data are extracted from the scaled stiffness matrix $[K]_s$. The cross section adopted was cross-shape. The spar is tapered and variable thickness to adapt to the wing internal volume.

CAD model is produced to send the spar to the workshop for manufacturing.

The skin is designed to be: 1) modular to mitigate the costs and to replace sections for different configurations, 2) 3D printed as a continuum alternating rigid and elastic pods and 3) as light as possible to better distribute the mass afterwards and match the full scale dynamics

Fig. 6.1.: XB-2 wind tunnel model design and manufacturing workflow (1/2)

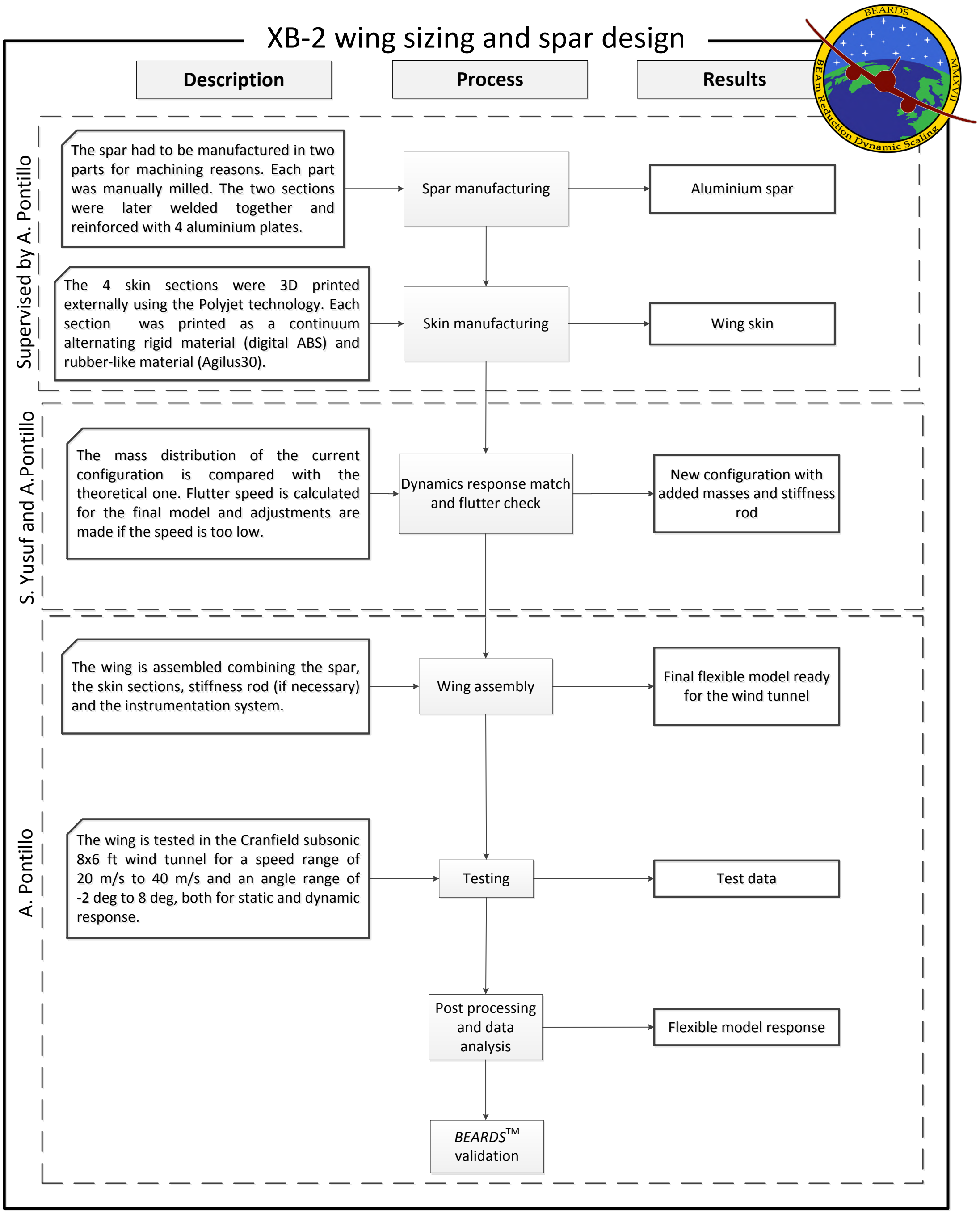

The spar had to be manufactured in two parts for machining reasons. Each part was manually milled. The two sections were later welded together and reinforced with 4 aluminium plates.

The 4 skin sections were 3D printed externally using the Polyjet technology. Each section was printed as a continuum alternating rigid material (digital ABS) and rubber-like material (Agilus30).

The mass distribution of the current configuration is compared with the theoretical one. Flutter speed is calculated for the final model and adjustments are made if the speed is too low.

The wing is assembled combining the spar, the skin sections, stiffness rod (if necessary) and the instrumentation system.

The wing is tested in the Cranfield subsonic 8x6 ft wind tunnel for a speed range of 20 m/s to 40 m/s and an angle range of -2 deg to 8 deg, both for static and dynamic response.

Fig. 6.2.: XB-2 wind tunnel model design and manufacturing workflow (2/2)

4. The skin of the model is designed and 3D printed. The same process applied for the XB-1 was considered for the XB-2. However it features a new window design, a modular architecture and reinforced leading and trailing edges.
5. The wing is assembled and throughout the assembly process lumped weights are distributed along the spar to appropriately scale the mass distribution.
6. The aeroelastic static and dynamic response of the flexible model are assessed through a wind tunnel test campaign in the Cranfield 8x6 ft wind tunnel.
7. Wind tunnel data are processed and compared with the BEaRDS^{TM} output.

In this chapter the reader will find details on the design process of the flexible wing model. Firstly, the design process of both spar and stiffness are discussed. Secondly, the manufacturing process of the spar and the skin are detailed. Lastly, Ground Vibration Test (GVT) are performed on the model and then natural frequencies are compared with the numerical prediction.

6.1 XB-2 full scale design

The design of the XB-2 wing was carried out by Hayes [79]. However, a brief description of the full-scale XB-2 HARW design process is given here to complete the BEaRDS analysis. The XB-2 aircraft is based on the geometry of the AIRBUS A320, where standard wings are replaced with optimized HARW. In fact, the aim of the study was to assess the dynamic response to gust input of a medium-haul commercial aircraft with high aspect ratio wings.

The process of the XB-2 wing design assumed the followings:

$$\begin{aligned} \text{MTOW}|_{A320} &= \text{MTOW}|_{XB\text{-}2} \\ \text{Wing load}|_{A320} &= \text{Wing load}|_{XB\text{-}2} \end{aligned}$$

These two conditions constrain the geometry of the wing imposing the XB-2 aircraft to have the same wing area of the A320. Hayes obtained the optimized XB-2 wingspan (namely the aspect ratio, as the wing area is constrained) applying the principle of minimum exergy destruction. While the wingspan optimization process considered the wing as rigid, the mass and inertia distribution definitions took into account the fact that the wing was flexible. In fact, the latter distributions were designed targeting a minimum of 22% wingtip displacement with respect to the wing semispan subject to cruise load. Hayes found that the exergy destruction is proportional to the gradient of the circulation, Γ [79]. Therefore, in order to minimize the exergy loss of the system, the cost function for the optimization problem was defined as:

$$J(s) = K\mu \int_0^b \left(\frac{\partial \Gamma}{\partial y}\right)^2 dy \tag{6.1}$$

subject to the constraints:

$$\underbrace{\rho u_\infty \int_0^{b_0} \Gamma(y) dy}_{L_{A320}} = \underbrace{\rho u_\infty \int_0^{b} \Gamma(y) dy}_{L_{XB\text{-}2}} \tag{6.2}$$

$$\underbrace{\rho u_\infty \int \int_0^{b_0} \Gamma(y) dy^2}_{M_{A320}} = \underbrace{\rho u_\infty \int \int_0^{b} \Gamma(y) dy^2}_{M_{XB\text{-}2}} \tag{6.3}$$

where b is the optimized XB-2 wingspan, k, μ are constants related to the geometry of the wing. Equations 6.2 and 6.3 represent constraints on the lift and the bending moment. For more details on the variables and the equations, the reader is referred to Hayes et al. [79]. The result of the optimization problem provided the following for the XB-2 aircraft:[2]

$$\begin{aligned} \text{wingspan} &= 48 \text{ m} \\ \text{AR} &= 18.8 \end{aligned}$$

Details of the fulll-size XB-2 parameters are given in Table 6.1 and the resulting wing planform is shown in Figure 6.4, while a comparison between the A320 and the XB-2 wing planforms is shown in Figure 6.3. It is important to stress that the XB-2 wing has a zero 1/4-chord sweep and a lower cruise Mach. The former was important in order to simplify the wind tunnel model manufacturing while the latter was chosen in order to adopt a more efficient propulsion system such as turboprop engines.

The XB-2 full-size structure was therefore a reduced order model for which the mass and stiffness matrices, $\boldsymbol{M}_{ff}$ and $\boldsymbol{K}_{ff}$ respectively, were extracted and fed into BEaRDS^{TM}.

The mass and stiffness distribution of the XB-2 were optimized to meet the requirements for the wing-tip displacement and aeroelastic modes[3]. BEaRDS^{TM} loads analysis for the full scale XB-2 aircraft in cruise flight provided a 22% wing-tip displacement, while the eigenproblem solution provided the first 6 natural modes detailed in Table 6.2.

6.2 Aeroelastic dynamic scaling

As for the XB-2 full-size design process, a brief overview of the dynamic scaling is provided in this section. The XB-2 dynamic scaling was carried out by Yusuf and detailed in References [191, 192]. The first step was to isolate the wing from the rest of the aircraft as the wind tunnel

---

[2] The use of exergy is one of the methods that could have been applied to optimize aerodynamically the span of the wing. However, as shown in [79] different approaches would have led to the same results. The benefit of using an energetic approach was to highlight the physical meaning of the optimization process.

[3] Requirements for the wing design were set on the displacement, to be at least 22% of the wing semispan subject to cruise load and on the structural natural frequencies. This latter point required the modal design of the wing structure such that the first bending frequency overlapped the flight dynamics frequency domain, specifically the short period mode

	Parameter	Symbol	Units	A320	XB2
Performance	Operating Weight Empty	OWE	kg	42,100	42,100
	Maximum Take-Off Weight	$MTOW$	kg	73,500	73,500
	Maximum Payload Weight	W_{pay}	kg	20,400	20,400
	Cruise Altitude	h	m	11,280	11,280
	Cruise Velocity	u_{∞}	Ma	0.78	0.6
	Range (typical)	R	km	4,800	4,800
	Powerplant (x2)			CFM56	gFan+2
	Thrust (x2)	T	kN	111.2	102.3
	Specific Fuel Consumption	SFC	$g/kN/s$	16.88	13.27
	Fuel Consumption (cruise)	$\dot{M}_f$	kg/h	2100	
Body	Length	f_l	m	37.57	37.57
	Fuselage height	f_z	m	4.14	4.14
	Fuselage width	f_y	m	3.95	3.95
Aerofoil	Aerofoil			BAC 449	NACA
	Thickness ratio	$\frac{t}{c}$	$-$	0.113	0.150
	Lift at zero AoA	C_{l_0}	$-$	0.208	0.125
	Zero lift AoA	α_0	rad	0.031	-0.022
Planform	Span	b	m	34.09	48.00
	Aspect Ratio	AR	$-$	9.5	18.8
	Reference area	S_{ref}	m^2	122.4	122.4
	Sweep (LE)	Λ_{LE}	rad	0.471	0.026
	Sweep ($\frac{c}{4}$)	$\Lambda_{\frac{c}{4}}$	rad	0.436	0.000
	Root Chord	c_b	m	6.10	3.78
	Streamwise c_b position	x_b	m	12.55	-
	Tip Chord	c_t	m	1.62	1.32
	Streamwise c_t position	l_t	m	20.35	
	Taper Ratio	λ	$-$	0.240	0.350
	MAC	$\bar{c}$	m	4.29	2.75

Tab. 6.1.: Airbus A320 aircraft vs full-size XB-2 aircraft parameters

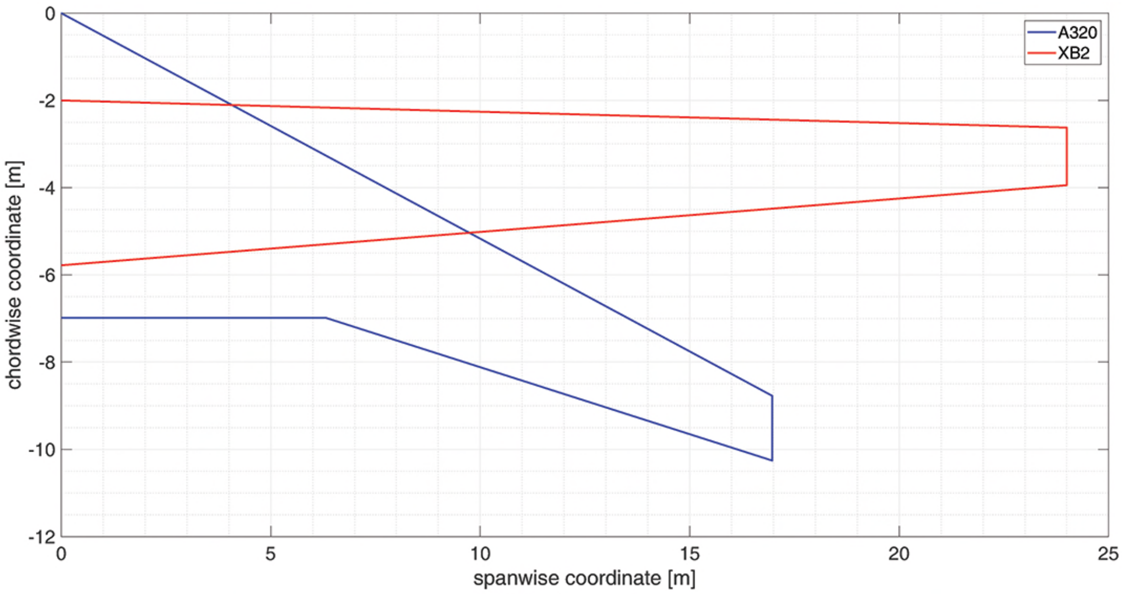

Fig. 6.3.: A320 and XB-2 wing planform comparison

test focused on the cantilever wing only. The second step was to define the equations of motion of a generic aeroelastic model as:

$$\underbrace{[\boldsymbol{M}]\ddot{\boldsymbol{x}}+[\boldsymbol{K}]\boldsymbol{x}}_{structure}=\underbrace{[\boldsymbol{A}_k]\boldsymbol{x}+[\boldsymbol{A}_c]\dot{\boldsymbol{x}}+[\boldsymbol{A}_m]\ddot{\boldsymbol{x}}}_{aerodynamics}+\underbrace{[\boldsymbol{M}]a_g}_{gravity} \tag{6.4}$$

Mode no.	Frequency		Mode
	rad	Hz	
1	4.4	0.69	1st Bending
2	21.7	3.46	2nd Bending
3	21.8	3.50	1st Torsion
4	38.5	6.13	3rd Bending
5	56.8	9.03	4th Bending
6	89.9	14.31	Coupled

Tab. 6.2.: Eigenvalue analysis of full-size XB-2 aircraft.

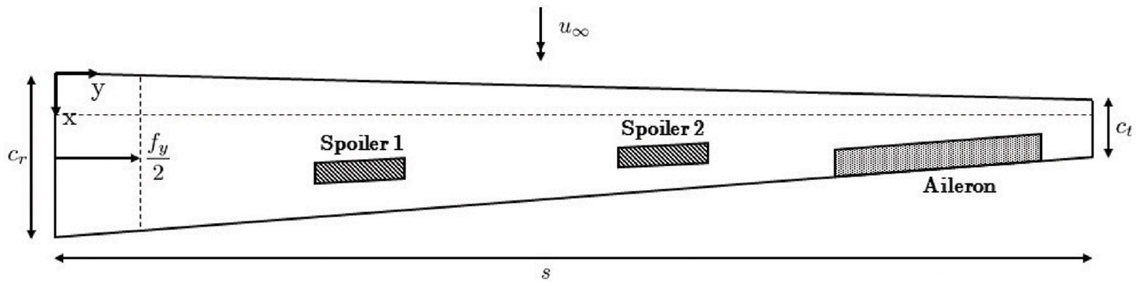

Fig. 6.4.: XB-2 wing planform.

where $[\boldsymbol{A}_k]$, $[\boldsymbol{A}_c]$, $[\boldsymbol{A}_m]$ are the aerodynamic stiffness, damping and mass respectively, ***[M]*** is the mass matrix, ***[M]*** is the stiffness matrix and $\boldsymbol{x}$ the state vector. Working on the EoMs defined in Equation 6.4, to derive the scaled model characteristics, the methodology developed by Ricciardi [147, 146], based on the non-dimensional analysis [58] was adopted. The scaling procedure led to non-dimensional EoMs (not reported here for brevity). The non-dimensional analysis provides three coefficients that can be used to estimate the reference scaling factors based on the basic dimensions of length, mass and time. The three coefficients from the non-dimensional analysis were defined as:

$$\pi_1 = \frac{M}{\rho b^5} \tag{6.5}$$

$$\pi_\omega = \frac{\omega b}{U} \tag{6.6}$$

$$F_r = \frac{V}{\sqrt{bg}} \tag{6.7}$$

The coefficient π_1 represents the inertia ratio, π_ω is the reduced frequency and F_r is the Froude number[4]. Equations 6.5-6.7 provide the scaling laws which are applied to design the mass and stiff distribution of the scaled model, along with the following requirements:

- Since the model is designed to be tested in the Cranfield 8x6 ft wind tunnel (details of the facility can be found in Table 7.1), the maximum wingspan is constrained by the tunnel test section geometry. The maximum wingspan is bounded to be no more than 80% of the wind tunnel test section to avoid interactions with the tunnel wall boundary

---

[4] The Froude number is a dimensionless parameter which plays a critical role in dynamics tests. The parameter represents the ratio of the inertia force and the gravity force

layer [20]. This requirement sets the model span to 1.5 m, resulting in a geometrical scale factor of 1:16.

- The maximum velocity in the tunnel is 50 m/s and thus the Froude number velocity scale factor of 1:4 is imposed.
- The ratio between the full scale target altitude (35000 ft) and the wind tunnel test condition (sea level), sets the air density ratio to 3.23:1.

Adoption of these requirements allows to find reference scaling factors π_g, π_ρ, π_U that are later used in the non-dimensional analysis to derive the remaining scaling factors, as detailed in Table 6.3 [191, 192]. The Mach number[5] similarity was considered in the early stage of the study. However, due to the characteristics of the Cranfield wind tunnel facility, such as maximum speed and nature of the gas (air), it was not possible to achieve it. The Reynolds number[6] similarity was considered as well. In this case as well, due to the nature of the fluid, wind tunnel maximum speed and model dimension, matching the Reynolds number proved not to be possible. Reynolds number referred to the root chord for the full scale XB-2 aircraft in the chosen flight condition is $\mathrm{Re}_{\mathrm{ff}} = 5.4e7$ while for the scale model at 40 m/s is $\mathrm{Re}_{\mathrm{ss}} = 6.3e5$. It was decided not to use any trip wire on the wing and to allow free-to-laminar boundary layer transition. However, in order to promote boundary layer transition, the skin surface roughness from the 3D printing was retained instead of smoothing it. Furthermore, the full scale elastic bending and torsional rigidity were matched by the scaled design. As result of

			Scaling factor	
Dimension	**Unit**	π	**Scaled XB-2**	**Full scale XB-2**
Length	L	π_g	1	16
Air density	ML^{-3}	π_ρ	3.23	1
Velocity	LT^{-1}	π_U	1	4
Mass	M	$\pi_M = \pi_\rho \pi_g^3$	1	16^3
Inertia	ML^2	$\pi_I = \pi_\rho \pi_g^5$	1	16^5
Structural stiffness	MT^{-2}	$\pi_K = \pi_\rho \pi_U^2 \pi_g$	1	79.33
Torsional stiffness	$\mathrm{ML}^2\mathrm{T}^{-2}$	$\pi_G = \pi_\rho \pi_U^2 \pi_g^2$	1	$2.03\mathrm{x}10^4$
Non-dimensional time	T	$\pi_T = \frac{\pi_g}{\pi_U}$	4	1
Structural damping	T^{-1}	$\pi_\zeta = \frac{\pi_U}{\pi_g}$	1	4

Tab. 6.3.: XB-2 scaling factors (from [191]).

---

[5] Mach number is defined as:

$$\mathrm{Ma} = \frac{v}{a}$$

where v is the flow velocity and a is the speed of sound. Mach number is relevant when considering the impact of the compressible effect on the model aerodynamics.

[6] Reynolds number is defined as:

$$\mathrm{Re} = \frac{vL}{\nu}$$

where L is a characteristic length of the model and ν is the kinematic viscosity. Reynold number defines the ratio between inertial and viscosity forces, which defines the aerodynamic nature of the flow (laminar or turbulent).

the scaling procedure, the main parameters of the XB-2 scaled model as result of the scaling process are given in Table 6.4.

	Value
Wingspan	1.5 m
Root chord	0.236 m
Tip chord	0.083 m
Area	0.180 m^2
LE sweep	1.5 deg
AR	18.8

Tab. 6.4.: XB-2 scaled model main characteristics.

6.3 Spar design

The chosen option to build the wing was the classic spar+shell configuration, following the same manufacturing process adopted for the XB-1. First step of the XB-2 wing model design was to define the spar cross-shape to reflect the stiffness properties derived from the scale matrix ***[K]***. The spar design process can be divided into the following steps:

1. First, the available volume was calculated to estimate the inner space available to contain the spar, instrumentation and servos.
2. Second, the stiffness properties of the wing were extracted for the matrix *[K]* as a function of the span coordinate.
3. Finally, the spar cross-section dimensions were estimated by matching the bending and in-plane inertia properties of the dynamically scaled model with the stiffness characteristics of the spar.

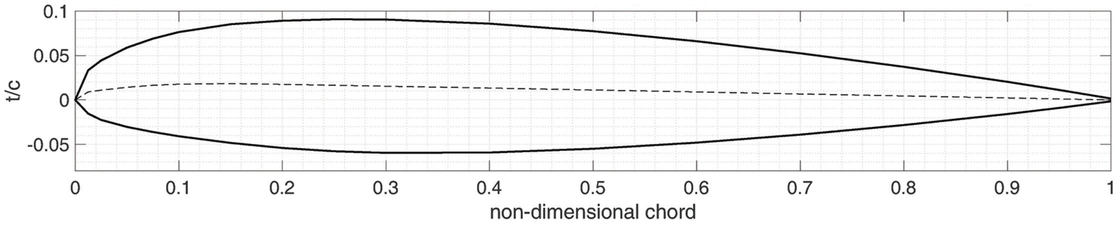

Fig. 6.5.: NACA 23015 aerofoil profile.

The aerofoil adopted for the XB-2 model was the NACA 23015, shown in Figure 6.5. Once the aerofoil was known, the available volume was simply calculated by projecting the profile root section over the chord distribution. The spar was designed to be placed at 25% of the chord to exploit the maximum thickness of the aerofoil at 15% of the chord and considering the need of space on the chordwise coordinate as well [7]. The spar numerical model was

---

[7] Unfortunately, as discussed in more detail later in the chapter, this choice led to a low flutter speed due to the early divergence of the first torsional mode.

discretised into 25 nodes for the shape design, as inherited from the original numerical beam model of the wing structure. Furthermore, although the model span is 1.5 m, the spar length is 1.45 m to allow the connection with the skin.

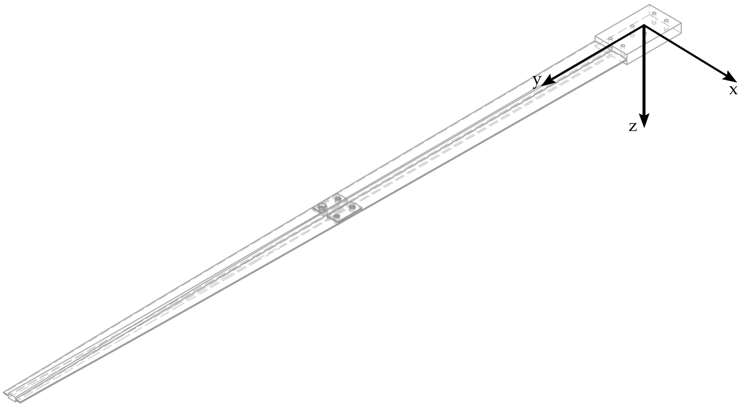

Fig. 6.6.: XB-2 spar axis system.

As already mentioned, the design of the local shape of the spar is driven by the bending and in-plane stiffness requirements. Thus, to define the local cross section dimensions, the conditions imposed at each node were defined as (refer to Figure 6.6):

$$(EI_{xx})^{model} = (EI_{xx})^{spar} \tag{6.8}$$

$$(EI_{zz})^{model} = (EI_{zz})^{spar} \tag{6.9}$$

Equation 6.8 was defined because the bending dynamics dominate the wing response in the bandwidth of interest (0-50 Hz) as shown from the properties of the XB-2 wing modes (see Table 6.2) while Equation 6.9 guaranteed to suppress any unwanted in-plane dynamics.

The Young's modulus of the theoretical model, E_K, and that of the spar, E_{spar}, are different as the full-size XB-2 wing box was made of composite materials, while the spar is manufactured using aluminium alloy 6082T6. The two Young's moduli are then defined as:

$$E^K = 5.2e10 \quad \text{Pa}$$

$$E^{spar} = 6.9e10 \quad \text{Pa}$$

Before proceeding with the search of the cross-section dimensions, two different shapes were assessed considering the manufacturing process, the available volume and the machining requirements of the solution. These are shown in Figure 6.7. The general shape of both sections consists of a horizontal flange in the XY plane mostly responsible for the in-plane stiffness, and a vertical web in the YZ plane which contributes to the bending stiffness. The T-shape section is easier to manufacture, however the bending axis is more difficult to identify. This would complicate the process of aligning the spar elastic axis to the aerofoils 1/4 chord

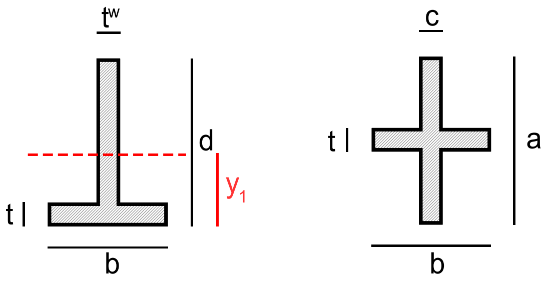

Fig. 6.7.: Two different shapes were considered as spar cross section: (left) T-shape and (right) cross-shape.

line. The cross-shape section overcomes this problem due to its symmetry. Since the section has two axes of symmetry, the elastic axis passes through the barycentre of the section. However, the manufacturing procedure can be more complicated. Considering all these aspects the cross-shape section was chosen for the spar.

The second moment of area of the cross-shape section is defined as:

$$I_{xx} = \frac{1}{12}\left((a^3 - t^3)c + t^3 b\right) \tag{6.10}$$

$$I_{zz} = \frac{1}{12}\left((a - t)c^3 + t b^3\right) \tag{6.11}$$

Equations 6.10-6.11 are substituted in Equations 6.8-6.9 providing the new set of equations to be solved to define the spar shape as:

$$(EI_{xx})_i^{model} = E^{spar}\frac{1}{12}\left((a_i^3 - t_i^3)c_i + t_i^3 b_i\right) \qquad i = 1, ..., 25 \tag{6.12}$$

$$(EI_{zz})_i^{model} = E^{spar}\frac{1}{12}\left((a_i - t_i)c_i^3 + t_i b_i^3\right) i \qquad i = 1, ..., 25 \tag{6.13}$$

Equations 6.12-6.13 are solved at each section independently. The components of the vector [*a,b,c,t*] represent the unknown variables, while the left hand side of the equations is known by evaluating the bending and in-plane inertia from the stiffness matrix ***[K]***. However, this requires a priori knowledge of ***[K]***. The matrix is built by discretising the spar as a beam model applying the Timoshenko theory [173], as described in Chapter 4. The matrix ***[K]*** reflects the inertial, geometric and material properties of the structure at each node.

An example of the definition of ***[K]*** is given considering a two-node element as shown in Figure 6.8. The mass of the element is modelled on the two nodes while the stiffness properties are represented by the bar that connects them. Each node has 6 degrees of freedom, three translations and three rotations. Hence the size of the matrix is 12x12 where the 6x6 top left elements refer to the first node and the 6x6 bottom right refer to the second node. The off-diagonal matrix elements define the interaction between the nodes. The general representation of ***[K]*** is given in Equation 6.14. The numerical value of the matrix elements are functions of the geometric properties such as the area of the local section, A, the distance between the nodes, l, and second moment of area, $[I, J]$, and function of the material prop-

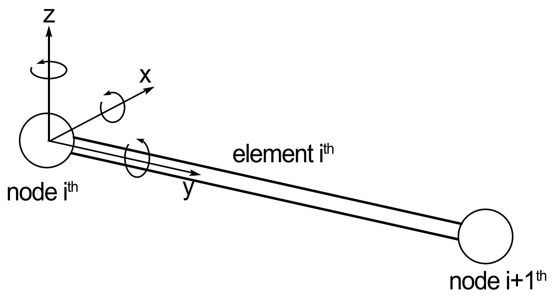

Fig. 6.8.: Two-node beam element and reference system representation

$$
[K]=\begin{bmatrix}
\frac{EA}{l} & & & & & & & & & & & \\
0 & \frac{12EI_z}{l^3(1+\phi_y)} & & & & & & & & & & \\
0 & 0 & \frac{12EI_y}{l^3(1+\phi_z)} & & & & & & \mathit{sym} & & & \\
0 & 0 & 0 & \frac{GJ}{l} & & & & & & & & \\
0 & 0 & \frac{-6EI_y}{l^2(1+\phi_z)} & 0 & \frac{(4+\phi_z)EI_y}{l(1+\phi_z)} & & & & & & & \\
0 & \frac{6EI_z}{l^2(1-\phi_y)} & 0 & 0 & 0 & \frac{(4+\phi_y)EI_z}{l(1+\phi_y)} & & & & & & \\
\frac{-EA}{l} & 0 & 0 & 0 & 0 & 0 & \frac{EA}{l} & & & & & \\
0 & \frac{-12EI_z}{l^3(1+\phi_y)} & 0 & 0 & 0 & \frac{6EI_z}{l^2(1+\phi_y)} & 0 & \frac{12EI_z}{l^3(1+\phi_y)} & & & & \\
0 & 0 & \frac{-12EI_y}{l^3(1+\phi_z)} & 0 & \frac{6EI_y}{l^2(1+\phi_z)} & 0 & 0 & 0 & \frac{-12EI_y}{l^3(1+\phi_z)} & & & \\
0 & 0 & 0 & \frac{-GJ}{l} & 0 & 0 & 0 & 0 & 0 & \frac{GJ}{l} & & \\
0 & 0 & \frac{-6EI_y}{l^2(1+\phi_z)} & 0 & \frac{(2-\phi_z)EI_y}{l(1+\phi_z)} & 0 & 0 & 0 & \frac{6EI_y}{l^2((1+\phi_z)} & 0 & \frac{(4+\phi_z)EI_z}{l(1+\phi_y)} & \\
0 & \frac{6EI_z}{l^2(1+\phi_y)} & 0 & 0 & 0 & \frac{(2-\phi_y)EI_z}{l(1+\phi_y)} & 0 & \frac{-6EI_z}{l^2(1-\phi_y)} & 0 & 0 & 0 & \frac{(4+\phi_y)EI_z}{l(1+\phi_y)}
\end{bmatrix} \tag{6.14}
$$

erties as well, such as Young's modulus, E, and shear modulus, G. The matrix ***[K]*** can be summarised as made of four 6x6 sub-matrices:

$$
[K]=\begin{bmatrix} K_{11} & K_{12} \\ K_{21} & K_{22} \end{bmatrix} \tag{6.15}
$$

Fig. 6.9.: Four-node beam element schematics

However, the problem is more complex when considering a multi-node beam. Figure 6.9 shows a four-node beam structure where its associated stiffness matrix ***[K]*** is described as [138, 77]:

$$
[K]=\begin{bmatrix} K_{11} & K_{12} & 0 & 0 \\ K_{21} & K_{11}+K_{22} & K_{23} & 0 \\ 0 & K_{32} & K_{22}+K_{33} & K_{34} \\ 0 & 0 & K_{43} & K_{44} \end{bmatrix} \tag{6.16}
$$

Equation 6.16 shows that for beams of more than two nodes it is not possible to use diagonal terms to identify elastic parameters because the nodes share their properties. Therefore, local elastic properties of the beam were extracted from the off-diagonal terms. Inertia values for each section are presented in Table B.1 in Appendix B.

The thickness of the flange, t, was set constant and equal to 0.002 m while the height of the web, a, was defined as:

$$a = \begin{cases} 0.02m & for\ y < 0.81m \\ \frac{y-y_{14}}{y_{tip}-y_{14}}\left(a_{tip}-0.02\right)+0.02m & for\ 0.81 < y < 1.5m \end{cases} \tag{6.17}$$

where a_{tip} is the chosen value of the web height at the tip. Ideally the value of a was required to be constant to not complicate the manufacturing process. However, as shown in Figure 6.10, the dimension of a must adapt to the distribution of the chord and the thickness of the XB-2 aerofoils along the wingspan. Hence the definition of Equation 6.17.

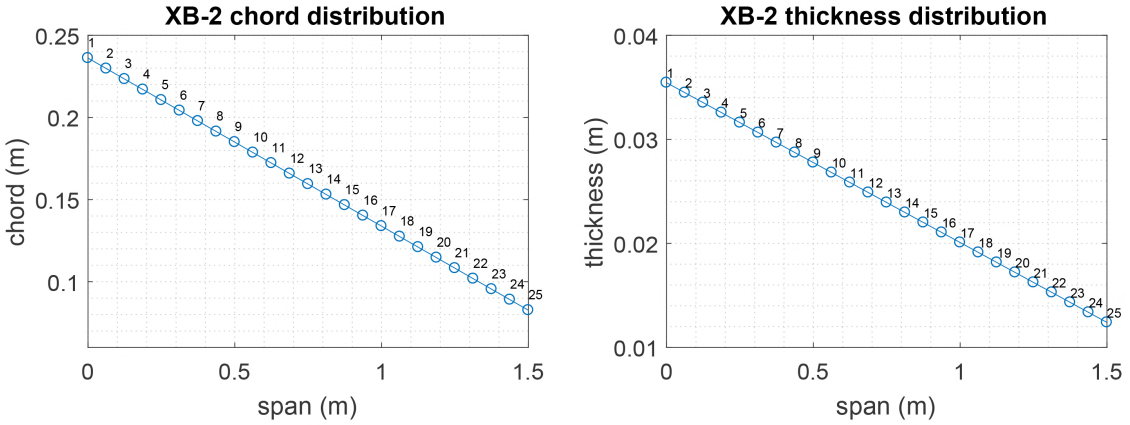

Fig. 6.10.: XB-2 chord distribution (left) and maximum thickness distribution (right)

Boundary conditions were defined as:

$$0.001m < b < 0.14m \tag{6.18}$$

$$0.001m < c < 0.13m \tag{6.19}$$

applied to constrain the spar dimensions to remain within the skin boundaries. A second constraint was defined as:

$$b > c + 0.005 \tag{6.20}$$

to guarantee the numerical solution to be physically viable.

For each section, the problem was defined as:

where J is the function to minimize at each section, i, and defined as:

$$J_i = \left([EI]_{xx}^{K} - [EI]_{xx}^{spar}\right)_i^2 + \left([EI]_{zz}^{K} - [EI]_{zz}^{spar}\right)_i^2 \quad i = 1,..,25 \tag{6.21}$$

$$\begin{array}{ll} \textit{minimize} & J \\ \textit{subject to} & 0.001\text{ m} < b < 0.14\text{ m} \\ & 0.001\text{ m} < c < 0.13\text{ m} \\ & b > c + 0.005 \\ & \text{Equation 6.17} \end{array}$$

The solution of the problem was found solving the following equations:

$$\frac{\partial J_i}{\partial b_i} = 0 \quad i = 1,..,25 \tag{6.22}$$

$$\frac{\partial J_i}{\partial c_i} = 0 \quad i = 1,..,25 \tag{6.23}$$

Figure 6.11 shows dimensions of the spar cross-section along with the volume constraints. Numerical values of the section parameters can be found in Table B.2 in Appendix B. The top-left plot shows the width of flange and thickness of the web compared with the length of the local chord of the wing. The flange is 0.074 m at the root and 0.038 m at the tip, while the web is 0.003 m thick at the root and 0.015 m at the tip. The web thickness increases towards the end to compensate for the reduction in a. Top-right figure highlights the trend of a decreasing from section 14 onwards as dictated by Equation 6.17. The bottom plots show the final cost function value at each section (right) and the inertia ratio between the numerical value and the optimized value.

6.4 Spar manufacturing

Each section of the spar is sized as result of the solution of Equations 6.22-6.23 and then virtually extruded to connect with the following section though a series of spline curves, providing the final tapered shape shown in Figure 6.12. The first three nodes of the spar were constrained in all 6 degrees of freedom as representing the section of the wing connected to the fuselage of the aircraft. Therefore the section was modelled as a square, solid volume (0.110 m x 0.020 m). This metal block hosted the 6 holes used to attach the model to the wind tunnel structure. The technical drawings of the spar can be found in Appendix C.

The viable manufacturing solution to have the spar manufactured as one piece was to use Computer Numerical Controlled (CNC) milling because of the tapered shape of the main section and the irregular shape of the vertical reinforcement. However the spar was manufactured by manually milling the final piece for which the spar had to be divided in two halves with a cut made 750 mm from the root. Moreover, a compromise on the web parameter a had to be found. The parameter a was kept constant and equal to 20 mm in the first half of the spar ($0 < y < 0.750$ m). The second half of the spar was instead machined following the original optimised shape. After the two halves of the spar were completed they were welded together and reinforced with four L-shaped aluminium plates bolted to the spar. Figure 6.12 shows drawings of the theoretical (left) and the manufactured and welded spar (right). In

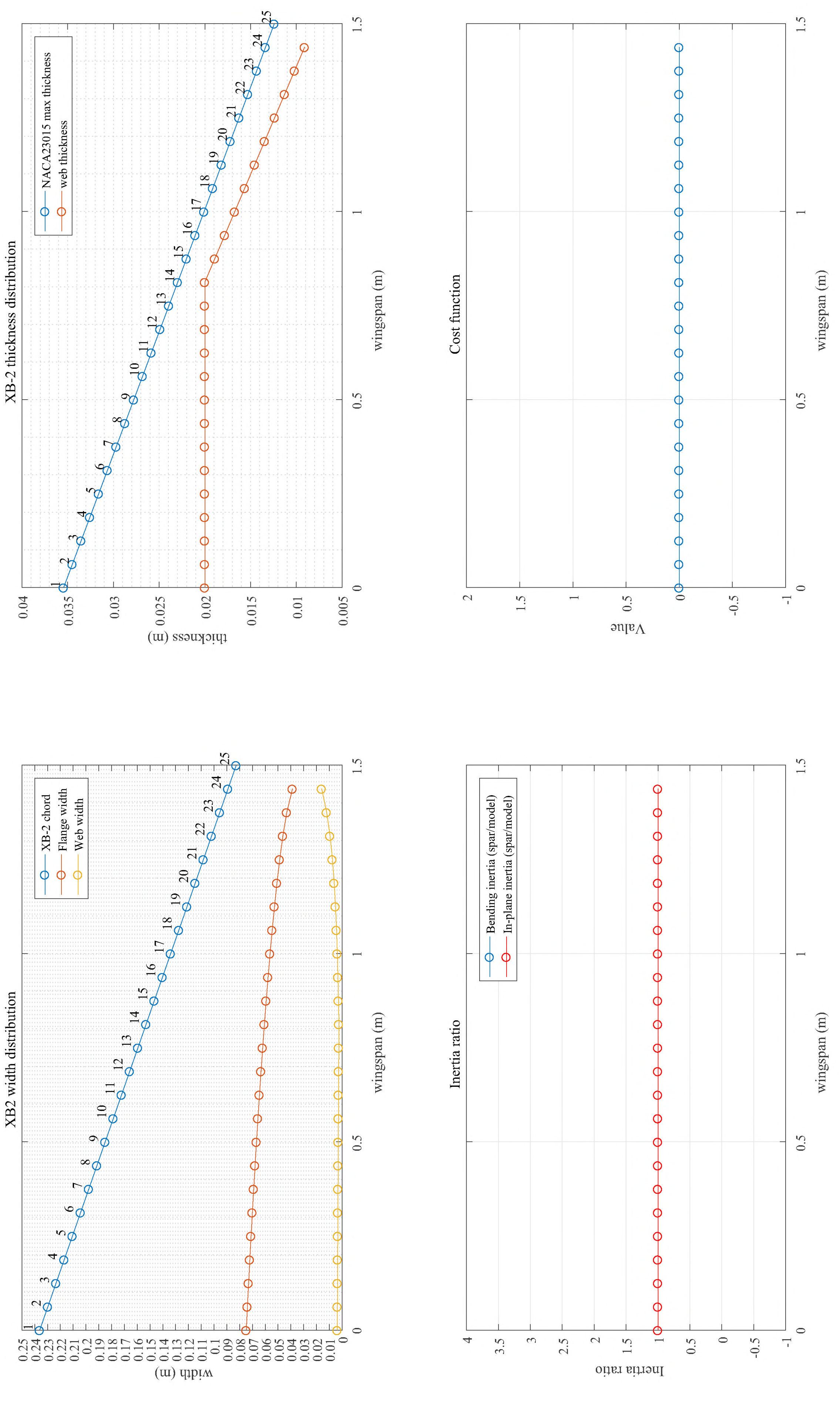

Fig. 6.11.: Plots of the optimal distribution of the optimization parameters.

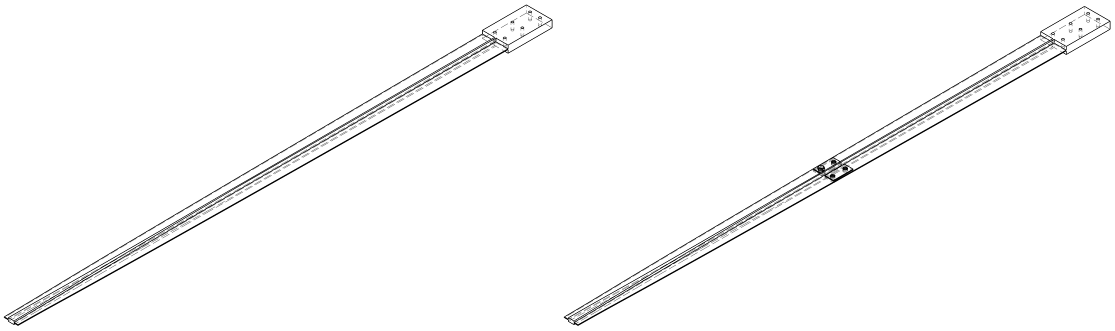

(a) CAD drawing of the optimized spar shape. **(b)** CAD drawing of the manufactured spar shape.

Fig. 6.12.: Drawing of the ideal optimized spar shape and the manufactured solution. In the latter option it is visible at half span the presence of a bolted aluminium plate which strengthens the structure across the welded section.

the latter case, aluminium plates and bolts were placed at the middle of the spar. The assessment of the impact of the weld and the plates was carried out numerically and the numerical model was afterwards validated via ground vibration tests.

6.5 Ground Vibration Test (GVT) and spar characterisation

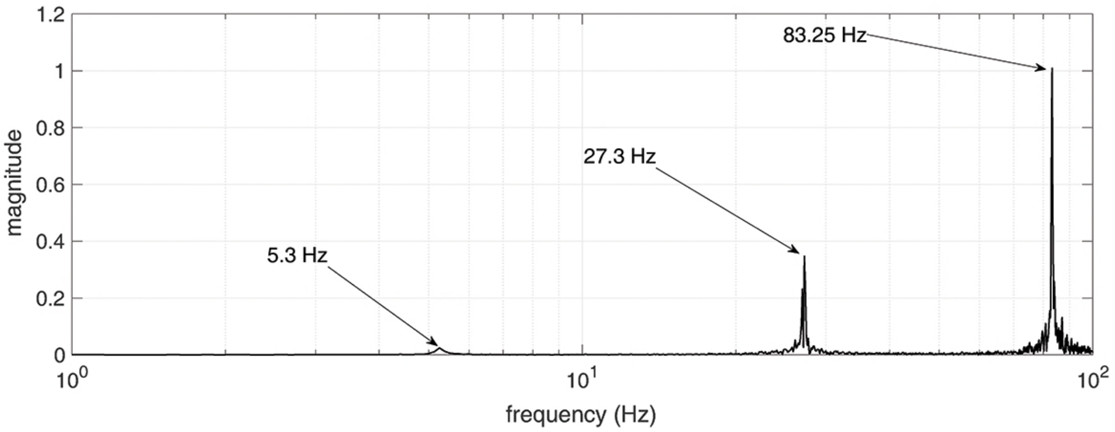

Fig. 6.13.: Frequency response of GVT performed on XB-2 spar. Data represented are acquired from the tip accelerometer.

The first set of structural tests were carried out on the aluminium spar for validating the Finite Element (FE) numerical model and for characterising the frequency response of the metal structure. The FE model was built as a beam element structure in the *punch card* format to be fed into the NASTRAN solver. The solver used for the modal characterisation was the SOL 103 [14], which simply solves the eigenvalue and eigenvector problem as follows:

$$\left([\boldsymbol{K}]-\omega^2[\boldsymbol{M}]\right)\bar{\boldsymbol{\Gamma}}=0 \tag{6.24}$$

where $[\boldsymbol{M}]$ and $[\boldsymbol{K}]$ are the mass and stiffness matrices, ω the natural frequencies and $\bar{\boldsymbol{\Gamma}}$ the eigenvector solution associated to each mode. The numerical approach adopted to calculate the natural frequencies was the Lanczos method [97]. The natural frequencies were calculated for both the ideal optimal solution and for the manufactured one to estimate the impact of the welded section and the addition of aluminium plates with screws and nuts. The plates and bolts were modelled as lumped masses in the FE model.

Figure 6.13 shows the spar frequency response obtained from the structural tests. The GVT was done placing 4 mono-axial accelerometers (Bruel and Kjaer Delta Tron Type 4507[8]) along the spar with the sensitive axis oriented perpendicular to the spar horizontal plate. Thus, results shown in the figure can only be representative of the bending modes. The first bending mode was identified at 5.3 Hz, while the second occurs at 27.3 Hz.

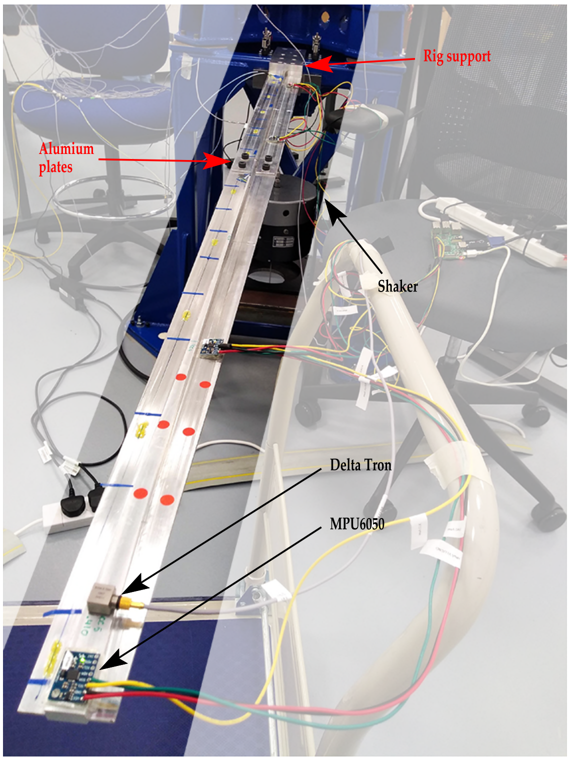

Fig. 6.14.: XB-2 spar GVT test setup

Figure 6.14 shows the set up for the XB-2 GVT test. The spar was rigged to a rigid structure with 6 bolts and an aluminium block specifically designed to support the model. The shaker used to excite the spar was placed under the spar and connected to it through a stinger at the base of the vertical web. The input of the test was a Random on Random (RoR) signal with a bandwidth of 100 Hz.

Table 6.5 shows the results from the numerical simulation compared with the structural test. The first 6 modes were considered. Modes are ordered by magnitude of the natural fre-

---

[8] Some of the specification of the accelerometer are listed here: **Sensitivity** = 9.769 mV/ms^{-2} (95.8 mV/g), **Frequency range** from 0.3 Hz to 6 kHz, **Resonance frequency** = 17.7 Hz.

		Finite Element		Test	
	Type	**Ideal** [Hz]	**Bridge** [Hz]	**GVT** [Hz]	Δf [%]
1st	B	5.6	5.6	5.3	5.4
2nd	L	28.7	28.0	-	-
3rd	B	32.5	31.1	27.3	13.3
4th	T	66.1	62.7	-	-
5th	B	87.6	87.1	83.25	4.5
6th	L	153.7	147.3	-	-

Tab. 6.5.: Natural frequencies and mode shapes identification for the first 6 modes of the spar for the ideal and manufactured spar. B = bending, L = lagging (in-plane) and T = torsion.

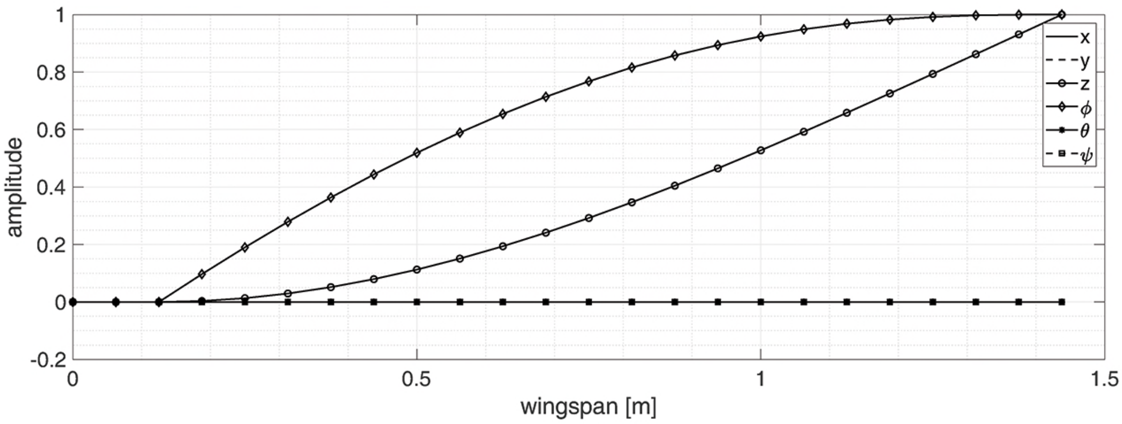

Fig. 6.15.: Normalised displacement and rotation associated to the 6 degrees of freedom of the first mode of the XB-2 spar.

quency. The second column of the table defines the mode type. The eigenvectors associated with each mode were plotted and analysed in all the 6 degrees of freedom to characterise the nature of the modes. Referring to the spar axis system shown in Figure 6.6, the possible numerical mode shapes are: the bending mode, in the y-z plane, the torsion mode, around the y-axis and finally the in-plane mode, in the x-y plane. An example of the mode characterisation is shown in Figure 6.15 where the first mode is identified: the plot represents the normalised displacements, (x,y,z), and rotations, (ϕ, θ, ψ), in the spar axis system against the span coordinate. In this specific case, the spar deforms in the z-direction and rotates around the x-axis. The mode is then identified as bending. The same procedure is applied to the first 6 modes and the associated plots can be found in Appendix C.

The third and fourth column of Table 6.5 show the estimated natural frequencies as a result of the numerical analysis for the ideal configuration and the bridged configuration with bolts and aluminium plates. As expected, the introduction of the plate did not change the order of the modes. In fact, the first bending mode occurs at the same frequency for both the models because of the nature of the mode, which shows only one *node*[9] at the root of the spar. Hence, the introduction of plate does not interfere with the modal displacement of

---

[9] The meaning of node in this case is not related to the structural modelling. When considering the spacial displacement representation of the modes, the node is defined as the point that has zero amplitude of oscillation, while the anti-node is the point whit the maximum amplitude.

the first bending mode (see Figure 6.16) and its frequency. However, going towards the sixth mode, the frequency gap between the two configurations increases to a maximum of 4.2% for the 6^{th} mode, which was considered to be an acceptable deviation from the optimal solution. Another aspect to consider from the frequency analysis is that the natural frequencies of the ideal configuration are always higher than the ones of the bridged solution. This is due to the fact that the limited area of the bridges plates does not affect considerably the stiffness of the spar, while the plates and bolts mass increases the weight resulting in lower values of modal frequencies.

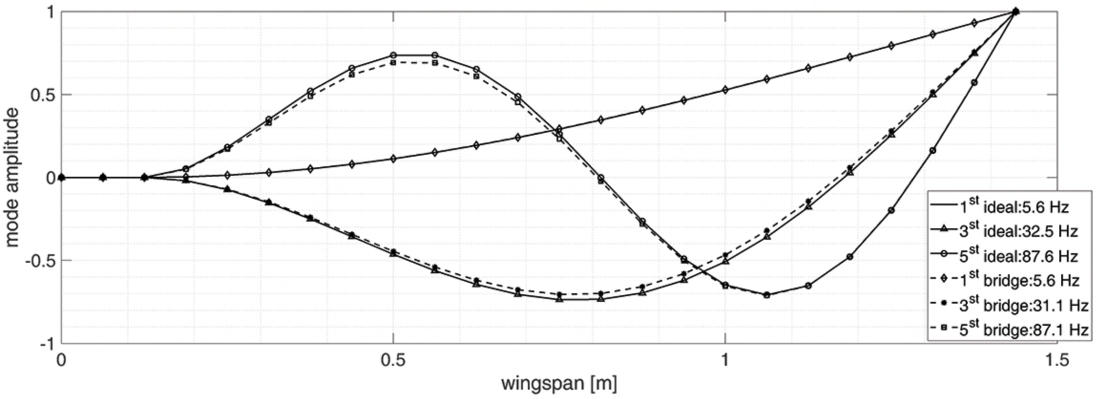

Fig. 6.16.: Comparison of the three first bending mode shapes and frequencies of the ideal theoretical configuration and the manufactured one.

The last two columns of Table 6.5 show the natural frequencies obtained from the GVT and the difference with the numerical model. This step is part of the structural model validation. Results show agreement for the first and third modes, with an error of 5.4% and 4.5% respectively. The error is higher for the second bending mode with a deviation of 13.3%. Figure 6.16 shows the impact of the bridge on the bending mode shapes of the spar. While for the first bending mode the bridge does not impact the shape, for the third and fifth modes instead (2^{nd} and 3^{rd} bending respectively) the bridge is placed either at the anti-node (2^{nd} bending) or at the node (3^{rd} bending), affecting the final modal shape of the spar.

6.6 Skin design and manufacturing

The design of the XB-2 skin followed the same principles and experience gained from the XB-1 one. Requirements for the XB-2 skin were as follows:

1. *To limit the impact of the skin on the model overall stiffness.* Applying the results obtained from the XB-1 test (refer to Chapter 5), the skin was again designed to have a minimal impact on the model overall stiffness.

2. *To be modular.* Including modularity into the design of the wing skin was crucial for several reasons. First, as specified in Section 1.1, the manufacturing of the wing can be expensive, therefore the need to mitigate the costs by producing a low-cost model. Sec-

ondly, it adds design flexibility for future tests as it is always possible to re-design and replace single sections of the wing to test specific technologies, such as folding wing-tip mechanisms [59, 62]. Finally, more practically, modularity facilitates the assembly of the wing.

3. *To be as light as possible.* In order to match the dynamic response of the full scale model, the mass distribution along the wing is crucial. The model was built to be as light as possible so that the target mass distribution could be achieved by adding weights along the spar during the assembly phase. This concept requires the *clean*[10] configuration to be as light as possible. Furthermore, this allows the model to be used to test different mass cases, such as engines or fuel distribution. The limit to the design is the available inner volume of the wing.

4. *To be accessible.* Access to the inner volume of the model must be considered to connect the spar to the skin, to access the instrumentation and servos and to place lump masses.

The 3D CAD drawings of the assembled wing are shown in Figure 6.17. The model skin was divided into four different sections. Each section was printed with PolyJet 3D technique as for the XB-1 model. The succession of rigid and flexible pods is clearly visible in Figure 6.18. The black strips are printed with elastic material (the Agilus30) and the white areas with digital-ABS[11]. The photo of the skin section shows the continuity of the rigid and flexible sections along the spar. Metal dowels were used to guarantee the alignment between sections and they are visible as well. All the dowel holes are reinforced with metal inserts to ensure that assembling and disassembling of the wing does not deform the holes. These also increase the strength of the connection between sections and prevent the ABS from cracking.

Figure 6.19 shows the load pillars used to connect the skin to the spar and the window. The load pillars are 3D printed with digital-ABS and reinforced with threaded metal inserts. It is the metal insert therefore that hosts the screw that connects the skin section to the spar. The load pillars are also responsible for transferring the aerodynamic load from the skin to the spar. Each of them is connected to the spar with two screws to avoid unwanted shear stress due to the pivoting of the pillar around the screw. To size the diameter of the pillars, a simple evaluation of the stress was done. It was assumed that the screws sustain the load and that the glue ideally transfers 100% of the load from the screw insert to the 3D printed pillar. The load acting of the section was calculated assuming an elliptical lift distribution derived from the monoplane equation developed by Prandtl [137] and described as follows [152]:

$$\mu\left(\alpha_0-\alpha\right)=\sum_{n=1}^{N} A_n \sin(n\theta_i)\left(1+\frac{\mu n}{\sin\theta_i}\right) \tag{6.25}$$

---

[10] Clean configurations means in this case the wing model made only of the spar and the skin, without other mass contributions such as servos or lumped masses.

[11] Material properties are specified in Table 5.4 in Chapter 5.

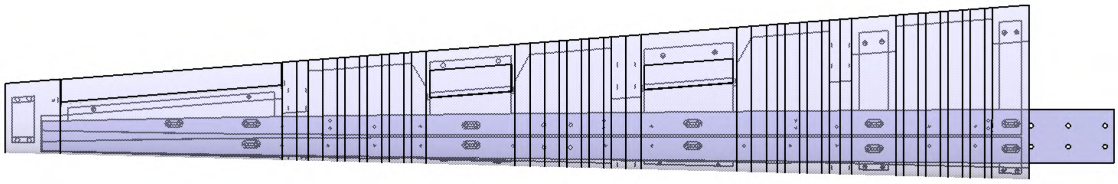

(a) Top view of the assembled wing.

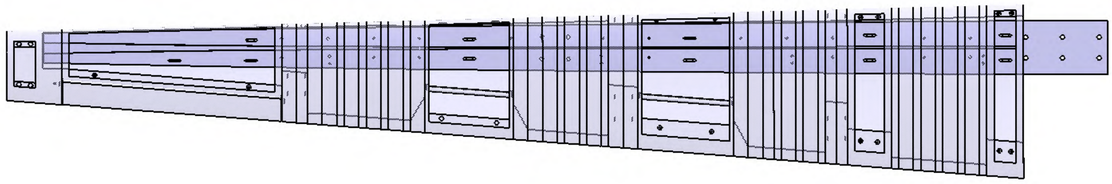

(b) Bottom view of the assembled wing. The 5 windows used to access the inner volume of the model are here visible and open.

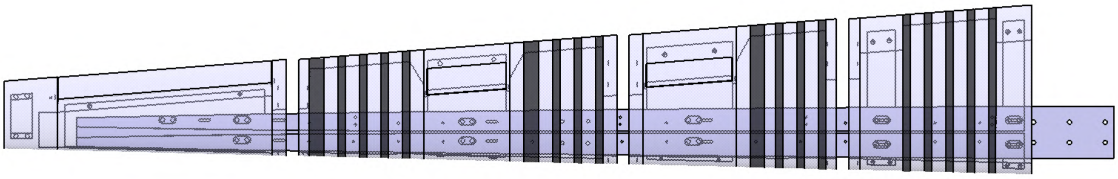

(c) The figure shows the 4 skin sections of the wing.

Fig. 6.17.: CAD sketches of the assembled wing.

Fig. 6.18.: Section of the skin with the connection dowels and the flexible stripes well visible.

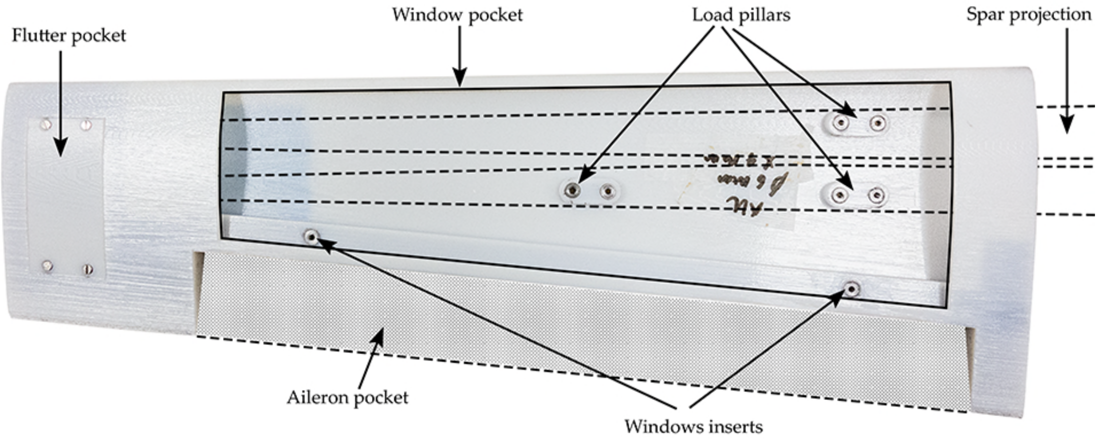

Fig. 6.19.: Bottom view of the tip section of the wing.

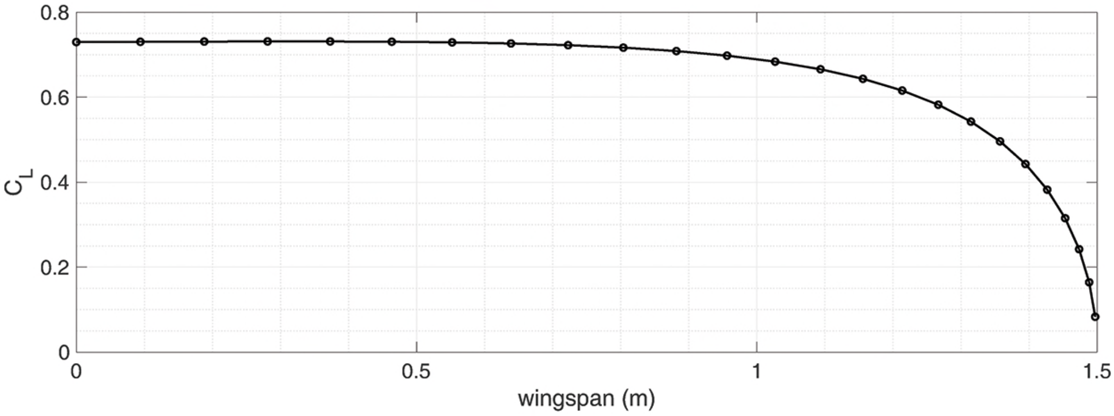

Fig. 6.20.: Elliptical lift distribution estimation of the XB-2.

where

$$\mu = \frac{\bar{C}_i C_{l_\alpha}}{4b}. \tag{6.26}$$

The unknown parameters are the coefficients A_n, while $\bar{C}_i$ is the mean geometric chord, θ is the local lifting-line theory angle and N is the number of nodes along the wing. The number of nodes for XB-2 is N=25. The obtained C_l distribution is shown in Figure 6.20. To evaluate the load on the section, the lift distribution is first integrated over the span where the section is located as:

$$L = qS \int_{y_i}^{y_o} C_l(y)dy \tag{6.27}$$

where y_i and y_o are the inboard and outboard span location of the section respectively, q is the dynamic pressure, ρ is the air density at sea level, $v = 45$ m/s is the test target velocity and the considered angle of attack is $\alpha = 6$ deg. Applying Equation 6.27 for the root section of the wing ($0.125 < y < 0.32$ m), the lift on the upper skin was estimated to be 30 N. It is engineering practice to consider each of the two screws to take 2/3 of the overall load. Therefore, the load on each screw was assumed to be P = 20 N. The bolt diameter was sized on the tensile stress value, defined as:

$$\sigma = \frac{P}{A_t} \tag{6.28}$$

where A_t is the tensile-stress area of the bolt. Considering the bolt made of steel, the yield strength is assumed to be $\sigma_Y = 250$ MPa. From Equation 6.28, the value of the tensile-stress area of the bolt was calculated to be $A_t = 0.08 mm^2$. Referring to available bolt-stress-analysis tables [12], the right size of the bolt would have been M1. However, to simplify the manufacturing of the metal inserts it was chosen a M3 bolt, while the diameter of the 3D printed pillar was set to 10 mm to host the insert.

Each of the skin sections is printed to feature a bottom opening which can be closed with a rigid 3D-printed cover. The cover follows the shape of the local aerofoil and it is screwed in position when the wing is tested. The holes that host the window screws are reinforced with threaded metal inserts. The flutter pocket is also visible in Figure 6.19. The pocket was designed to host extra weights to lower the flutter speed if needed.

6.7 Data acquisition system

The acquisition system used for the XB-2 test is the same as that installed on the XB-1 with some new features (the system's schematic is shown in Figure 6.22). First, connection wires were glued with epoxy to avoid accidental detachment due to the cables being very thin (AWG 28). The glue also prevented short circuits between wires. The second improvement consisted of adding a LCD screen to the system (Figure 6.21). The LCD is used to show the IP address of the Raspberry Pi in order to communicate wirelessly with the board. The screen can also be used to display data from the test. For the XB-2 wind tunnel test, four sensors were used to acquire acceleration and rotation at specific spanwise positions. Locations of the sensors are listed in Table 6.6 and shown in Figure 6.23. The requirement adopted to place sensors along the spar was to avoid to overlap the IMUs with modal nodes associated

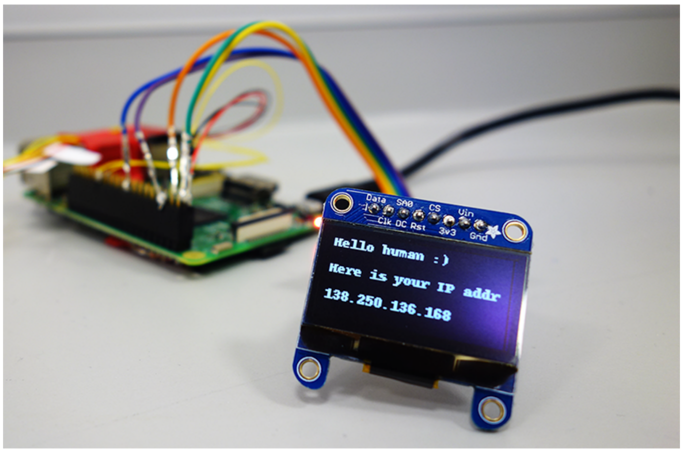

Fig. 6.21.: The LCD screen shows the Raspberry Pi IP address.

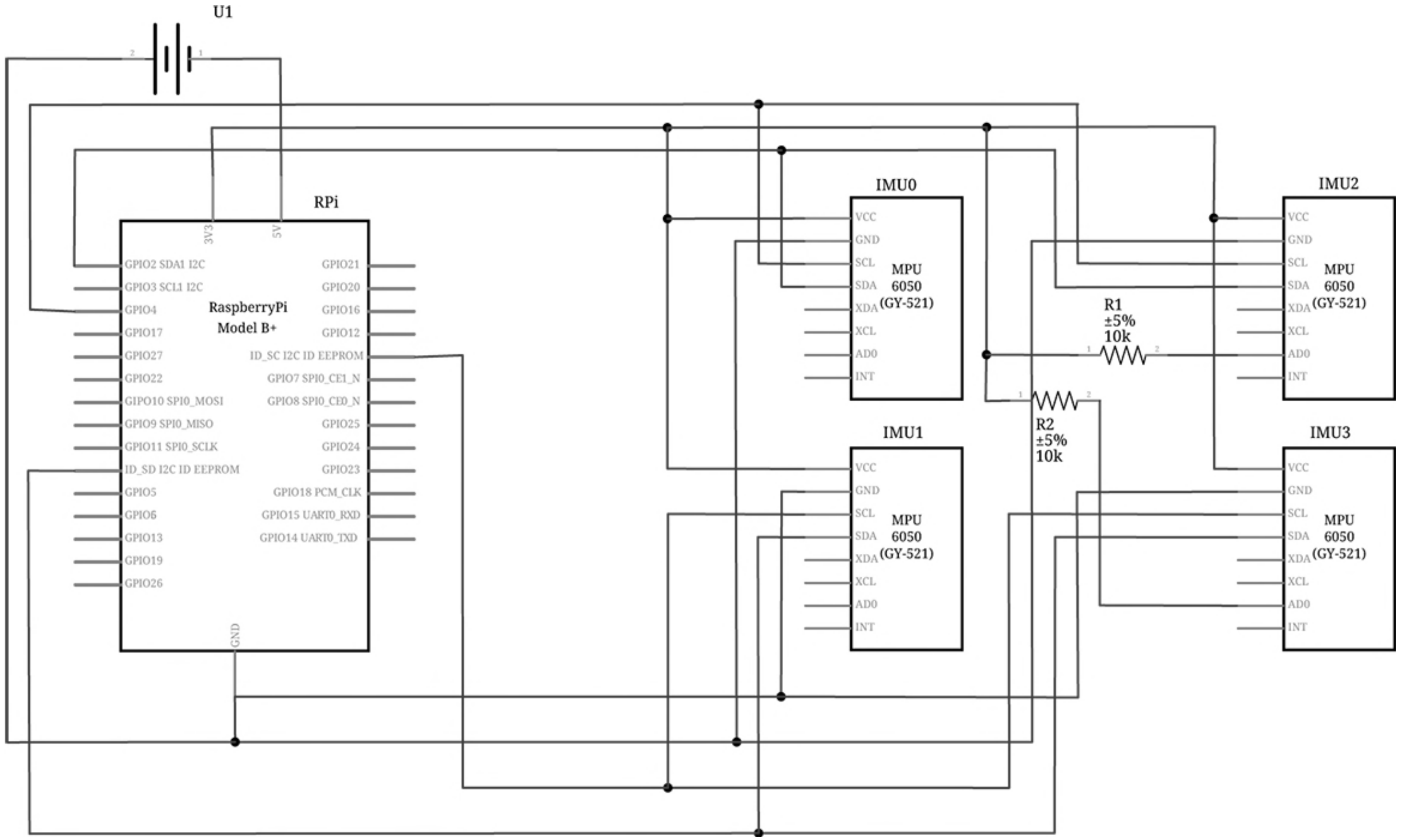

Fig. 6.22.: Sketch of the instrumentation system. For each I2C bus, one of the MPU6050 sensors features a pull-up resistor to change the device address from 0x68 to 0x69.

Sensor	I2C bus	Distance from the root [m]
IMU0	Bus 1	1.4
IMU1	Bus 1	0.965
IMU2	Bus 0	0.620
IMU3	Bus 0	0.360

Tab. 6.6.: XB-2 sensor placement and related I2C bus.

to the first and second bending mode. In fact the aim of the placement was to maximise the SNR of the reading of the nodal velocity and acceleration.

6.8 Assembly and mass distribution

The assembly process was designed to comply with two main requirements: i) to match the mass distribution along the spar to replicate the dynamic response of the full scale wing and ii) to provide a flutter speed higher than the targeted test speed of 45 m/s.

To address the first point, the mass distribution was required to match the one provided by the theoretical model. Figure 6.24 shows the mass and inertia distribution of the numerical model compared with the ones of the spar+skin model configuration [191]. To obtain the additional weight at each section of the wing, the theoretical optimal distribution (result of the scaling process) is compared with the mass distribution evaluated from the wing FE numerical model (spar+skin configuration). In the latter model, the spar is again modelled as beam elements structure while the skin is distributed over the spar as a series of lumped masses. The value of those skin masses is derived from the CAD model of the skin and corrected by physically weighing each skin section. The vector of the additional required weights is defined as the difference between the theoretical and the numerical mass distribution. Figure 6.24 also shows a peak in the FE mass and inertia distribution at $y = 1.3125$ m. This section represents the midspan location of the aileron. In fact, the 3D printed aileron

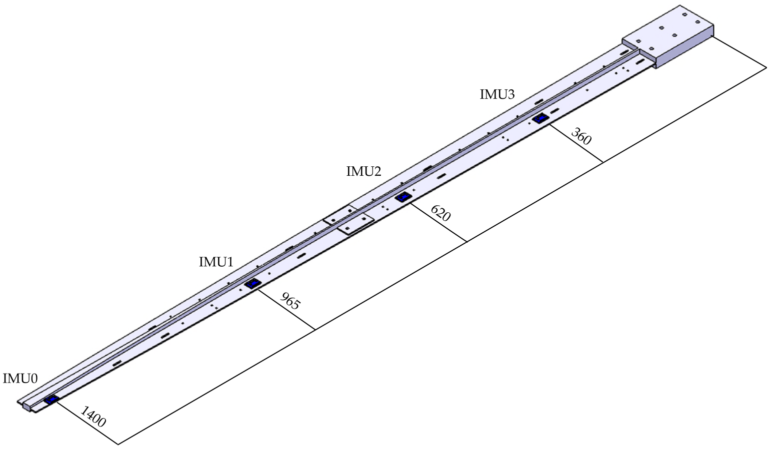

Fig. 6.23.: XB-2 CAD and sensors placement.

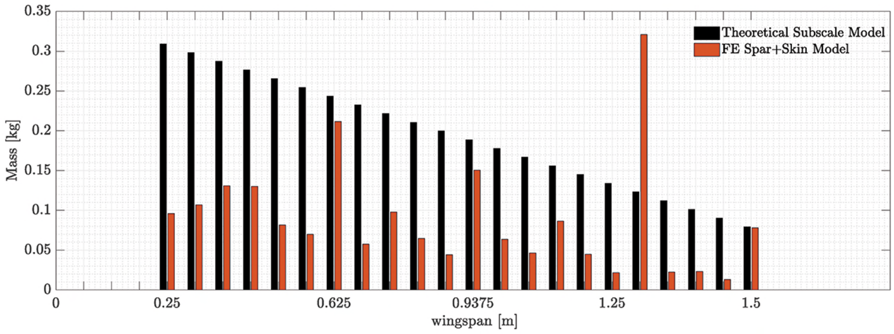

(a) XB-2 theoretical mass distribution derived from the scaling process

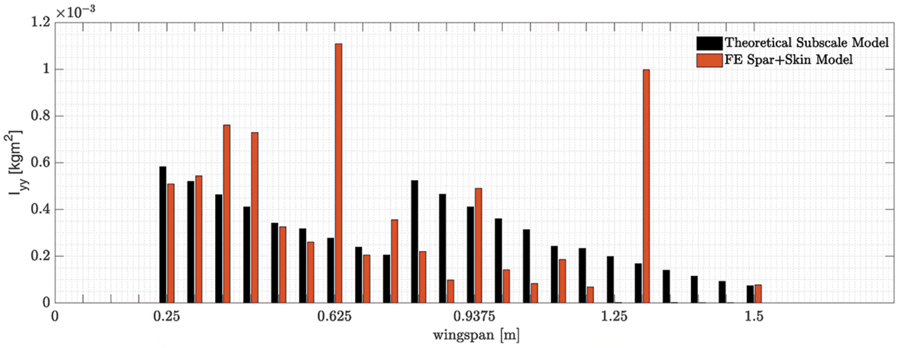

(b) XB-2 theoretical torsional inertia distribution derived from the scaling process

Fig. 6.24.: XB-2 mass and inertia distribution derived from the scaling process.

section density is higher than the rest of the wing sections because it was printed as a full volume piece.

The result of the comparison is given in Table 6.7, where location, mass and position of the additional weights is listed. Position of the masses is referred to a local axis system whose origin is the local section CoG. For each spar section, the position of the weights was estimated by matching the torsional inertia distribution of the original theoretical model. Although to reproduce the dynamic response of the full-scale model the whole wing mass distribution should match, weights were physically distributed only up to 75% of the span due to volume restriction [12].

The main requirement to manufacture the additional weights, due to the volume restrictions, was to be machined out a material as dense as possible. Therefore, they were manufactured using brass (grade CZ121). A 3D CAD of the final distribution of the weights along the spar is shown in Figures 6.25 and 6.26. Some of the sections are characterised by having two weights in order to place the CoG of the overall mass in the required position. Figure 6.26a shows a picture of the weights placed on the spar while Figure 6.26b shows the distribution of the weights along the spar.

---

[12] One could argue that in this case the dynamic response does not match the full scale model one. However, this aspect of the response is discussed in detail later in this chapter as it becomes a secondary problem when a new feature, a stiffening rod, is added to the model.

			Position		
Section	**Distance from root** [m]	**Mass** [kg]	**x** [m]	**y** [m]	**z** [m]
4	0.1875	0.213	-0.059	0	0
5	0.2500	0.191	0	0	-0.013
6	0.3125	0.156	0	0	-0.013
7	0.3750	0.146	0	0	-0.013
8	0.4375	0.184	-0.053	0	0
9	0.5000	0.185	-0.051	0	0
10	0.5625	0.032	0	0	-0.015
11	0.6250	0.175	-0.048	0	0
12	0.6875	0.124	0	0	-0.011
13	0.7500	0.146	-0.046	0	-0.010
14	0.8125	0.156	-0.049	0	-0.010
15	0.8750	0.038	0	0	-0.010
16	0.9375	0.114	-0.044	0	-0.009
17	1.0000	0.120	-0.044	0	-0.009
18	1.0625	0.070	-0.036	0	0
19	1.1250	0.100	-0.041	0	-0.008

Tab. 6.7.: XB-2 weights and their position with respect the quarter chord placed on the spar to match the wing dynamic response.

An FE model of the scaled wing including the weights was built in order to predict the flutter speed. Figure 6.27 shows the results from the flutter analysis predicting a flutter speed of 31.5 m/s, much lower than the target speed for the wind tunnel test of 45 m/s. The lower flutter speed occurred due to the difficulties of matching the torsional inertia [191, 192]. In the early design stage of the model, the spar was designed to be placed at quarter chord of the NACA 23015 profile to take advantage of the maximum thickness of the aerofoil. The idea proved to be wrong and it is actually common to place the spar at about 40% of the profile chord to prevent low torsional inertia and torsional instabilities such as those found in the XB-2 model [104]. In fact, the order of the natural modes for the final configuration of XB-2 is different from the one predicted for the full scale aircraft, where the first torsional mode for the scaled model is actually the second mode of the structure[13] (rather than the fifth). This torsional mode is the cause of the early onset of the flutter as it couples with first bending mode. Unfortunately once the design error was found, it was too late to move the spar back to 40% of the chord due to volume restriction.

Therefore it became clear that the full scale model dynamics could not be reproduced within the work done in this study. Different mass distributions were evaluated in order to increase the flutter speed. However, such configuration resulted in a maximum value of the flutter speed of 36 m/s, still too low for the wind tunnel test campaign. It was therefore decided to stiffen the wing by introducing a metallic rod parallel to the spar centreline. The mass distribution was left as the optimal distribution while three aluminium supports were manufactured and installed on the spar. The aim of the supports is to rig the stiffening rod to

---

[13] The nature of the modes is detailed later in the chapter where the FE numerical predictions are combined with GVT data.

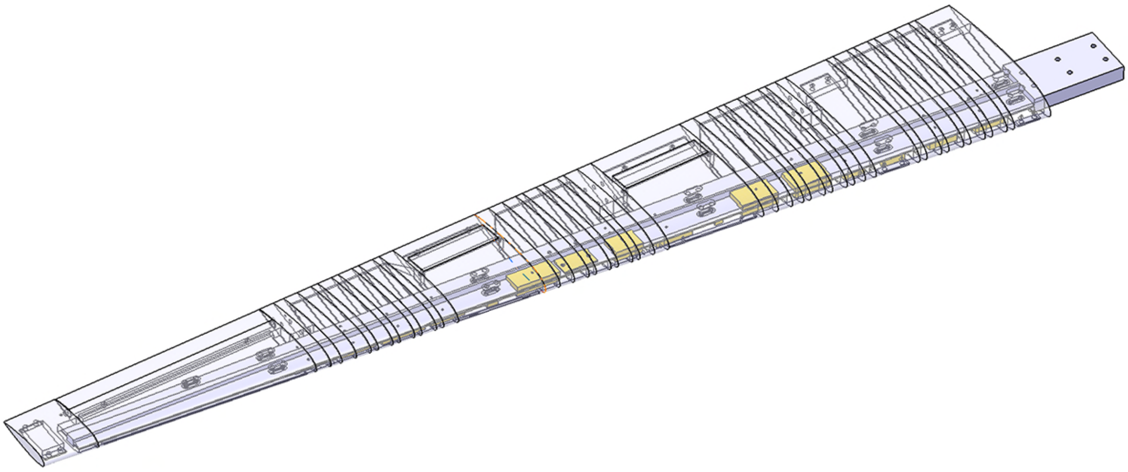

(a) XB-2 full wing CAD with the weights highlighted in yellow.

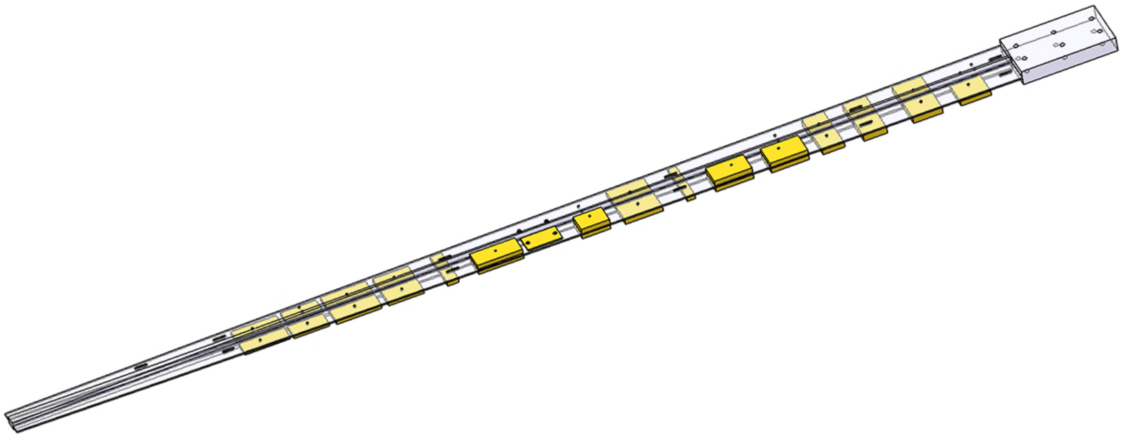

(b) XB-2 spar CAD with the weights highlighted in yellow.

Fig. 6.25.: XB-2 CAD representation of the weights (yellow) distribution.

the spar. These supports were placed at 0.17 m, 0.43 m and 0.69 m from the root respectively. Different combinations of the rod length were considered in order to achieve higher flutter speed keeping the wing as flexible as possible. Eventually 10 mm diameter hollow stainless steel rod of 1 mm thickness was used. It extended along the spar from 0.17 m to 0.69 m, for a total length of 0.52 m. Figure 6.28 shows the rod mounted on the spar. The flutter speed calculation of the stiffened model is shown in Figure 6.29. Flutter occurred when the second mode (torsion) diverged. The flutter speed of the stiffened model was estimated to be 47 m/s and for safety reasons the maximum test speed was set to 40 m/s. The FE model of the rod was built assembling NASTRAN *pbeam* elements and connecting them to the spar structure at the bracket locations.

The FE numerical model frequency analysis was compared with the outcome of GVT tests carried out on the full wing model (spar+skin+weights+rod) to validate the flutter speed. Five uni-axial Delta Tron accelerometers were placed on the skin to read vertical acceleration. The analysis of the response is carried out by processing the data from the tip accelerometer. Figure 6.30 shows the response of the full assembled wing for RoR input covering 0-60 Hz. As

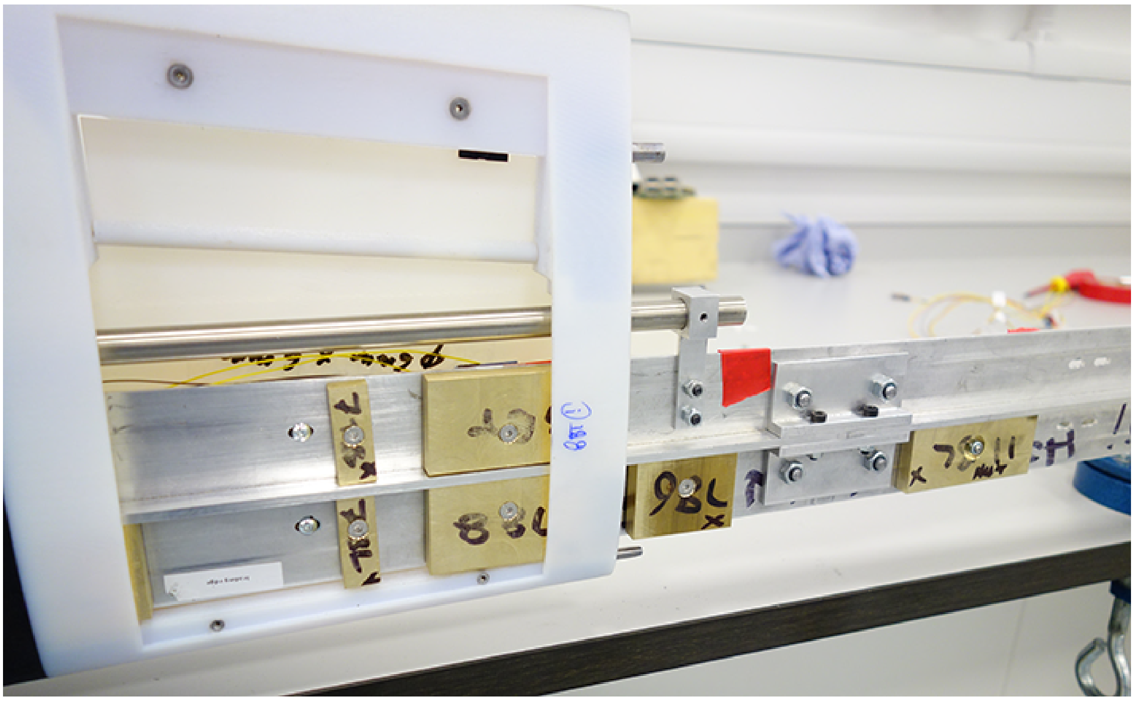

(a) XB-2 photo of the wing assembly process.

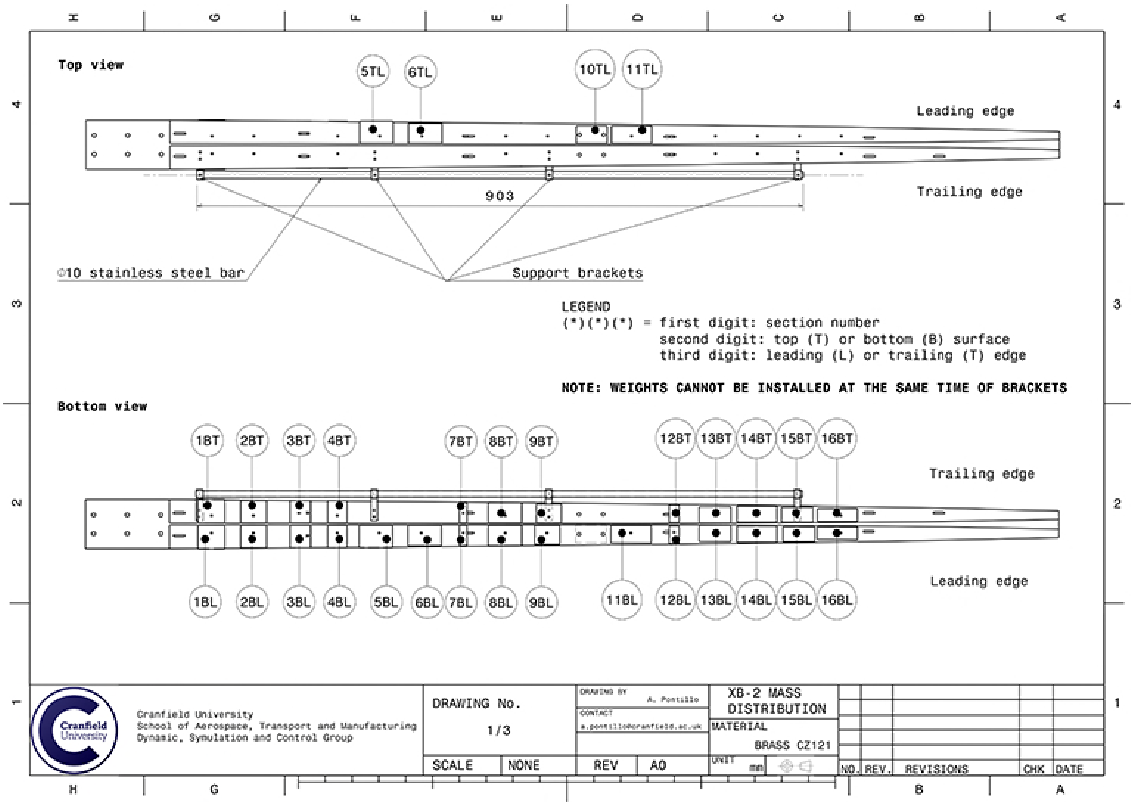

(b) One out of three XB-2 drawings of the wing model used to manufacture the weights for matching the full model dynamics.

Fig. 6.26.: XB-2 weights distribution

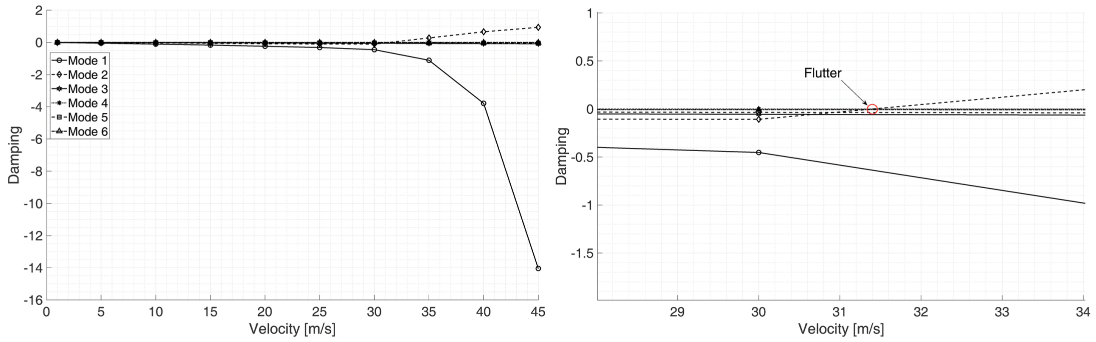

(a) Damping of the XB-2 first 6 modes with weights deployed along the spar.

(b) Zoom of damping of the XB-2 first 6 modes with weights deployed along the spar.

Fig. 6.27.: Flutter analysis of XB-2 NASTRAN model with brass weights along the spar.

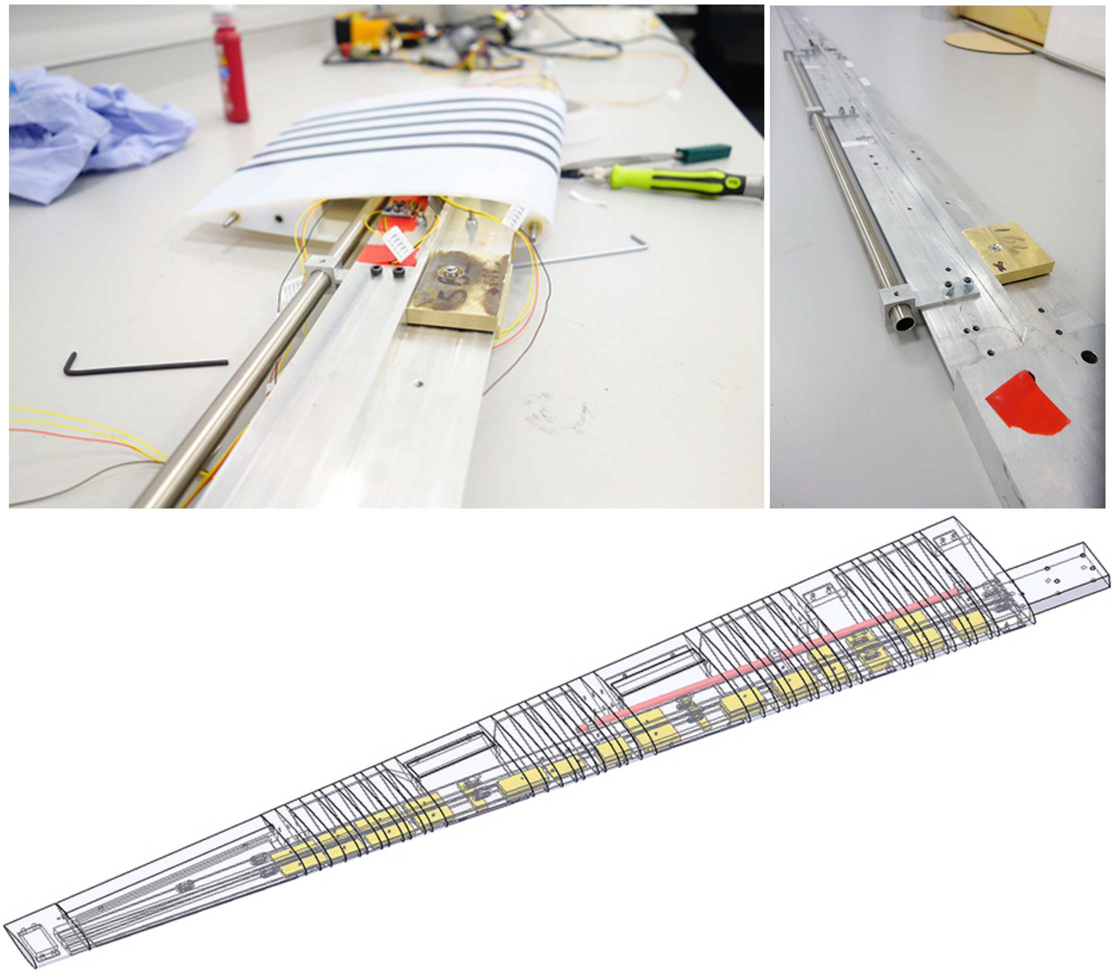

Fig. 6.28.: XB-2 final configuration with stiffening rod (in red).

before, the identified response can only be related to the bending modes due to the nature of the accelerometers used. Four peaks were identified: at 3.03 Hz, 3.25 Hz, 14.7 Hz and 38.3 Hz. The first two peaks can be probably identified as the same mode. The choice of RoR as input of GVT leads to have a non-constant energy associated with different frequencies. This leads to the possibility of having some natural modes more evident than others due to the SNR

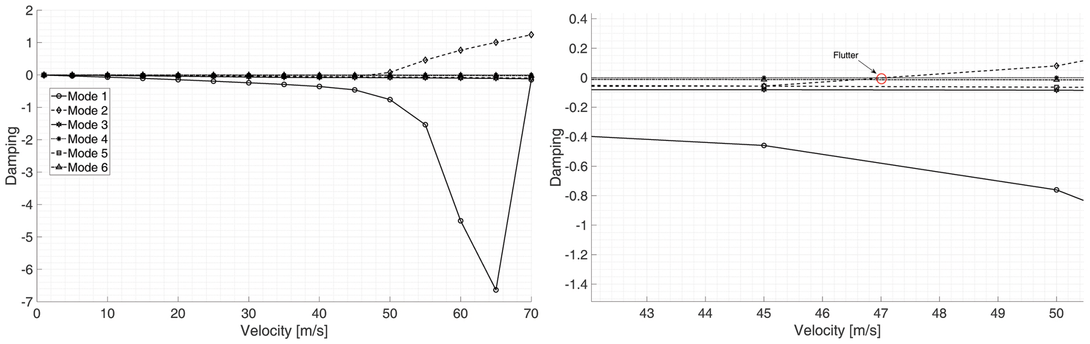

(a) Damping of the XB-2 first 6 modes with the stiffening rod.
(b) Zoom of damping of the XB-2 first 6 modes with stiffening rod.

Fig. 6.29.: Flutter analysis of the stiffened XB-2 NASTRAN model with the stainless steel rod.

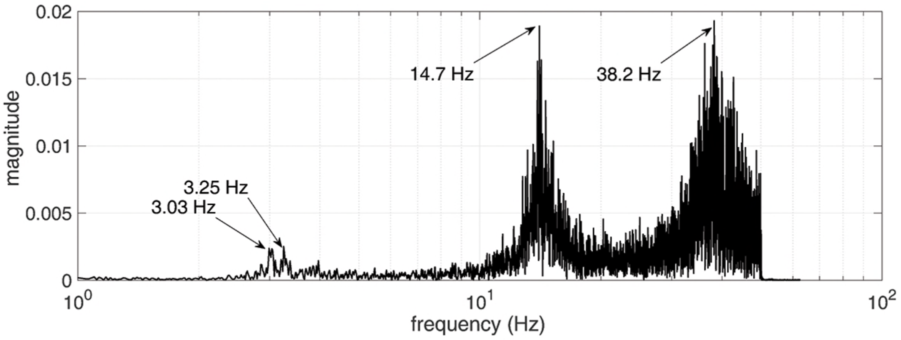

Fig. 6.30.: Frequency response of the XB-2 model for RoR input during the structural assessment.

associated with the specific frequency tested [63]. This is even more likely in the lower part of the spectrum due to the associated low frequencies. However, the comparison made in this work is only qualitative to assess the fidelity of the FE model. Therefore, for this specific case, no further analysis was carried out and the first bending frequency was chosen to be $f_1 = 3.25$ Hz.

Frequencies derived from the GVT were compared with those obtained from the FE eigenproblem analysis. However, the nature of the modes was not as clear as in the case of the spar analysis because the full wing was a more complex structure due the presence of the rod. Thus, it was hard to clearly work out the nature of the modes and associate them with the related natural frequencies. Furthermore, the modes were never *pure*, but always coupled. Plots of the mode DOF are shown in Appendix C for the full wing analysis. Table 6.8 shows the comparison between the FE prediction and the structural test results[14]. The maximum difference between the structural test and the numerical prediction was 14.5% for the first mode. The first and the sixth modal frequencies were overestimated by the FE model since the masses of the brackets were not modelled in the numerical model. Thus, the FE model was lighter and higher natural frequencies were expected. The second modal frequency instead was underestimated by the FE model.

---

[14] The natural frequencies of the XB-2 are in agreement with the structural response of flexible models with the same geometric characteristics and mass [104].

	Type	**FE** [Hz]	**GVT** [Hz]	Δf [%]
1^{st}	**B**/T	3.8	3.25	+ 14.5
2^{nd}	**B**/T	13.7	14.7	- 6.9
3^{rd}	-	17.5	-	-
4^{th}	**L**/T	18.7	-	-
5^{th}	T	24.1	-	-
6^{th}	B	42.5	38.3	+ 9.9

Tab. 6.8.: Natural frequencies and mode shapes identification for the full assembled XB-2 model. In bold the dominant identified mode.

6.9 Discussion and next step

In this chapter the reader was presented with an insight of the XB-2 wind tunnel flexible model. Firstly the design and manufacturing processes were described in detail. The model was designed and built following the common spar+skin configuration, 3D printing the skin with Polyjet technology. The spar instead was manufactured in aluminium alloy and its cross-section shape designed to match the dynamic response of the full-scale model.

Secondly, the chapter presented the challenges faced to match the mass distribution along the spar. Whilst the right mass distribution was obtained placing lumped masses along the spar, it was not possible to match the scaled inertia distribution provided by the scaling process due to the position of the spar along the chord. This, along with the lower model torsional stiffness compared to the full-scale model, led to a lower flutter speed with respect to the test target speed. A stiffening rod was therefore introduced to increase the torsional stiffness and delay the flutter onset.

In the next chapter results of the testing of the XB-2 model are discussed. The test focused on evaluating the static and dynamic response of the wing. Results were used to assess the fidelity of the BEaRDS^{TM} software outcome, hence to validate CA^{2}LM framework.

7

eXperimental BeaRDS 2: testing (XB-2)

The XB-2 wing model was tested in the Cranfield subsonic closed-circuit closed-section 8x6 ft wind tunnel. Details of the facility are listed in Table 7.1, and the wind tunnel setup is shown in Figure 7.1. The wing model was rigged to the force and moment balance through an aluminium support specifically designed and manufactured for the test. The balance was located at the top of the tunnel. The ceiling-wing-support-balance rotates as one body in order to change the angle of attack of the model. A fuselage was added to simulate the wing-fuselage interference and to prevent the build-up of the boundary layer on the roof of the tunnel. The shape of the fuselage is a simple cylindrical body, with a spherical nose and a conical tail. The vertical and horizontal tail planes were not included for this specific test as the response of the aircraft as a whole was considered beyond the scope of this study. The model was mounted on the roof to avoid the effect of gravity on the wing deformations. Figure 7.2 shows photos of the wind tunnel setup: the top left image shows the wing-balance mounting (the fuselage is removed) and the top right photo shows the rotating roof. The bottom photo shows the XB-2 model in its test configuration.

Designation	Low speed, closed return	**Max Mach No**	0.15
Contraction ratio	7:1	**Flow speed** [m/s]	5-50
Max Reynolds No	3.6×10^6/m	**Pressure**	Ambient
Test Section [m]	2.4 x 1.8	**Turbulence intensity**	<0.1%
Dynamic Pressure [kN/m^2]	up to 1.5		

Tab. 7.1.: Cranfield 8x6 ft wind tunnel specification

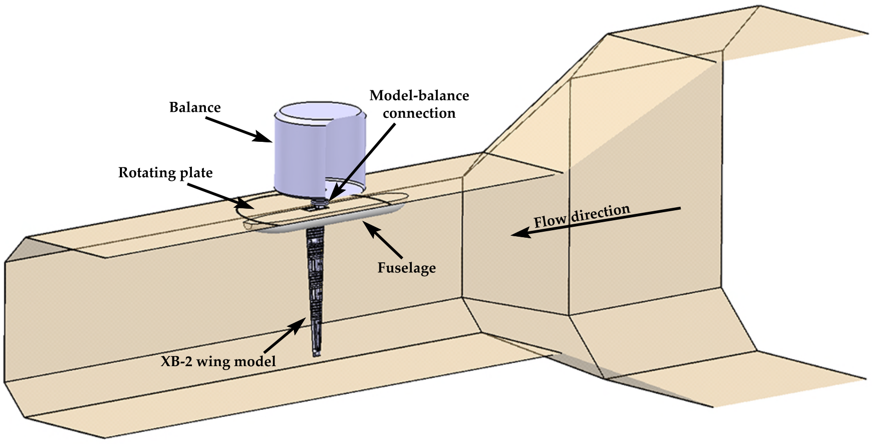

Fig. 7.1.: CAD representation of the XB-2 wind tunnel setup

Fig. 7.2.: XB-2 wind tunnel test setup

The aim of the test was to assess the limitation of BEaRDS^{TM} and consequentially of the CA^{2}LM framework. The experiment evaluated the static aeroelastic response of the XB-2 wing (measuring forces and static deflections in different conditions) and the dynamic aeroelastic response of the model (to estimate the overall wing damping). In order to perform dynamic tests, a metal string was fixed from the spar tip to the control room through the floor using a system of pulleys. By pulling the wire the initial displacement of the wingtip could be set for assessing so that upon release the dynamic response could be excited. The same wire was used to secure the model in case of structural failure.

A set of six angles of attack, from -2 deg to 8 deg, and five different velocities, from 20 m/s to 40 m/s, was tested. Repeatability was tested for all angles and velocities, providing consistent output throughout the test matrix. The force balance output consisted of an average of the 10 s recording, directly provided by the balance software (along with the standard deviation of each dataset). The time histories of the force readings were not available to be collected. Data from the IMU sensors were instead recorded as time histories, which required processing before analysis.

7.1 Static aeroelastic response: forces

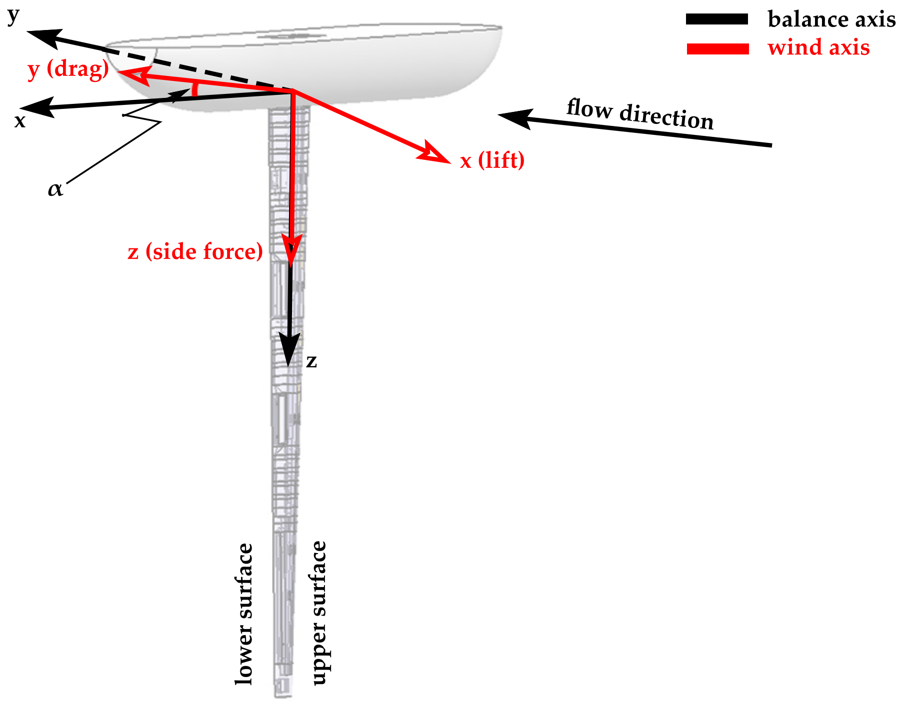

Fig. 7.3.: Representation of the body (balance) and the wind frames of reference adopted for the XB-2 test.

Experimental forces were measured in the balance (wing-body) axis system and then transferred to the wind axis system. Figure 7.3 shows the two axis systems and their relative positions depending on the angle of attack, α. The relationship between the forces in balance axis and wind axis was derived as follows:

$$\begin{bmatrix} L^w \\ D^w \\ Z^w \end{bmatrix} = \begin{bmatrix} -\cos\alpha & -\sin\alpha & 0 \\ -\sin\alpha & \cos\alpha & 0 \\ 0 & 0 & 1 \end{bmatrix} \begin{bmatrix} L^B \\ D^B \\ Z^B \end{bmatrix} \tag{7.1}$$

where L, D, and Z are lift, drag and sideforce respectively. The superscripts w and B indicate wind and body axis respectively. The sideforce is defined as the force that develops along the spar, positive in the root-to-tip direction. A similar relationship is derived for BEaRDS^{TM} to evaluate forces in wind axis from the node body axis system. As well as in the experimental setup, BEaRDS^{TM} also evaluates forces in the body axis system. The transformation of coordinates from the body to wind axis system in BEaRDS^{TM} is defined follows:

$$\begin{bmatrix} L^w \\ D^w \end{bmatrix} = \begin{bmatrix} \cos\alpha & -\sin\alpha \\ \sin\alpha & \cos\alpha \end{bmatrix} \begin{bmatrix} L^B \\ D^B \end{bmatrix} \tag{7.2}$$

In Equation 7.2, the sideforce element is not considered because the model does not implement follower forces. Therefore, the lift is always vertical and does not follow the wing deflection. This approximation prevents the forces to generate a spanwise component. However, the assumption is acceptable for small deflections and must be assessed for flexible structures.

The aerodynamic forces considered for the analysis are lift, drag and side force, following the axis convention shown in Figure 7.3. Only the difference between experimental data and numerical prediction is discussed here to be consistent with the aim of the test [1]. The magnitude of the forces is plotted in Figure 7.4 to provide an idea of the load that the model structure is able to sustain. In fact, one of the objectives of the test was to prove that the BEaRDS manufacturing process is suitable and safe for wind tunnel tests. Forces are as well compared with BEaRDS^{TM} prediction to assess the accuracy of the numerical model output. The error on the force was estimated using the standard error of the mean, σ_ϵ, defined as:

$$\sigma_\epsilon = \frac{\sigma}{\sqrt{n}} \tag{7.3}$$

where σ is the standard deviation on the force data collected from the balance and n is the number of runs of each experimental case. Note that the error is often close to zero. The force data points were plotted along with the related error, although often the error bar is not visible as σ_ϵ is small. The application of a correction coefficient was considered in order to account for blockage effect in the wind tunnel. The correction for solid and wake blockage can be estimated as [20]:

$$\epsilon = \frac{1}{4}\frac{\textit{model frontal area}}{\textit{test-section area}} \tag{7.4}$$

---

[1] The summary of the experimental data is given in Table C.1 in Appendix C.

For this specific test, the correction considered the wing coefficient, ϵ_w, and the fuselage coefficient, ϵ_f. The overall correction coefficient was obtained as follows:

$$\epsilon = \epsilon_w + \epsilon_f = \frac{1}{4}\frac{b\,t_{8\text{deg}}}{S_{\text{tunnel}}} + \frac{1}{4}\frac{d\,h}{S_{\text{tunnel}}} = 0.012 = 1.2\% \tag{7.5}$$

where b is the model span, $t_{8\text{deg}}$ is the frontal profile thickness at $\alpha = 8$ deg, d is the fuselage diameter while h is the fuselage thickness. Equation 7.5 shows that the blockage effect related to the model is in this case minimal, affecting measurement by 1.2%. Therefore, the correction coefficient were not applied to the aerodynamic data.

The lift force for different angles of attack is shown in Figure 7.4a. The error between the numerical prediction and experimental data is detailed in Table 7.2. The trend in error is evident in Figure 7.5 for different velocities and angles of attack. The analysis of the data shows good agreement between the numerical prediction and the wind tunnel test results. The biggest difference were seen for $\alpha = -2$ deg and v = 20 m/s where the error is 31.4%.

α	$\Delta_{20\,m/s}$ [%]	$\Delta_{25\,m/s}$ [%]	$\Delta_{30\,m/s}$ [%]	$\Delta_{35\,m/s}$ [%]	$\Delta_{40\,m/s}$ [%]
-2	-31.4	-26.5	-18.5	-12.8	-7.2
0	-11.3	-10.3	-10.6	-13.8	-22.2
2	-8.7	-4.62	-4.6	-6.9	-12.1
4	-13.4	-7.7	-5.1	-5.3	-7.3
6	-10.3	-6.9	-4.1	-2.4	-1.3
8	-0.7	0.8	2.3	5.4	11.4

Tab. 7.2.: Error between lift force evaluated with BEaRDS^{TM} and experimental results (wind tunnel test data taken as reference).

An interesting point to stress is that in most cases the numerical prediction underestimates the experimental results. However, for $\alpha = 8$ deg, and v > 20 m/s, the opposite is seen where BEaRDS^{TM} overestimates the forces. This may be a clear sign of the need for including a model that considers follower forces[2]. In fact, as the wing deforms, a component of lift is generated towards the root and subtracted from the lift vector. This spanwise component is not considered in the numerical model. Thus, when wing deflection is not negligible, the physical lift decreases while it is overestimated by the numerical model which still considers lift to be fully vertical.

The BEaRDS^{TM} prediction of drag on the other hand is less accurate. The comparison is shown in Table 7.3 and trend of the errors are shown in Figure 7.6. The computed error for drag is much higher than the one for lift. The average error is around 40%-50% (fairly constant across the velocity range). This result was expected because of the nature of the numerical drag estimation.

---

[2] This aspect was already clear by the literature where it has been stressed the importance of follower forces model for flexible structures analysis [161].

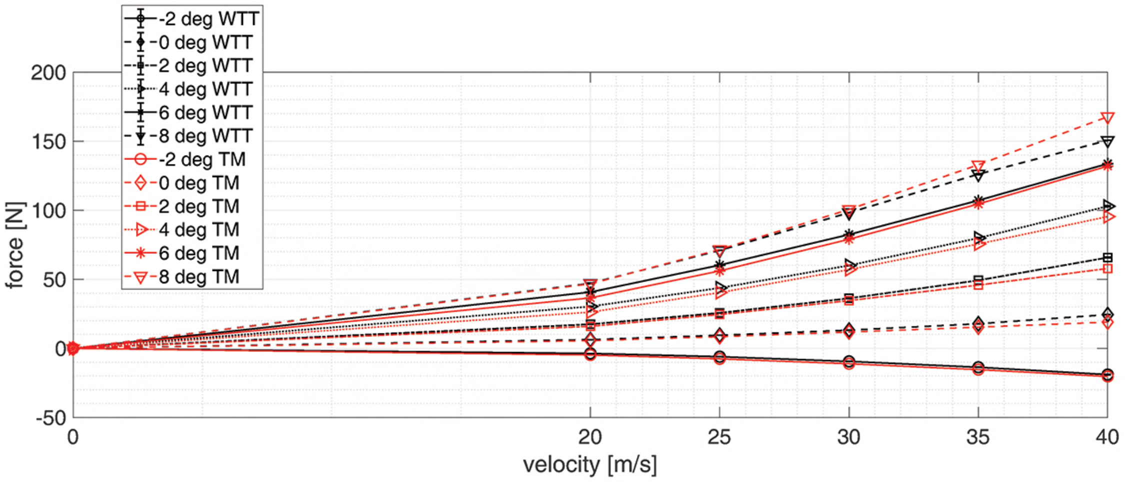

(a) XB-2 lift force vs velocity.

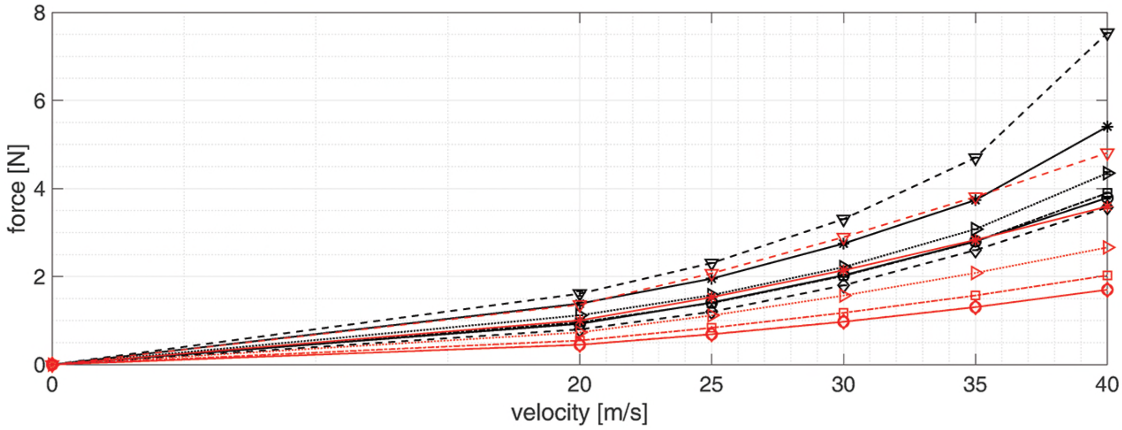

(b) XB-2 drag force vs velocity.

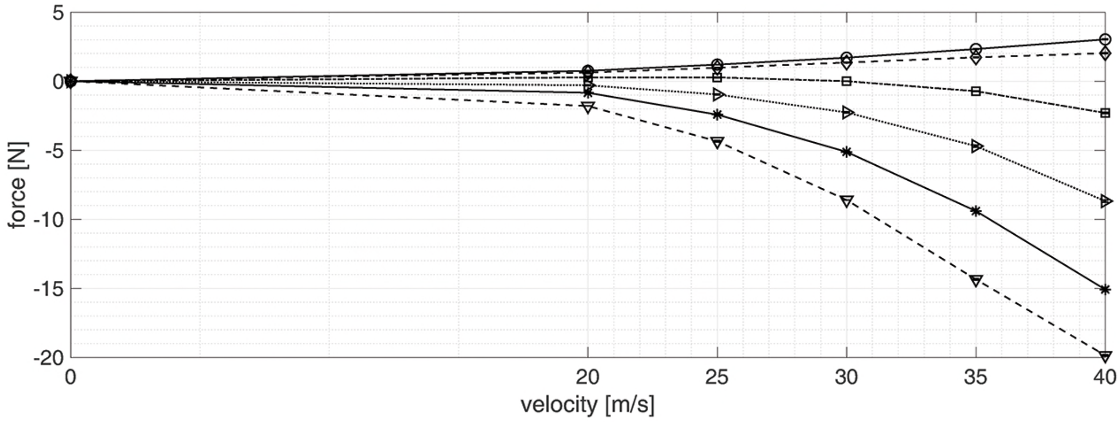

(c) XB-2 side force vs velocity.

Fig. 7.4.: XB-2 static lift (*top*), drag (*middle*) and side (*bottom*) forces for different velocities. In black wind tunnel test (WTT) and in red BEaRDS^{TM} (TM).

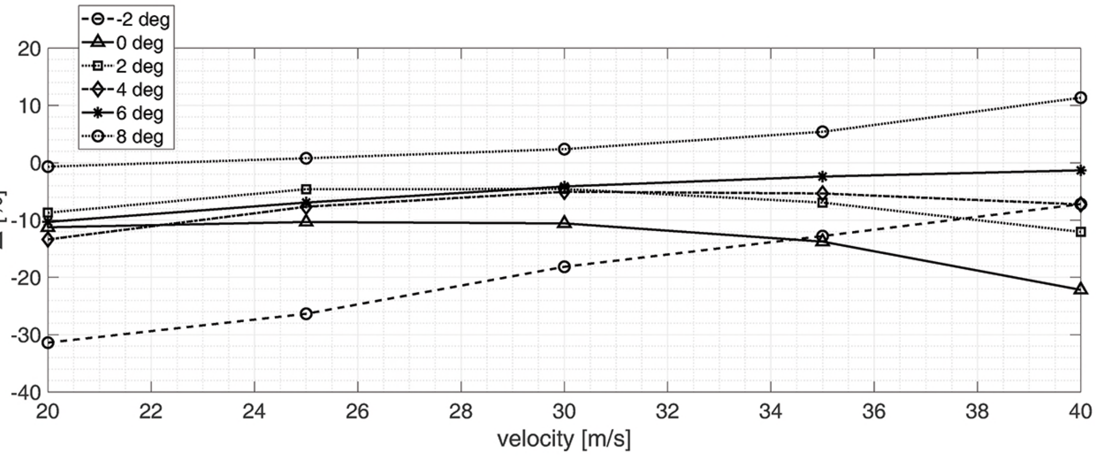

Fig. 7.5.: XB-2 lift error trend against velocity.

α	$\Delta_{20\,m/s}$ [%]	$\Delta_{25\,m/s}$ [%]	$\Delta_{30\,m/s}$ [%]	$\Delta_{35\,m/s}$ [%]	$\Delta_{40\,m/s}$ [%]
-2	-51.5	51.2	-52.1	-53.4	-55.1
0	-43.3	-42.2	-45.7	-49.7	-52.4
2	-43.0	-40.2	-41.6	-43.8	-48.0
4	-34.6	-29.2	-29.2	-32.3	-38.8
6	-27.6	-21.6	-22.1	-24.2	-33.6
8	-15.4	-10.1	-12.4	-18.9	-36.2

Tab. 7.3.: Error between drag force evaluated with BEaRDS^{TM} and experimental results (wind tunnel test data taken as reference).

The BEaRDS^{TM} drag look-up tables are built using AVL. The AVL software, as every panel method, estimates the induced drag while neglecting form drag due to the pressure distribution on the profile (vortex lattice method considers the wing as zero-thickness flat plate) and friction drag. In order to account for the issue, several approaches can be followed, such as using X-Foil software to compute the missing drag data and add them to the AVL drag com-

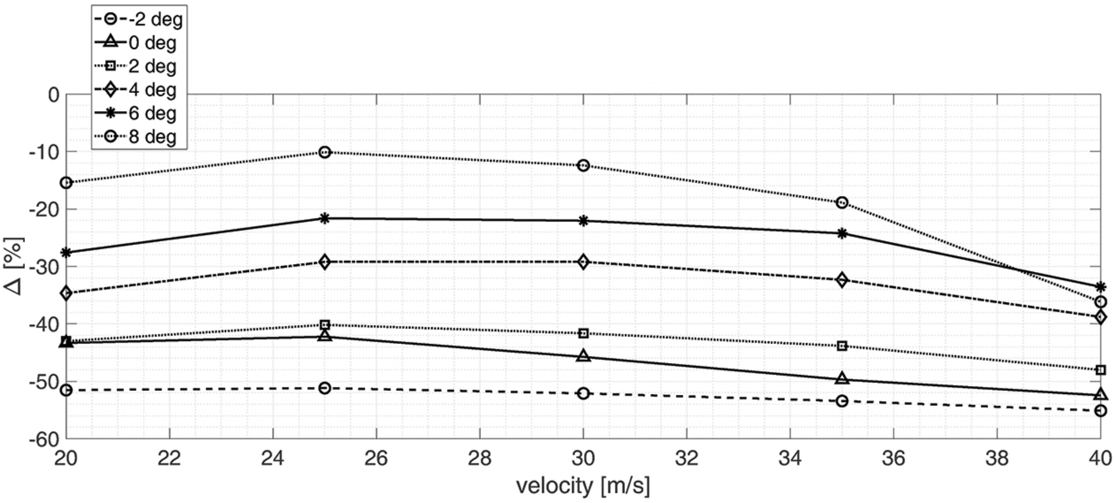

Fig. 7.6.: XB-2 drag error trend against velocity.

ponent or to correct the AVL drag estimation with empirical data from ESDU datasheet. In BEaRDS^{TM} the friction drag was estimated using XFoil [31]. However, the roughness of the 3D printed skin also has a contribution that cannot be modelled in XFoil, causing the difference in the estimation. In fact, while the trend of the two drag distributions is the same, there is an offset between the two datasets which leads to an error in the zero-lift drag component, C_{D_0} (this is more clear in the drag coefficient plot, Figure 7.8b). The difference between the two drag estimations is also shown in Figure 7.4b.

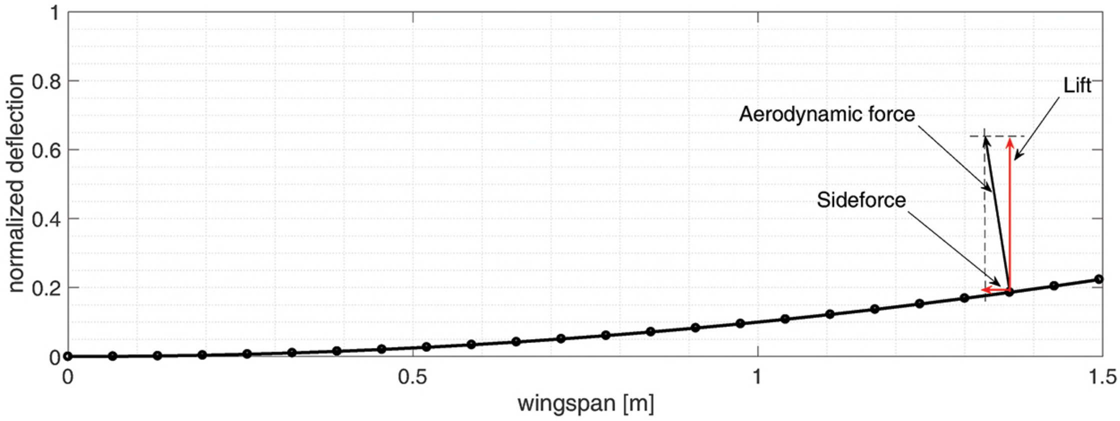

Fig. 7.7.: Diagram showing the origin of the sideforce

Figure 7.4c shows the absolute value of the side force acting along the span. The component of the force along the span depends both on velocity and angle of attack. Referring to Figure 7.7, the more the wing deflects, the higher the lift component along the span. For $\alpha = 8$ deg and $v = 40$ m/s, the value of the side force accounts for 13% of the overall lift. This aspect proves the need to include an extra layer of design when considering flexible wings. From a structural point of view, the wing root bending moment might be less severe due to the component of the load along the span and the subsequent reduction of lift. This could lead to lighter design of the wing root section and weight saving on the overall wing structure. The flight dynamics implications are instead the reduction of lift at the tip section, which could result in a reduction in control surface effectiveness and to a degradation of the controllability of the aircraft. A possible solution could be to reduce the size of the ailerons and rely more on secondary control surfaces such as spoilers for control, as these would be distributed along the wing and less likely to be affected by wing deformation. Error between wind tunnel results and BEaRDS^{TM} numerical prediction could have been reduced by upgrading the structural modelling of the XB-2 model by using results from GVT. Although this is common practice, it was beyond the scope of this work as the purpose of BEaRDS^{TM} was to be used only to evaluate limitations of the aeroelastic framework.

The aerodynamic coefficients are shown in Figure 7.8 where a comparison between the numerical and experimental data is also presented. The coefficients were calculated making the force dimensionless as follows:

$$C_x = \frac{X}{1/2 \rho S V^2} = \frac{X}{qS} \tag{7.6}$$

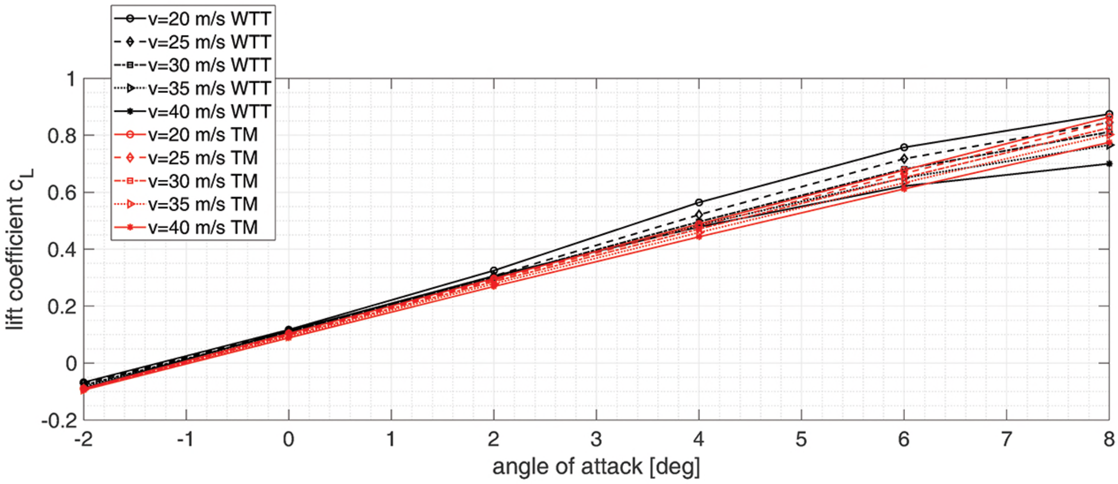

(a) XB-2 lift coefficient.

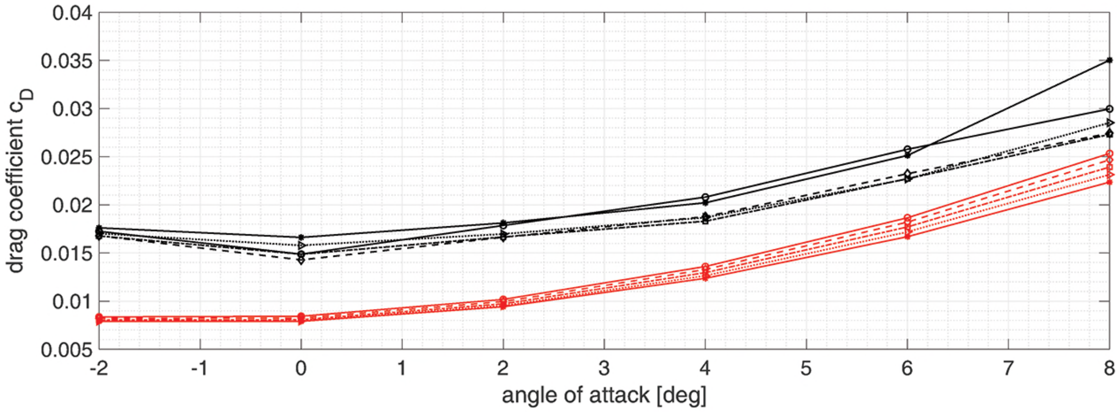

(b) XB-2 drag coefficient.

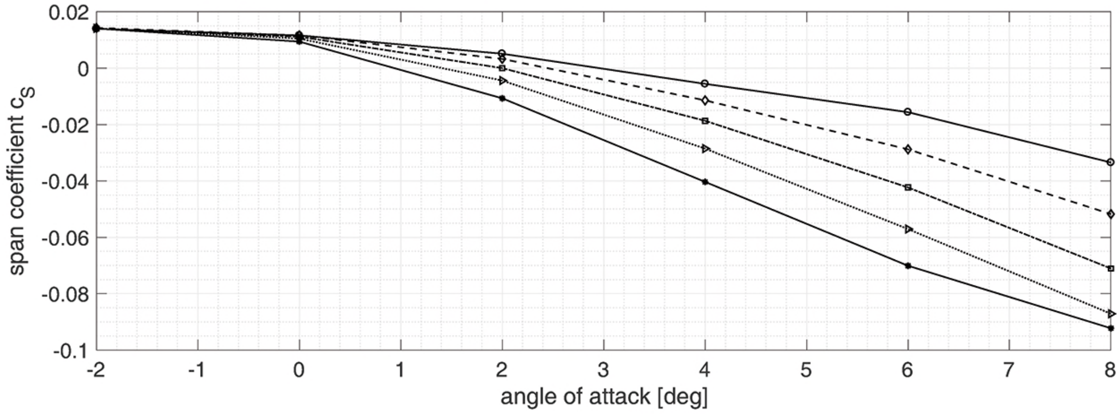

(c) XB-2 sideforce coefficient.

Fig. 7.8.: XB-2 static lift (*top*), drag (*middle*) and sideforce (*bottom*) coefficient for different velocities. In black data from wind tunnel test (WTT) and in red the ones from BEaRDS^{TM} (TM).

where X represents the specific aerodynamic force. Air density, velocity and reference area are the same for both cases.

The lift coefficient is shown in Figure 7.8a. The limitation of the numerical model is the first aspect to emerge from the plot: while the experimental C_L is only linear in the range of -2 deg < α < 4 deg due to the adverse pressure gradient phenomena (which eventually leads to stall), the numerical lift coefficient is linear across the entire angle range. Limitations of the model about the evaluation of lift coefficient in the non-linear region was indeed known as detailed in Section 4.1.2 and corrections to account for stall phenomena are among the CA^{2}LM and BEaRDS^{TM} future work. The lift coefficient shows higher value for lower velocities, while the coefficient slope C_{L_α} reduces with speed. The latter aspect is particularly important for HARW. In fact, the result can be explained by the dependency of the aerodynamic characteristics of the wing on the value of the aspect ratio. In its simplest formulation, the dependency can be defined as follows [4]:

$$C_{L_\alpha} = \frac{C_{L_\alpha}^{2D}}{1 + \frac{C_{L_\alpha}^{2D}}{\pi AR}} \tag{7.7}$$

where $C_{L_\alpha}^{2D}$ represents the lift coefficient slope of the 2D airfoil, the NACA 23015. Equation 7.7 states that a decrease in the aspect ratio would reduce the lift curve slope of the wing. From the XB-2 plots the lift slope can be estimated in the linear region, defined by two points A and B, as:

$$C_{L_\alpha} = \frac{C_L^B - C_L^A}{\alpha^B - \alpha^A} \tag{7.8}$$

Applying this relation to the case of $\alpha = 8$ deg and $v = 40$ m/s, the resulting lift curve slope is:

$$C_{L_\alpha}^{40m/s\text{-}8^\circ} = 5.41$$

Rewriting Equation 7.7 in terms of aspect ratio as:

$$AR = \frac{-C_{L_\alpha} C_{L_\alpha}^{2D}}{\pi (C_{L_\alpha} - C_{L_\alpha}^{2D})}. \tag{7.9}$$

and substituting the value of $C_{L_\alpha}^{40m/s\text{-}8^\circ}$, the aspect ratio would be:

$$AR^{40m/s\text{-}8^\circ} = 17.2$$

assuming $C_{L_\alpha}^{2D} = 6.01$. This result shows a reduction of 8.6% of the AR with respect to the original case. Such analysis might be simplistic in its approximation, but provides an insight into how flexibility could impact the aerodynamic performance. Considering a rigid structure, the aerodynamic properties of the aircraft are not expected to change. However, this is an aspect that must be taken into consideration when dealing with high aspect ratio flexible wings due to the reduced wing planform area induced by the deformation.

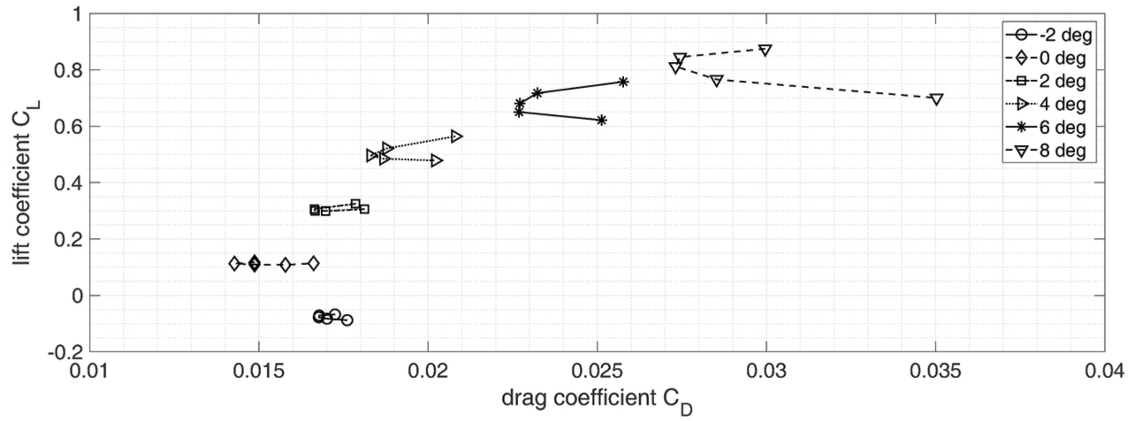

Fig. 7.9.: XB-2 drag polar plot for different test conditions.

Figure 7.8b shows the drag coefficient comparison. As expected, the trend is similar for the numerical prediction and experimental results. The difference is mostly in the C_{D_0} component of the drag. As already mentioned , this was predictable because C_{D_0} is representative of the combination of friction and pressure drag, which are not modelled in panel methods.

Figure 7.8c shows the span coefficient C_S against angle of attack for different velocities. The interesting aspect here is that the value of C_S is of the same order of magnitude as drag coefficient. Thus, when considering flexible structures, the effects of the deformation should have been taken in account as much as the drag effects.

To complete the analysis, the drag polar plot is shown in Figure 7.9. Assuming that the aerodynamic efficiency L/D can be seen as the angle of the line that goes through the origin and it is tangent to the polar curve, the plot shows that the most efficient case is for $\alpha = 4$ deg.

7.2 Static aeroelastic response: deformations

The deformed shape of the wing was estimated by applying the same methodology adopted for the XB-1 model, where four different sensors were used to read angular and linear accelerations at specific spanwise location (positions of the sensors are shown in Figure 6.23). The displacement in time is calculated again by applying the complementary filter. More details about the filter can be found in Section 5.5.

The wing tip displacement for different test conditions is given in Table 7.4. Deformation of the wing tip for $\alpha = -2$ deg is missing as data went corrupted and it was not possible to process the estimated shape of the wing for this specific condition. However data for 0 deg $< \alpha <$ 8 deg provide some insight into the structural deformation. The maximum deflection of the model tip was 13.7% of the model span (0.21 m). Projecting this data on the full scale XB-2 aircraft, it is equivalent to a vertical tip deflection of 3.3 m.

Experimental data is then compared with BEaRDS^{TM} numerical prediction. The difference between the two datasets is significant. BEaRDS^{TM} always underestimates the experimental

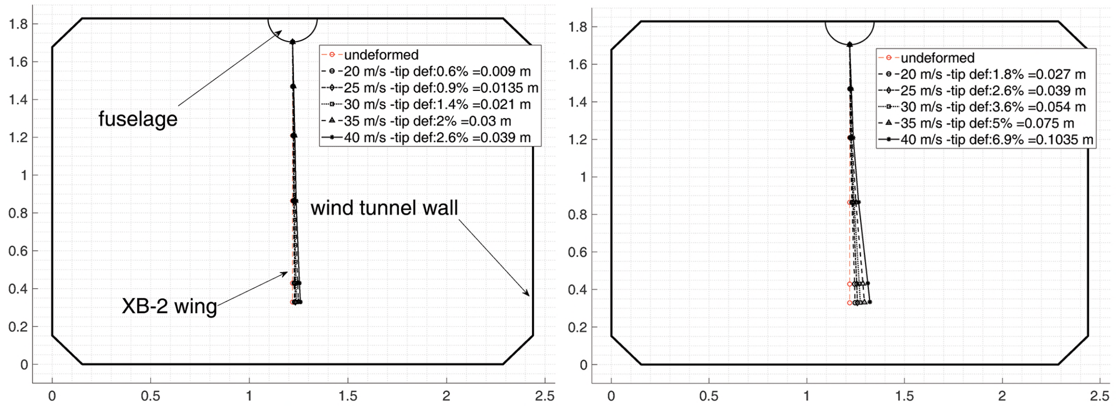

(a) Deformation of the XB-2 model for different velocities at $\alpha = 0$ deg.

(b) Deformation of the XB-2 model for different velocities at $\alpha = 2$ deg.

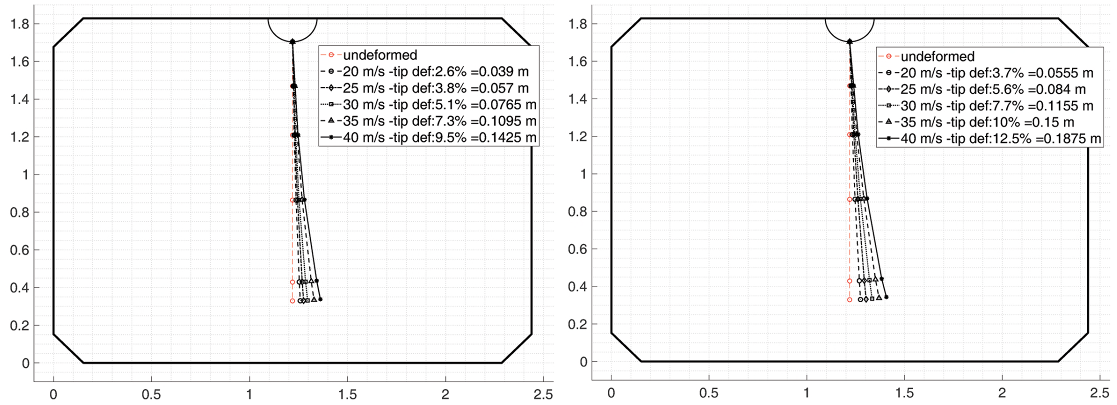

(c) Deformation of the XB-2 model for different velocities at $\alpha = 4$ deg.

(d) Deformation of the XB-2 model for different velocities at $\alpha = 6$ deg.

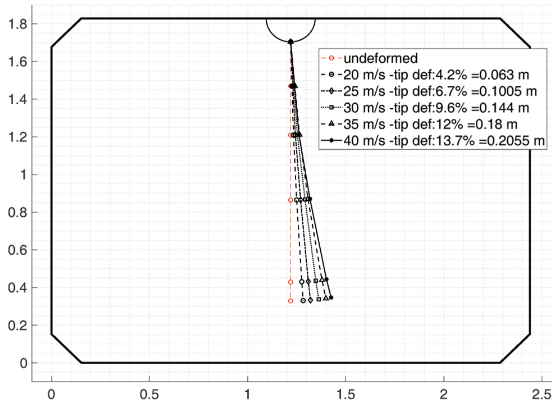

(e) Deformation of the XB-2 model for different velocities at $\alpha = 8$ deg.

Fig. 7.10.: Front view sketch of the wind tunnel showing the displacement of the XB-2 wing for different angles of attack and velocities. Displacement of the wing was calculated from wind tunnel data.

Velocity [m/s]	WTT	BEaRDS^{TM}	**Error**
$\alpha = 0$ deg			
20	0.6 %	0.2 %	67.9 %
25	0.9 %	0.3 %	67.8 %
30	1.4 %	0.4 %	69.8 %
35	2.0 %	0.5 %	73.6 %
40	2.6 %	0.6 %	76.1 %
$\alpha = 2$ deg			
20	1.8 %	0.6 %	68.0 %
25	2.6 %	0.9 %	65.7 %
30	3.6 %	1.3 %	65.3 %
35	5.0 %	1.6 %	67.3 %
40	6.9 %	2.0 %	70.3 %
$\alpha = 4$ deg			
20	2.6 %	1.0 %	63.1 %
25	3.8 %	1.5 %	60.4 %
30	5.1 %	2.1 %	59.3 %
35	7.3 %	2.7 %	62.4 %
40	9.5 %	3.4 %	63.7 %
$\alpha = 6$ deg			
20	3.7 %	1.4 %	63.2 %
25	5.6 %	2.1 %	62.9 %
30	7.7 %	2.9 %	62.0 %
35	10.0 %	3.8 %	61.6 %
40	12.5 %	4.8 %	61.4 %
$\alpha = 8$ deg			
20	4.2 %	1.7 %	58.9 %
25	6.7 %	2.7 %	60.5 %
30	9.6 %	3.7 %	60.9 %
35	12.0 %	4.9 %	58.8 %
40	13.7 %	6.2 %	54.9 %

Tab. 7.4.: XB-2 tip deformation as percentage of the model span. The estimated deformation from wind tunnel test and the one from BEaRDS^{TM} are shown along with the error related to the WTT data.

data from a minimum of 54.9% to a maximum of 76.1%, compared to the wind tunnel tip displacement. The source of this error lies in the numerical approximation. Further investigation is required in order to better quantify the error, although some assumptions can be made, as the same problem was found in the XB-1 data analysis as well even though less severe. It is likely that the error is a consequence of a range of modelling assumptions. The first and most reasonable is the inaccurate prediction of wing torsion due to the addition of the stiffness rod. In fact, when the rod was introduced numerically the model became more complicated. Furthermore, due to mono-axial nature of the accelerometers used in the GVT assessment, it was not possible to validate the torsional mode.

A second source of error could be the mismatch of stiffness distribution between physical and numerical model. Although the GVT results were found to be in agreement with

BEaRDS^{TM}, it only proved that the overall K/M values were matching. However, the k and m distributions could locally differ and introduce inaccuracies in the numerical estimation. These sources of error need further investigation that could be carried out in the next phase of the BEaRDS programme.

Figure 7.10 shows the estimated shape of the XB-2 model for different test conditions. In the plots a sketch of the front view of the wind tunnel is shown.

7.3 Dynamic aeroelastic response: damping

In order to evaluate the overall damping of the wing, the dynamic response of the XB-2 was excited. To induce the initial displacement of the wing, a metal string was attached to the tip of the wing and pulled manually from the control room through a series of pulleys. The amplitude of the dynamic motion could not be controlled with precision. However, since damping is independent of the initial conditions it can be estimated from the test data. Figure 7.11 shows an example of the recorded time history. Damping was evaluated across the entire velocity range, from 20 m/s to 40 m/s, at $\alpha = 6$ deg. For each of the velocity step, the dynamic excitation of the tip was performed 6 times to check repeatability and to estimate the standard error.

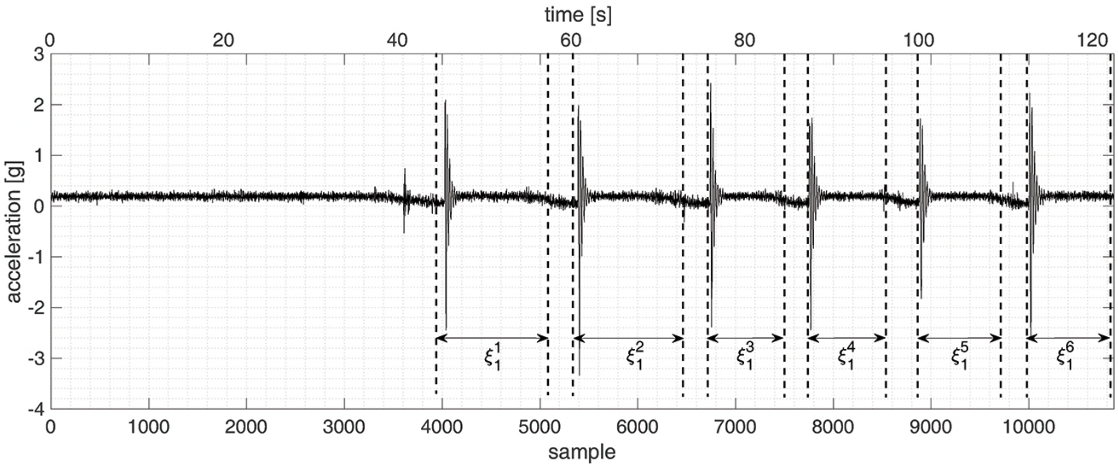

Fig. 7.11.: Example of time history used for damping evaluation. The figure shows data recorded for the case at 40 m/s.

The numerical method of the *half-power bandwidth* [172] was applied to estimate the damping. The method works in frequency domain and identifies the resonance peak associated with a specific mode, as shown in Figure 7.12d. The method identifies the peak A_n of the response and its resonance frequency f_n and looks for the frequencies f_a and f_b where the magnitude of the signal is halved, $A_n/\sqrt{2}$. Once these frequencies are found, damping is approximated as follows [172]:

$$\zeta = \frac{f_b - f_a}{2 f_n} \tag{7.10}$$

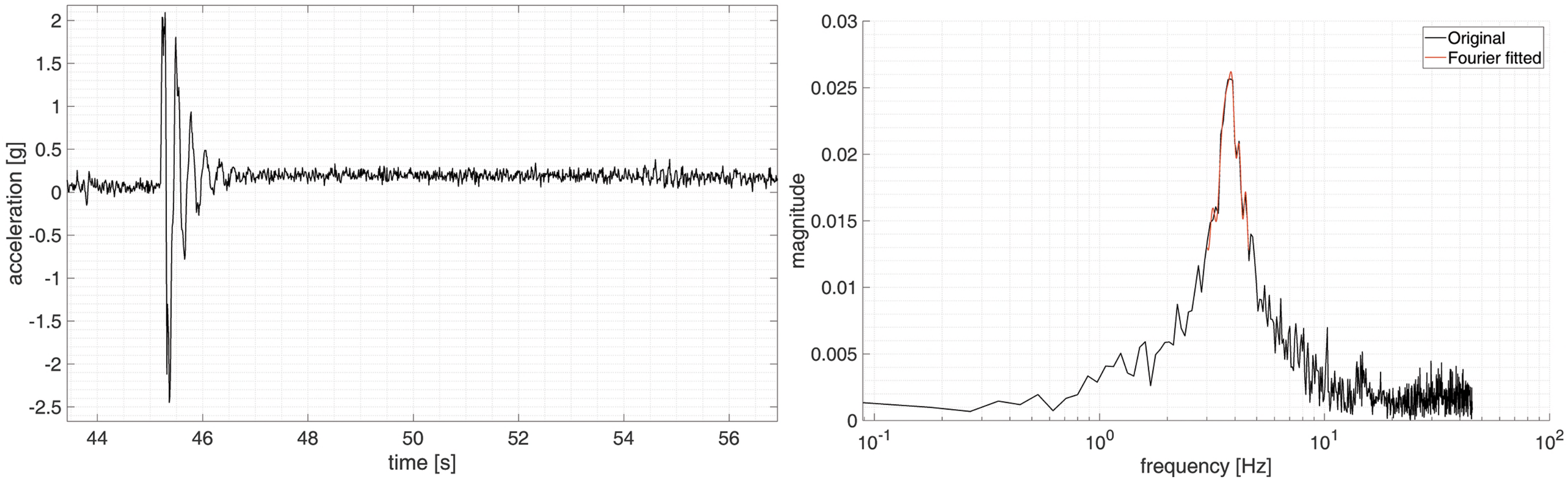

(a) Dynamic test zoomed on one of peaks used to estimate the damping for XB-2.

(b) Frequency response of the selected peak shown in plot a).

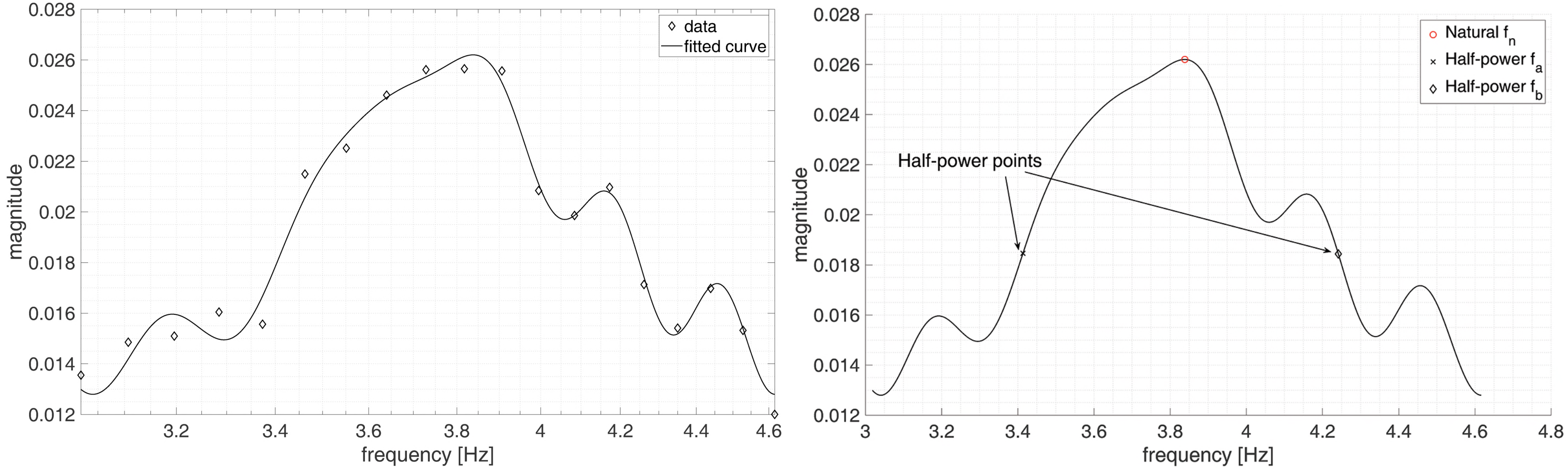

(c) Frequency response fitted trough the use of the Fourier Series approximated to the 6th term.

(d) Half power points evaluation for the estimation of damping linked to the first mode.

Fig. 7.12.: The figure shows the steps of the procedure used to estimate XB-2 overall damping.

Peaks and frequencies were found following different steps for this specific test:

1. The frequency response was obtained from the time history of the signal. The required data samples are isolated and extracted from the dataset, as shown in Figure 7.11. Figure 7.12a shows an example of the selected time samples used to estimate damping.

2. Once the time samples are selected, the Matlab Fast Fourier Transform algorithm is applied to the input and the frequency response is obtained (represented by the black line in Figure 7.12b).

3. The adopted sampling frequency (90 Hz) of the signal proved to not be sufficient to provide a clear peak of the wing tip frequency response. To account for this limitation, a 6^{th} order Fourier Series was used to approximate the frequency response, as shown in Figure 7.12c. The equation of the approximation adopted for the estimation, along with the Fourier coefficients, is given as:

   $$x(\omega) = a_0 + \sum_{i=1}^{6} a_i \cos(i \cdot x w) + \sum_{i=1}^{6} a_i \sin(i \cdot x w) \tag{7.11}$$

   Therefore, the Fourier approximation provides a function that can be used to find the required frequencies (Figure 7.12c-d).

Table 7.5 shows the summary of the estimated values of the overall XB-2 damping.

Input	**20 m/s [%]**	**25 m/s [%]**	**30 m/s [%]**	**35 m/s [%]**	**40 m/s [%]**
1	16.7	19.2	28.6	28.2	21.3
2	16.4	22.7	26.5	28.7	24.9
3	19.8	15.8	27.1	27.1	24.2
4	19.0	19.6	25.8	23.9	24.7
5	17.8	21.1	24.3	27.8	26.6
6	17.3	21.5	26.5	25.8	23.6
$\bar{\zeta}$	17.8	20.0	26.5	26.9	24.2
σ	1.2	2.2	1.3	1.6	1.6

Tab. 7.5.: XB-2 estimated overall damping and associated error

The same approach was used to estimate the structural damping associated with the first bending mode of the structure. Data were extracted by the GVT structural characterisation of the model described in Section 6.4. The calculation provided an estimated damping of $\zeta^{struct} = 6.9\%$.

Figure 7.13 shows trends of the different components of the damping over the airspeed range. The overall damping is not constant and increases with velocities up to 35 m/s as aerodynamic forces are more dominant at higher speeds. However, for $v > 35$ m/s it decreases as flutter speed is approached (estimated in 47 m/s).

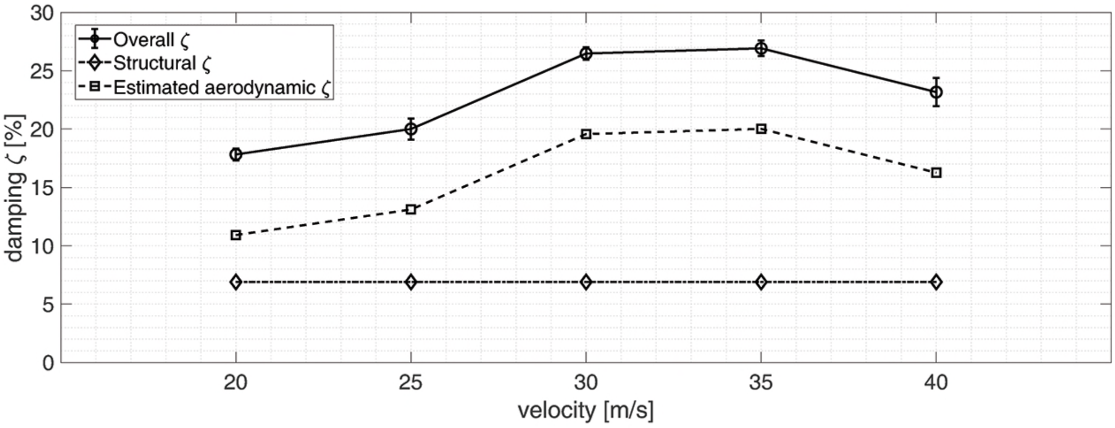

Fig. 7.13.: XB-2 overall damping trend calculated with frequency analysis focusing on the response of the first bending mode.

The structural damping, as previously explained, is derived from the GVT test and it is constant throughout the airspeed range. This is an assumption as it is considered that the elastic characteristics of the model, such as stiffness, do not change with deformation. Non-linear effects associated with deformations, such as the increase of stiffness due to the structure deformation, are well-known phenomena in literature [187]. However, such limitation of the modelling is not considered in this work as beyond the scope of assessing the overall aeroelastic response of the model.

The estimated aerodynamic damping is calculated as the difference between the overall and structural damping. The analysis shows that aerodynamic damping accounts for a minimum of 61% (at 20 m/s) to a maximum of 74% (at 35 m/s) of the overall damping.

Velocity [m/s]	BEaRDS^{TM}	**WTT**	Δ
20	34.3%	17.8%	92%
25	35.6%	20.0%	78%
30	37.1%	26.5%	40%
35	32.4%	26.9%	20%
40	32.0%	24.2%	32%

Tab. 7.6.: BEaRDS^{TM} overall XB-2 damping against wind tunnel test estimated damping

The same method was applied to the BEaRDS^{TM} response to estimate the overall damping of the numerical model and therefore allow comparison with experimental data. Damping was estimated from the acceleration data of the wing-tip node. This data is presented in Table 7.6. The BEaRDS^{TM} damping trend is similar to the experimental, although it consistently overestimates (from a maximum of 92% at 20 m/s, to a minimum of 20% at 35 m/s)[3].

---

[3] However, the impact of damping on the gust load alleviation is relatively small as the focus of the analysis is on the first and second peak of the transient response. The two peaks represent less than one cycle of the dynamic response of the structure. Thus, the more important parameter to consider is the frequency content of the response.

7.4 Discussion and next step

This chapter presented the reader with the analysis of the wind tunnel test data of the eXperimental BEaRDS 2 model. Data collected from the test were compared with the output of BEaRDS^{TM} to assess the limitation of the numerical model. Some considerations are discussed here:

- BEaRDS^{TM} uses a linear model of the lift slope curve. While this is not an issue for small deflection of the structure, it could be instead for flexible wings such as HARW. The impact of this aspect might be relevant especially at the tip of the wing. In fact, when considering high deformation, the tip could stall before of the rest of the wing due to the induce angle of attack associated with the wing deformation. In this case, the linear model would overestimate the lift.
- BEaRDS^{TM} lift prediction was found in good agreement with the experimental data.
- BEaRDS^{TM} drag prediction was found to be far off from the experimental data, always underestimated relative to the wind tunnel data.
- Overall the BEaRDS^{TM} structural solver underestimates the structural deflection of the wing. This however appears to be linked to the inaccurate modelling of the wing. This limitation should be overcome with a more detailed model.

Considering all these aspects, the use of CA^{2}LM is considered viable in order to evaluate the response of a flexible aircraft to gust response and to design a GLA system. In fact, limitations in the drag estimation do not particularly impact the response of the aircraft in the transient response of the gust as the dynamics is dominated by the lift force.

In the next chapter a full assessment of the HARTEN concept aircraft will be shown. The presented aircraft will be used within the boundaries of this work and represents a medium-haul HARW flexible aircraft.

Spoiler modelling and HARTEN aircraft

8

Within the scope of this work, the CA^{2}LM framework is used to simulate the effects of a Gust Load Alleviation (GLA) system specifically designed for the flexible HARW HARTEN aircraft. As previously mentioned, the control surfaces originally modelled in the CA^{2}LM framework include ailerons, rudder and elevator, but not spoilers. As spoilers are crucial in order to design an effective load alleviation system, CA^{2}LM was extended to include this type of control surface. Spoilers are fully-nonlinear devices and their aerodynamic contribution is usually quantified through methods such as CFD, wind tunnel testing or analysis of flight test data. Due to the nature of the CA^{2}LM aerodynamics modelling, based mainly on strip theory, the main obstacle in modelling spoilers was to parametrize the spoiler effect with respect flight to conditions and characteristics of the geometry. As shown in Chapter 2, this is a common problem found in literature. In this work, a novel approach of modelling spoilers is proposed where empirical formulas, derived from ESDU datasheets, are merged with strip theory for steady aerodynamic and Wagner model to reproduce the unsteady effects introduced by the spoilers deflection. Such an approach allows as well accounting for spoiler non-linear effects while satisfying the real-time simulation requirement for the CA^{2}LM framework.

In this chapter, the HARTEN concept aircraft is introduced. HARTEN is later used as a test case for the GLA system design and assessment. The aircraft is defined in two different structural configurations: flexible, where the wing structural dynamics bandwidth is compatible with the rigid-body dynamics and stiff, where the structural and rigid-body dynamics are well separated and not interacting. Following the HARTEN section, the methodology to model the non-linear aerodynamic of spoilers into CA^{2}LM is detailed.

8.1 HARTEN

The High Aspect Ratio Technology ENabler (HARTEN) was adopted as a case study for the GLA design process and gust assessment analysis. HARTEN is a 50 m wingspan aircraft, with an aspect ratio of $AR = 17.7$ and MTOW of 93500 kg. Its target market is the same as that of the Boeing 737 or Airbus A320 family. HARTEN is a low-wing T-tail aircraft powered by two engines placed at the rear of the vehicle.[1] Details of the aircraft are given in Table 8.1 and a 3-view drawing is shown in Figure 8.1. The engines have a frontal area of 7 m^2 and they are

---

[1] The longitudinal mass distribution is obtained by discretizing the overall mass over the fuselage in 11 points as:

	N1	**N2**	**N3**	**N4**	**N5**	**N6**	**N7**	**N8**	**N9**	**N10**	**N11**
Position [m]	0	4	8	12	16	20	24.6	29	33	38.3	43.9
Mass [kg]	200	350	500	2350	5000	23318	15000	2470	500	350	200

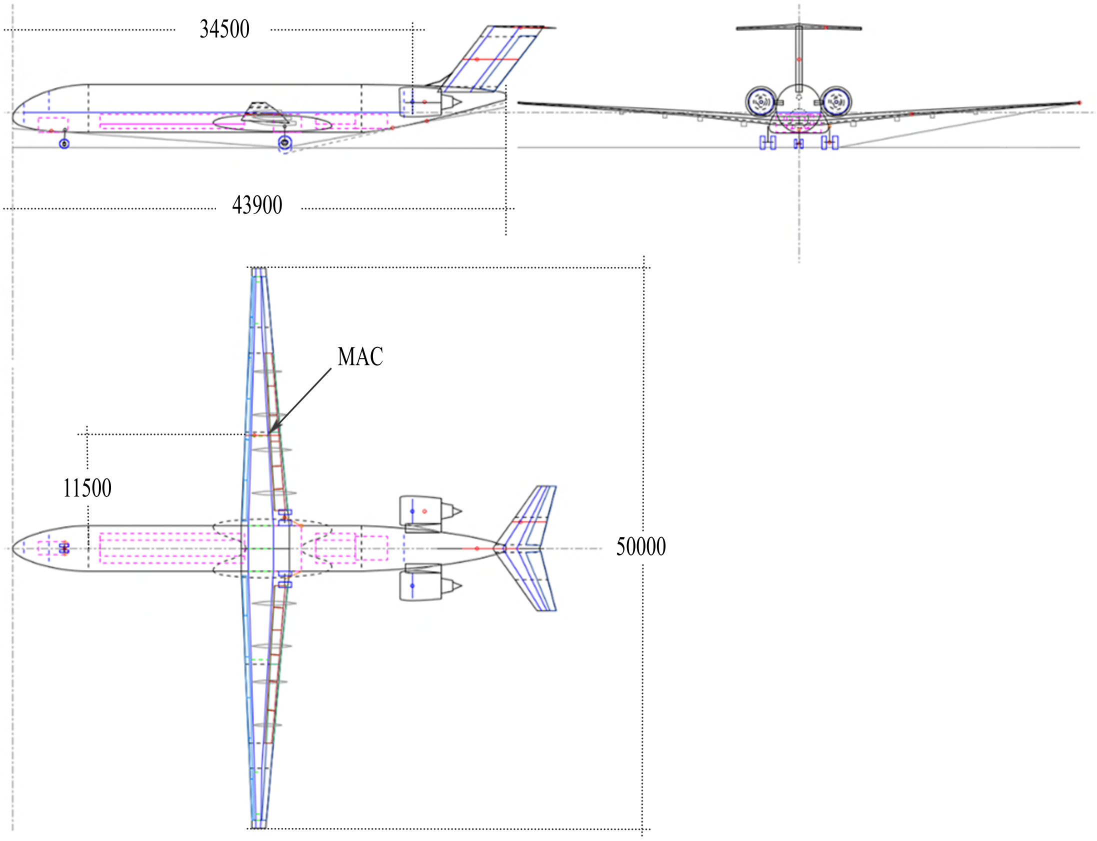

Fig. 8.1.: HARTEN concept aircraft 3-view drawing (dimensions in mm).

placed 38.3 m from the nose. The centre of gravity is placed at 20% of the MAC (23.96 m from the nose). In order to achieve that, an appropriated mass distribution was provided.

Although the gust load assessment along with the GLA design focuses on the flexible aircraft, a *stiff* version of HARTEN was also provided to better understand the impact of the flexible wing structure on the HARTEN performance.

Details of the two structural configurations are given in Table 8.2. While in both cases the fuselage, HTP and VTP are modelled with a high value of Elastic Modulus (practically they can be considered as rigid), the wing structure was modelled differently in the two cases: in the flexible case, the Elastic Modulus, E, of the wing structure is set to be $E = 40$ MPa, while in the stiff configuration the Elastic Modulus is $E = 500$ MPa.

A first difference between the two configurations can be noticed in the deformation under the static aerodynamic load in cruise flight ($\mathrm{v} = 200$ m/s, $\mathrm{h} = 26000$ ft): while the wing tip deformation is 4.4% of the wing semispan in the stiff configuration (1.1 m), when the wing is assumed flexible the wing tip static deformation is 16.8% of the wing semispan (corresponding to 4.2 m). Figure 8.2 shows the deformed structure for both the stiff and flexible configuration, where the difference in the wing shape is clear.

Main specifications

Aircraft category	short range (A320-like)
Pax	165
Range	4600 km
OWE	55269 kg
MTOW	93500 kg
MZFW	78700 kg
MLW	78420 kg

Cruise flight conditions

Mach	0.75
Altitude	26000 ft
C_L	0.65

Lift surfaces

	Wing	**HTP**	**VTP**
Area [m^2]	141.1	32.9	59.1
Span [m]	50	11.2	5.9
MAC [m]	3.14	3.10	5.02
AR	17.7	3.8	1.17
Taper Ratio	0.27	0.4	1

Fuselage

Length	43.9 m
Diameter	4 m

Tab. 8.1.: HARTEN main dimensions

Section	**Stiff**	**Flexible**
Wing	500 GPa	40 GPa
Fuselage	6.9e15 Pa	6.9e15 Pa
HTP	6.9e15 Pa	6.9e15 Pa
VTP	6.9e15 Pa	6.9e15 Pa

Tab. 8.2.: Elastic modulus of stiff and flexible HARTEN configurations

The different structural response of the two configurations is stressed when the first 12 natural frequencies and mode shapes were calculated for the stiff and the flexible wing. The natural frequencies are given in Table 8.3. First aspect to stress is the value of the natural frequencies in both the HARTEN configurations. The structural dynamics of the stiff configuration is unlikely to couple with the short period rigid-body dynamics. In fact, the first HARTEN natural frequency is 4.4 Hz, well separated from the short period frequency, estimated to be in the range of 0.15-1.5 Hz[2]. The first natural frequency of the flexible configuration instead overlaps potentially the short period, coupling the elastic response with the rigid-body one.

---

[2] In Chapter 9 the HARTEN short period frequency is estimated and the rigid-body characterization provides a value of the short period frequency $f_S = 0.4$ Hz.

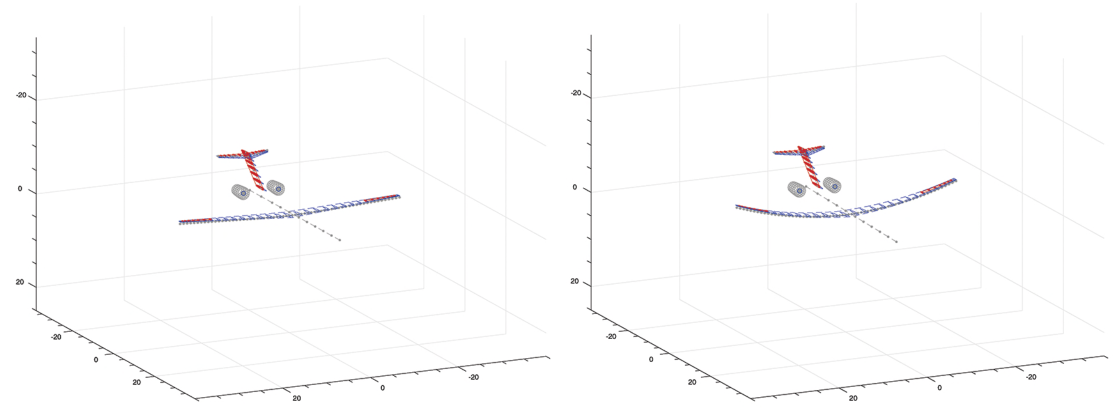

(a) HARTEN stiff configuration **(b)** HARTEN flexible configuration

Fig. 8.2.: Stiff vs flexible configurations trim deflection.

	Flexible		Stiff	
Mode	**Frequency**	**Description**	**Frequency**	**Description**
1	1.3 Hz	1^{st} sym wing bending	4.4 Hz	-
2	2.2 Hz	1^{st} asym wing bending	7.9 Hz	-
3	3.6 Hz	2^{st} sym wing bending	12.6 Hz	-
4	4.6 Hz	2^{st} asym wing bending	16.4 Hz	-
5	4.8 Hz	3^{st} sym wing bending	17.1 Hz	-
6	5.6 Hz	3^{st} asym wing bending	19.7 Hz	-
7	7.1 Hz	-	25.0 Hz	-
8	8.2 Hz	-	28.8 Hz	-
9	12.1 Hz	-	42.8 Hz	-
10	12.7 Hz	-	45.0 Hz	-
11	14.6 Hz	-	51.6 Hz	-
12	14.7 Hz	-	51.7 Hz	-

Tab. 8.3.: HARTEN natural structural modes for flexible and stiff case.

The second important aspect to discuss derives from the analysis of the nature of the modes of the flexible configuration, plotted in Figure 8.3[3]. All the flexible modes are dominated by the wing response, while the fuselage, HTP and VTP response reflect the one of a rigid body. This behaviour was expected as the wing is five orders of magnitude *less stiff* than the other aircraft components. Therefore the elastic response of the aircraft is dominated by the wing response. This aspect plays a crucial role when considering the full-aircraft response to a gust as detailed in the next chapter.

8.1.1 Control surfaces

In the previous section it was found that the elastic response of HARTEN is dominated by the flexible wing. In this section, the wing geometry along with its main characteristics is described. The geometry of the HARTEN wing is shown in Figure 8.4 and details are given in

---

[3] Analysis of the nature of the natural modes was performed only on the flexible configuration as the one chosen for the GLA design and gust load assessment.

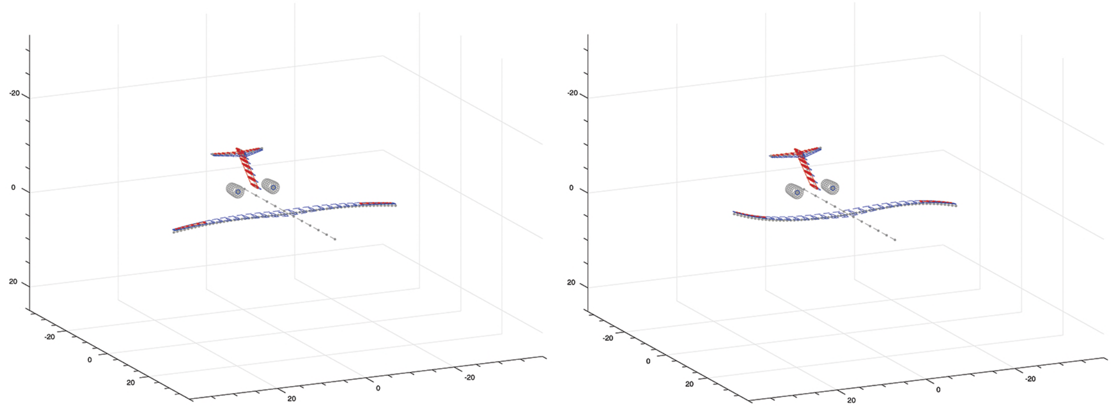

(a) HARTEN flexible mode 1, $f = 1.3$ Hz **(b)** HARTEN flexible mode 2, $f = 2.2$ Hz

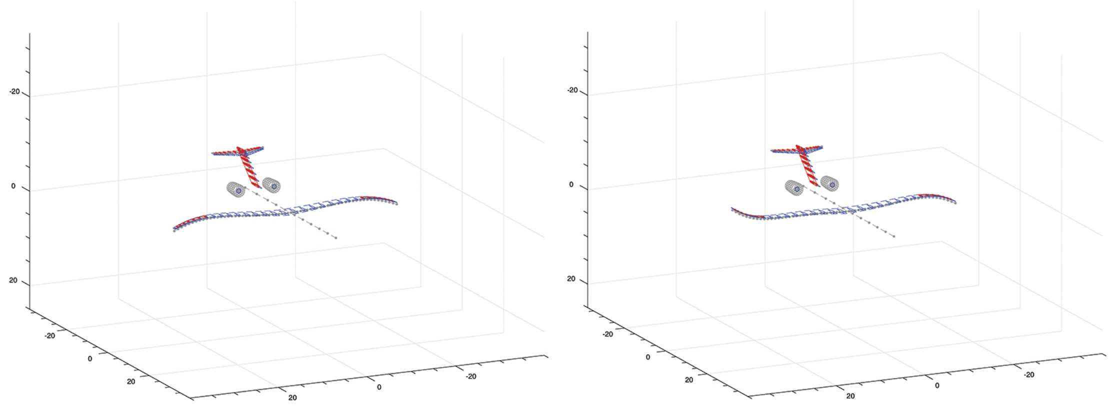

(c) HARTEN flexible mode 3, $f = 3.6$ Hz **(d)** HARTEN flexible mode 4, $f = 4.6$ Hz

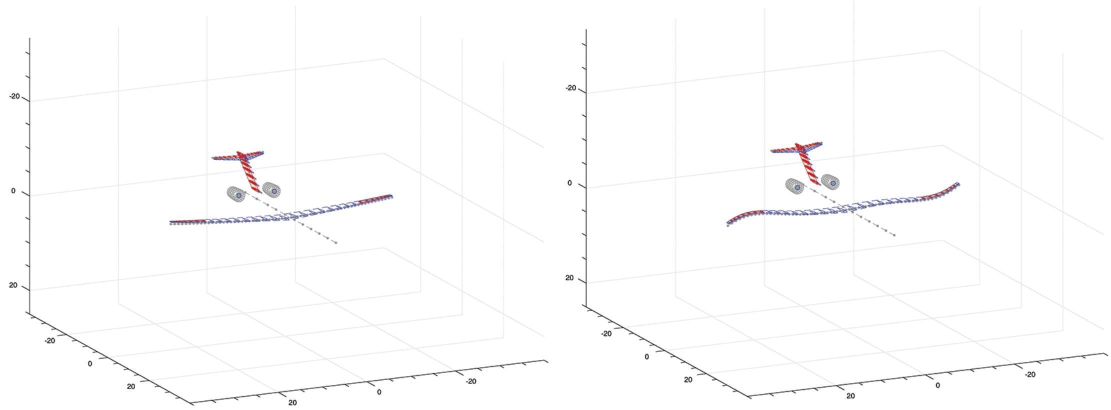

(e) HARTEN flexible mode 5, $f = 4.8$ Hz **(f)** HARTEN flexible mode 6, $f = 5.6$ Hz

Fig. 8.3.: HARTEN flexible first 6 modes.

Table 8.4. The wing is equipped with a set of primary control surfaces (ailerons) and a set of secondary control surfaces, composed of six separated spoilers.

Details of the location and geometry of the control surfaces are shown in Table 8.5. The size of the aileron area and its position are dictated by the roll performance requirements provided by the MIL-F-8785c[13]. An extract of the requirements for roll control are given in Table 8.6. The required roll performance of an aircraft depend on the category and the size of the vehicle. HARTEN is assumed to be a Class II (medium weight transport aircraft) land-based (L) aircraft. The Level 1 row describes a situation of *flying qualities clearly adequate for the mission Flight Phase*, while category B indicates *manoeuvres accomplished gradually and without precision tracking*. Based on the appropriate aircraft category, the requirement for the HARTEN aileron design is to provide a roll turn of 45 deg in 1.9 s with full aileron deflection.

A left turn of flexible HARTEN is simulated at the maximum aileron deflection of 25 deg. The flight condition for the manoeuvre is $v = 200$ m/s and $h = 26000$ ft. Time history of the ailerons deflection along with the required parameters, p and ϕ, are shown in Figure 8.5. The manoeuvre develops as follows: at t = 6 s the aircraft ailerons are deflected to 25 deg. The aircraft reaches 45 deg bank at t = 7.12 s, 1.12 s after ailerons are deflected. After 1.9 s from the start of the manoeuvre, the aircraft reaches a bank angle of 96.5 deg, more than double the required angle. Although control surfaces effectiveness must be assessed in a wider range of flight conditions (as specific scenarios determine and drive the design parameters), the output of the simulation indicates that HARTEN ailerons might be oversized. In fact, regarding aileron design, Sandraey [153] suggests for civil aircraft that an aileron-to-wing-area ratio, S_a/S, of 5% and an aileron-to-wing-span ratio, b_a/b, of 20-30% should be adopted. Considering the HARTEN wing specifications, the size of the ailerons meets these requirements as $S_a/S = 3.6\%$ and b_a/b=25.1%. The roll rate necessary to meet MIL-F-8785c for this class of aircraft is [153]:

$$p = \frac{2\phi}{t^2} = \frac{2 \cdot 45 deg/s}{1.9^2} \approx 24.5 deg/s \tag{8.1}$$

about half of the value achieved of 66 deg/s reached after 0.8 s from the start of the manoeuvre. As the size of the HARTEN ailerons is in line with the design principles, the reason behind the excessive effectiveness is believed to lie in the non-standard wing configuration of HARTEN. In fact, Sandraey specifies that the design laws apply for civil aircraft, which have a typical wing aspect ratios of 7-10 while HARTEN's aspect ratio is 17.7.

The rolling moment, L_A, generated by the ailerons deflection is [153]:

$$L_A = 2\Delta L \cdot y_a \tag{8.2}$$

where y_a is the distance of the aileron from the longitudinal axis and ΔL is the extra lift generated by the deflection. Assuming the moment necessary to satisfy roll requirement, while the lift generated by the HARTEN ailerons is the one expected by Equation 8.2, the extra rolling moment is due to the excessive distance of the ailerons from the longitudinal axis introduced

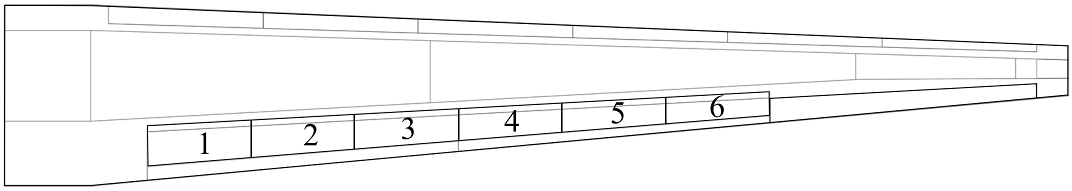

Fig. 8.4.: HARTEN wing with control surfaces.

Spec	**Value**
Reference area	141.1 m^2
Span	50 m
Aspect ratio	17.1
Root chord	4.24 m
Tip chord	1.17 m
Dihedral angle	3.5 deg
1/4 sweep angle	0.5 deg
LE sweep angle	2.4 deg
TE sweep angle	-5.4 deg
Nose to 25% MAC	21.5 m

Tab. 8.4.: Wing main characteristics

	In edge [% b]	**Out edge** [% b]	**Chord** [m]	**Hinge** [% c^{local}]	**Area (one wing)** [m^2]
spoiler 1	14	23.14	0.8990	68	2
spoiler 2	23.14	32.29	0.8990	68	2
spoiler 3	32.29	42.64	0.7653	67	1.98
spoiler 4	42.64	52.38	0.7653	67	1.86
spoiler 5	52.38	62.14	0.6355	66	1.55
spoiler 6	62.14	71.9	0.6355	66	1.55
aileron	71.9	97	0.8310	72	3.24

Tab. 8.5.: Geometry details of HARTEN spoilers and aileron.

		Category A		Category B		Category C	
Class	**Level**	60°	45°	60°	45°	30°	25°
II-L	1	-	1.4	-	**1.9**	1.8	-
II-L	2	-	1.9	-	2.8	2.5	-
II-L	3	-	2.8	-	3.8	3.6	-

Tab. 8.6.: Extract of MIL-F-8785c roll performance requirements for max time to complete turn at given bank angle[13].

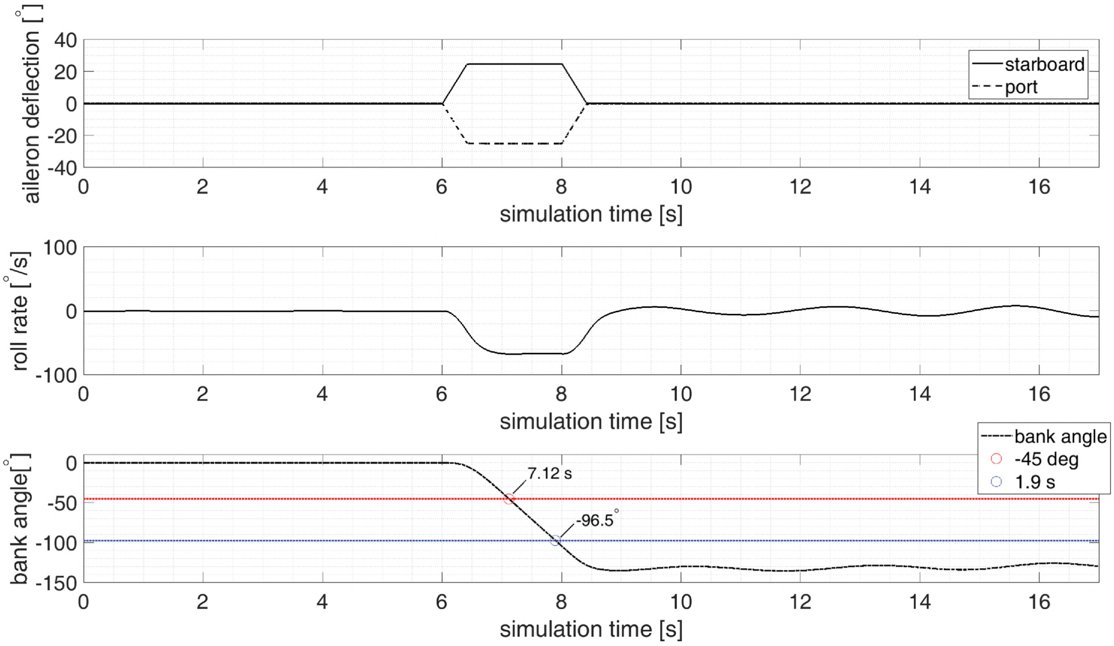

Fig. 8.5.: Aileron effectiveness assessment: HARTEN roll manoeuvre.

by the HARW configuration. In order to generate an adequate rolling moment, it would be necessary either to reduce the size of the aileron or place the control surface closer to the longitudinal axis.

The aim of this work is however to design a GLA system that is effective on the provided aircraft. Thus, the effectiveness of the ailerons will be taken into account when analysing the GLA results, although the aircraft configuration will not change from the one provided. Within the scope of the analysis of the impact of ailerons on GLA performance, aeroelastic effects such as aileron reversal or aerodynamic phenomena such as adverse yaw should be considered. Aileron reversal is an undesired effect typical of elastic wings where an increase of lift due to a positive deflection of the aileron causes a nose down twist of the wing [22] (and vice-versa for a negative deflection of the aileron). As result, the effectiveness of the aileron can be compromised. At a specific speed, known as reversal speed, the aileron is totally ineffective. This static instability is worse towards the wingtip due to the elastic properties of the HARW configuration. Such an aeroelastic phenomena must be taken in account when evaluating the use of outboard ailerons for GLA purposes. Adverse yaw instead is described as the undesired yaw moment opposite to the rolling motion induced by an asymmetric deflection of ailerons. The yaw moment is caused by the different increase in drag on the two wings. As well as aileron reversal, this phenomena is related to the use of ailerons and the greater is the wingspan the more important is the impact on the flight dynamics characteristics of the aircraft.

8.2 Spoilers modelling

As seen in Chapter 2, the use of spoilers results in a local loss of lift and an increase in drag. The resulting flow separation means that spoilers are fully-nonlinear devices that cannot be modelled via linear methods such as strip theory. An important feature of such control surfaces is that such devices can be actuated very quickly [167] making them ideal candidates for load alleviation. Spoilers were not previously modelled in CA^{2}LM because of their nonlinear nature and lack of data[4].

The novel solution proposed in this work was to develop a generalised method for modelling spoilers by merging empirical data provided by ESDU 14004 [167] with the output of the theoretical CA^{2}LM aerodynamic model. However, the ESDU datasheet provides an overall value of ΔC_L due to the spoiler deflection. Therefore, the control surfaces were implemented such that the spoiler effect is actually distributed along the wing, affecting the local lift distribution. As a result this method allows spoiler contribution to be coupled with the CA^{2}LM aeroelastic model.

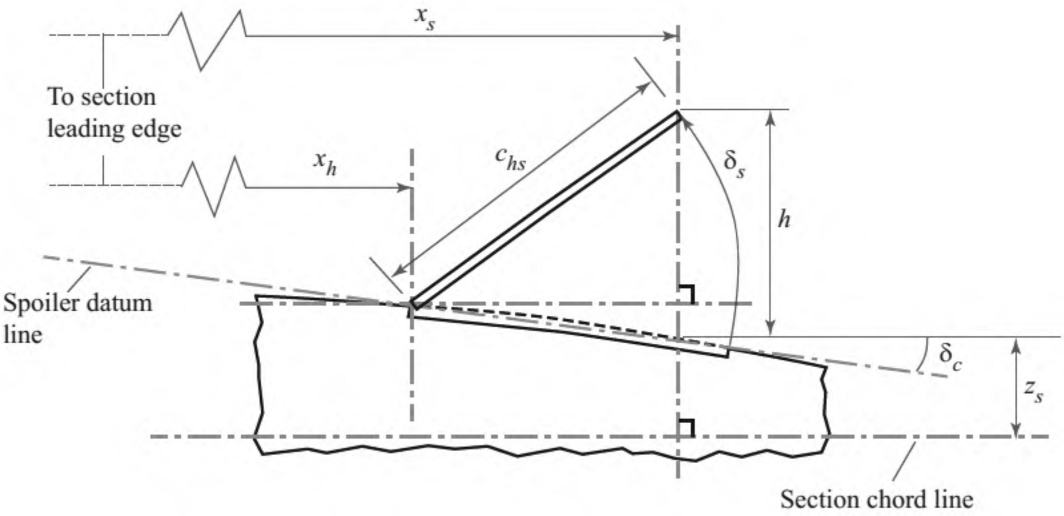

Fig. 8.6.: Flat-type spoiler representation and main geometry parameters [167].

ESDU 14004 provides a method to simulate the effect of several types of spoilers such as vented-spoilers, flat-plate spoilers, circular-arch spoilers and flap-type spoilers. Flat-type spoilers are the device modelled in CA^{2}LM as they represent the most common solution adopted

---

[4] A possible approach to assess the impact of spoilers is to use CFD analysis. However, coupling CA^{2}LM with a CFD software would compromise the ability of the framework to run in real time.

for commercial aircraft. Figure 8.6 shows the representation of the spoiler along with the main geometry parameters. The overall impact of the spoiler deflection on the lift coefficient and roll rate coefficient, is derived from interpolating look-up tables provided by the ESDU 14004 and depends on spoiler geometry, such as chord, spanwise extension, hinge position, porosity[5] and deflection angle, and on flight conditions.

The spoiler contribution that is eventually fed into the CA^{2}LM aerodynamic block is evaluated in three steps:

1. overall ΔC_L^{ESDU} contribution of the single spoiler is calculated from ESDU 14004 datasheet as follows [167]:
$$\Delta C_L^{ESDU} = \Phi_{ps} \Delta C_{LsF} \tag{8.3}$$
where Φ_{ps} is the part-span factor that accounts for spoiler position along the wingspan, while ΔC_{LsF} is the lift increment due to a fullspan spoiler and is defined as:
$$\Delta C_{LsF} = \frac{\Delta C_{Ls\infty}}{2\pi} a_{1w} \tag{8.4}$$
where $\Delta C_{Ls\infty}$ is local 2D aerofoil contribution and a_{1w} is the lift-slope for the finite wing, obtained using ESDU 70011 [169]. All the parameters in Equations 8.3 and 8.4 are extracted from look-up tables and derived through an extensive experimental campaign which tested several wing and spoiler configurations (detailed in Ref [167, 169])..

2. overall ΔC_L^{ESDU} is distributed over the spoiler aerodynamic nodes as local $\Delta c_{L_i}^{spoiler}$ such that
$$\sum_{i=y_1}^{y_2} \Delta c_{L_i}^{spoiler} \Delta y = \Delta C_L^{spoiler} \tag{8.5}$$
where y_1, y_2 are the inboard and outboard spanwise edges of the spoilers respectively. Doing so, the effect of the spoiler on the local lift distribution can be evaluated and therefore propagated in the wake through the unsteady aerodynamic indicial model. However the impact of spoilers on spanwise aerodynamics is not uniform. This consideration is necessary as the edge of the spoiler that lies in between aerodynamic nodes might be closer to one node than another. The weight χ accounts for this specific requirement and it is calculated as the ratio of the local spoiler area and the local wing area. The sum of all weights related to the same spoilers is equal to one:
$$\sum_{i=1}^{m} \chi^i = 1 \tag{8.6}$$
where m is the number of nodes related to the spoilers.

---

[5] The porosity of the spoiler, σ, is defined as
$$\sigma = \frac{S}{S_f}$$
where S is the spoiler wetted area and S_f is the rectangular area defined by the spoiler's edges. In this study the porosity is equal to one since the spoiler is not perforated.

As the ΔC_L^{ESDU} derived from Equation 8.3 is referred to the overall wing area, in order to limit its contribution on the spoiler area, the following constant is defined:

$$\Delta C_L^{ESDU} b = \Delta C_L^{spoiler} b_s \tag{8.7}$$

where b is the wingspan and b_s is the spoiler span. The spoiler local contribution is then calculated as:

$$\Delta C_L^{spoiler} = \frac{\Delta C_L^{ESDU}}{2} \frac{b}{b_s} \tag{8.8}$$

where it is divided by two because ESDU 14004 assumes both wings deflect the spoilers.

Once the spoiler local contribution is known, this is distributed on the related aerodynamic nodes by using appropriate weighting as follows:

$$\Delta c_L^i = \underbrace{\frac{\Delta C_L^{ESDU}}{2} \frac{b}{b_s}}_{\Delta C_L^{spoiler}/2} \chi^i c_s^i \tag{8.9}$$

where c_s is the local spoiler chord. In fact, all contributions are multiplied by the local spoiler chord to maintain consistency with the CA^{2}LM aerodynamic code which calculates the local lift distribution as $c\,C_L$ (see Equation 4.21).

3. Finally, nodal $\Delta c_{L_i}^{spoiler}$ is added to the nodal unsteady c_{L_i}.

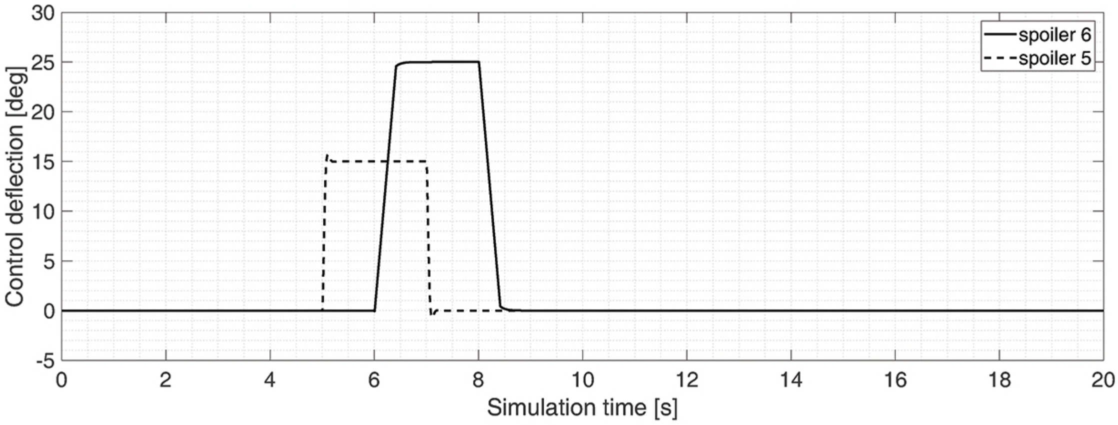

Fig. 8.7.: Spoilers deflection for the first example

To show the impact of the spoiler modelling on the CA^{2}LM framework, two example are here presented. In both cases, the flexible HARTEN was used as a model, flying at $v = 200$ m/s and $h = 26000$ ft. In the first example, the impact of the spoiler deflection on the local lift distribution is presented. Spoilers used for the assessment are port spoiler number 5 (covering 52% and 62% of the wing semispan), and port spoiler number 6 (covering 62% to 72% of the semispan[6]). The simulation is designed to overlap for 1 s the effect of the two spoilers to analyse the interaction between the two. The input of the simulation is defined as:

$$\begin{aligned} spoiler\,5 \quad &\rightarrow \delta_s = 15°, \quad for \quad 5s < t < 7s \\ spoiler\,6 \quad &\rightarrow \delta_s = 25°, \quad for \quad 6s < t < 8s \end{aligned}$$

The simultaneous deflection of the two spoilers is simulated for $6s < t < 7s$, while 1 second before and 1 second after this interval, the spoilers work independently. Figure 8.7 shows the time history of the spoilers deflection, where the overlap is clear for $6s < t < 7s$.

Figure 8.8 shows the lift distribution over the wing for the presented simulation. Figure 8.8a shows the lift distribution against the simulation time. When spoilers are deflected, the decrease in local lift is evident along with the transient response due to the coupling of the spoilers aerodynamics model with CA^{2}LM aerodynamics model. This aspect is more clear in Figure 8.8b, where a snap-shot of the lift distribution at three different times is presented: i) t = 5.5 s, when only spoiler 5 is deflected, ii) t = 6.5 s, when both spoilers are deflected and iii) t = 7.5 s when only spoiler 6 is deflected. At t = 5.5 s, the ΔC_L is entirely placed on one node, as the only aerodynamic node associated with spoiler 5. When spoiler 5 is deflected, the reduction in the local lift (at node 8) is 40% with respect to the clean configuration. At t = 6.5 s, spoiler 6 is deflected as well and the effect of the two spoilers combine and extends to three aerodynamic nodes: two associated with spoiler 6 and one with spoiler 5. Finally, at t = 7.5 s, spoilers 6 is the only device to be activated: only two nodes are affected and the reduction in local lift is 37% with respect to the clean configuration.

The second example presented here is a left turn performed by deflecting the port outer spoilers number 5 and number 6[7]. To complete the turn, the two port spoilers were deflected to 15° each for 2 seconds simultaneously, in the interval $5s < t < 7s$. The roll rate and roll angle time histories are shown in Figure 8.9.The roll rate plot shows that, once the deflection is triggered at t = 5 s, it quickly reaches a maximum value of $3.8°/s$. At t = 7 s, when the input is removed, the roll rate returns to the initial value and oscillates around zero. The roll angle follows the same trend of p quickly reaching a maximum value of 7°. As soon as the spoilers were retracted ϕ settles around 7°.

To model the spoiler actuator dynamics some assumptions were made as relatively little data on the topic is available in the open literature. Firstly, it was assumed that the spoiler actuator dynamics is defined by a second order transfer function in a similar way to the aileron actuator dynamics. Secondly, it was assumed that spoilers deploy twice as fast as the aileron. Hence, the bandwidth of the spoiler actuator was chosen to be twice that of the aileron. Main-

---

[6] Spoiler 5 and spoiler 6 are next to each other. Considering their position with respect of the aerodynamic nodes, only one node (node number 8) was assigned to spoiler 5, while two nodes (node number 9 and 10) were assigned to spoiler 6. The assignment of nodes to a specific spoiler depends both on the spanwise extent of the spoiler and the density of the aerodynamic grid.

[7] For consistency, the same spoilers of the previous example are used for this second case.

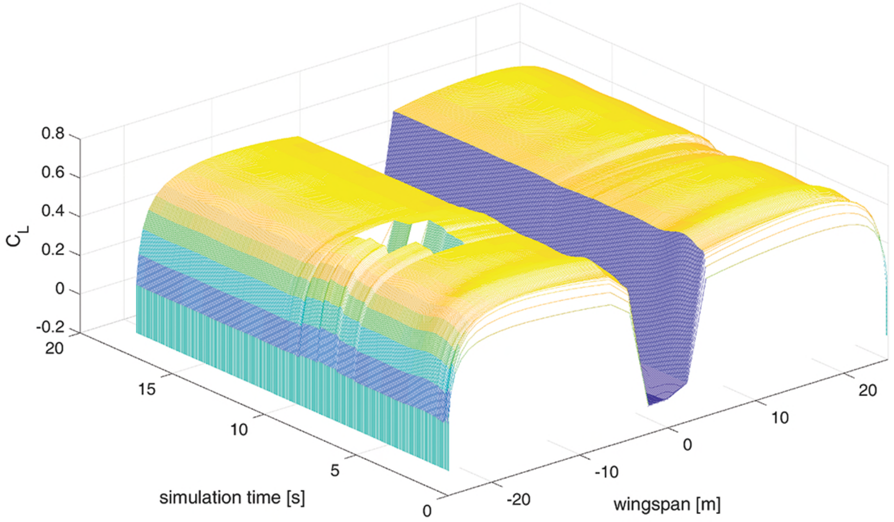

(a) HARTEN lift distribution against time.

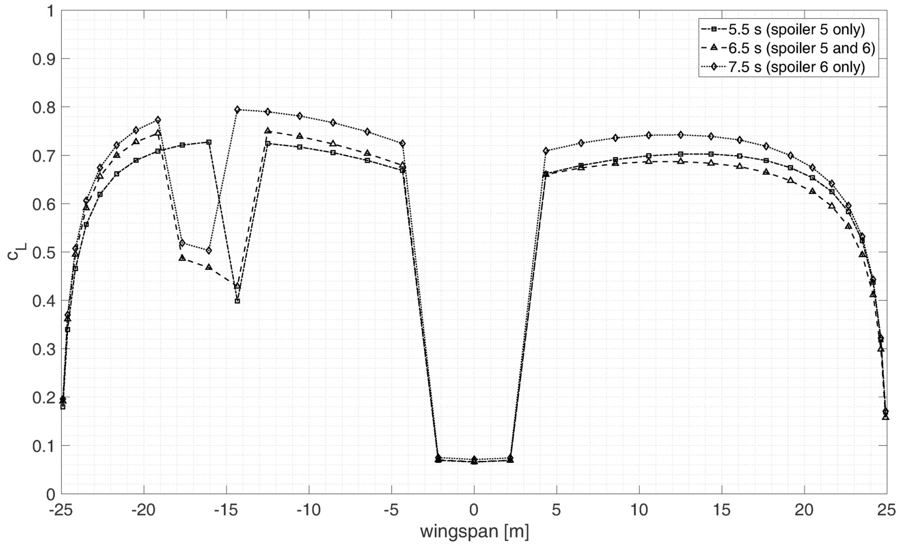

(b) HARTEN lift distribution for different spoilers deflection.

Fig. 8.8.: HARTEN lift distribution visualization for spoiler deflection manoeuvre ($v = 200$ m/s, $h = 26000$ ft).

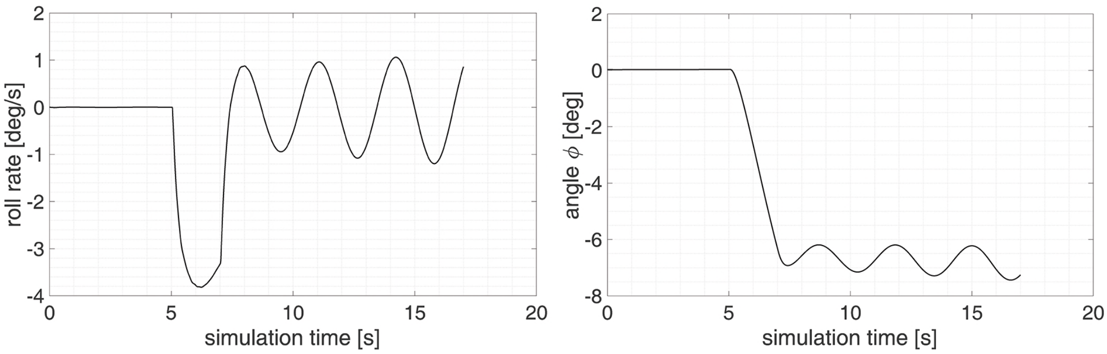

(a) Roll rate time history for the left turn manoeuvre.

(b) Roll angle time history for the left turn manoeuvre.

Fig. 8.9.: Roll angle and roll rate of a left turn manoeuvre performed with outboard spoilers ($v = 200$ m/s, $h = 26000$ ft).

taining the same damping ($\zeta = 0.7$), the spoiler actuator dynamics was therefore defined as:

$$H(s) = \frac{\delta_s}{\delta_{s_d}} = \frac{1600}{s^2 + 56s + 1600} \tag{8.10}$$

In order to be able to implement a variable number of spoilers in the initialization process, the transfer function given in Equation 8.10 is converted into a state-space model as:

$$H(s) = C(sI - A)^{-1}B + D \tag{8.11}$$

where A, B, C, D are the state matrix, input-to-state matrix, state-to-output matrix and feedthrough matrix respectively, of the state-space system defined as:

$$\dot{x} = \boldsymbol{A}x + \boldsymbol{B}u \tag{8.12}$$

$$\dot{y} = \boldsymbol{C}x + \boldsymbol{D}u \tag{8.13}$$

For this specific work, such matrices are defined as:

$$\boldsymbol{A} = \begin{bmatrix} -56 & 50 \\ 36 & 0 \end{bmatrix} \tag{8.14}$$

$$\boldsymbol{B} = \begin{bmatrix} 8 \\ 0 \end{bmatrix} \tag{8.15}$$

$$\boldsymbol{C} = \begin{bmatrix} 0 & 6.25 \end{bmatrix} \tag{8.16}$$

$$D = 0 \tag{8.17}$$

Therefore, the state-space dynamics of n number of spoilers is modelled by the following matrices:

$$\boldsymbol{A} = \begin{bmatrix} \boldsymbol{A}_1 & \boldsymbol{0} & \cdots & \boldsymbol{0} \\ \boldsymbol{0} & \boldsymbol{A}_2 & \cdots & \boldsymbol{0} \\ \vdots & & & \\ \boldsymbol{0} & \boldsymbol{0} & \cdots & \boldsymbol{A}_n \end{bmatrix} \tag{8.18}$$

$$\boldsymbol{A} = \begin{bmatrix} \boldsymbol{B}_1 & \boldsymbol{0} & \cdots & \boldsymbol{0} \\ \boldsymbol{0} & \boldsymbol{B}_2 & \cdots & \boldsymbol{0} \\ \vdots & & & \\ \boldsymbol{0} & \boldsymbol{0} & \cdots & \boldsymbol{B}_n \end{bmatrix} \tag{8.19}$$

$$\boldsymbol{C} = \begin{bmatrix} \boldsymbol{C}_1 & \boldsymbol{0} & \cdots & \boldsymbol{0} \\ \boldsymbol{0} & \boldsymbol{C}_2 & \cdots & \boldsymbol{0} \\ \vdots & & & \\ \boldsymbol{0} & \boldsymbol{0} & \cdots & \boldsymbol{C}_n \end{bmatrix} \tag{8.20}$$

$$\boldsymbol{D} = \boldsymbol{0} \tag{8.21}$$

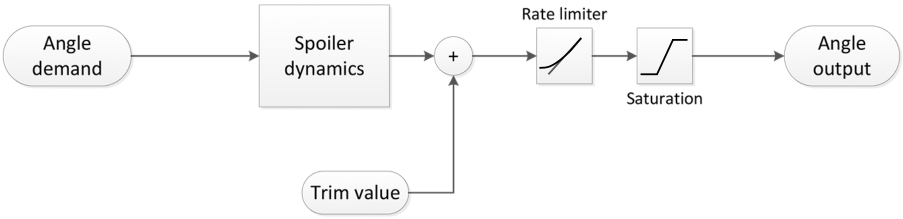

Fig. 8.10.: Spoiler actuator dynamics as implemented in CA^{2}LM .

assuming $A_1 = \cdots = A_n = A, B_1 = \cdots = B_n = B$, $C_1 = \cdots = C_n = C$.

The implementation of the spoilers actuator dynamics in CA^{2}LM is shown in Figure 8.10. A rate limiter is modelled to limit the dynamics to a max of 300 deg/s, along with a saturation which bounds the deflection to a maximum of 40 deg[8].

8.2.1 Limitations of ESDU 14004 coupled with CA^{2}LM framework

Being able to simulate the spoiler non-linear aerodynamic effects into low fidelity, real time frameworks, which are required to be computationally inexpensive, represents the main benefit of the proposed spoiler modelling approach. However, limitations of the method, which originate either from the adoption of the ESDU datasheet or from the implementation into CA^{2}LM , must be considered as follows:

- Because the ESDU 14004 provides the global variation in lift coefficient due to the deflection of one isolated spoiler, two aspects might influence the local lift distribution:

    i) Since CA^{2}LM is able to evaluate the contribution of multiple spoilers, it is currently not considering the possible aerodynamic interference between adjacent spoilers. At the moment, it is unknown whether this interference is constructive or destructive, thus a further investigation on this aspect is required. Currently, CA^{2}LM evaluates each spoiler contribution as isolated from the others.

    ii) While the ESDU 14004 provides an overall ΔC_L, CA^{2}LM distributes this contribution along the spoiler aerodynamic nodes as local Δc_L. Such local change could lead to a variation in the rolling coefficient different from the one predicted by ESDU 14004 because of the high aspect ratio wing geometry of the case aircraft and its potentially non-linear geometric displacements.

- The spoiler actuator dynamics is not available in literature and was not provided for the concept aircraft used in this study. The actuator bandwidth was assumed to be twice as fast as the aileron one. This approximation needs to be validated with either experimental or manufacturer data.

- The ESDU prediction is only valid for Mach number $\mathrm{Ma} < 0.7$, spoiler sweep-back angle up to 45° and porosity of up to 0.38.

---

[8] The HARTEN actuator characteristics and control surfaces maximum deflection were provided.

- The spoiler is effective for deployment height, $\bar{h}$, constrained to be $\bar{h}/c > 0.02$, where c represents the spoiler local chord (Figure 8.6). This is defined as the minimum distance between the spoiler trailing edge and the wing surface. This constraint is introduced to model the interaction between the spoiler and the boundary layer: if $\bar{h}/c < 0.02$, the spoiler still lies inside the wing boundary layer and it is unable to disturb the flow. Since ESDU 14004 suggests to use the model for values $0.02 < \bar{h}/c < 0.04$ with caution, the spoiler was modelled in CA^{2}LM to be effective for $\bar{h}/c > 0.04$. This aspect is stressed here as particularly important in the gust load alleviation optimization design process (Chapter 9). In fact, this might lead to *computationally*-valid deflections that do not translate into a physical aerodynamic effect if $\bar{h}/c < 0.04$. To better understand the impact of $\bar{h}/c$ on the spoiler performance, two different deflection angles were simulated and the results are shown in Figure 8.11. The spoiler which was selected for the example is the spoiler number 3, which is placed between 32% and 43% of the wing semispan. Flight conditions are again $v = 200$ m/s and $h = 26000$ ft (Ma=0.65). The top row of the figure shows a deflection demand, δ_s, of 6° initiated at $t = 5s$. The top middle plot shows that the demanded deflection never crosses the minimum threshold of $\bar{h}/c = 0.04$. Therefore the $\Delta C_L^{spoiler}$ is set to zero and the demanded deflection does not affect the lift distribution (top right). The bottom row shows the same dynamics, although this time the deflection angle is $\delta_s = 10°$. The bottom middle plot shows that in this case the demanded input crosses the threshold $\bar{h}/c = 0.04$, therefore the spoiler affects the lift distribution locally at the related aerodynamic nodes (bottom right). Furthermore, spoilers are usually not deployed for very small gust inputs to reduce wear and tear whilst not achieving a significant impact.

- The increase in drag due to spoiler deflection is not modelled by the ESDU 14004. Although CA^{2}LM accounts for the variation in drag due to the lift change as result of the spoiler deployment (induced drag), other drag components related to the spoilers (such an increase in local profile drag) are not currently modelled.

8.3 Discussion and next step

In this chapter a novel method to model the effects of spoiler non-linear aerodynamics and implement it within an aeroelastic simulation framework has been presented. The spoiler effect is evaluated using empirical data extracted from ESDU data sheet, which provides an overall ΔC_L contribution due to the deflection of an isolated spoiler. The novelty lies in the way the ΔC_L is included into the CA^{2}LM framework. In fact, the spoiler contribution is distributed along the spoiler span, affecting the local lift distribution in spoiler sections of the wingspan. Such a modelling technique allows the framework to account for unsteady aerodynamic effects and transient flow response due to the finite time taken for the spoiler to deploy. The change in the aerodynamic force due to spoiler deflection propagates downstream of the wing and affects the aerodynamics of the HTP and VTP, which is modelled as a lag force. Some examples were presented to prove the effectiveness of the spoiler modelling.

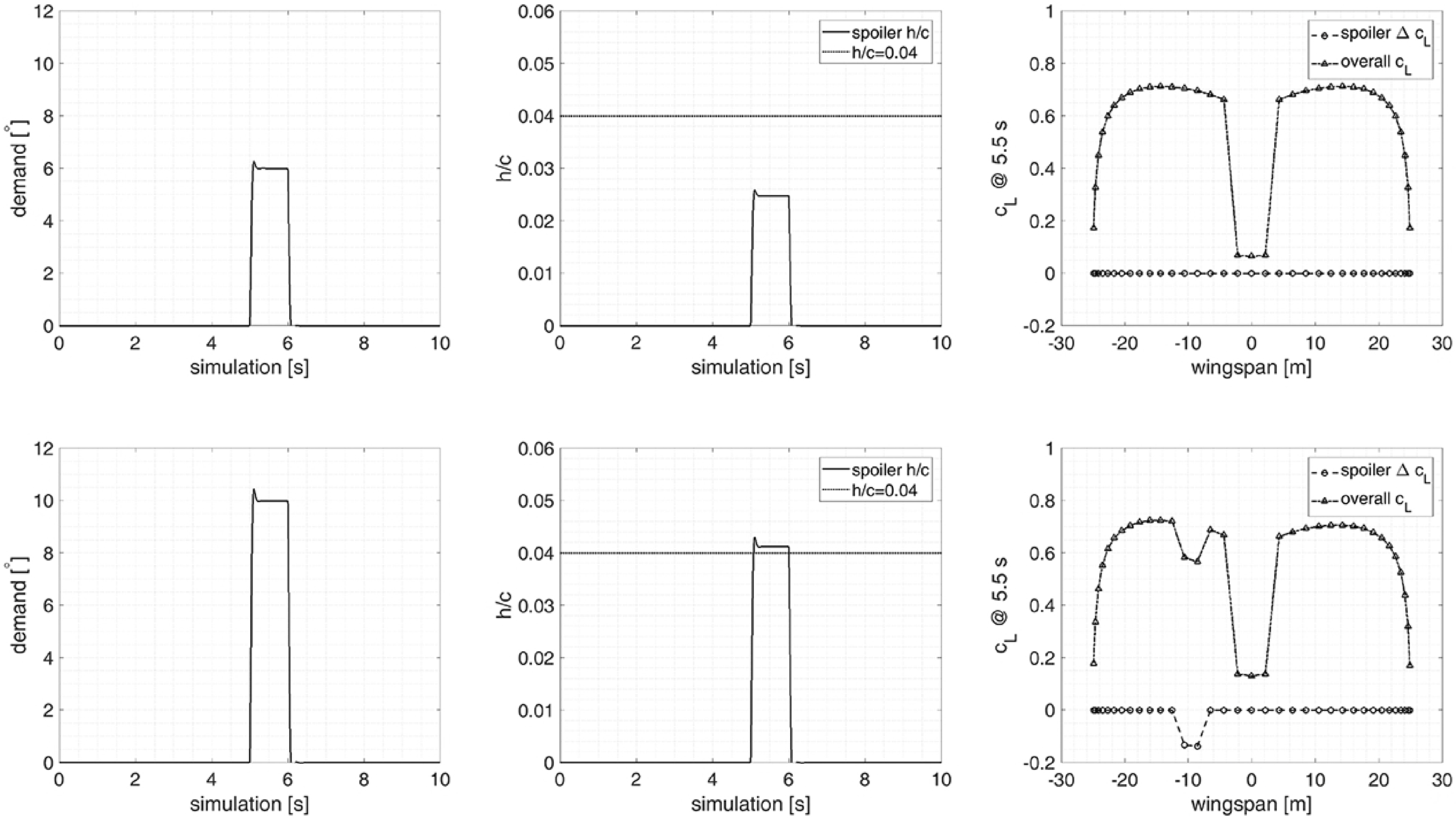

Fig. 8.11.: Impact of $\bar{h}/c$ on the spoiler Δc_L for two different port spoiler deflection (M=0.65, h=26000 ft).

The HARTEN concept aircraft was as well introduced in the chapter. HARTEN is a conceptual HARW aircraft and it is used as a test case for the GLA system design. During the aircraft assessment, the ailerons were found to be oversized at the considered flight point. This aspect is of importance as the efficiency of the GLA along with the optimal solution to reduce the gust load depends on the control surface effectiveness. Results from the GLA system design will be discussed considering the impact of oversized ailerons on the GLA performance.

The final step consists in designing a viable GLA system for HARW commercial aircraft. The next chapter focuses on the design of the GLA system and optimization of its parameters combining the knowledge acquired throughout the this work on the benefits and limitations of the CA^{2}LM framework and on the HARTEN aircraft.

9

Gust Load Alleviation (GLA) system

The load induced by a gust on the aircraft structure is of critical importance for the load and fatigue design [194]. In order to alleviate the load on the wing and reduce the weight of the structure, a GLA system is desired. For more details on GLA systems and gust induced load the reader is referred to Chapter 2. Such problem is even magnified when considering HARW configuration. In this chapter, a GLA system for the HARTEN aircraft is designed. Requirements for the HARTEN GLA were defined as:

1. to rely on available technologies,
2. to account for the flexibility of the structure, and
3. to focus on the wing root bending moment.

At this point the designer has two main choices: either a closed-loop or an open-loop control system. Advantages and performance of different GLA closed-loop (either feedback or feedforward) systems were previously discussed in Chapter 2, where some of these systems were shown to be able to alleviate up to 50% of the wing root bending moment, $\bar{M}_0$. However, implementation of a closed-loop control system may lead to significant increases in the cost of and complexity of the certification. Although every new system must go through a certification process, the feedback system certification would be more time consuming in comparison to an open loop system. In fact, several aspects of the closed-loop control system are not present in the open-loop one: the sensitivity of the control system to parameter change in the system, the stability of the closed-loop system and the ability of disturbance rejection of the control system. Furthermore, the increase in complexity of the closed-loop control system must be considered as well.

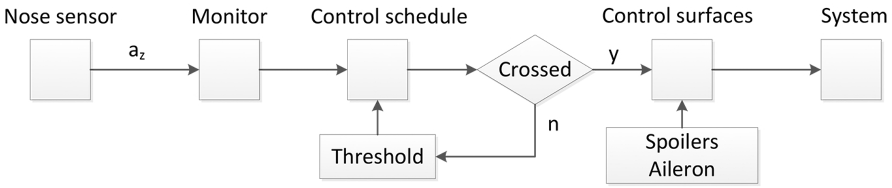

Fig. 9.1.: Open-loop control system architecture.

Considering all these aspects, an open-loop control system was developed mainly for its simplicity of implementation and its inclination for the industrial use. Figure 9.1 shows the architecture of the designed HARTEN open-loop control system which continuously monitors the acceleration at the nose. Such value of the vertical acceleration is compared with a reference value (threshold). Once the value of a_z become greater than the threshold, the wing control surfaces are deployed for a specific and fixed time, independently from the evolution of the acceleration and the structural load induced by the gust velocity profile.

This chapter provides insights on the gust alleviation problem for HARW commercial aircraft. Firstly, the HARTEN aircraft response is assessed for a range of discrete *1-cosine* gust conditions at one example flight condition. Secondly, an open-loop GLA system is developed in order to alleviate the $\Delta\bar{M}_0$ induced by the gust. Finally, the GLA is tested in the same range of gust conditions and the impact of the control system is discussed.

9.1 HARTEN gust response

Before designing the GLA system, the response of the HARTEN to a gust input was assessed. The analysis was performed following the CS-25 requirements [9] on the discrete gust load design criteria. The reader is referred to Section 2.5 for the adopted formulation and definition of gust. The CS-25 requirements dictate that the number of gust gradients, H, required for a complete analysis, must be a *sufficient number in the range 9-107 m in order to find the critical response* [9]. Eleven gust gradients were identified to be sufficient for the HARTEN configuration at the specific chosen flight condition. The parameters used to evaluate the gust velocity profiles are given in Table 9.1. By the time of this study, the development of HARTEN was still at the early stage and some of the aircraft characteristics were derived from a more generic A320-like vehicle. To account for the uncertainty in the HARTEN specifications, the amplitude of the gust velocity profile derived from the CS-25 was increased by 30%. Figure 9.2 shows the 11 gust profiles adopted for the GLA system design at the flight point described above.

Altitude	26000 ft (7920 m)
TAS	200 m/s
EAS	131 m/s
Mach number	0.65
α_{trim}	4 deg
Dynamic pressure	10600 kg/(ms^2)
MLW	84200 kg
MTOW	93500 kg
MZFW	78700 kg
Mass during gust encounter	79200 kg
Z_{mo}	41000 ft

Tab. 9.1.: HARTEN reference values for gust profiles derivation.

The response of the aircraft to the gust input is dictated by the increase of the angle of attack induced by the vertical gust velocity, w_g. In this work only the longitudinal response of the aircraft is considered. Thus, only heave and pitch degrees of freedom are considered in the analysis. Since the HARTEN is a T-tail configuration aircraft, the change in incidence

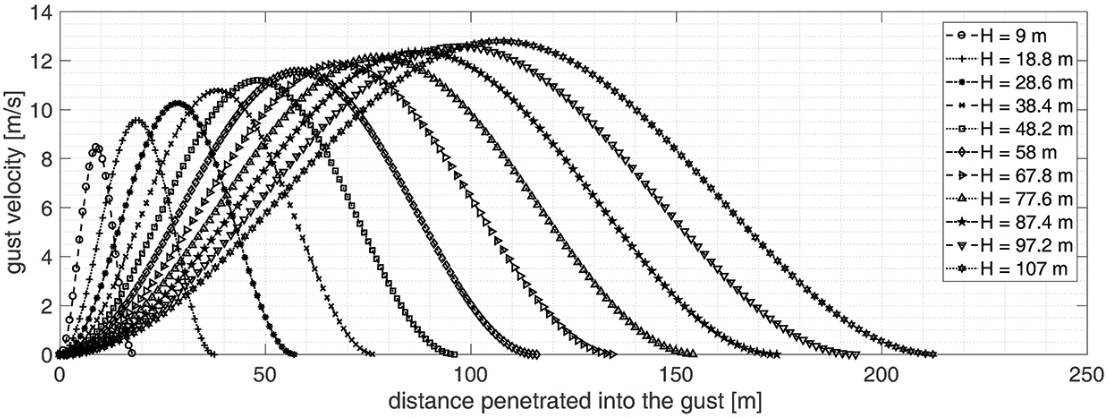

Fig. 9.2.: HARTEN gust profiles from CS-25 requirements at 26000 ft and cruise speed of 200 m/s.

for a specific time t for wing and tail plays an important role in the aircraft response due to the vertical distance of the tail from the longitudinal axis. The change in AoA for the tail due to the gust penetration effect is delayed by a time l/V with respect to the wing, where l is the distance between wing and tail and V is the speed of the aircraft. The change in angle of attack for both the wing and the tail is defined as [187]:

$$\Delta\alpha_{Wg}(t) = \frac{w_g(t) + \dot{z}_W}{V} + \Delta\theta \tag{9.1}$$

$$\Delta\alpha_{Tg}(t) = \frac{w_g(t - l/V) + \dot{z}_T}{V} + \Delta\theta \tag{9.2}$$

where w_g is the vertical component of the velocity, V is the absolute value of the aircraft speed, θ is the pitch angle and the vertical acceleration, $\dot{z}$, is different for the wing and the tail due to their distance from the CoG and defined as:

$$\dot{z}_W = \dot{z}_{\mathrm{CG}} - l_w\dot{\theta} \tag{9.3}$$

$$\dot{z}_T = \dot{z}_{\mathrm{CG}} - l_T\dot{\theta} \tag{9.4}$$

where l_w and l_T are the distance of the wing and tail aerodynamic centre from the aircraft centre of gravity respectively. The increase in lift for the wing and the tail is therefore defined as:

$$\Delta L_w(t) = \frac{1}{2}\rho S_W V^2 C_{L_{\alpha W}}\left[\frac{w_g(t) + \dot{z}_{\mathrm{CG}} - l_W\dot{\theta}}{V} + \theta\right] \tag{9.5}$$

$$\Delta L_T(t) = \frac{1}{2}\rho S_W V^2 C_{L_{\alpha T}}\left[\frac{w_g(t - l/V) + \dot{z}_{\mathrm{CG}} - l_T\dot{\theta}}{V} + \theta\right] \tag{9.6}$$

where three main factors can be identified to affect the change in lift: the gust effect (w_g/V), the heave effect ($\dot{z}_{\mathrm{CG}}/V$) and the rotation (pitch) effect ($l\dot{\theta}/V$).

Figure 9.3 shows the HARTEN CoG maximum and minimum acceleration for the stiff and flexible configuration. The first aspect to notice is that the stiff and flexible acceleration re-

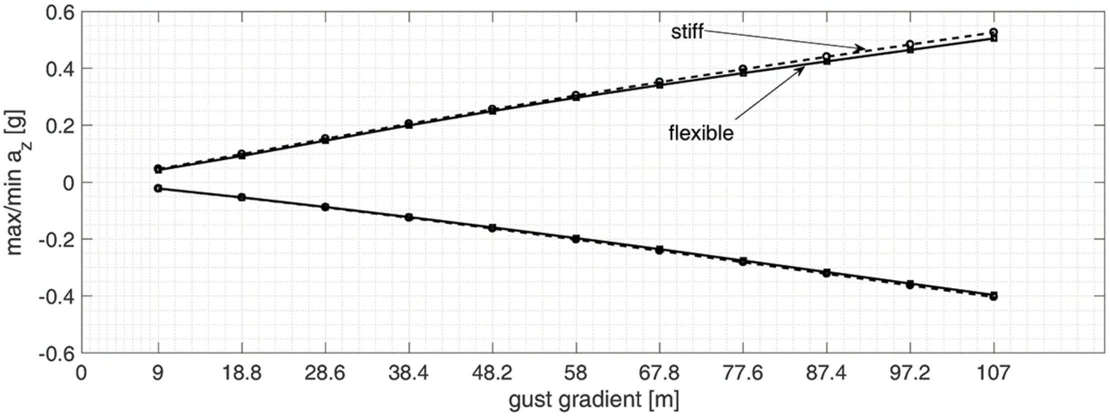

Fig. 9.3.: HARTEN max and min CoG acceleration for all gust gradients.

sponses follow the same trend and they are similar in magnitude, with a maximum difference of 3.9% at H=107 m. The impact of the structural flexibility on the CoG acceleration is therefore minimal in terms of maximum *g*s induced by the gust. A second and more important element to consider is that the magnitude of a_z increases with the gust gradient.

Figures 9.2-9.3 show an increased response of the aircraft CoG acceleration for increasing values of the gust intensity. However, considering a tuned-gust input, it was expected to observe a peak in the aircraft response within the range of the evaluated gust gradients, followed by a decrease of the response amplitude [80]. Such behaviour was not noticed in the current study, suggesting that for flexible HARW configuration requirements dictated by the CS-25 documentation might not cover the whole dynamic range of the aircraft response. Assessment of the adequacy of the CS-25 for such category of aircraft is however beyond the scope of this work, although further investigation into the topic is suggested as possible future work.

The impact of the overlapping between the rigid-body dynamics and the structural dynamics is more evident in the transient response of the aircraft and its structure. Figure 9.4 shows the HARTEN response for three different gust conditions at H=9 m, H=48.2 m and H=107 m. The CoG and wing-tip vertical acceleration along with the pitch rate are plotted against the simulation time. The transient response of the CoG vertical acceleration (top) does not show a coupling between the structural and rigid-body dynamics. The response initially oscillates and finally settles for t > 14 s. The gust gradient impacts only the magnitude of the response. However, for H=48.2 m the a residual of the short period mode is superimposed to the aircraft response. An approximation of the longitudinal rigid-body natural frequencies is given in Table 9.2[1]. A similar behaviour is shown by the pitch rate, q (bottom). The magnitude of the q response is again higher for higher values of H. In this case as well the structural flexi-

---

[1] The short-period and phugoid natural frequencies were evaluated using the reduced-order approach for the two mode responses. The approximated short-period natural frequency is defined as [45]:

$$\omega_s = \sqrt{\frac{-M_w V}{I_{yy}}} \tag{9.7}$$

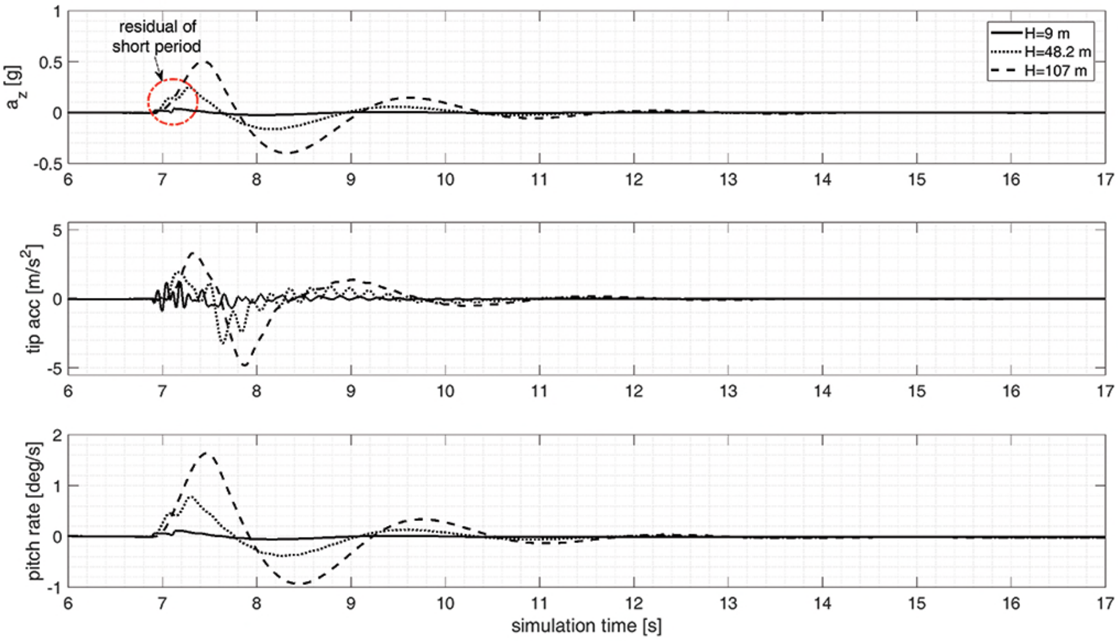

Fig. 9.4.: HARTEN gust response for H = 9 m, 48.2 m and 107 m (flexible configuration).

bility do not affects the transient response of the pitch dynamics. The wing-tip acceleration (middle) instead is strongly affected by the flexible nature of the wing structure. The transient response is oscillatory and the flexible contribution is superimposed to the rigid body response. However, this is true only for H=9 m and H=48.2 m. The response for H=107 m is not affected by the structural flexibility. The reader should notice that the tip acceleration is calculated in the body axis reference system, therefore does not includes the contribution of the CoG acceleration. The wing-tip behaviour can be explained by analysing the nature of the *1-cosine* gust excitation. In fact, such gust model is also called *tuned* gust as it is designed to excite specific frequencies of the aircraft response. When considering only the rigid-body dynamics, the gust design targets the rigid-body dynamics such as short period and phugoid mode (for the longitudinal case). However, when the structure is flexible *enough*, the lower value of the structural frequencies can be compatible with the ones excited by the gust. In this case, the structural dynamics is excited along with the rigid-body dynamics. The specific dynamics frequency excited by the gust depends on the flight speed and the gust gradient and it is defined as [45]:

$$\omega_g = \frac{\pi V_0}{2H} \tag{9.9}$$

---

where M_w is the aerodynamic stiffness, V the velocity and I_{yy} the inertia around the y-axis. The estimation of M_w was carried out considering the response as linear and applying the superposition principle. More details on the M_w estimation can be found in Appendix D.

The phugoid natural frequency is defined by following the Lanchester approach as [45]:

$$\omega_p = \frac{g\sqrt{2}}{V} \tag{9.8}$$

The lower is the Mach number, the more accurate is the approximation of the natural frequencies [45]. In this case, the flight Mach number is $Ma = 0.65$, representing the upper limit of the subsonic flight, thus these values of the frequencies are considered only as representative of the HARTEN rigid-body response.

			structural		rigid-body	
H	ω_g	**mode**	**flexible**	**stiff**	**short-period**	**phugoid**
9 m	5.5 Hz	1	1.3 Hz	4.4 Hz	0.4 Hz	0.01 Hz
18.8 m	2.7 Hz	2	2.2 Hz	7.9 Hz		
28.6 m	1.7 Hz	3	3.6 Hz	12.6 Hz		
38.4 m	1.3 Hz	4	4.6 Hz	16.4 Hz		
48.2 m	1.1 Hz	5	4.8 Hz	17.1 Hz		
58.0 m	0.9 Hz	6	5.6 Hz	19.7 Hz		
67.8 m	0.7 Hz	7	7.1 Hz	25 Hz		
77.6 m	0.6 Hz	8	8.2 Hz	28.8 Hz		
87.4 m	0.57 Hz	9	12.1 Hz	42.8 Hz		
97.2 m	0.51 Hz	10	12.7 Hz	45 Hz		
107 m	0.46 Hz	11	14.6 Hz	51.7 Hz		

Tab. 9.2.: Gust frequencies (ω_g) along with rigid and flexible structural natural frequencies for HARTEN evaluated for the specific case study.

Table 9.2 shows the structural natural frequencies excited by the tuned gusts along with the HARTEN structural frequencies for the rigid and flexible configurations. Highlighted in red are the structural frequencies that overlap with ω_g. For example, for H = 9 m, ω_g excites the 6^{th} flexible structural mode, while for H = 38.4 m and H = 48.2 m, the gust is able to excite the dominant first bending mode. As shown in the plots, the rigid-body motion of the CoG is not affected by the structural flexibility. This is due to the fact that the aircraft is modelled as stiff, considering only the wing as flexible.

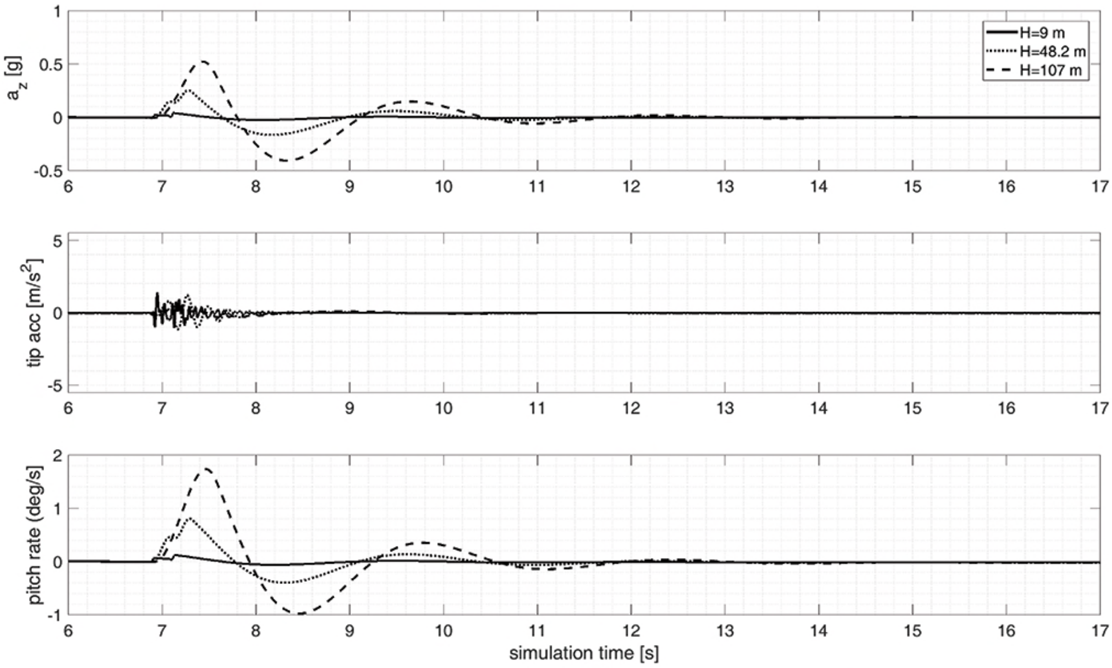

Fig. 9.5.: HARTEN gust response for H = 9 m, 48.2 m and 107 m (stiff configuration).

The phenomena are more clear when considering the HARTEN stiff configuration. The response in this case in shown in Figure 9.5. While the difference in the aircraft pitch rate and vertical acceleration for the stiff configuration is minimal with respect to the flexible case, the wing-tip acceleration response is clearly different. Firstly, the magnitude of the response is definitely lower, about 70%, of the flexible response. Secondly, the transient response is much shorter. In fact, while in the flexible case the response settles for t>14 s, in the stiff case the response converges for t > 9 s. This behaviour affects the ability of the structure to sustain dynamics load and to be resilient to fatigue.

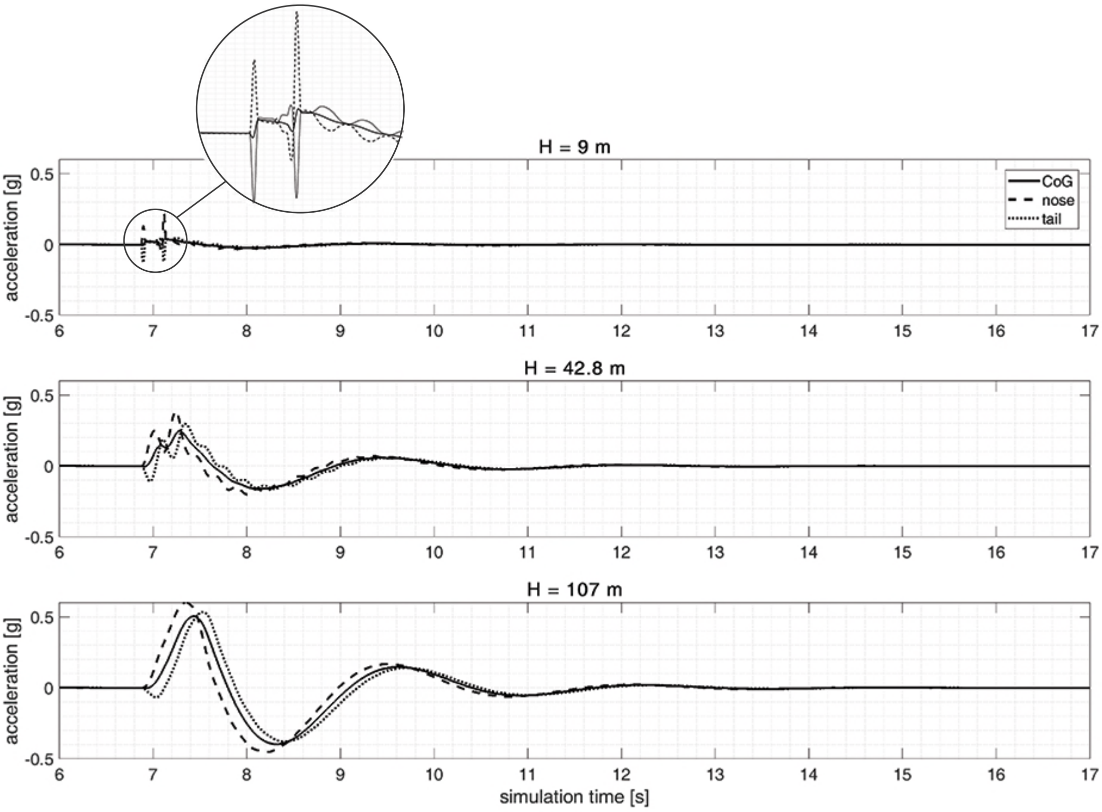

Fig. 9.6.: HARTEN vertical acceleration at the CoG, nose and tail for H = 9 m, 48.2 m and 107 m (flexible configuration).

Figure 9.6 shows the vertical acceleration at HARTEN nose, tailplane and CoG for three different gust gradients for the flexible configuration. The structural transient response is superimposed to the rigid-body one for H=9 m and H=42.8 m and clearly visible in the plot. The three signals are out of phase: the nose response anticipates the CoG response, while the tail response follows the CoG one, where the time lag is $\tau_N = 0.087$ s and $\tau_T = 0.090$ s for nose and tail respectively. Such aspect plays an important role in the open-loop strategy adopted in this work. In fact one of the general possible limitations of the GLA is the reaction time of the control and the ability of affecting the early aircraft transient response due to the gust induced load. For this reason, research is investigating the possibility of anticipate the gust-induced $\Delta\alpha$, as previously explained in Chapter 2. Although the most common way to do it is to detect the $\Delta\alpha$ at the nose through an AoA sensor, for the control strategy developed in this study the acceleration is assumed constantly monitored at the nose of the aircraft through the use of an accelerometer. Such choice is based on the fact that the open-loop strategy is triggered based on the value of the aircraft vertical acceleration rather than its angle of attack. Although monitoring the acceleration at the nose is not a common practice for GLA systems, such strategy was already implemented successfully in different studies [105, 82]. By detecting the acceleration on the nose, the GLA can benefit from a prediction time of 87 ms to deploy the control surfaces before the gust hits the wing.

The $\bar{M}_0$ response is calculated by firstly evaluating the forces due to the motion of the aircraft, L_M, and the forces induced by the gust, L_G. The bending moment of a generic wing section at distance y_k from the fuselage centre line is therefore defined as (adapted from [187]):

$$\bar{M}(y,t)=\sum_{k=1}^{n} F_{\text{inertia}_k}(t)\left(y_k+\frac{\Delta y}{2}\right)-F_{\text{applied}}(t)\frac{b}{4} \tag{9.10}$$

where n is the number of structural nodes between the wing element k and the wing centre line, Δy is the distance between following nodes, b is the wingspan and

$$F_{\text{applied}}(t)=L_M(t)+L_G(t) \tag{9.11}$$

Finally, the wing root bending moment of the overall wing is derived from Equation 9.10 and defined as:

$$\bar{M}_0(t)=\bar{M}(b/2,t) \tag{9.12}$$

Figure 9.7 shows the transient response of $\bar{M}_0$ at different gust gradients for the flexible and stiff HARTEN configuration. The value of $\bar{M}_0$ is represented as relative change with respect to the value calculated at the cruise flight point. An important aspect to stress is the overlapping

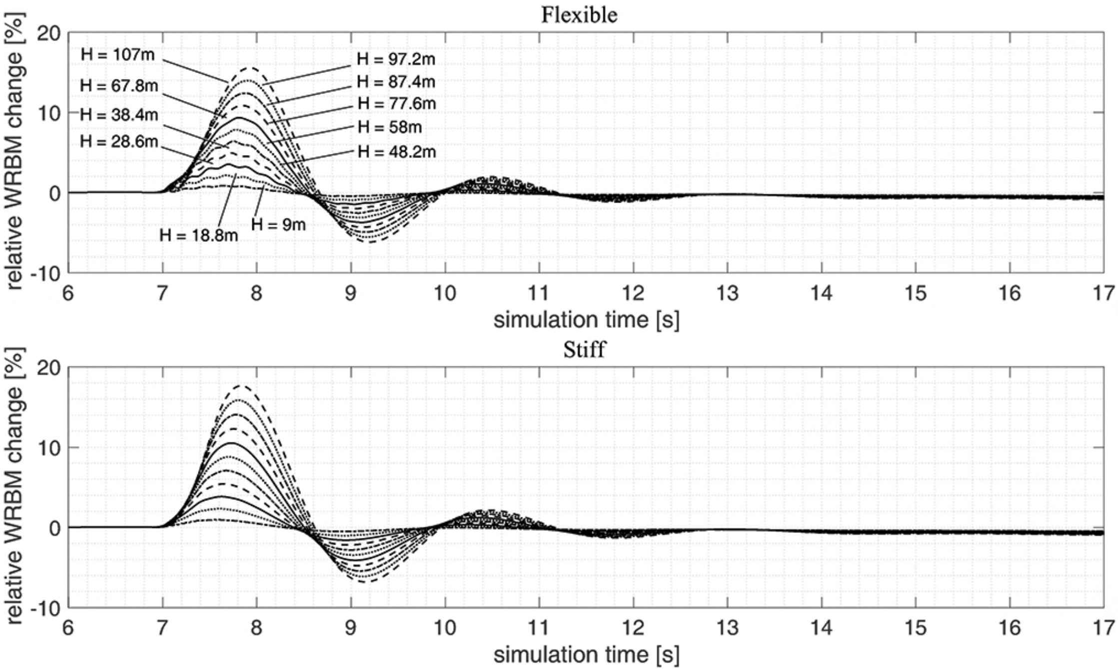

Fig. 9.7.: HARTEN open loop wing root bending moment at the simulated gust profile conditions for flexible (top) and stiff (bottom) case.

of the structural dynamics with the wing response in the flexible configuration, as noticed already in the previous analysis. The superimposition of the flexible dynamics is evident when the gust frequency aligns with the resonance frequency of the structure, i.e. 9 m < H < 48.2 m (refer to Table 9.2). Such behaviour is not observed in the stiff-configuration response because of the higher bandwidth of the dynamics associated with this specific configuration. Furthermore, the higher is the gradient, the higher is the maximum value of $\bar{M}_0$.

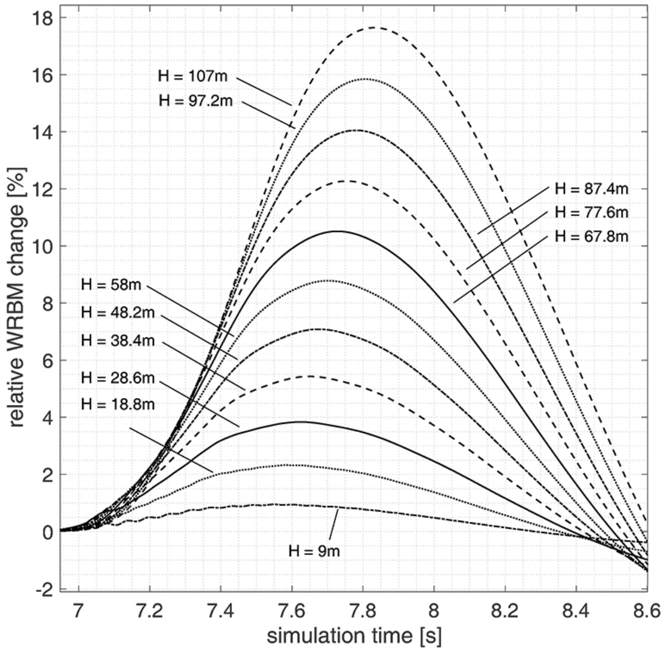

Fig. 9.8.: Zoom on the positive peaks for the stiff response.

Figure 9.8 shows a zoom of the positive peak of the transient response for the stiff case. The plot highlights the fact that the peaks of the response for different gust gradients are not aligned but actually slightly shifted. The higher is the gust gradient, the later the peak occurs. The time shift between the peak response at H = 9 m and H = 107 m is about 200 ms. This aspect can be relevant in the design of the GLA system as although lower gradients lead to lower loads, the response actually peaks faster. For this specific study, this aspect is not considered.

Figure 9.9 shows the trend of the maximum and minimum relative $\bar{M}_0$ change for all the gust gradients. As already seen, an increase in the gust intensity leads to an increase in the wing load. Furthermore, the plot also shows that the stiff-configuration wing is actually more loaded than the flexible one. The gap between the two trends increases with the gust gradient.

9.2 Open-loop GLA control system

The working principles of the open-loop GLA control system are shown in Figure 9.10. The activation of the GLA system is based on the constantly monitored value of the vertical accel-

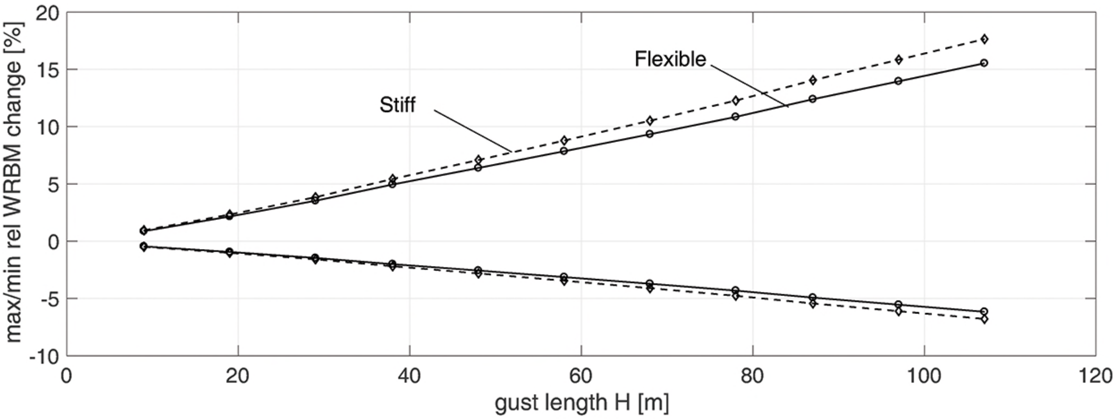

Fig. 9.9.: HARTEN maximum and minimum wing root bending moment over simulated gust profiles for flexible and stiff case.

eration, a_z, measured at the nose of the aircraft. When a_z crosses a specific threshold, the GLA system is activated for a specific time, τ, called *hold time*. Once activated, the control signal, $\boldsymbol{u}$, is generated by the GLA and fed into the system. The control is defined as:

$$\boldsymbol{u}(t) = \begin{bmatrix} \boldsymbol{\delta}_s \\ \xi \end{bmatrix} \left(\text{sign}(t-\bar{t}) - \text{sign}(t-\bar{t}-\tau)\right) \tag{9.13}$$

where $\boldsymbol{\delta}_s$ is the vector of the spoiler deflections, $\bar{t}$ is the time of the deployment and ξ is the aileron deflection.

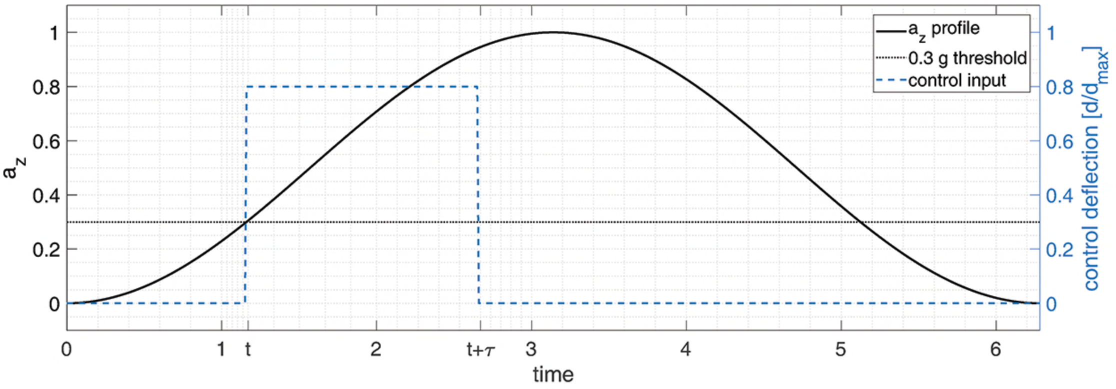

Fig. 9.10.: Schematic of the control strategy applied for GLA on HARTEN.

However, the simplicity of this GLA system represents as well its biggest limitation. In fact, once the GLA is activated, the control surfaces deflection and the hold time are insensitive to the induced gust load or the aircraft attitude. Hence, the GLA cannot adapt to the different gust scenarios. To overcome this limitation, the idea is to generate a database of optimal control surfaces deflections, hold time and threshold values, for a specific gust gradient set at several flight points, which can be interpolated to provide the GLA response in any combination of gust and flight condition. Once this database of optimal parameters has been calculated in N discrete conditions, any point in the flight and gust domain can be interpolated to fed parameters into the GLA system. The database dimension is *NxNxN* (assuming the same size for each dimension) where the first dimension represents the different flight conditions, function of speed and altitude, representative of the dynamic pressure. The second dimension represents the simulated gust gradients. The range of gust gradients is 9 m to 107 m as required by the CS-25. Finally, the last dimension of the database contains the optimal displacement of the control surfaces. Any point within the boundaries of this 3D-space can be then interpolated to provide the optimal control surfaces deflection as function of flight conditions and gust intensity. The study carried out in this work however, does not focus on the entire search space of flight conditions, but analyses just one point of the potential database in order to detail the procedure to generate all the necessary points.

An optimization algorithm was developed in order to derive the set of the optimal parameters for each gust length at the flight condition defined in Table 9.1. As the choice of the optimizer was not an object of this work, the only requirements for the solver were to be a global solver, in order to search for the optimum in the entire search domain and to be computationally viable with respect to the available hardware. Therefore, after a short review on the available optimizer literature, the *particleswarm* optimizer was chosen. The particleswarm tool adopted for the analysis was an embedded MATLAB function [8].

The *particleswarm* optimization (PSO) algorithm[91, 116, 131] is considered as a subset of the evolutionary algorithms and it is a stochastic optimizer. The optimization algorithm search for a global solution implements the following steps:

1. it first generates an initial set of N particles assigning them a prescribed initial velocity v. Unless differently assigned, the set of particles is generated randomly and constrained to be within the given upper and lower boundaries. Initial velocities are randomly generated as well. The algorithm then records the position $x(i)$ of each particle i and assigns the best evaluation b to the swarm as $b = \min(fun(p(i)))$ and its location d. A new variable, stall counter c, is created and initialized to zero.

2. A random subset S of N particles is chosen (neighbours) and the best objective function *fbest(S)* is found along with its position $g(s)$. New velocities are chosen based on the current velocity, particles' individual best locations and best location of their neighbours. The new velocity v is defined as follow:

$$v = W v + y_1 u_1 (p - x) + y_2 u_2 (g - x) \tag{9.14}$$

   where W is the inertia of the particle, y_1, y_2 are weights and $u_1, u_2 \in (0,1)$.

3. The new position of the particle is found based on the old position, new velocities and neighbours as $x = x + v$. However boundaries are enforced if the x falls outside a bound.

In this specific case, $x(i)$ is set equal to the bound and $v(i) = 0$. The objective function is evaluated in x as $f = fun(x)$. If $f < fun(p)$, then $p = x$.

4. The best optimum value of the cost function in the swarm is found. The algorithm considers the smallest $f = \min(f(j))$ among the N particles of the swarm. If $f < b$, then $b = f$ and $d = x$.If in the previous iteration the best value was lowered, the counter flag is set to *true*, otherwise stays as default as *false*. Iterations stop when the stopping criteria are met.

Swarm size and stop criteria were evaluated as a compromise between accuracy of the solution and the time required for each simulation to be completed. As result, the swarm size was set to be 5 elements wide while the stop criterion consisted in the residual of the cost function lower than 10^{-3} for 12 consecutive iterations.

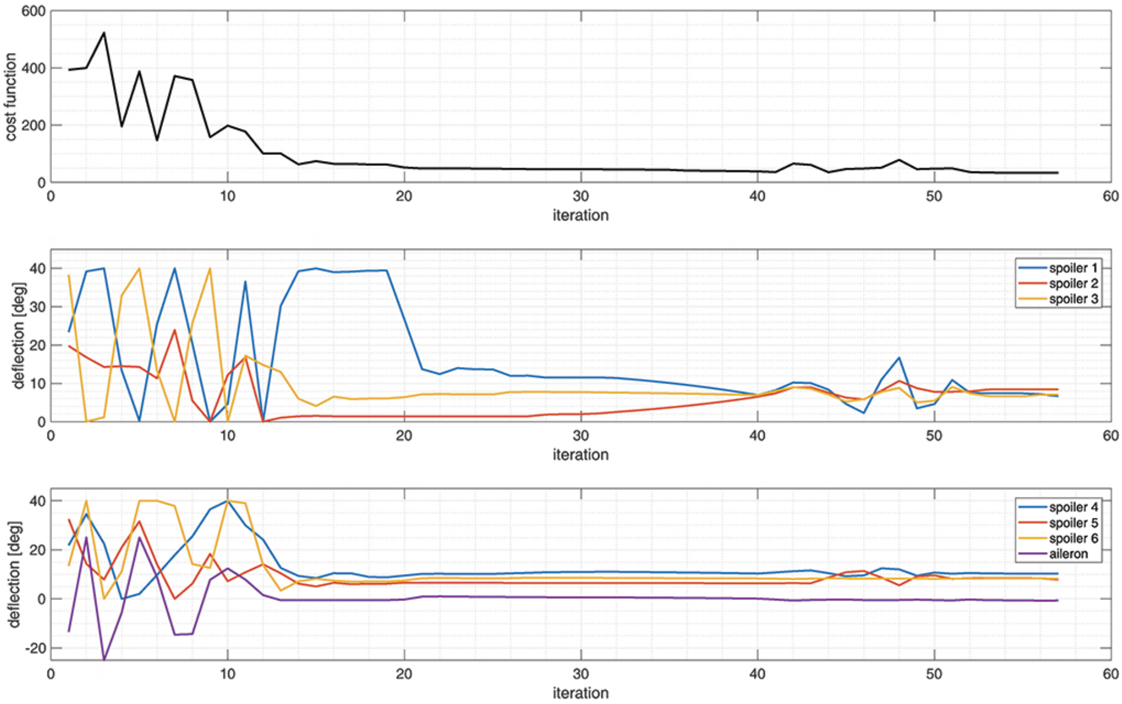

Fig. 9.11.: Example of optimization parameters history: cost function (top), inboard spoilers (middle) and outboard spoilers and aileron (bottom) iteration evolution.

Figure 9.11 shows an example of the optimization process history for a gust length of 67.8 m and $\tau = 0.3$ s. The top figure shows the cost function value plotted against the number of iterations. The value of J as expected decreases without however reaching the zero. This is a foreseen behaviour, because the cost function J reflects the increase in $\bar{M}_0$ due to the gust load (more details in the next section). Therefore, a value of $J = 0$ would mean the effect of the gust on the wing structure is zero. The last two plots show the variation of the free-parameters of the optimization vector, $\boldsymbol{u}$. The trend of the lines show that in this case the role of the spoilers is more important than the one played by the aileron.

9.2.1 Cost function definition

As previously said, the sudden increase (either positive or negative) of the aerodynamic load on the wing due to the induced change of angle of attack leads to an increase of the wing root bending moment due to the higher wing load. Likewise, the attitude of the aircraft may be degraded due to the transitory effect of the change in aerodynamic forces and moments. Acceleration of the aircraft centre of gravity is affected as well experiencing a variation proportional to the intensity of the gust, influencing the passenger comfort. In fact, recalling Equation 4.12, the vertical acceleration of the aircraft is given by:

$$a_z = \frac{L}{M} + qu - pv \tag{9.15}$$

where the vertical force f_B^z is considered to be equal to the lift force. Assuming the product pv to be small with respect to qu, the vertical acceleration of the CG is given as:

$$a_z = \frac{L}{M} + qu. \tag{9.16}$$

Therefore, initially, the problem of finding the optimum control surfaces deflection vector was solved twice, either considering the minimization of $\Delta\bar{M}_0$ only or trying to minimize both $\Delta\bar{M}_0$ and Δa_z at the same time, and the results compared. Two different cost functions were used for the two problems. The general definition of the two cost functions is given as:

$$J_1(x) = \min \Delta\bar{M}_0(x,t) + \min a_z(x,t) \tag{9.17}$$

$$J_2(x) = \min \Delta\bar{M}_0(x,t) \tag{9.18}$$

The use of the cost function J_1 was the preferred option as, the passenger comfort could benefit from the GLA system along with the structural load reduction. However, as shown in Equation 9.16 and detailed in the gust response analysis of the HARTEN aircraft, the pitch moment plays a dominant role in the aircraft response and in the increase of a_z. To com-

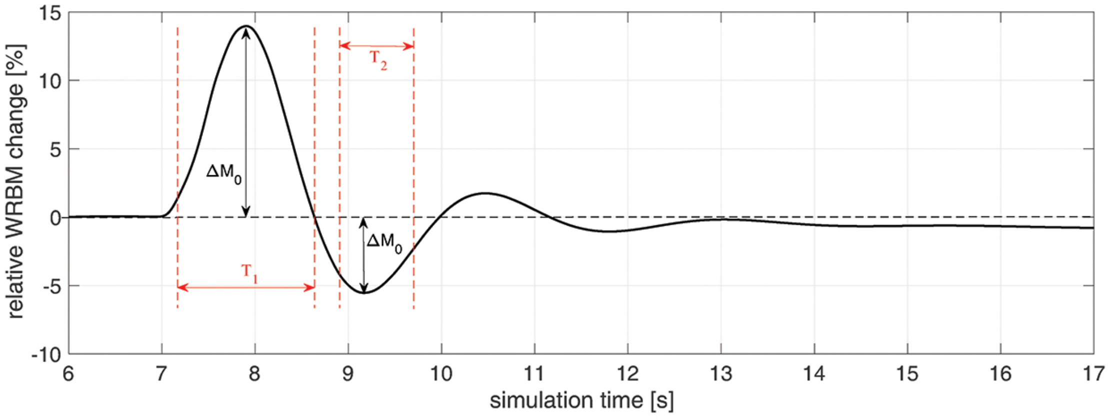

Fig. 9.12.: $\Delta WRBM$ identification for the cost function definition

pensate the increase in q and therefore limit the increase of Δa_z, a FCS along with the use of the elevator would be needed. Such choice is common to have in modern GLA systems. However, the present study focuses mainly on the flexible response of the wing structure and therefore does not consider the use of control surfaces other than spoilers and ailerons. Thus, when trying to minimize J_1, the solver could not converge to any solution as it was not able to reduce both $\bar{M}_0$ and a_z simultaneously with the use of only wing control surfaces. Furthermore, it was seen that the maximum a_z reached over the investigated gust gradient range was 0.5 g, which represents the maximum load factor as well, n_z being defined as:

$$n_z = \frac{L}{W} = \frac{m a_z}{m g} = \frac{a_z}{g} \tag{9.19}$$

The common load factor envelope upper limit for commercial aircraft is between $2.5 < n_z < 3.2$ [187, 9]. Thus, for this specific study, the gust induced load does not represent a critical n_z for the aircraft structure. For all these reasons, the cost function adopted for the analysis is the one given in Equation 9.18 and expanded as:

$$J(x) = \min_{t \in T_1} |\Delta \bar{M}_0(t,x)| + \min_{t \in T_2} |\Delta \bar{M}_0(t,x)| \tag{9.20}$$

where the time T_1 and T_2 are defined as shown in Figure 9.12. The second term of the cost function aims to limit the second peak of the $\bar{M}_0$ transient response.

Considering this premise, the optimization problem can be formally stated as follows:

$$\min_{\boldsymbol{x}_L < \boldsymbol{x} < \boldsymbol{x}_U} \quad J(\boldsymbol{x}) \tag{9.21}$$

where $\boldsymbol{x}$ is the vector of the design parameters defined as

$$\boldsymbol{x} = [\delta_{s1}, \delta_{s2}, \delta_{s3}, \delta_{s4}, \delta_{s5}, \delta_{s6}, \xi] \tag{9.22}$$

The vector of the design parameters contains the deflections of the spoilers (a vector of six variables because they are assumed to deploy symmetrically), and the deflection of the aileron (assumed to deflect symmetrically as well). The upper and lower boundaries of the vector $\boldsymbol{x}$ are defined as:

$$\boldsymbol{x}_L = [0, 0, 0, 0, 0, 0, -25] \tag{9.23}$$

$$\boldsymbol{x}_U = [40, 40, 40, 40, 40, 40, 25] \tag{9.24}$$

In the following sections the impact of the different parameter on the GLA performance is evaluated considering the effect of one parameter at time. A summary of the different GLA systems analysed and the assumptions on the parameters is given in Table 9.3.

Ref number	Note	Configuration	τ	$\bar{n}_z$	τ_2	$(\bar{n}_z)_2$
I	Reference	flexible	1.5 s	0.3 g	-	-
II	Flex impact	rigid	1.5 s	0.3 g	-	-
III	Hold time	flexible	2.5 s	0.3 g	-	-
IV	Threshold	flexible	1.5 s	0.2 g	-	-
V	Enhanced	flexible	opt	opt	-	-
VI	Second threshold	flexible	1.5 s	0.3 g	opt	opt

Tab. 9.3.: Summary of all the assessed GLA systems

9.2.2 Reference GLA system

For the first case to be considered is the GLA system the following assumptions were made:

$$\tau = 1.5s \tag{9.25}$$

$$n_z \quad \text{threshold} = 0.3g \tag{9.26}$$

$$\text{configuration} = \text{flexible} \tag{9.27}$$

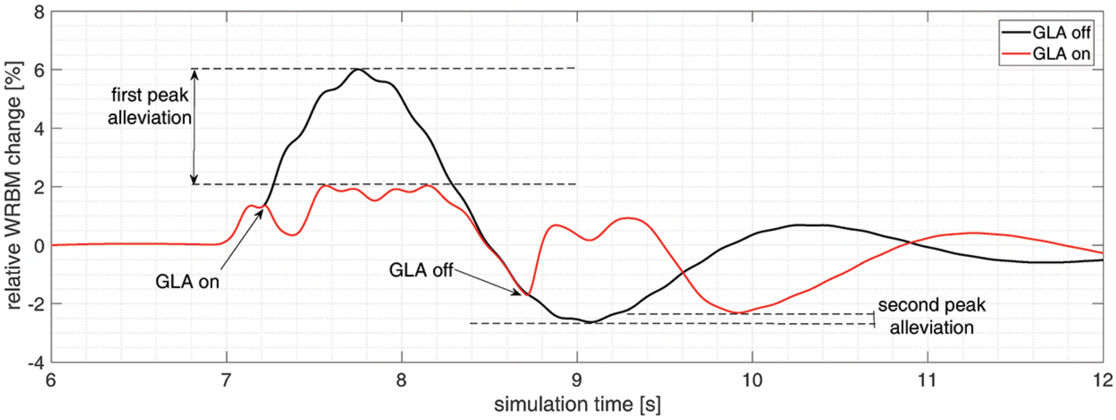

Fig. 9.13.: GLA system design: WRBM alleviation convention (test case $t = 1.5$ s, threshold 0.3 g and gust length = 48.2 m).

This GLA system will be considered as the reference case for the rest of the work. Before discussing the results, Figure 9.13 shows the convention on the WRBM alleviation: the GLA system alleviates the load (minus sign in the WRBM alleviation plots) if the *absolute* value of the peak associated with GLA system activated is *smaller* than the absolute value of the peak with the GLA off. In other words, the GLA system is effective if the alleviated peaks are closer to the trim value than the non alleviated peaks. An example of the WRBM alleviation summary plot is shown in Figure 9.14. The WRBM alleviation coefficient, $\bar{M}_0^S$, is estimated as:

$$\bar{M}_0^S = \frac{\Delta\bar{M}_0^{GLA\,ON} - \Delta\bar{M}_0^{GLA\,OFF}}{\Delta\bar{M}_0^{GLA\,OFF}} \tag{9.28}$$

Therefore the alleviation is evaluated with respect to the maximum value of the WRBM of the aircraft non alleviated response.

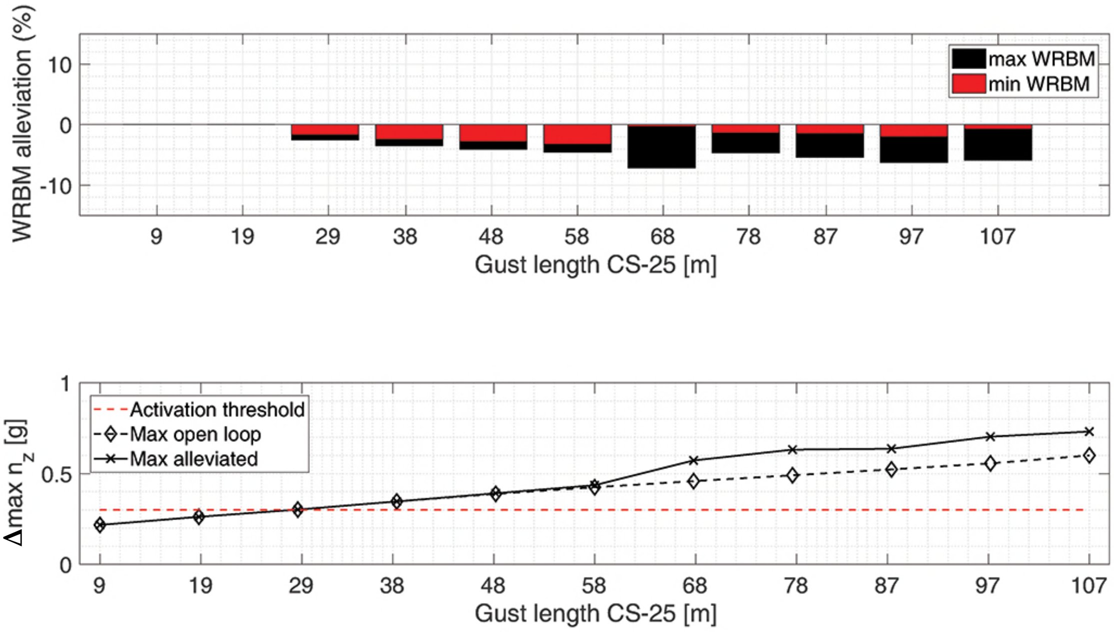

Fig. 9.14.: GLA reference: HARTEN WRBM alleviation plot (top) and maximum load factor increment Δn_z (bottom) for optimized control surfaces deflection against gust lengths.

Figure 9.14 shows the impact of the reference GLA system. The first two gust lengths (H = 9 m and H = 18.8 m) do not excite any response of the GLA system as the maximum n_z does not cross the threshold of 0.3 g. For H > 28.6 m, max n_z is always greater than 0.3 g and the GLA system is always able to attenuate both the positive and negative WRBM peaks. The alleviation is not constant for all the gust lengths: for the positive peak, it reaches the maximum at H = 67. 8 m, alleviating the WRBM by 7.6%. The minimum of the alleviation is at H = 29 m, where WRBM is alleviated by 2.5%. The negative peak as well is always attenuated from a maximum of 3.2% at H = 58 m to a minimum of 0.3% at H = 67.8 m. The same figure (bottom) shows the impact of the GLA system on the vertical load factor. As predicted the vertical load factor increases when the load alleviation is activated, increasing n_z up to 29.8% at H = 78 m.

Figure 9.15 shows the control surface deflections as a result of the optimization process. These deflections are simply the numerical solution found by the optimizer, although, as previously explained, such deflections are not necessarily reflected in the physical problem. They affect the solution only if the spoiler height, h, is $h/c > 0.04$[2]. Instead, when considering ailerons, the numerical solution corresponds to the physical one. Figure 9.16 shows control surfaces actually used by the aircraft to alleviate the load induced by the gust along with their deflection. The first thing to notice is that ailerons play an important role in the alleviation by being deflected at all alleviated gust lengths. Their deflection goes from a minimum of 0.9

---

[2] Refer to Section 8.2.1 for more details.

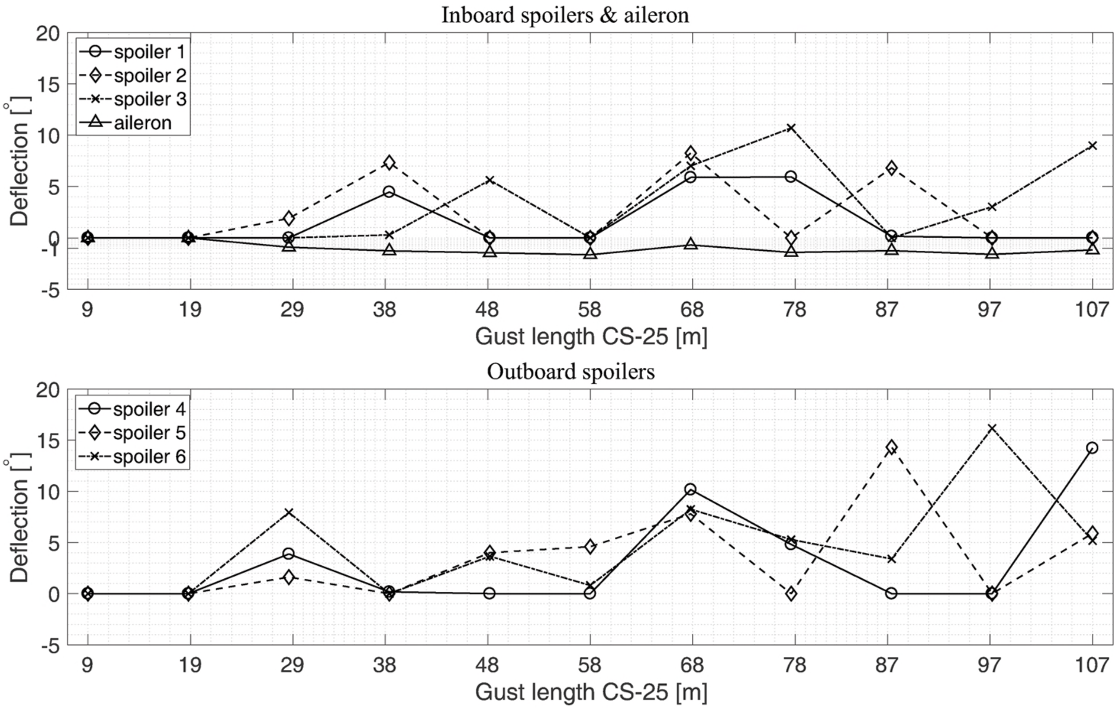

Fig. 9.15.: GLA reference: HARTEN optimized computational control surface deflections.

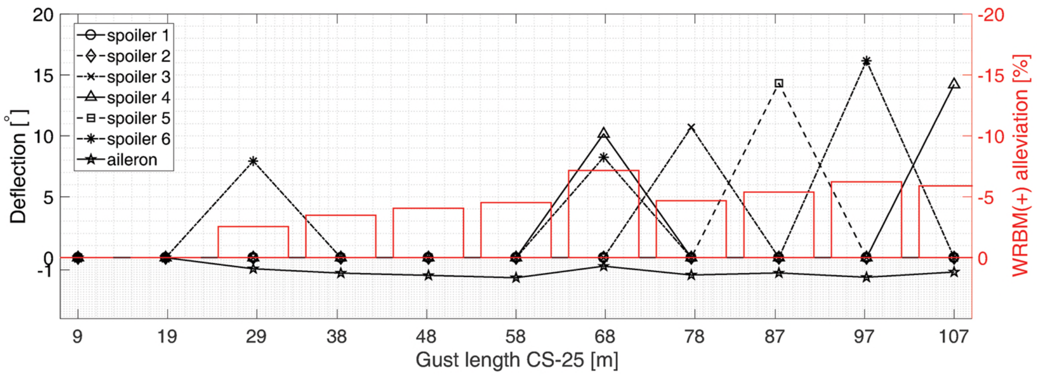

Fig. 9.16.: GLA reference: HARTEN *true* optimized deflections.

deg for H = 28.7 m to a maximum of 1.6 deg for H = 58 m. Spoilers instead are not always used and their maximum deflection is 16 deg and throughout the gust range only outer spoilers were used. Spoiler 1 and spoiler 2 , which go from 14% to 32.2% of the wingspan, were never considered by the optimizer. This is something we might expect as the optimizer tries to shift the lift from the outboard wing to the inboard section to reduce the bending moment. When the spoilers were not used, for H = 38 m, H = 48 m and H = 58 m, the WRBM reduction is always under the 5%. The biggest reduction is for H = 68 m, where spoiler 3 and spoiler 4 were deployed along with the aileron.

Overall two main aspects can be stressed: i) the ailerons, as predicted, are over-effective. In fact, although deflected of just one degree, they have a big impact on the wing load. This aspect definitely affects the optimum solution of the work done by the spoilers. ii) The inboard spoilers were never used throughout the optimal solutions.

9.2.3 Impact of flexibility

In this section only, differently from the rest of the chapter, the GLA system is optimized for the HARTEN stiff configuration in order to assess the impact of the flexible wings on the GLA response. The optimization process assumed the following:

$$\tau = 1.5s \tag{9.29}$$

$$n_z \quad \text{threshold} = 0.3g \tag{9.30}$$

$$\text{configuration} = \text{rigid} \tag{9.31}$$

Figure 9.17 shows the WRBM alleviation plot for this scenario. The fact that the aircraft is more rigid than the reference configuration does not impact considerably the action of the GLA system. The alleviation in this case follows the same trend and magnitude of the reference case. Small differences are at H = 67.8 m and H - 107 m, where in this case the positive peak alleviation are 4.38% rather than 7.2% and 6.5% rather than 5.9% respectively. The negative peak as well follows the same trend except for H = 97.2 m where the performance of the GLA system is worse than the non alleviated case, worsening the response by 3.2%. The vertical load factor as well is in line with the reference case, except again at H = 97.2 m, where $\max n_z = 0.8g$. This last case might be one of the numerical solutions as it appears to be a

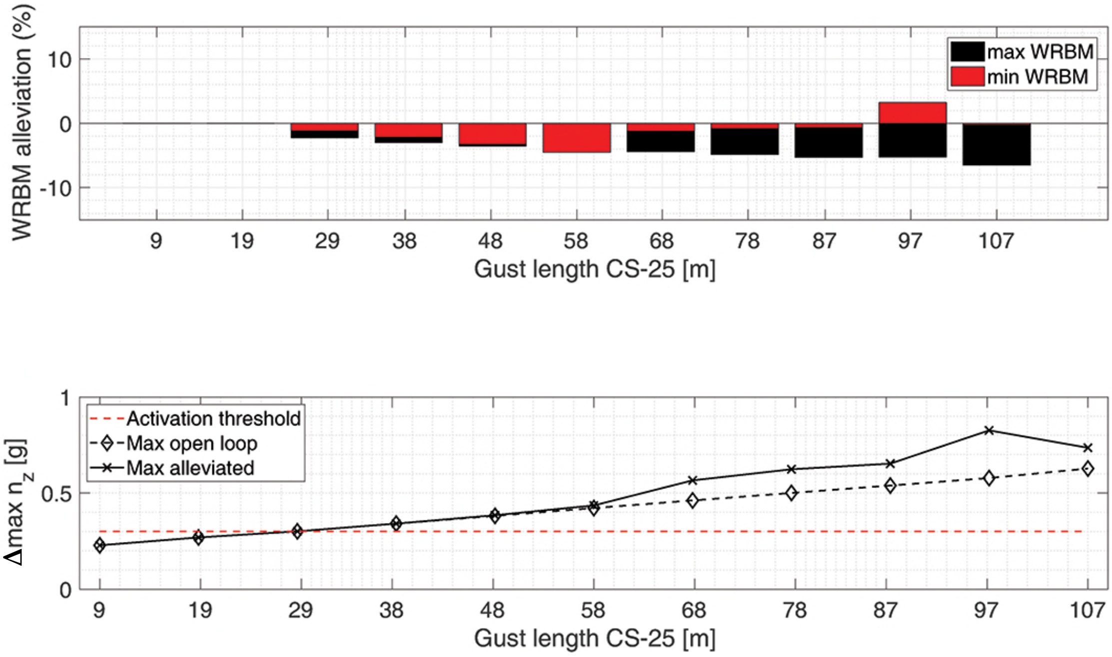

Fig. 9.17.: Impact of the flexibility: HARTEN WRBM alleviation plot (top) and maximum load factor increment Δn_z (bottom) for optimized control surfaces deflection against gust lengths, rigid case.

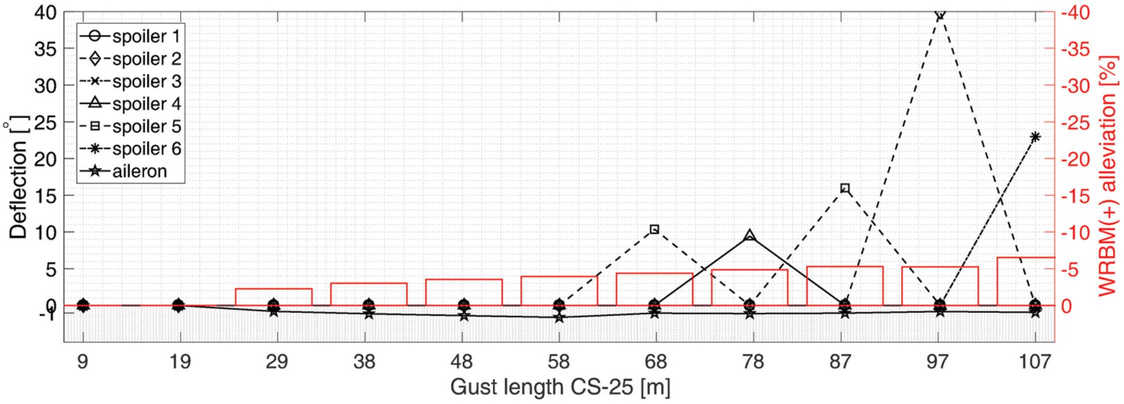

Fig. 9.18.: Impact of the flexibility: HARTEN *true* optimized deflections, rigid case.

local minimum rather than a global one. To verify the source of error, a new optimization might be required.

The optimal control surface deflections are shown in Figure 9.18. Inboard spoilers number 1 and 2 are again never used, while the worst performance of the simulation set is linked to full deflection of the mid spoiler 3.

Overall, the analysis shows that the effect of the structural flexibility do not affect substantially the action of the GLA system, although a modest improvement has been seen for some gust lengths. More plots on the numerical deflections can be found in Appendix D.

9.2.4 Impact of hold time

The aim of this section is to assess the impact of the hold time τ on the performance of the GLA system. Increasing the control surfaces deployment time might allow the GLA system to catch the second peak as well. Simulations assumptions for this case were the as follows:

$$\tau = 2.5s \tag{9.32}$$

$$n_z \quad \text{threshold} = 0.3g \tag{9.33}$$

$$\text{configuration} = \text{flexible} \tag{9.34}$$

Figure 9.19 shows the WRBM alleviation plot. As expected, the performance for the second negative peak worsen considerably as the wing is partially unloaded for 2.5 s due to the action of the GLA system. The negative peak is never alleviated and leads to a maximum difference with the reference case of 11.07% at H = 28. 6 m. For H = 77.6 m, the second peak response worsen by 8.37%. The effect of a longer hold time does not benefit the first (positive) peak generally. The GLA system provides an improved response for H = 28.6 m (reduction of 9.1% with respect of 2.5% of the reference case) and it is in line with the reference performance for the rest of the simulation. The behaviour of n_z as well is not clearly different from the reference case.

Figure 9.20 shows the optimal control surfaces deflection. Differently from the other cases, this time the GLA system barely uses spoilers. In fact, they are used singularly in only two cases: H = 28.6 m and H = 77.6 m. Again inner spoilers are never considered.

Overall, the impact of a longer hold time worsens the general performance of the GLA system. The reason behind this is the excessive unloading that the activation of the GLA system causes on the aircraft wings.

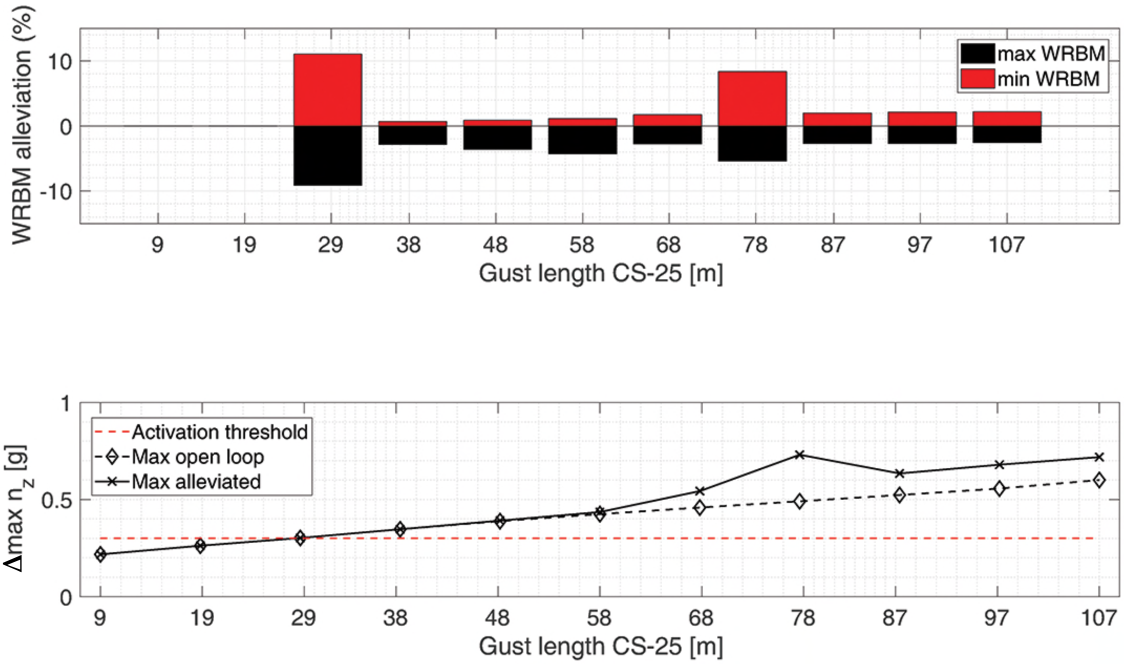

Fig. 9.19.: $\tau = 2.5$ s: HARTEN WRBM alleviation plot (top) and maximum load factor increment Δn_z (bottom) for optimized control surfaces deflection against gust lengths.

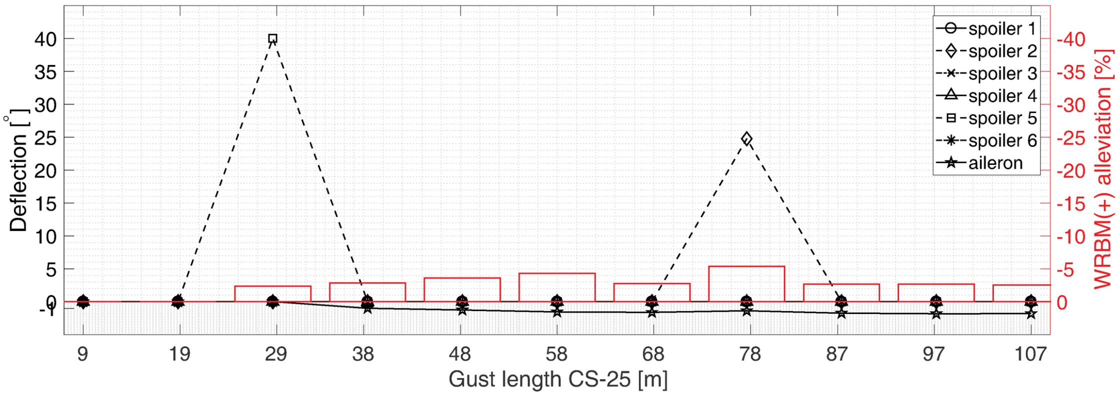

Fig. 9.20.: $\tau = 2.5$ s: HARTEN *true* optimized deflections.

9.2.5 Impact of activation threshold

For this last case the impact of the threshold on the GLA system performance is assessed. The threshold is lowered in order to sense the gust dynamics earlier. Assumptions for this simulation were the followings:

$$\tau = 1.5s \tag{9.35}$$

$$n_z \quad \text{threshold} = 0.2g \tag{9.36}$$

$$\text{configuration} = \text{flexible} \tag{9.37}$$

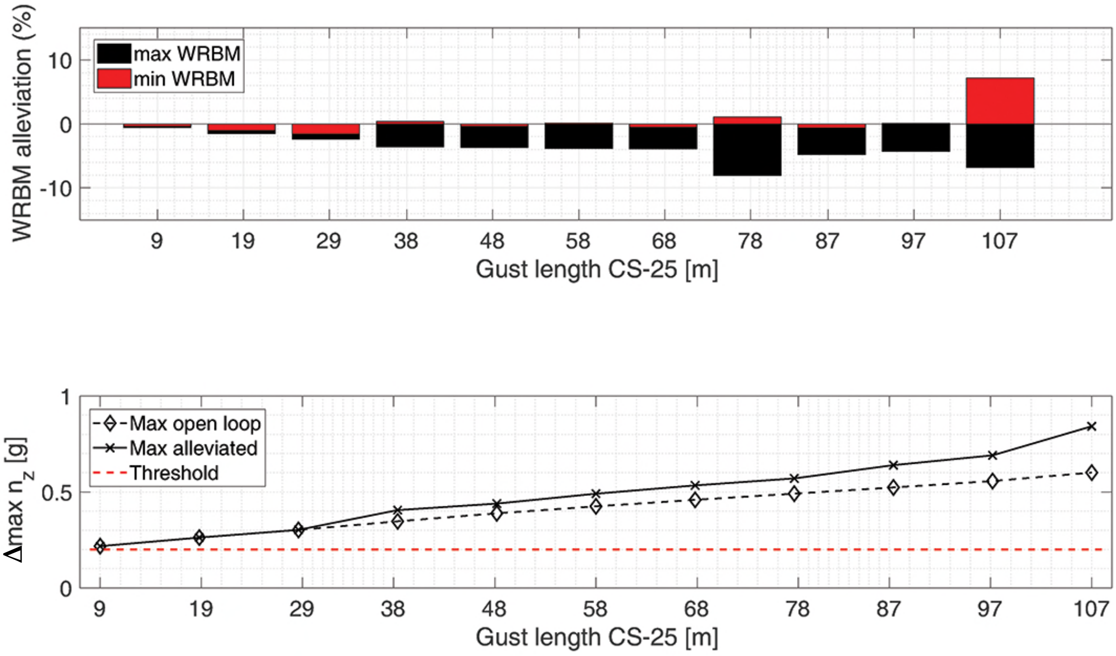

Fig. 9.21.: Threshold = 0.2 g: HARTEN WRBM alleviation plot (top) and maximum load factor increment Δn_z (bottom) for optimized control surfaces deflection against gust lengths.

Figure 9.21 shows the WRBM alleviation plot. Differently from the other cases previously discussed, the case H = 9 m and H =18.8 m are alleviated as well. The overall performance of the GLA are not improved compared to the reference case. In fact, the alleviation for the first two gust lengths is minimal (0.5% and 1.5% for the positive peaks respectively), and it induces a deterioration of negative peak performance at H = 107 m by 7.2%. There is improvement at H = 77.6 m where the WRBM is reduced by 8.1% with respect the 4.1% of the reference case. The behaviour of the load factor n_z is constant throughout the range of simulation and in line with the reference case.

Figure 9.22 shows the optimal control surfaces deflections. The GLA alleviation this time makes greater use of the spoilers, while it reduces the use of the ailerons. For H = 78 m, the

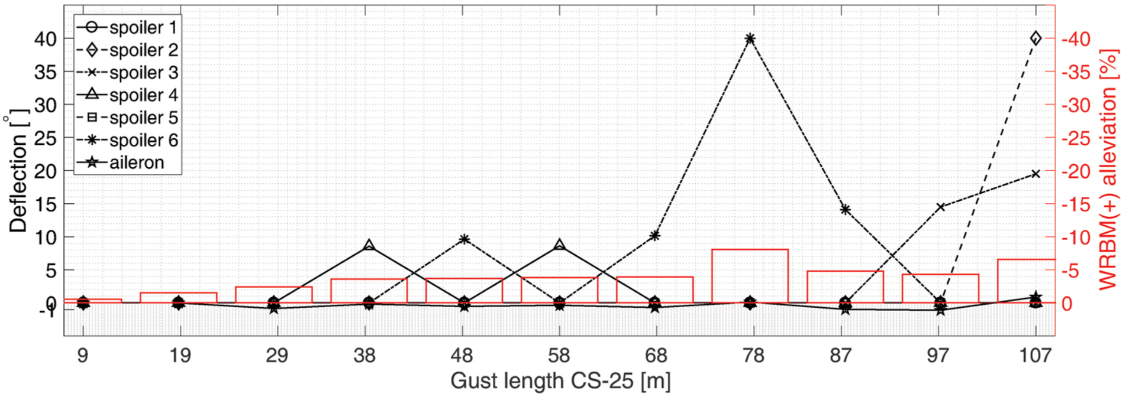

Fig. 9.22.: Threshold = 0.2 g: HARTEN *true* optimized deflections threshold of 0.2 g.

outer spoiler number 6 is deflected to its maximum angle of 40 deg, while in the other cases the use of the control surfaces is not massive, as reflected by the WRBM reduction trend.

9.3 Enhanced open-loop GLA system

In this last section, two enhanced open-loop GLA systems are presented: in the first one, the hold time and the threshold value are not constant any more but optimized along with the control surfaces deflection. In the second one instead, a second (deactivation) threshold is introduced into the architecture of the GLA system.

9.3.1 Optimized time and threshold

In the design of the first enhanced version of the GLA system, the values of the threshold and hold time were set as free parameters to be optimized by the solver. The numerical problem is still formally defined by Equations 9.21-9.24. However, the new free parameter vector is defined as:

$$\boldsymbol{x} = [\delta_{s1}, \delta_{s2}, \delta_{s3}, \delta_{s4}, \delta_{s5}, \delta_{s6}, \xi, \tau, \bar{n}_z] \tag{9.38}$$

while the upper and lower boundaries changes as:

$$\boldsymbol{x}_L = [0, 0, 0, 0, 0, 0, -25, 0.5, 0.1] \tag{9.39}$$

$$\boldsymbol{x}_U = [40, 40, 40, 40, 40, 40, 25, 2.5, 0.4] \tag{9.40}$$

where $\bar{n}_z$ is the optimized threshold value. The parameter analysis in Section 9.2 has shown that ultimately the best GLA system option is the reference one, as it is able to alleviate consistently the WRBM across the gust length domain, without compromising the second gust peak alleviation. When setting up the particle swarm optimizer, it is possible to define an initial value of the swarm. Considering the assumptions above, the initial value for the optimization was set to be the optimum free parameter vector of the reference GLA system. It is not surprising then the solution is an improved version of the reference GLA system[3].

The WRBM alleviation trend is presented in Figure 9.23. As expected, the trend of the saving is similar to the one obtained by the reference GLA system. Generally, the alleviation of the first peak is slightly better than the reference case, with the maximum benefit obtained at H = 97.2 m where the WRBM is alleviated by 8.3% rather than 6.2% of the reference GLA system. The benefits on the second peak instead are more evident, with a constant improvement distributed along the gust length domain. The increment in vertical load factor (bottom figure) does not present any major deviation from the reference study

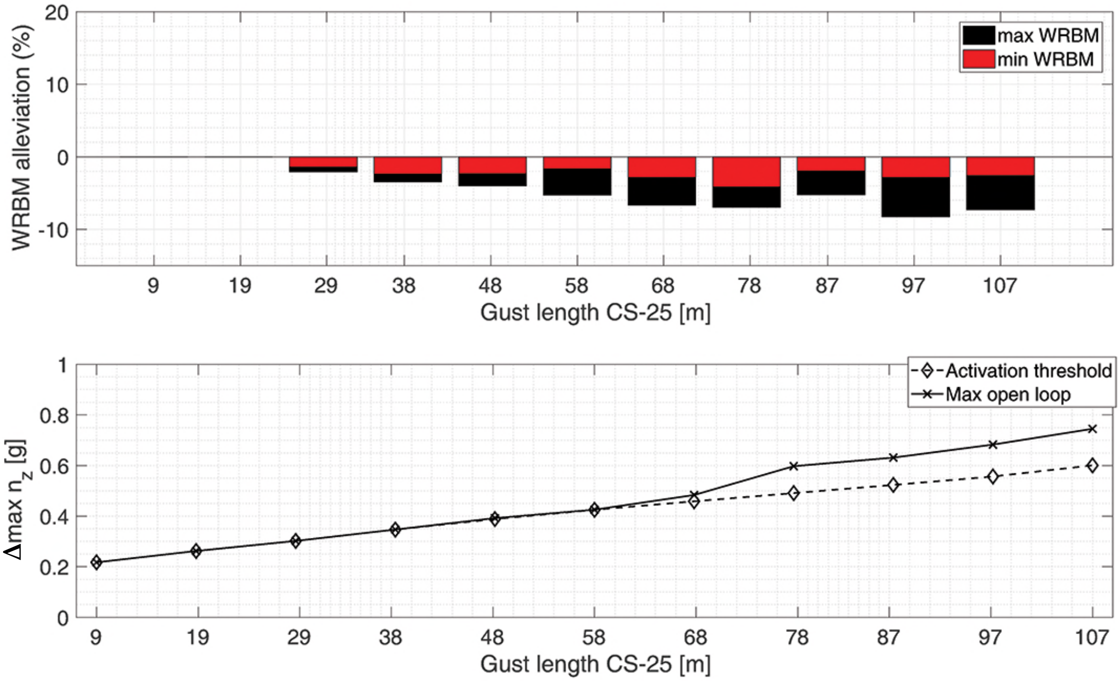

Fig. 9.23.: Variable τ and threshold: HARTEN WRBM alleviation plot (top) and maximum load factor increment Δn_z (bottom) for optimized control surfaces deflection against gust lengths.

Figure 9.24 shows the control surfaces deflection. Interestingly, spoilers are not used up to H = 67.8 m. Until this point the GLA system relies on the aileron deflections only. In the same pattern as before, when spoilers are included in the alleviation system it is only one at time and never the first two inner spoilers.

Figure 9.25 shows the optimized values of the hold time and threshold. It is interesting to notice that for the first two gust lengths the optimal threshold was 0.3 g and the WRBM was not alleviated in these cases. However, from the analysis of the GLA system with threshold

---

[3] The same problem was approached using a random initial value for the optimizing process. Results are not presented here for the sake of brevity and can be found in Appendix D. However, this case proved the sensitivity of the solution to the initial point. In fact, the optimal solution found could not benefit the WRBM alleviation as much as the GLA system presented here. Specifically, it was unable to alleviate any gust load for H < 58 m as the optimal threshold value tended to converge to the highest value of the domain boundaries, settling to 0.4 g.

of $n_z = 0.2$ g, it is known that the WRBM for these gust length values can be alleviated. The analysis of this result proves once again that, although a global optimizer will converge to the global optimum in an infinite time, for a time-limited problem the choice for the initial point plays a crucial role in the search of the optimal solution. The optimum hold time value oscillates around 1.5 s while the optimal threshold mostly settles around 0.3 g. In three cases it instead assumes the maximum value of 0.4 g in the effort to delay the deployment of the

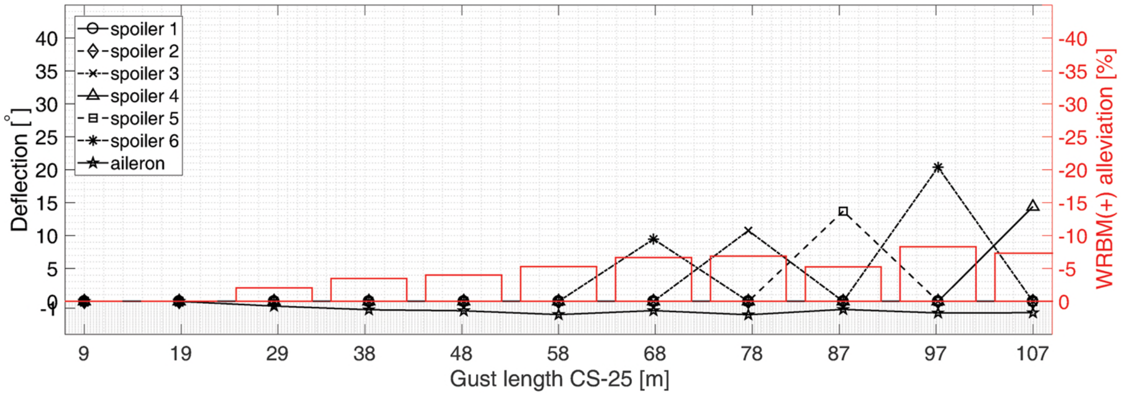

Fig. 9.24.: Variable τ and threshold: HARTEN *true* optimized deflections.

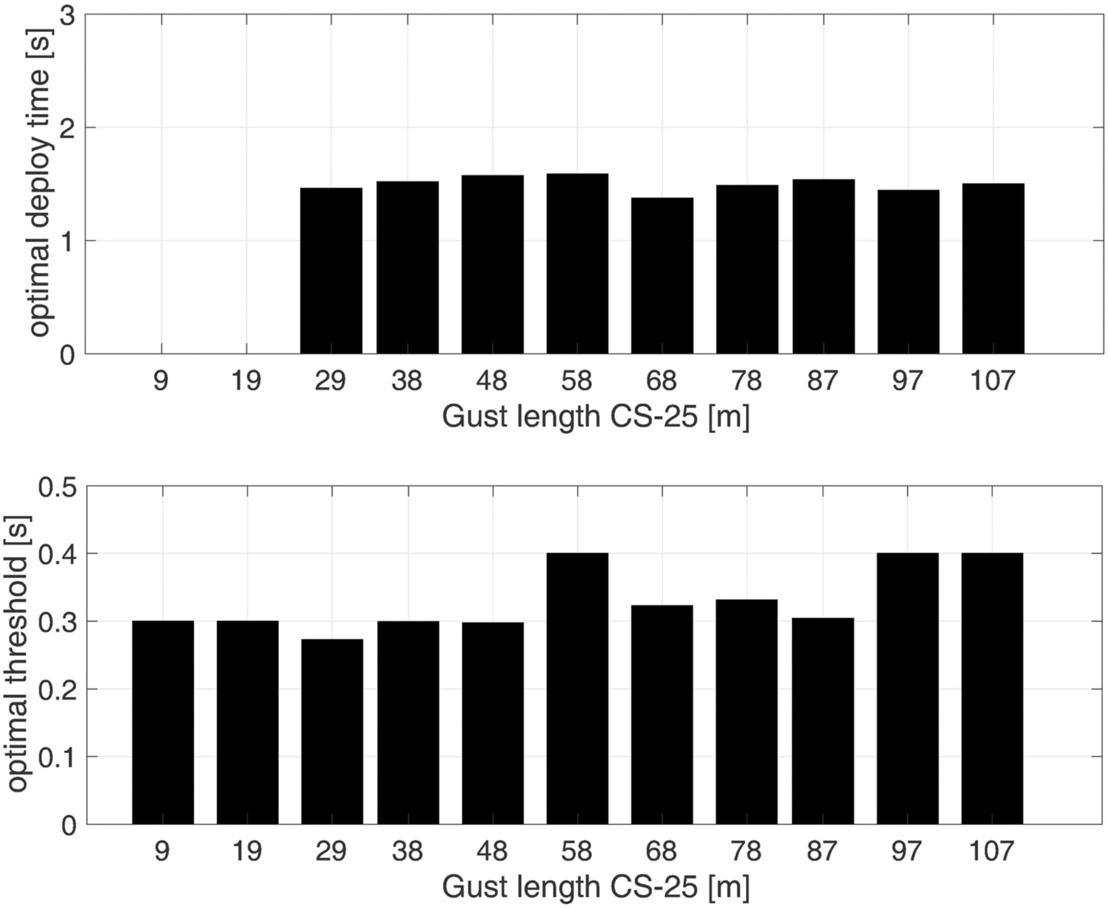

Fig. 9.25.: Variable τ and threshold: optimized hold time and threshold values.

control surfaces. Actually, the best GLA performance and improvement from the reference case happens to be with this value of the threshold.

Overall, the enhanced GLA system performs better than all other configurations considered until now. However, it was seen that the solution is highly sensitive to the initial conditions.

9.3.2 Two-threshold enhanced GLA

The idea behind the second enhanced GLA system option was to delay the end of the GLA action to after the load factor was below a new introduced second threshold. Figure 9.26 shows the GLA system working principle. The first original threshold, the one that activates the the GLA system, is constant and set to 0.3 g. Once n_z crosses it, the GLA system is activated. Now, differently from before, n_z is monitored. The conditions for the GLA system to turn off is the n_z to stay below the newly introduced second threshold for a minimum prescribed time, τ, continuously. The condition is given as:

$$GLA\,off \quad if \quad n_z < \bar{n}_z^{2nd\,thr} \quad for \quad \Delta t > \tau \tag{9.41}$$

The optimization problem is again formally stated as for the previous introduced enhanced GLA system, but the value of τ refers in this case to the hold time the signal is required to stay below the second threshold, $\bar{n}_z$, which is itself a free parameter to optimize. Therefore, only the lower threshold is defined as a parameter to be optimized.

Figure 9.27 shows the WRBM alleviation plot for the optimized solution. The WRBM alleviation is in line with the reference GLA and does not improve the performance of system. An improvement in the second peak alleviation is seen for most of the gust lengths. However, this aspect does not justify the increase in the GLA system complexity. The impact of the GLA system on the vertical load factor is minimal up to H = 58 m and in line with the reference case for other gust lengths. The deflection of spoilers and ailerons is shown in Figure 9.28.

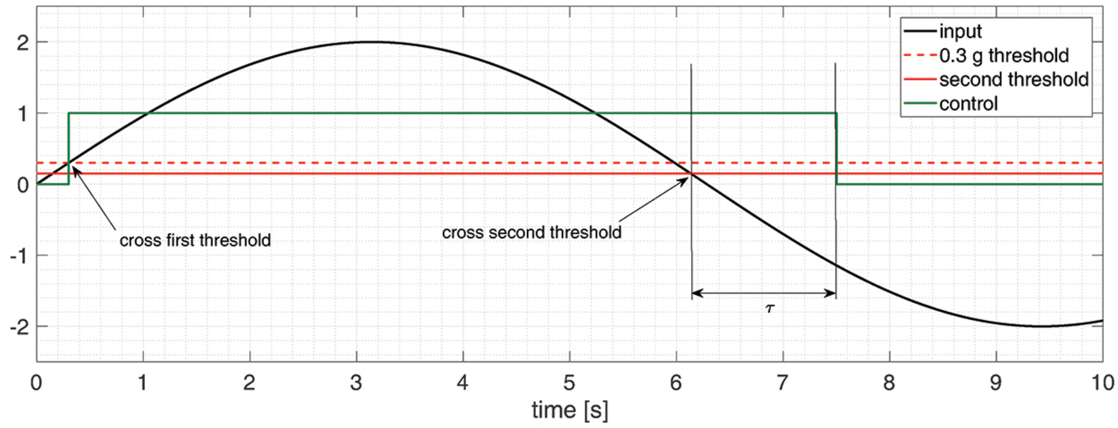

Fig. 9.26.: Second threshold GLA system principles.

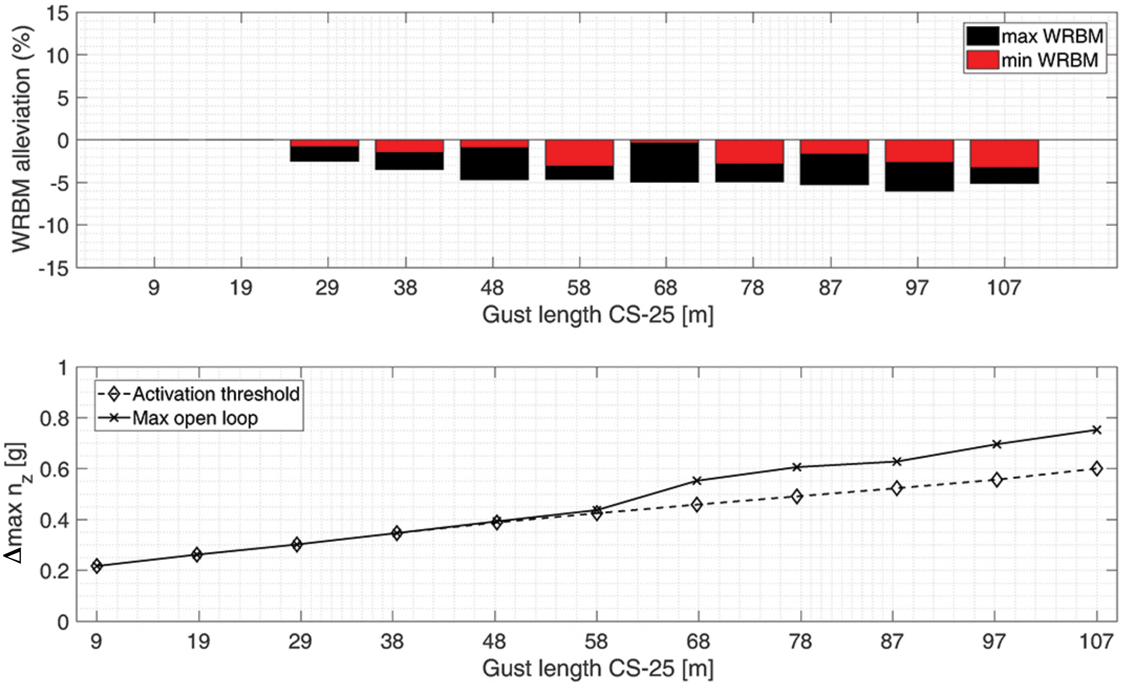

Fig. 9.27.: Second threshold: HARTEN WRBM alleviation plot (top) and maximum load factor increment Δn_z (bottom) for optimized control surfaces deflection against gust lengths.

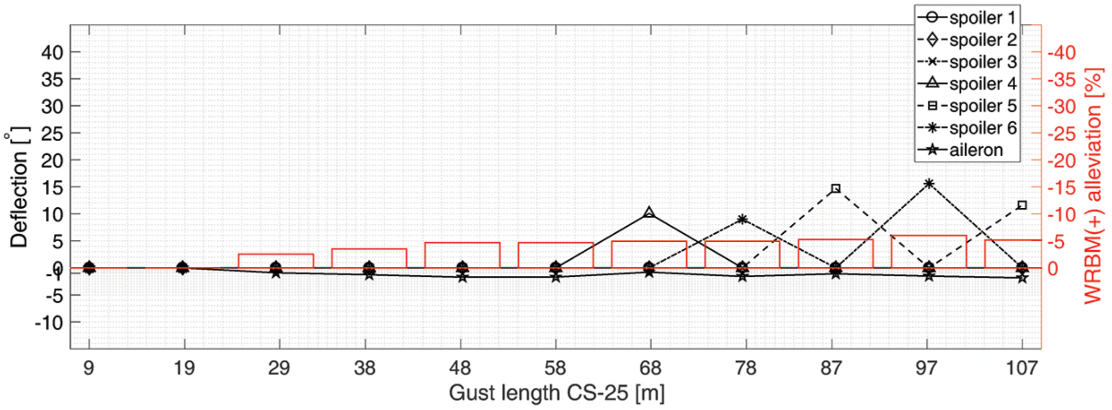

Fig. 9.28.: Second threshold: HARTEN *true* optimized deflections.

As all the other cases, while ailerons are always deployed, outer spoilers are deployed again only for the highest values of the gust length.

Finally, the hold time and the second threshold value are shown in Figure 9.29. The second threshold is often close to the activation threshold of 0.3 g. This aspect limits the potential of this strategy as the closer the second threshold is to the activation threshold, the more the current GLA system converges to the reference one. One optimal value of the threshold was found to be 0.38 g, at H = 97.2 m. Thus, in this case, the GLA system behaves potentially as the reference one. To support this theory, hold time values are close to the reference values, showing the tendency of the solution to *converge* to the optimal reference GLA system.

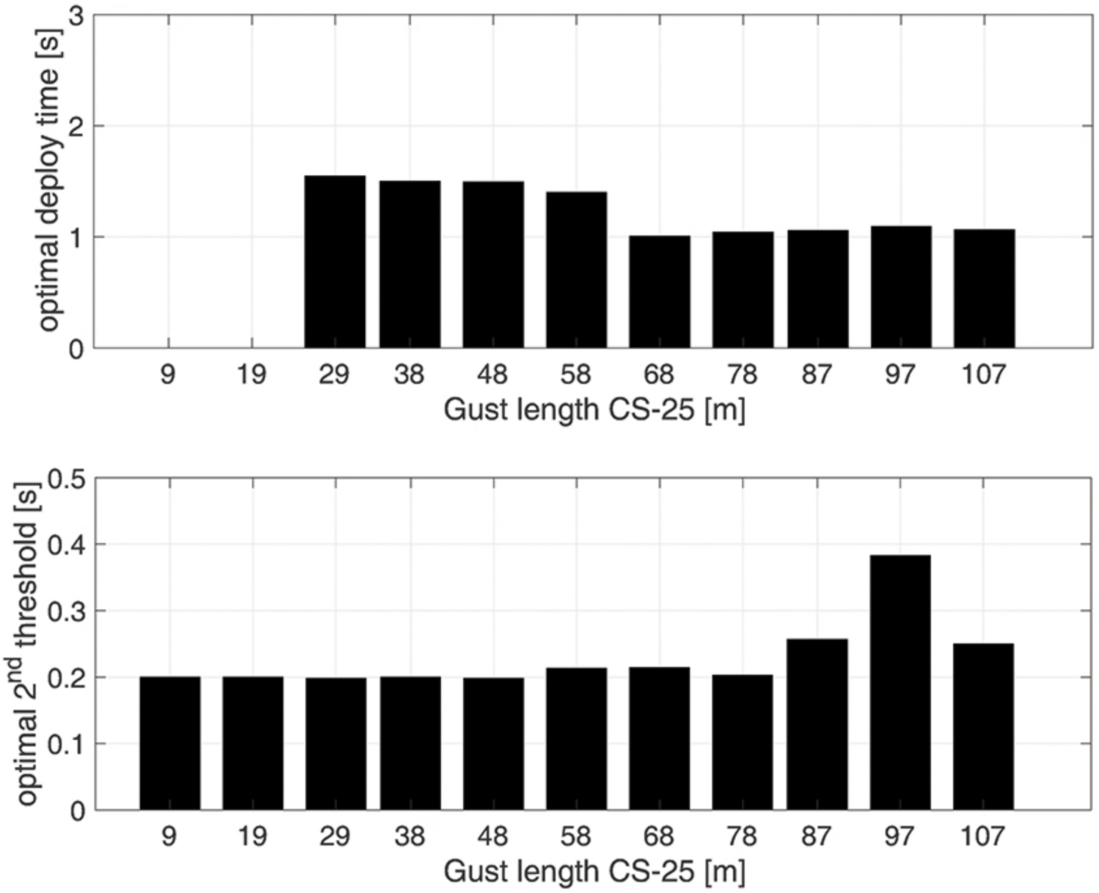

Fig. 9.29.: Second threshold: optimized hold time and threshold values.

9.4 Discussion

This chapter proposed an open-loop GLA system as an alternative to a closed-loop system for HARW aircraft. Different open-loop GLA strategies were proposed and evaluated. For each of the GLA configurations proposed, 11 different 1-cosine discrete gusts responses were assessed using the HARW HARTEN concept aircraft as test bed. The data analysis focused on the alleviation of the wing root bending moment and estimated the change of the vertical load factor to ensure it did not exceed 1.5 g.

The application of the method proposed in this chapter for the optimum GLA must consider some limitations:

- the optimal solution depends on the gust lengths, thus the system must be able to detect the magnitude of the gust profile. Two possible solutions might be implemented to overcome this problem. The first would be to consider the local angle of attack at the wing nose. The velocity profile induced by the gust, w_g, is known. Therefore, the $\Delta\alpha$ associated with a specific gust profile can be estimated as:

$$\Delta\alpha = \frac{w_g}{V} \tag{9.42}$$

Hence, the angle of attack can then be related to the gust profile through $\Delta\alpha$. However, this specific GLA system is based on the estimation of the nose acceleration. Thus, the gust profile might be evaluated looking at the gradient of the load factor profile. Figure 9.30 shows the load factor associated with two gust profiles, 9 m and 107 m, and their gradients. While the system is monitoring the load factor to detect the gust encounter through the use of an accelerometer, it could estimate its gradient in real time. Turning the GLA system on when $n_z >$ threshold value, the right GLA system dataset can be selected based on the calculated gradient.

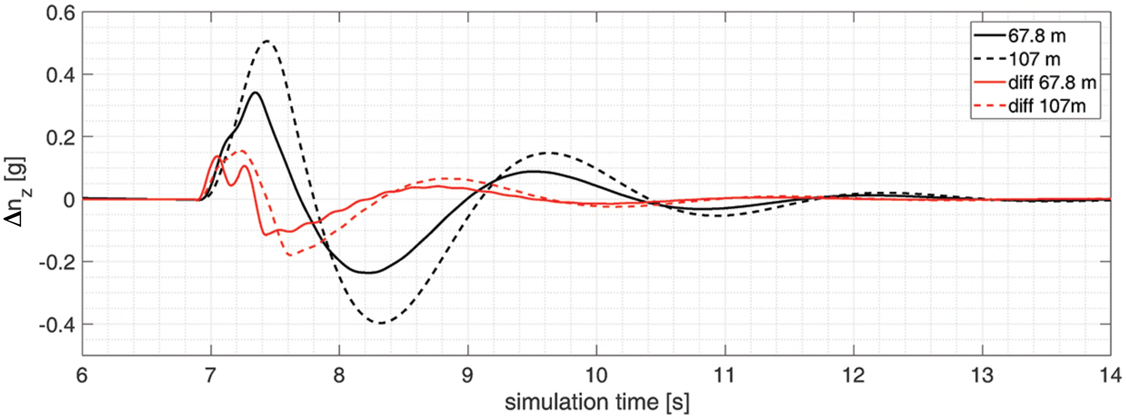

Fig. 9.30.: Load factor increment (black) and gradient estimation (red).

- The study is specific to the described mass distribution and overall weight. In order to consider more cases, the study can be extended to multiple weight configuration.
- The 1-cosine gust is just an approximation of the real scenario, which is better represented by a stochastic turbulence model.

By extending the analysis to more cases and tuning the numerical model of the aircraft, the outcome of this study can be further improved and is perhaps worthy of industrial consideration. The WRBM alleviation for the different strategies against the gust lengths is given in Table 9.4.

Although while considering specific gust lengths the highest alleviation for each gust gradient value, H, is distributed across the different GLA systems considered, overall, it was established that the most effective GLA system is the one that implements constant hold time (case I, $\tau = 1.5$ s, Δn_z threshold equal to 0.3 g). The WRBM alleviation effectiveness varies over the gust length domain. However, for case I, the GLA system is able to alleviate the WRBM by a minimum of 2.5% to a maximum of 7.2%. When considering the enhanced GLA systems, optimizing the hold time and threshold values does improve performance of the GLA with respect to the reference case (maximum WRBM alleviation of 8.3%), while introducing a second threshold increases the level of complexity of the system without clearly affecting performance of the GLA system when compared to the reference case.

Gust length	Case I	Case II	Case III	Case IV	Case V	Case VI
9 m	-	-	-	-0.6 (-0.4)	-	-
18.8 m	-	-	-	-1.5 (-1.0)	-	-
28.6 m	-2.5 (-1.7)	-2.3 (-1.2)	-9.1 (+11.1)	-2.4 (-1.6)	-2.1 (-1.4)	-2.5 (-0.8)
38.4 m	-3.5 (-2.4)	-3.0 (-2.2)	-2.8 (+0.7)	-3.6 (+0.4)	-3.5 (-2.4)	-3.5 (-1.5)
48.2 m	-4.1 (-2.8)	-3.2 (-3.0)	-3.6 (+0.9)	-3.7 (-0.4)	-4.0 (-2.3)	-4.7 (-0.9)
58.0 m	-4.5 (-3.2)	-4.5 (-4.5)	-4.3 (+1.2)	-3.8 (+0.2)	-5.3 (-1.7)	-4.6 (-3.5)
67.8 m	-7.2 (-0.3)	-4.4 (-1.2)	-2.8 (+1.7)	-3.9 (-0.5)	-6.7 (-2.8)	-5.0 (-0.3)
77.6 m	-4.7 (-1.4)	-4.8 (-0.8)	-5.4 (+8.4)	-8.1 (+1.1)	-7.0 (-4.1)	-4.9 (-2.8)
87.4 m	-5.4 (-1.5)	-5.3 (-0.6)	-2.7 (+2.0)	-4.7 (-0.6)	-5.2 (-1.9)	-5.3 (-1.6)
97.2 m	-6.2 (-2.0)	-5.2 (+3.2)	-2.7 (+2.1)	-4.3 (+0.0)	-8.3 (-2.8)	-6.0 (-2.6)
107 m	-5.9 (-0.7)	-6.5 (+0.0)	-2.5 (+2.2)	-6.8 (+7.2)	-7.3 (-2.6)	-5.1 (-3.2)

Tab. 9.4.: Summary of the GLA system effectiveness for different configurations: I) reference, II) rigid, III) $\tau = 2.5$ s, IV) threshold = 0.2 g V) optimized τ and threshold and VI) second threshold. In brackets the alleviation for the negative peak.

The analysis of the results stresses the impact of ailerons on the GLA performance. In fact, while spoilers are not always adopted by the optimal GLA system, ailerons are always present. However, as discussed previously in this thesis, the adoption of ailerons on HARW configurations may lead to aeroelastic and aerodynamics instabilities such as aileron reversal and adverse yaw. A possible solution to overcome this limitation could be the adoption of spoilers as primary control surface for GLA purposes along with a strong limitation on the use of outboard ailerons (eventually neglecting the use of ailerons implemented in GLA systems). Such strategy could see the use of outer spoilers for load alleviation and inner spoilers (never used in the current study in the optimal GLA system) used for ride quality control. Further investigation into this topic is however recommended as beyond the scope of this study due to time constraint.

Furthermore, results showed in this chapter are limited to the assumptions made on gust design and GLA system assessment method. The gust considered for the study was uniform and designed following the CS-25 requirements. Therefore the analysis did not considered a possible extension of the maximum value of the gust gradient considered or the impact of non-uniform gust load along the wingspan. As mentioned in the previous point, all these aspect are worth to be considered although they were not addressed here due to time constraint and their assessment is suggested in possible future studies.

Conclusions and further work

10

A general conclusion regarding the findings of the thesis is given herein. For more in-depth conclusions on specific aspects of the work, the reader is referred to the single chapters where the topic is discussed. The reader can find discussion of aim and objectives of this work in Section 1.1. The study focused on the assessment of the impact of flexible High Aspect Ratio Wings (HARW) on commercial aircraft. It was shown that aircraft aerodynamic performance can benefit by the adoption of higher Aspect Ratios (AR) because of the reduction in induced drag. However, such longer and slender wings are structurally very flexible, lowering considerably the first wing mode frequency. These wing configurations are therefore characterised by a possible overlap of the wing structural dynamics with the rigid-body dynamics. The overlap of the two dynamics may results in the deterioration of flight qualities, Flight Control System (FCS) performance or in higher Wing Root Bending Moment (WRBM) among the other aspects to be considered. Due to their aerodynamic characteristics, HARW are widely used in vehicles where the aerodynamic design is driven by achieving the highest aerodynamic efficiency possible, like gliders or High Altitude Long Endurance (HALE) aircraft, with values of aspect ratio up to 40. However, the average modern civil aircraft aspect ratio is not higher than 10, hence the need to consider the impact of HARW on this category of aircraft. The approach followed by this study is a mix of numerical analysis and experimental validation. Main findings of the study are given here provided as follows:

- Firstly, a comprehensive assessment of the impact of structural flexibility on the aircraft flight dynamics was made. The study was carried out by enhancing a rigid-body point-mass model, the Generic Transport Model (GTM), a 5.5% scaled numerical model publicly available and provided by NASA. Augmentation of the model dynamics was performed by adapting the approach discussed by Waszak and Schmidt [179] and adding a new set of second order differential equations designed to model the aircraft flexibility. Four symmetric and one asymmetric mode were used to simulate the aircraft flexible structural response. Interaction between the flexible structure and rigid-body dynamics was implemented through the force and moment terms. Therefore, a sensitivity analysis was run, where both structural natural frequencies and damping were varied within a specified range. Results have shown that reducing the gap between the aircraft first bending structural mode and the short period mode frequencies leads to an unstable behaviour of the aircraft response when an external disturbance acts on the aircraft. The analysis has shown as well that the impact of such interference is more severe on the longitudinal response rather than the lateral one. Instead, the impact of structural damping on the aircraft dynamics is less significant. Results are however affected by the fact that flexible forces and moments had to be scaled down to be compatible with the size of the GTM model as modal characteristics of the GTM are not publicly accessible. Therefore, the choice of the scaling factors has to be carefully design. However, the use of scaling factors is not necessary if modal characteristics of the aircraft are available.

- Secondly, a series of wind tunnel tests was run in order to evaluate reliability and limitations of low-fidelity numerical aeroelastic framework in modelling highly flexible structures. The BEAm Reduction and Dynamic Scaling programme (BEaRDS) aimed to provide a methodology to design, dynamically scale, manufacture and test highly flexible wing tunnel models. The wing model was designed following the common spar and skin approach, where a metal spar sustains the structural load and the skin guarantees the aerodynamic shape and transfers the load from the external surface to the spar. However, a novel approach to the skin manufacturing was applied: the skin was 3D printed with PolyJet technology which allowed to provide a continuous aerodynamic shape without the typical gaps necessary for flexible models to allow bending. It was as well proved that such approach is able to limit the impact of the skin stiffness below 12.5% with respect to the overall model stiffness. Two models were manufactured and tested within the BEaRDS programme: the first model was used as proof-of-concept of the new skin manufacturing technology. The model was tested in the Cranfield Weybridge wind tunnel at 27 m/s ($\mathrm{Re} = 3.5\mathrm{e}5$) and $\alpha = 6^\circ$. The model span was 0.840 m, with $\mathrm{AR} = 12$. Aim of the test was to show that the skin was able to retain the aerodynamic shape and sustain the load under large deformation. The wing tip model deflected 32% of the model span. The second model was built following the same spar and skin approach. The model was tested in the Cranfield 8x6 ft wind tunnel in the speed range of 20 m/s to 40 m/s ($3.1\mathrm{e}5 < \mathrm{Re} < 6.2\mathrm{e}5$) at $-2^\circ < \alpha < 8^\circ$. The model span was 1.5 m and $\mathrm{AR} = 18.8$. Forces and displacements were acquired during the test. Main results showed the importance of modelling follower forces for flexible models. In fact, in the most severe aerodynamic load scenario ($v = 40$ m/s and $\alpha = 8^\circ$), the spanwise force coefficient was $c_S = 0.09$, about 10% of the wing overall C_L and 2.5 times higher than C_D.

  The overall damping was as well estimated for different velocities and $\alpha = 6^\circ$, reaching a maximum of 26.9% at 35 m/s and a minimum of 17.8% at 20 m/s. The aerodynamic damping was estimated to account for a minimum of 61% to a maximum of 74% of the overall damping. Maximum displacement of the wing tip was 13.7% of the model span (0.21 m). In both tests a low-cost acquisition system built with off-the-shelf components was adopted. Core of the system was a Raspberry Pi board able to acquire accelerations and rotations from four MPU6050 IMU sensors. It was shown that for high Signal to Noise ratio (SNR) this system performance are comparable with the one of professional sensors, being however limited in the sampling frequency. Main benefit of the system lies in the small size of the sensors, which are able to fit tiny volumes typical of HARW wing tunnel models.

Limitations of the Cranfield Accelerated Aircraft Loads Model (CA^{2}LM) aeroelastic framework were as well discussed by comparing numerical prediction with experimental results. Main limitation is in the drag estimation which proved to be considerably underestimated by the numerical model. Lift estimation instead is in good agreement in the linear region, being CA^{2}LM unable to model stall. Error on lift increases with the wing deformation due to the absence of spanwise forces estimation.

- Thirdly, a novel method was developed to model the non-linear aerodynamic effects of spoiler deflection into low-fidelity aeroelastic frameworks. The method consists in *adjusting* the lift distribution provided by the strip theory method with empirical data extracted from the ESDU 14004 datasheet. The method was implemented in CA^{2}LM where the aircraft is reduced to a series of aerodynamic and structural nodes. Strip theory is used to calculate the aerodynamic load in each aerodynamic and node. The spoiler modelling method takes the overall ΔC_L due to the spoiler deflection, estimated through an extensive series of wind tunnel tests and provided by the ESDU 14004, and distribute this value over the wing surface taken by the spoiler. In this way the spoiler effect can be included in the framework's aerodynamic load estimation and impacts the lift distribution along the wing. Results has shown that the method is able to locally change the lift distribution according to the spoiler deflection while benefiting of the low-fidelity characteristics of the CA^{2}LM framework, such as the ability to run real-time and the low computational power required to run.
- Finally, an open-loop GLA system for HARW commercial aircraft was designed and evaluated across a range of discrete gust gradients at one specific flight point (v = 200 m/s and h = 26000 ft). The aircraft used for the analysis was the High Aspect Ratio Technology ENabler (HARTEN) concept aircraft developed in partnership with the project partners. HARTEN is a medium-range single-aisle HARW aircraft. Prior to the GLA design, an assessment of the HARTEN flight dynamics response to gust input was carried out applying CS-25 requirements for the discrete gust input design. Two different configurations were simulated for this purpose: a rigid-wing configuration and a highly-flexible one. Results showed that for the flexible configuration the tuned gust is able to excite not only rigid-body dynamics but structural dynamics as well due to shift of the wing structural frequencies towards the rigid-body frequency domain. Therefore it was suggested that CS-25 gust requirements may need to be extended to include rigid body/structure interaction.

Although the literature showed that close-loop GLA are effective in reducing the Wing Root Bending Moment (WRBM), the open-loop strategy was chosen in order to design an industrially viable controller able to be implemented with available technologies. The open-loop GLA system was designed to deploy a combination of spoilers and ailerons for a fixed time independent from the gust load (known as hold time, τ) once the vertical load factor crossed a specific threshold. The design process explored different combinations of these parameters by implementing an optimization routine which aimed to minimize the WRBM by optimizing control surfaces deflections. Results show that the impact of the aileron is of primary importance in the GLA system performance. For the purpose of the GLA system design, both the first and second WRBM peak were targeted in the optimizer cost function. Results has shown that the alleviation system performance varies depending on hold time and threshold values. However, except few cases, the open-loop GLA system is always able to reduce the first peak across the gust gradient range tested. Best GLA performance is achieved when hold time and the threshold values were optimized along with control surfaces deflection. In this case, the WRBM alleviation goes from a minimum of 2.4% to a maximum of 8.1% with respect to the non-alleviated scenario.

10.1 Further work

Although aim and objectives were met, several aspects of the work can be improved. Therefore, a list of future works is suggested here to continue the work described in this thesis:

- The spoiler model must be validated against flight data or experimental data. Limitations of the spoiler modelling must be evaluated. In particular the evaluation of the effect of having multiple spoilers and the way this impacts the ΔC_L generated by each spoiler requires to be addressed.

- To include a Flight Control System (FCS) into the CA^{2}LM framework in order to account for the pitch dynamics of the aircraft induced by the gust encounter coupled with the GLA system action.

- To be able to include the acceleration term in the GLA optimization cost function. A possible option may be to run a multi-objective optimization problem and compromise between the WRBM alleviation and the passenger comfort (vertical acceleration).

- Reduce the size of the HARTEN aileron and perform a new GLA parameters optimization to find a new set of optimal control gains. Smaller ailerons should results in a heavier use of the spoilers.

- To consider the use of spoilers as primary control surfaces assuming no ailerons are present on the wing. Such analysis would explore the benefit of using a distributed set of control surfaces along the wingspan for manoeuvring and load alleviation purposes and would address aerolastic instabilities problems related to the use of ailerons on highly flexible wings.

- Include servos and control surfaces in the XB-2 model for future wind tunnel tests. The use of control surfaces would allow test input design for frequency analysis and assessment of the flexible structure aeroelastic response.

- To assess the impact of non-uniform gusts on HARW aircraft response. The effect of non-uniform gust may have a more relevant impact on HARW than on conventional wing due to the influence of flexibility on the aircraft response. Evaluation of the impact of non-conventional gust input on the aircraft flight qualities may suggest the need of extending CS-25 requirements to consider rigid body/flexible wing interaction typical of HARW configurations.

10.2 Dissemination of research

10.2.1 Journal articles

- **Alessandro Pontillo**, Sezsy Yusuf, Guillermo Lopez, Dominic Rennie and Mudassir Lone, *"Investigating pitching moment stall through dynamic wind tunnel test"*, Proceeding IMechE Part G: Journal of Aerospace Engineering (2019), doi: 10.1177/0954410019861853

  Experimental characterisation of aircraft dynamic stall can be a challenging and complex system identification activity. In this article, the authors present a method that combines dynamic wind tunnel testing with parameter estimation techniques to study the nonlinear pitching moment dynamics of a 1/12 scale Hawk model undergoing moment stall. The instrumentation setup allows direct calculation of angular acceleration terms, such as pitch acceleration, and avoids post-processing steps involving differentiation of signals. Data collected from tests,carried out at 20 m/s and 30 m/s, are used for a brief aerodynamic analysis of the observed stall hysteresis. Then an output-error-based parameter estimation process is used to parametrise dynamic stall models and furthermore, illustrate that in a scenario where the model's heave motion is constrained. The observed nonlinear behaviour arises from the nonlinear angle of attack and linear pitch rate components.

- Momtaz Abadir, Sezsy Yusuf, **Alessandro Pontillo** and Mudassir Lone, *Parameters estimation methodology for the nonlinear rolling motion of finned cylindrical body*, Aerospace, Science and Technology (2019), Volume 84, Pages 782-798, doi: 0.1016/j.ast.2018.11.013

  Identification of nonlinear roll dynamics of finned cylindrical bodies is a critical step when assessing free motion stability and trajectories of aerially dispensed munitions or decoys. In this paper the authors present a parameter estimation process that focuses on identifying nonlinear aerodynamic models that characterize the roll dynamics of a cylindrical body with wrap around fins using data from a series of dynamic wind tunnel tests. This is a three step approach that combines ordinary least squares, stepwise regression and the augmented output-error method, and it is initially tested using simulation data corrupted by white Gaussian noise and then applied to the wind tunnel data. Roll and roll rate dynamics were captured through a series of high angle of attack free-to-roll tests carried out at an airspeed of corresponding to a Reynolds number of 800,000. The results and discussion in this paper demonstrate how simulation can be used to develop and mature a system identification routine followed by its assessment through wind tunnel test data. It is shown that high order nonlinear models with up to 14 terms can be *parameterized to provide high levels of agreement with roll and roll rate dynamics observed in the dynamic wind tunnel tests.*

- Martin A. Carrizales, Gaétan Dussart, Vilius Portapas, **Alessandro Pontillo** and Mudassir Lone, *Verification of a low fidelity fast simulation framework through RANS simulations*, CEAS Aeronautical Journal (2019), doi: 10.1007/s13272-019-00409-x

  Verification and validation of simulation models are critical steps in engineering. This paper aims at verifying the suitability of reduced order aerodynamic models used in an aeroservoelastic framework designed to analyze the flight dynamics of flexible aircraft, known as the Cranfield Accelerated Aircraft Loads Model. This framework is designed for rapid assessment of aircraft configurations at the conceptual design stage. Therefore, it utilizes or relies on methods that are of relatively low fidelity for high computational speeds, such as modified strip theory coupled with Leishmann-Beddoes unsteady aerodynamic model. Hence, verification against higher order methods is required. Although low fidelity models are widely used for conceptual design and loads assessments, the open literature still lacks a comparison against higher fidelity models. This work focuses on steady-trimmed flight conditions and investigates the effect of aerodynamic wing deformation under such loads on aerodynamic performance. Key limitations of the reduced order models used, namely fuselage and interference effects, are discussed. The reasons for the overall agreement between the two approaches are also outlined.

- Joris R Duran, James F Whidborne, Martin Carrizales and **Alessandro Pontillo**, *A benchtop flight control demonstrator*, International Journal of Mechanical Engineering Education (2019), doi: 10.1177/0306419019852688

  A feedback control demonstrator is described. The demonstrator is intended for the demonstration of control principles applied to flight control of fixed-wing aircraft and hence is suitable for aeronautical programmes. The demonstrator consists of a two degree-of-freedom wing assembly where the wing is free to pitch in an airflow provided by a simple, benchtop wind tunnel. The second degree-of-freedom is provided by a hinged elevator which is actuated by a servomotor. The wing pitch angle is measured with a potentiometer attached to a pivot shaft, thus allowing feedback control of the elevator pitch to be implemented. The aerodynamics of the wing are modelled, the wind tunnel design is described and computational fluid dynamics analysis presented. An embedded controller that implements a proportional-integral-derivative controller and a graphical interface has been developed. Some details of these are also given.

10.2.2 Book chapter

- Gaétan Dussart, Vilius Portapas, **Alessandro Pontillo** and Mudassir Lone, *Flight Dynamic Modelling and Simulation of Large Flexible Aircraft*, Flight Physics - Models, Techniques and Technologies, IntechOpen (2018), doi: 10.5772/intechopen.71050

The drive for aircraft efficiency and minimum environmental impact is requiring the aerospace industry to generate technologically innovative and highly integrated aircraft concepts. This has changed the approach towards conceptual design and highlighted the need for modular low fidelity aircraft simulation models that not only capture conventional flight dynamics but also provide insight into aeroservoelasticity and flight loads. The key aspects that drive the need for modularity are discussed alongside integration aspects related to coupling aerodynamic models, flight dynamic equations of motion and structural dynamic models. The details of developing such a simulation framework are presented and the utility of such a tool is illustrated through two test cases. The first case focuses on aircraft response to a gust that has a spanwise varying profile. The second investigates aircraft dynamics during control surface failure scenarios. The Cranfield Accelerated Aeroplane Loads Model (CA2LM) forms the basis of the presented discussion.

10.2.3 Conference papers

- **Alessandro Pontillo**, Gaétan X. Dussart, Mohammad M. Lone, Dominique Fleischmann and Etienne Coetzee, *Control surface modelling for fast simulation of large flexible aircraft*, 2017 AIAA Atmospheric Flight Mechanics Conference, 9-13 January 2017, AIAA 2017-0017, doi: 10.2514/6.2017-0017

- **Alessandro Pontillo**, David Hayes, Gaétan X. Dussart, Guillermo E. Lopez Matos, Martin A. Carrizales, Sezsy Y. Yusuf and Mohammad M. Lone, *Flexible high aspect ratio wing: Low cost experimental model and computational framework*, 2018 AIAA Atmospheric Flight Mechanics Conference, 8-12 January 2018, AIAA 2018-1014, doi: 10.2514/6.2018-1014

- Sezsy Yusuf, **Alessandro Pontillo**, Simone Weber, David Hayes and Mudassir Lone, *Aeroelastic Scaling for Flexible High Aspect Ratio Wings*, AIAA Scitech 2019 Forum, AIAA 2019-1594, 7-11 January 2019, doi: 10.2514/6.2019-1594

- David Hayes, **Alessandro Pontillo**, Sezsy Y. Yusuf, Mohammad M. Lone and James Whidborne, *High Aspect Ratio Wing Design Using the Minimum Exergy Destruction Principle*, AIAA Scitech 2019 Forum, AIAA 2019-1592, doi: 10.2514/6.2019-1592

- Martin Carrizales, Gaetan Dussart, Vilius Portapas, **Alessandro Pontillo** and Mudassir Lone, *Comparison of reduced order aerodynamic models and RANS simulations for whole aircraft aerodynamics*,2018 AIAA Atmospheric Flight Mechanics Conference, 8-12 January 2018, AIAA 2018-0773 doi: 10.2514/6.2018-0773

Bibliography

[1]A. Abbas, J. De Vicente, and E. Valero. „Aerodynamic technologies to improve aircraft performance“. In: *Aerospace Science and Technology* 28.1 (2013), pp. 100–132 (cit. on pp. 1, 2, 9–12).

[2]F. Afonso, J. Vale, E. Oliveira, F. Lau, and A. Suleman. „A review on non-linear aeroelasticity of high aspect-ratio wings“. In: *Progress in Aerospace Sciences* 89 (2017) (cit. on pp. 14, 21).

[3]T. Allen, B. Sexton, and M. J Scott. „SUGAR Truss Braced Wing Full Scale Aeroelastic Analysis and Dynamically Scaled Wind Tunnel Model Development“. In: *56th AIAA/ ASCE/ AHS/ ASC Structures, Structural Dynamics, and Materials Conference* January (2015), pp. 1–8 (cit. on pp. 2, 14).

[4]J. D. Anderson. *Fundamental of aerodynamics - 5th edition*. McGrow-Hill, 2010 (cit. on pp. 1, 12, 138).

[5]S. Andrews. „Modelling and Simulation of Flexible Aircraft: Handling qualities and active load control“. PhD thesis. Cranfield University, 2011, p. 292 (cit. on pp. 22, 57, 59, 61–63, 65).

[6]S. Andrews and A. Cooke. „An Aeroelastic Flexible Wing Model for Aircraft Simulation“. In: *48th AIAA Aerospace Sciences Meeting Including the New Horizons Forum and Aerospace Exposition* January (2010) (cit. on pp. 22, 57, 63).

[7]Anon. *AVL - Athena Vortex Lattice*. `http://web.mit.edu/drela/Public/web/avl/`. Accessed: 26/07/2019 (cit. on p. 70).

[8]Anon. *Comparison of Six Solvers - MathWorks documentation*. `https://uk.mathworks.com/help/gads/example-comparing-several-solvers.html`. Accessed: 26/04/2019 (cit. on p. 175).

[9]Anon. *CS-25 Large Aeroplanes, Amendment 22*. EASA, 2018 (cit. on pp. 27, 166, 178).

[10]Anon. „Flightpath 2050 Europe“. In: *Directorate-General for Research and Innovation and Directorate-General for Mobility and Transport* (2011) (cit. on p. 1).

[11]Anon. *IATA Forecast Predicts 8.2 billion Air Travelers in 2037*. `https://www.iata.org/pressroom/pr/Pages/2018-10-24-02.aspx`. Accessed: 2019-09-23 (cit. on p. 1).

[12]Anon. *Mechanical Analysis Bearings and Screws, Prof Ahmed Kovacevic, City University London*. `http://www.staff.city.ac.uk/~ra600/ME2105/Analysis/ME2104-A-2.pdf`. Accessed: 02/06/2020 (cit. on p. 119).

[13]Anon. *MIL-F-8785c: Flying qualities of piloted airplanes*. US Military Specs, 1982 (cit. on pp. 152, 154).

[14]Anon. *MSC.Nastran 2001 - Quick Reference Guide*. MSC Software Corporation, 2001, p. 1598 (cit. on p. 112).

[15]Anon. *Styles of Wing Construction for Flying Model Aircraft.* `https://www.airfieldmodels.com/information_source/math_and_science_of_model_aircraft/rc_aircraft_design/styles_of_wing_construction.htm`. Accessed: 26/04/2018 (cit. on p. 31).

[16]S. A. Araujo-Estrada and M. H. Lowenberg. „Evaluation of Aircraft Model Upset Behaviour Using Wind Tunnel Manoeuvre Rig“. In: *AIAA SciTech 2015-0750* January (2015), pp. 1–20 (cit. on p. 30).

[17]S. A. Araujo-Estrada, Z. Gong, M. Lowenberg, S. Neild, and M. Goman. „Wind Tunnel Manoeuvre Rig : A Multi-DOF Test Platform for Model Aircraft“. In: *Aiaa Scitech 2016-2119* January (2016), pp. 1–11 (cit. on p. 30).

[18]P Argüelles, M Bischoff, and P Busquin. „European Aeronautics: A vision for 2020. Report of the Group of Personalities“. In: *Office for Official Publications of the European Communities* January (2001) (cit. on p. 1).

[19]N Baghdadi, M H Lowenberg, and A T Isikveren. „Analysis of Flexible Aircraft Dynamics Using Bifurcation Methods“. In: *Journal of Guidance, Control, and Dynamics* 34.3 (2011), pp. 795–809 (cit. on p. 41).

[20]J. Barlow, H. William, and A. Pope. *Low wind tunnel testing - 3rd ed.* John Wiley and Sons, 1999 (cit. on pp. 104, 132).

[21]R. E. Bartels, R. C. Scott, and B. Allen T.and Sexton. „Aeroelastic Analysis of SUGAR Truss-Braced Wing Wind-Tunnel Model Using FUN3D and a Nonlinear Structural Model“. In: *56th AIAA /ASCE /AHS /ASC Structures, Structural Dynamics, and Materials Conference* January (2015), pp. 1–15 (cit. on p. 14).

[22]Bisplinghoff, R. and Holt, A. and Halfman, R. *Aeroelasticy.* Courier Corporation, 1996 (cit. on pp. 2, 17, 31, 62, 73, 154).

[23]C. Black, K.V. Singh, S. Goodman, A. Altman, and R. Kolonay. „Design, fabrication and testing of 3D printed wings for rapid evaluation of aeroelastic performance“. In: *AIAA/ASCE/AHS/ASC Structures, Structural Dynamics, and Materials Conference, 2018* 210049 (2018), pp. 1–17 (cit. on p. 33).

[24]K. M. Bradley and Droney K. C. *Subsonic Ultra Green Aircraft Research Phase II: N+4 Advanced Concept Development.* Tech. rep. NASA, 2012 (cit. on p. 14).

[25]K. M. Bradley and C. K. Droney. *Subsonic Ultra Green Aircraft Research: Phase I.* Tech. rep. NASA, 2011, p. 207 (cit. on pp. 2, 14).

[26]R. T. Britt, S. B. Jacobson, and T. D. Arthurs. „Aeroservoelastic analysis of the B-2 bomber“. In: *Journal of Aircraft* 37.5 (2000), pp. 745–752 (cit. on p. 17).

[27]Edward L. Burnett, Christopher Atkinson, Jeff Beranek, et al. „NDOF simulation model for flight control development with flight test correlation“. In: *AIAA Modeling and Simulation Technologies Conference 2010* August (2010), pp. 1–14 (cit. on p. 18).

[28]D. E. Calderon, J. E. Cooper, M. Lowenberg, S. A. Neild, and E. B. Coetzee. „Sizing High-Aspect-Ratio Wings with a Geometrically Nonlinear Beam Model“. In: *Journal of Aircraft* 56.4 (2019), pp. 1455–1470 (cit. on pp. 14, 21).

[29]S. Carnduff, S. Erbsloeh, A. Cooke, and M. Cook. „Development of a Low Cost Dynamic Wind Tunnel Facility Utilizing MEMS Inertial Sensors“. In: *46th AIAA Aerospace Sciences Meeting and Exhibit* January (2008), pp. 1–17 (cit. on p. 30).

[30]S. D. Carnduff, S. D. Erbsloeh, A. K. Cooke, and M. V. Cook. „Characterizing Stability and Control of Subscale Aircraft from Wind-Tunnel Dynamic Motion“. In: *Journal of Aircraft* 46.1 (2009), pp. 137–147 (cit. on p. 30).

[31]M. Carrizales, E. Bragado, and M. Lone. „Non-elliptic lift distribution wings to decrease vertical tailplane size in commercial aircraft“. In: *Proceedings of AIAA Scitech Forum, 7-11 January 2019* (2019) (cit. on pp. 70, 136).

[32]M Carrizales, G Dussart, V Portapas, A Pontillo, and M Lone. „Verification of a low fidelity fast simulation framework through RANS simulations“. In: *CEAS Aeronautical Journal* (2019) (cit. on pp. 57, 64).

[33]A. Castrichini, V. Hodigere Siddaramaiah, D. E. Calderon, et al. „Nonlinear folding wing tips for gust loads alleviation“. In: *Journal of Aircraft* 53.5 (2016), pp. 1391–1399 (cit. on p. 29).

[34]A. Castrichini, V. Hodigere Siddaramaiah, D. E. Calderon, et al. „Preliminary investigation of use of flexible folding wing tips for static and dynamic load alleviation“. In: *Aeronautical Journal* 121.1235 (2017), pp. 73–94 (cit. on p. 29).

[35]L. Cavagna, S. Ricci, and L. Travaglini. „NeoCASS: An integrated tool for structural sizing, aeroelastic analysis and MDO at conceptual design level“. In: *Progress in Aerospace Sciences* 57.8 (2011), pp. 621–635 (cit. on p. 68).

[36]L. Cavagna, S. Ricci, and L. Riccobene. „Structural Sizing, Aeroelastic Analysis, and Optimization in Aircraft Conceptual Design“. In: *Journal of Aircraft* 48.6 (2011), pp. 1840–1855 (cit. on p. 68).

[37]J. Cecrdle J.and Malecek. „Design and development of new whirl flutter aeroelastic demonstrator“. In: *55th AIAA/ ASMe/ ASCE/ AHS/ SC Structures, Structural Dynamics, and Materials Conference* January (2014) (cit. on p. 32).

[38]C. E. S. Cesnik and E. L. Brown. „Modelling of High Aspect Ratio Active Flexible Wings for Roll Control“. In: *43rd AIAA/ASME/ASCE/AHS/ASC Structures, Structural Dynamics, and Materials Conference* April (2002), pp. 1–15 (cit. on p. 22).

[39]J. Chambers. *Modeling flight : the role of dynamically scaled free-flight models in support of NASA's aerospace programs.* Tech. rep. NASA SP 2009-575., 2010 (cit. on p. 36).

[40]S. L. Chernyshev, A. Ph Kiselev, and A. P. Kuryachii. „Laminar flow control research at TsAGI: Past and present“. In: *Progress in Aerospace Sciences* 47.3 (2011), pp. 169–185 (cit. on p. 12).

[41]R. C.M. Cheung, D. Rezgui, J. E. Cooper, and T. Wilson. „Testing of folding wing-tip for gust load alleviation in high aspect ratio wing“. In: *AIAA Scitech 2019 Forum* January (2019), pp. 1–15 (cit. on p. 33).

[42]M. Civera, L. Zanotti Fragonara, and C. Surace. „Using Video Processing for the Full-Field Identification of Backbone Curves in Case of Large Vibrations“. In: *Sensors* 19 (2019) (cit. on pp. 90, 93).

[43]A R Collar. „The expanding domain of aeroelasticity“. In: *The Royal Aeronautic Society* (1946) (cit. on pp. 2, 16, 17).

[44]H. Consigny, A. Gravelle, and R. Molinaro. „Aerodynamic characteristics of a two-dimensional moving spoiler in subsonic and transonic flow“. In: *AIAA-83-1809* (1983) (cit. on p. 23).

[45]M. V. Cook. *Flight Dynamics Principles - 3rd Edition.* Oxford, UK: Elsevier, 2013 (cit. on pp. 19, 25, 26, 41, 43, 168, 169).

[46]R. G. Cook, D. E. Calderon, J. E. Cooper, et al. „Worst case gust prediction of highly flexible wings“. In: *58th AIAA/ASCE/AHS/ASC Structures, Structural Dynamics, and Materials Conference, 2017* January (2017) (cit. on p. 28).

[47]M Costes. „Comparison between experimental and computational results for airfoils equipped with a spoiler and a flap“. In: *AIAA-85-5008* (1985) (cit. on p. 23).

[48]K. Cunningham, D. E. Cox, D. G. Murri, and S. E. Riddick. „A Piloted Evaluation of Damage Accommodating Flight Control Using a Remotely Piloted Vehicle“. In: *AIAA Guidance, Navigation, and Control Conference, Guidance, Navigation, and Control and Co-located Conferences.* August. 2011, pp. 1–20 (cit. on p. 36).

[49]A. De Gaspari, S. Ricci, and L. Riccobene. „Design, Manufacturing and Wind Tunnel Validation ofa Morphing Compliant Wing“. In: *25th International Conference on Adaptive Structures and Technologies (ICAST 2014)* January (2014), pp. 1–12 (cit. on p. 32).

[50]J. DeYoung and C. W. Harper. *Theoretical symmetric span loading at subsonic speeds for wings having arbitrary plan form.* Tech. rep. NACA-TR-921, National Advisory Committee for Aeronautics, 1948 (cit. on p. 63).

[51]T. Dodt. *Introducing the 787.* Tech. rep. Boeing - Air Safety Investigation, 2011 (cit. on p. 25).

[52]Earl Dowell, John Edwards, and Thomas Strganac. „Nonlinear Aeroelasticity“. In: *Journal of Aircraft* 40.5 (2003) (cit. on p. 21).

[53]M. Drela. *ASWING 5.99 Techical Description Steady Formulation.* Tech. rep. March. 2015 (cit. on pp. 21, 22).

[54]M. Drela. „Integrated simulation model for preliminary aerodynamic, strucutral and control-law design of aircraft“. In: *AIAA-99-1934* (1999) (cit. on pp. 21, 22).

[55]M. Drela. „Low-Reynolds-number airfoil design for the M.I.T. Daedalus prototype- A case study“. In: *Journal of Aircraft* 25.8 (1988), pp. 724–732 (cit. on pp. 2, 14).

[56]M. Drela. *XFOIL - Subsonic Airfoil Development System.* `https://web.mit.edu/drela/Public/web/xfoil/`. Accessed: 26/07/2019 (cit. on p. 70).

[57]M. Drela. *XFOIL: An Analysis and Design System for Low Reynolds Number Airfoils.* Berlin: Springer, 1989 (cit. on p. 70).

[58]W. Duncan. *Physical Similarity and Dimensional Analysis: An Elementary Treatise.* Edward Arnold and Co, 1953 (cit. on p. 103).

[59]G. Dussart. „On the use of in-flight dihedral wingtip folding systems for large civil aircraft“. PhD thesis. Cranfield University, 2019, p. 475 (cit. on pp. 57, 116).

[60]G. Dussart, M. Lone, and R. Bailey. „Development of a Multi-Directional Manoeuvre for Unified Handling Qualities Investigation“. In: *Aerospace* 6.6 (2019) (cit. on p. 57).

[61]G. Dussart, V. Portapas, A. Pontillo, and M. M. Lone. „Flight Dynamic Modelling and Simulation of Large Flexible Aircraft“. In: *Flight Physics - Models, Techniques and Technologies.* 2018 (cit. on p. 21).

[62]G. Dussart, S. Yusuf, and M. Lone. „Identification of In-Flight Wingtip Folding Effects on the Roll Characteristics of a Flexible Aircraft“. In: *Aerospace* 6.6 (2019) (cit. on pp. 57, 116).

[63]D. J. Ewins. *Modal Testing: Theory, Practice and Application, 2nd Edition.* Philadelphia: Research Studies Press Ltd., 2000 (cit. on p. 127).

[64]Kubica F and T. Livet. „Flight control law synthesis for a flexible aircraft“. In: *AIAA Guidance, Navigation and Control Conference* 2 (1994) (cit. on p. 65).

[65]N. Fezans and H. Joos. „Combined Feedback and LIDAR-Based Feedforward Active Load Alleviation“. In: *AIAA Atmospheric Flight Mechanics Conference, 5-9 June 2017* June (2017) (cit. on p. 29).

[66]F. Fonte, A. De Gaspari, L. Riccobene, et al. „Development of a wind tunnel model for active flutter suppression studies“. In: *AIAA Scitech 2019 Forum* January (2019), pp. 1–14 (cit. on pp. 31, 32).

[67]F. Fonte, S. Ricci, and P. Mantegazza. „Gust Load Alleviation for a Regional Aircraft Through a Static Output Feedback“. In: *Journal of Aircraft* 52.5 (2015) (cit. on pp. 28, 29).

[68]C. Garcua, D. Prett, and M. Morari. In: *Automatica* 25.3 (1989), pp. 335–348 (cit. on pp. 2, 29).

[69]A. Gatto. „Application of a Pendulum Support Test Rig for Aircraft Stability Derivative Estimation“. In: *Journal of Aircraft* 46.3 (2009), pp. 927–934 (cit. on pp. 30, 33, 79).

[70]A. Gatto and M. Lowenberg. „Evaluation of a Three Degree of Freedom Test Rig for Stability Derivative Estimation“. In: *Journal of Aircraft* 43.6 (2006), pp. 1747–1761 (cit. on p. 30).

[71]H. Giesseler, M. Kopf, T. Faulwasser, P. Varutti, and R. Findeisen. „Gust Load Alleviation Based on Model“. In: *IFASD-2013-24A* (2013), pp. 1–18 (cit. on p. 29).

[72]H. Giesseler, M. Kopf, P. Varutti, T. Faulwasser, and R. Findeisen. „Model Predictive Control for Gust Load Alleviation“. In: *4th IFAC Nonlinear Model Predictive Control Conference* January (2012), pp. 27–32 (cit. on p. 29).

[73]G. C. Greene. „An entropy method for induced drag minimization“. In: *SAE Transactions* 98.1 (1989), pp. 1771–1780 (cit. on p. 13).

[74]I. M. Gregory, C. Cao, V. V. Patel, and N. Hovakirnyan. „Adaptive Control Laws for Flexible Semi-Span Wind Tunnel Model of High-Aspect Ratio Flying Wing“. In: *Proceedings of the AIAA Guidance, Navigation, and Control Conference and Exhibit* August (2007), pp. 1–11 (cit. on pp. 31, 32).

[75]S. Haghighat, H. Liu, and J. Martins. „Application of model predictive control to gust load alleviation systems“. In: *AIAA Atmospheric Flight Mechanics Conference* August (2009) (cit. on p. 29).

[76]S. Haghighat, H. Liu, and J. Martins. „Model-Predictive Gust Load Alleviation Controller for a Highly Flexible Aircraft“. In: *Journal of Guidance, Control, and Dynamics* 35.6 (2012), pp. 1751–1766 (cit. on pp. 3, 29).

[77]D. Hayes. „Exergy Methods for Commercial Aircraft: Integrating the Laws of Thermodynamics into all Disciplines of Aircraft Design“. PhD thesis. Cranfield University, 2018 (cit. on pp. 70, 92, 93, 97, 108).

[78]D. Hayes, M. Lone, J. Whidborne J.and Camberos, and E. Coetzee. „Adopting exergy analysis for use in aerospace“. In: *Progress in Aerospace Science* 93 (2017), pp. 73–94 (cit. on p. 97).

[79]D. Hayes, A. Pontillo, S. Y. Yusuf, M. M. Lone, and J. Whidborne. „High Aspect Ratio Wing Design Using the Minimum Exergy Destruction Principle“. In: *AIAA 2019-1592 - Aeroservoelastic (ASE) Control, Modeling, Simulation, and Optimization* (2019) (cit. on pp. 13, 15, 100, 101).

[80]Hoblit, F. M. *Gust Loads on Aircraft: Concepts and Applications.* AIAA Education Series, 1988 (cit. on pp. 2, 26, 27, 168).

[81]R. M. Hueschen. *Development of the Transport Class Model (TCM) Aircraft Simulation From a Sub-Scale Generic Transport Model (GTM) Simulation.* Tech. rep. August. NASA/TM-2011-217169, 2011, p. 61 (cit. on p. 35).

[82]K. L. Hull D. L. Roger. *B-52E CCV flight test data applicable to parameter estimation.* Tech. rep. Boeing Company, 1975, p. 462 (cit. on p. 172).

[83]A. Irving. „Evaluation of techniques for predicting static aeroelastic effects on flexible aircraft". In: *Journal of Aircraft* 9.1 (1972), pp. 43–47 (cit. on p. 21).

[84]L. James and L. Nash-Webber. *Motorless flight research.* Tech. rep. NACA CR2315, 1972 (cit. on p. 13).

[85]J. R. Jones and C. E.S. Cesnik. „Nonlinear aeroelastic analysis of the X-56A multi-utility aeroelastic demonstrator". In: *15th Dynamics Specialists Conference* January (2016), pp. 1–18 (cit. on p. 18).

[86]T. Jordan, W. Langford, C. M. Belcastro, et al. „Development of a Dynamically Scaled Generic Transport Model Testbed for Flight Research Experiments". In: AUVSI's Unmanned Systems North America 2004 Symposium and Exhibition. 2004 (cit. on p. 35).

[87]T. Jordan, W. Langford, C. Belcastro, et al. *Development of a Dynamically Scaled Generic Transport Model Testbed for Flight Research Experiments.* Tech. rep. NASA Langley Research Center, 2018 (cit. on pp. 35, 36).

[88]T. L. Jordan, W. M. Langford, and J. S. Hill. „Airborne Subscale Transport Aircraft Research Testbed - Aircraft Model Development". In: *Proceedings of the AIAA Guidance, Navigation, and Control Conference and Exhibit.* 2005, pp. 1–12 (cit. on p. 36).

[89]T. L. Jordan, J. V. Foster, R. M. Bailey, and C. M. Belcastro. „AirSTAR: A UAV Platform for Flight Dynamics and Control System Testing". In: June. 25th AIAA Aerodynamic Measurement Technology and Ground Testing Conference. 2006, pp. 1–15 (cit. on p. 36).

[90]R. T. Kawai, D. M. Friedman, and L. Serrano. „Blended Wing Body (BWB) Boundary Layer Ingestion (BLI) inlet configuration and system studies". In: *NASA/CR-2006-214534* (2006), pp. 1–26 (cit. on pp. 1, 11).

[91]J. Kennedy and R. Eberhart. „Particle Swarm Optimization". In: *Proceedings of the IEEE International Conference on Neural Networks* (1995), pp. 1942–1945 (cit. on p. 175).

[92]V. Kibens and W. W. Bower. „An overview of active flow control applications at the boeing company". In: *2nd AIAA Flow Control Conference* July (2004), pp. 1–17 (cit. on p. 12).

[93]T. Kimberly. „Tilt Sensing Using Linear Accelerometers". In: *Freescale semiconductor* Rev 2 (2007) (cit. on p. 89).

[94]S.A. Kravchenko. „Wing tip lifting surfaces aerodynamic design and comparative analysis". In: *AIAA-1995-3909* (1995) (cit. on p. 12).

[95]I. Kroo. „Drag due to lift: concepts for predicion and reduction". In: *Annual Review of Fluid MEchanics* 33 (2001), pp. 587–617 (cit. on p. 13).

[96]F. W. Lanchester. *Aerodynamics, constituting the first volume of a complete work on aerial flight.* London: A. Constable & Co. Ltd., 1907, p. 476 (cit. on p. 13).

[97]C. Lanczos. „An iteration method for the solution of the eigenvalue problem of linear differential and integral operators". In: *Journal of Research of the National Bureau of Standards* 45.5 (1950) (cit. on p. 113).

[98]J Leishman and T Beddoes. „A generalised model for airfoil unsteady aerodynamic behaviour and dynamic stall using the indicial method“. In: *42nd Annual forum of the American Helicopter Society. Washigton DC* (1986) (cit. on p. 62).

[99]J. G. Leishman. „Indicial lift approximations for two-dimensional subsonic flow as obtained from oscillatory measurements“. In: *Journal of Aircraft* 30.3 (1993), pp. 340–351 (cit. on p. 63).

[100]J. G. Leishman. „Unsteady lift of a flapped airfoil by indicial concepts“. In: *Journal of Aircraft* 31.2 (1994), pp. 288–297 (cit. on pp. 62, 65).

[101]J. G. Leishman and K. Q. Nguyen. „State-space representation of unsteady airfoil behavior“. In: *AIAA Journal* 28.5 (1990), pp. 836–844 (cit. on pp. 62, 63).

[102]R. Liebeck, M. Page, and B. Rawdon. „Blended-wing-body subsonic commercial transport“. In: *36th AIAA Aerospace Sciences Meeting and Exhibit* (1998) (cit. on p. 10).

[103]R. H. Liebeck. „Design of the Blended Wing Body Subsonic Transport“. In: *Journal of Aircraft* 41.1 (2004), pp. 10–25 (cit. on pp. 1, 10).

[104]Yi Liu, Changchuan Xie, Chao Yang, and Jialin Cheng. „Gust response analysis and wind tunnel test for a high-aspect ratio wing“. In: *Chinese Journal of Aeronautics* 29.1 (2016), pp. 91–103 (cit. on pp. 30–32, 66, 73, 123, 127).

[105]E. Livne. „Aircraft active flutter suppression: State of the art and technology maturation needs“. In: *Journal of Aircraft* 55.1 (2018), pp. 410–450 (cit. on pp. 18, 20, 172).

[106]M. Lone. „Pilot modelling for airframe loads analysis“. PhD thesis. Cranfield University, 2013 (cit. on p. 57).

[107]M. Lone and C. Alastair. „Pilot-model-in-the-loop simulation environment to study large aircraft dynamics“. In: *Journal of Aerospace Engineering* 3.277 (2014), pp. 637–650 (cit. on p. 57).

[108]M. Lone and G. Dussart. „Impact of spanwise non-uniform discrete gusts on civil aircraft loads“. In: *Aeronautical Journal* 123.1259 (2019), pp. 93–120 (cit. on p. 28).

[109]M. Lone, C. K. Lai, A. Cooke, and J. Whidborne. „Framework for Flight Loads Analysis of Trajectory-Based Manoeuvres with Pilot Models“. In: *Journal of Aircraft* 51.2 (2014), pp. 555–568 (cit. on p. 57).

[110]M. H. Love, P. S. Zink, P. A. Wieselmann, and H. Youngren. „Body freedom flutter of high aspect ratio flying wings“. In: *Collection of Technical Papers - AIAA/ ASME/ ASCE/ AHS/ ASC Structures, Structural Dynamics and Materials Conference* 3.April (2005), pp. 1808–1830 (cit. on p. 22).

[111]M. H. Lowenberg and H. L. Kyle. „Development of a Pendulum Support Rig Dynamic Wind Tunnel Apparatus“. In: *Aerospace Engineering* August (2002), pp. 1–10 (cit. on pp. 33, 79).

[112]Z. Lyu and J. Martins. „Aerodynamic design optimization studies of a blended-wing-body aircraft“. In: *Journal of Aircraft* 51.5 (2014), pp. 1604–1617 (cit. on p. 11).

[113]M D Mack, H C Seetharam, W G Kuhn, and J T Bright. „Aerodynamics of spoiler control devices“. In: *AIAA-79-1873* (1979) (cit. on pp. 22–24).

[114]Y. Madhwal and Z. Avdeeva. „Planning in Aircraft Industry based on prediction of Air Traffic“. In: *Procedia Computer Science* 122 (2017), pp. 1047–1054 (cit. on p. 1).

[115]B. S. de Mattos, A. P. Macedo, and D. H. da Silva Filho. „Considerations about winglet design“. In: *21st AIAA Applied Aerodynamics Conference* June (2003) (cit. on p. 12).

[116]E. Mezura-Montes and C. A. Coello. „Particle Swarm Optimization“. In: *Constraint-handling in nature-inspired numerical optimization: Past, present and future* (2011), pp. 173–194 (cit. on p. 175).

[117]P. Minguet and J. Dugundji. „Experiments and analysis for composite blades under large deflections Part I: Static behavior“. In: *AIAA Journal* 28.9 (1990), pp. 1573–1579 (cit. on p. 32).

[118]P. Minguet and J. Dugundji. „Experiments and analysis for composite blades under large deflections Part II: Dynamic behavior“. In: *AIAA Journal* 28.9 (1990), pp. 1573–1579 (cit. on p. 32).

[119]C. Nam, Y. Kim, and J. B. Layton. „Active Aeroelastic Wing Design For Gust Load Alleviation and Flutter Suppression“. In: *AIAA-97-1265* (1997), pp. 729–737 (cit. on p. 29).

[120]N. Nguyen, E. Ting, and S. Lebofsky. „Aeroelastic Analysis of Wind Tunnel Test Data of a Flexible Wing with a Variable Camber Continuous Trailing Edge Flap (VCCTEF)“. In: *AIAA 2015-1405 - 56th AIAA/ ASCE/ AHS/ ASC Structures, Structural Dynamics, and Materials Conference* January (2015), pp. 1–28 (cit. on p. 33).

[121]N. Nguyen, N. Precup, J. U. Sr, et al. „Experimental Investigation of a Flexible Wing with a Variable Camber Continuous Trailing Edge Flap Design“. In: *32nd AIAA Applied Aerodynamics Conference, AIAA AVIATION Forum*. June. 2014, pp. 1–37 (cit. on p. 36).

[122]N. Nguyen, M. Field, K. Trinh, et al. „Nonlinear Aeroelasticity of a Flexible Wing Structure Coupled with Aircraft Flight Dynamics“. In: *53rd AIAA/ASME/ASCE/AHS/ASC Structures, Structural Dynamics and Materials Conference, Structures, Structural Dynamics, and Materials and Co-located Conferences*. April. 2012 (cit. on p. 36).

[123]T. E. Noll, J. M. Brown, M. E. Perez-Davis, et al. „Investigation of the Helios Prototype Aircraft Mishap Volume I Mishap Report National Oceanic and Atmospheric Administration and“. In: *NOAA* I.January (2004), p. 100 (cit. on p. 24).

[124]A. M. Pankonien, G. W. Reich, N. Lindsley, and B. Smyers. „3D-Printed Wind Tunnel Flutter Model“. In: *58th AIAA/ ASCE/ AHS/ ASC Structures, Structural Dynamics, and Materials Conference* January (2017), pp. 1–17 (cit. on p. 33).

[125]M. J. Patil and D. H. Hodges. „Flight Dynamics of Highly Flexible Flying Wings“. In: *AIAA Atmospheric Flight Mechanics Conference and Exhibit* 43.6 (2006), pp. 1790–1799 (cit. on pp. 2, 25).

[126]M.J. Patil, D. H. Hodges, and C. E. S. Cesnik. „Nonlinear Aeroelasticity and Flight Dynamics of High-Altitude Long-Endurance Aircraft“. In: *Journal of Aircraft* 38.1 (2001), pp. 88–94 (cit. on pp. 2, 18, 25).

[127]J. Pattinson. „Development and evaluation of a wing tunnel manoeuvre rig“. PhD thesis. University of Bristol, 2010 (cit. on p. 79).

[128]J Pattinson and M H Lowenberg. „Characterisation of wind tunnel observed , large-amplitude pitch limit-cycles“. In: *AIAA Atmospheric Flight Mechanics Conference* August (2011), pp. 1–25 (cit. on p. 30).

[129]J. Pattinson, M. H. Lowenberg, and M. G. Goman. „Investigation of Poststall Pitch Oscillations of an Aircraft Wind-Tunnel Model“. In: *Journal of Aircraft* 50.6 (2013), pp. 1843–1855 (cit. on p. 30).

[130]J. Pattinson, M. H. Lowenberg, and M. G. Goman. „Multi-Degree-of-Freedom Wind-Tunnel Maneuver Rig for Dynamic Simulation and Aerodynamic Model Identification“. In: *Journal of Aircraft* 50.2 (2013), pp. 551–566 (cit. on pp. 30, 79).

[131]Pedersen, M. E. *Good Parameters for Particle Swarm Optimization*. Luxembourg: Hvass Laboratories, 2010 (cit. on p. 175).

[132]B. R Perkin and L. L. Erickson. *FLEXSTAB - A computer program for the prediction of loads and stability and control of flexible aircraft.* Tech. rep. 9. NASA CR-114712, 1974 (cit. on p. 21).

[133]A. Pontillo, G. Dussart, D. Fleischmann, M. Lone, and E. Coetzee. „Control surface modelling for fast simulation of large flexible aircraft“. In: *AIAA Atmospheric Flight Mechanics Conference, AIAA SciTech Forum, (AIAA 2017-0017)* (2017) (cit. on p. 62).

[134]V. Portapas. „Handling qualities of high aspect ratio wing aircraft“. PhD thesis. Cranfield University, 2018, p. 335 (cit. on pp. 17, 20, 57).

[135]V. Portapas, C. Alastair, and M. Lone. „Modelling framework for flight dynamics of flexible aircraft“. In: *Aviation* 20.4 (2016), pp. 173–182 (cit. on pp. 20, 22, 57).

[136]L. Prandtl. „Applications of modern hydrodynamics to aeronautics“. In: *Journal of the Franklin Institute* 193.3 (1922), p. 431 (cit. on p. 13).

[137]L. Prandtl. *Theory of lifting surface.* NACA TN 9, 1918 (cit. on pp. 13, 116).

[138]J. S. Przemieniecki. *Theory of Matrix Structural Analysis.* Dover Publications, Inc., 1985, p. 468 (cit. on pp. 68, 70, 108).

[139]N. Qin, A. Vavalle, A. Le Moigne, et al. „Aerodynamic studies for blended wing body aircraft“. In: *9th AIAA/ISSMO Symposium on Multidisciplinary Analysis and Optimization* September (2002), pp. 1–11 (cit. on p. 11).

[140]G. J. Rabadan, N. P. Schmit, T. Pistner, and W. Rehm. „Airborne lidar for automatic feedforward control of turbulent in-flight phenomena“. In: *Journal of Aircraft* 47.2 (2010), pp. 392–403 (cit. on pp. 3, 29).

[141]G. Redeker and G. Wichmann. „Forward sweep - A favorable concept for a laminar flow wing“. In: *Journal of Aircraft* 28.2 (1991), pp. 97–103 (cit. on p. 11).

[142]S. Ricci, A. De Gaspari, L. Riccobene, and F. Fonte. „Design and Wind Tunnel Test Validation of Gust Load Alleviation Systems“. In: *58th AIAA/ASCE/AHS/ASC Structures, Structural Dynamics, and Materials Conference* January (2017), pp. 1–12 (cit. on pp. 2, 28, 29).

[143]S. Ricci, A. De Gaspari, F. Fonte, et al. „Design and wind tunnel test validation of gust load alleviation systems“. In: *58th AIAA/ASCE/AHS/ASC Structures, Structural Dynamics, and Materials Conference, 2017* January (2017), pp. 1–12 (cit. on pp. 3, 31, 32).

[144]A. Ricciardi, R. A. Canfield, M. Patil, C. A Eger, and Ned J. L. „Nonlinear Aeroelastic Scaled Model Optimization Using Equivalent Static Loads“. In: *54th AIAA/ ASME/ ASCE/ AHS/ ASC Structures, Structural Dynamics, and Materials Conference* (2013) (cit. on p. 31).

[145]A. P. Ricciardi, R. A. Canfield, M. J. Patil, and N. Lindsley. „Nonlinear Aeroelastic Scaled-Model Design“. In: *Journal of Aircraft* 53.1 (2016), pp. 20–32 (cit. on p. 31).

[146]A. P. Ricciardi, R. P. Canfield, M. J. Patil, and N. Lindsley. „Nonlinear Aeroelastic Scaled-Model Design“. In: *Journal of Aircraft* 53.1 (2016), pp. 20–32 (cit. on pp. 68, 103).

[147]A. P. Ricciardi, C. A. G. Eger, R. A. Canfield, and M. J. Patil. „Nonlinear Aeroelastic-Scaled-Model Optimization Using Equivalent Static Loads“. In: *Journal of Aircraft* 51.6 (2014), pp. 1842–1851 (cit. on pp. 68, 103).

[148]RH Ricketts and RV Doggett. *Wind-tunnel experiments on divergence of forward-swept wings.* Tech. rep. NASA-TP-1685, 1980 (cit. on p. 11).

[149]K. L. Roger, G. E. Hodges, and L. Felt. „Active flutter suppression-A flight test demonstration“. In: *Journal of Aircraft* 12.6 (1975), pp. 551–556 (cit. on p. 17).

[150]J Roskam and A. Dusto. „A method for predicting longitudinal stability derivatives of rigid and elastic airplanes“. In: *Journal of Aircraft* 6.6 (1969), pp. 525–531 (cit. on p. 21).

[151]J Roskam and D L Kohlman. „Spoilers for roll control of light airplanes“. In: *AIAA-74-861* (1974) (cit. on p. 23).

[152]M H Sadraey. *Aircraft design: a system engineering approach.* Wiley, 2012 (cit. on pp. 116, 219, 220).

[153]Sadraey, M. H. *Aircraft Design: A Systems Engineering Approach.* John Wiley and Sons, 2012 (cit. on pp. 17, 29, 152).

[154]W. S. Saric, H. L. Reed, and D. W. Banks. „Flight Testing of Laminar Flow Control in High-Speed Boundary Layers“. In: *Meeting on Enhancement of NATO Military Flight Vehi- cle Performance by Management of Interacting Boundary Layer Transition and Separation* October 2004 (2004), pp. 4–7 (cit. on p. 12).

[155]D. K. Schmidt. *Modeling and Model Semplification of Aeroelastic Vehicles: an Overview.* Tech. rep. NASA Technical Memorandum, 1992 (cit. on p. 37).

[156]David K Schmidt. „Modal Analysis of Flexible Aircraft Dynamics with Handling Qualities Implications“. In: *Journal of Guidance, Control, and Dynamics* 8.2 (1985), pp. 194–200 (cit. on p. 37).

[157]A. Seitz, M. Kruse, T. Wunderlich, J. Bold, and L. Heinrich. „The DLR Project LamAiR: Design of a NLF forward swept wing for short and medium range transport application“. In: *29th AIAA Applied Aerodynamics Conference 2011* June (2011), pp. 1–14 (cit. on pp. 11, 12).

[158]C. M. Shearer and C. E.S. Cesnik. „Nonlinear Flight Dynamics of Very Flexible Aircraft“. In: *Journal of Aircraft* 44.5 (2007), pp. 1528–1545 (cit. on p. 18).

[159]R. J. Simpson, R. Palacios, H. Hesse, and P. Goulart. „Predictive Control for Alleviation of Gust Loads on Very Flexible Aircraft“. In: *55th AIAA/ ASMe/ ASCE/ AHS/ SC Structures, Structural Dynamics, and Materials Conference* January (2014), pp. 1–25 (cit. on p. 29).

[160]J. J. Spillman. „Use of Wing Tip Sails To Reduce Vortex Drag.“ In: *Aeronautical Journal* 82.813 (1978), pp. 387–395 (cit. on p. 12).

[161]W. Su and C. Cesnik. „Nonlinear aeroelasticity of a very flexible blended-wing-body aircraft“. In: *Journal of Aircraft* 47.5 (2010), pp. 1539–1553 (cit. on pp. 11, 14, 18, 30, 133).

[162]W. Su, J. Zhang, and C. E S Cesnik. „Nonlinear aeroelastic modeling and analysis of fully flexible aircraft“. In: *Collection of Technical Papers - AIAA/ASME/ASCE/AHS/ASC Structures, Structural Dynamics and Materials Conference* 7.April (2005), pp. 4472–4498 (cit. on p. 22).

[163]D. Tang and E. H. Dowell. „Experimental and Theoretical Study of Gust Response for High-Aspect-Ratio Wing“. In: *AIAA Journal* 40.3 (2002), pp. 419–429 (cit. on pp. 3, 30–33, 66, 79).

[164]D. Tang and E. H. Dowell. „Limit-cycle hysteresis response for a high-aspect-ratio wing model“. In: *Journal of Aircraft* 39.5 (2002), pp. 885–888 (cit. on pp. 31–33, 66, 79).

[165]D. Tang, A. Grash, and E. H. Dowell. „Gust response for flexibly suspended high-aspect ratio wings“. In: *AIAA Journal* 48.10 (2010), pp. 2430–2444 (cit. on pp. 3, 31, 32).

[166]The Royal Aeronautical Society. „ESDU 07003 - Modelling of wing viscous drag coefficient in shock-free attached flow“. In: *ESDU Series on Aerodynamics* December (2011) (cit. on p. 64).

[167]The Royal Aeronautical Society. „ESDU 14004 - Lift and rolling moment due to spoilers on wings at subsonic speeds with trailing-edge flaps undeployed“. In: *ESDU Series on Aerodynamics* November (2014) (cit. on pp. 24, 155, 156).

[168]The Royal Aeronautical Society. „ESDU 14005 - Lift and rolling moment due to spoilers on wings at subsonic speeds with trailing-edge flaps deployed“. In: *ESDU Series on Aerodynamics* November (2015) (cit. on p. 24).

[169]The Royal Aeronautical Society. „ESDU 70011 - Lift-curve slope and aerodynamic centre position of wings in inviscid supersonic flow“. In: *ESDU Series on Aerodynamics* September 1970 (1995) (cit. on p. 156).

[170]The Royal Aeronautical Society. „ESDU 87024 - Low-speed drag coefficient increment at constant lift due to full-span plain flaps“. In: *ESDU Series on Aerodynamics* August (2006) (cit. on p. 65).

[171]G. O. Thompson and G. J. Kass. „Active flutter suppression an emerging technology“. In: *Journal of Aircraft* 9.3 (1972), pp. 230–235 (cit. on p. 17).

[172]W. T. Thomson. *Theory of the vibration with application - 4th ed.* Stanley Thornes Ltd, 1993 (cit. on p. 142).

[173]S. Timoshenko and J. N. Goodier. *Theory of elasticity.* Third. McGraw-Hill, 1970, p. 567 (cit. on pp. 70, 107).

[174]E. Ting, T. Dao, and N. Nguyen. „Aerodynamic Load Analysis of a Variable Camber Continuous Trailing Edge Flap System on a Flexible Wing Aircraft“. In: *AIAA SciTech Forum.* January. 2015 (cit. on p. 35).

[175]I. Tuzcu. „Unsteady Aeroelasticity of Generic Transport Model“. In: *AIAA Atmospheric Flight Mechanics Conference.* August. 2011 (cit. on p. 36).

[176]M. C. Van Schoor and A. H. Von Flotow. „Aeroelastic characteristics of a highly flexible aircraft“. In: *Journal of Aircraft* 27.10 (1990), pp. 901–908 (cit. on p. 18).

[177]E. Vartio, A. Shimko, C. P. Tilmann, and P. M. Flick. „Structural modal control and gust load alleviation for a SensorCraft concept“. In: *Collection of Technical Papers - AIAA/ ASME/ ASCE/ AHS/ ASC Structures, Structural Dynamics and Materials Conference* 3.April (2005), pp. 1799–1807 (cit. on pp. 31, 32).

[178]Z. Wan and C. E.S. Cesnik. „Geometrically Nonlinear Aeroelastic Scaling for Very Flexible Aircraft“. In: *54th AIAA/ASME/ASCE/AHS/ASC Structures, Structural Dynamics, & Materials Conference* 52.AIAA 2013-1894 (2013), pp. 1–10 (cit. on p. 18).

[179]M. R. Waszak and D. K. Schmidt. „Flight dynamics of aeroelastic vehicles“. In: *Journal of Aircraft* 25.6 (1988), pp. 563–571 (cit. on pp. 18, 39, 195).

[180]M. R. Waszak and D.K. Schmidt. „On the flight dynamics of aeroelastic vehicles“. In: *Astrodynamics Conference, Fluid Dynamics and Co-located Conferences.* 1986 (cit. on pp. 18, 37, 55).

[181]M. R. Waszak, J. B. Davidson, and D. K. Schmidt. *A Simulation study of the Flight Dynamics of Elastic Aircraft - Volume One - Experiment, Results and Analysis.* Tech. rep. NASA Contractor Report 4102, 1987 (cit. on pp. 18, 37, 39).

[182]M. R. Waszak, J. B. Davidson, and D. K. Schmidt. *A Simulation study of the Flight Dynamics of Elastic Aircraft - Volume Two - Data.* Tech. rep. NASA Contractor Report 4102, 1988, p. 223 (cit. on pp. 37, 42).

[183]T. A. Weisshaar. „Divergence of Forward Swept Composite Wings“. In: *Journal of Aircraft* 17.6 (1980), pp. 442–448 (cit. on pp. 11, 12).

[184]J Weissinger. „The lift distribution of swept-back wings“. In: *NACA Report* 1120 (1947), p. 51 (cit. on p. 63).

[185]W. H. Wentz, C. Ostowari, and H. C. Seetharam. „Effects of Design Variables on Spoiler Control Effectiveness, Hinge Moments and Wake Turbulence.“ In: *AIAA-81-0072* (1981), pp. 418– (cit. on p. 24).

[186]B. A. Winther, W. A. Shirley, and R. M. Heimbaugh. „Wind-tunnel investigation of active controls technology applied to a DC-10 derivative“. In: *Journal of Guidance, Control, and Dynamics* 4.5 (1981), pp. 536–542 (cit. on p. 17).

[187]Wright, J. R. and Cooper, J. E. *Introduction to Aircraft Aeroelasticity and Loads, 2nd ed.* John Wiley and Sons, Ltd., 2015 (cit. on pp. 17, 19, 27, 145, 167, 172, 178).

[188]I. Wygnanski. „Boundary layer and flow control by periodic addition of momentum“. In: *4th Shear Flow Control Conference* (1997), pp. 1–38 (cit. on p. 12).

[189]J. I. H. Wykes, M. J. Klepl, and I. J. Brosnan. *Flight Test and Analyses of the B-1 Structural Mode Control System at Supersonic Flight Conditions.* Tech. rep. NASA-CR-170405, 1983 (cit. on p. 17).

[190]John I H Wykes. „Structural dynamic stability augmentation and gust alleviation of flexible aircraft“. In: *AIAA paper* 68-1067 (1968) (cit. on p. 18).

[191]S. Yusuf. „On Scaling and System Identification of Flexible Aircraft Dynamics“. PhD thesis. Cranfield University, 2019, p. 218 (cit. on pp. 57, 68, 70, 86, 97, 101, 104, 121, 123).

[192]S. Yusuf, A. Pontillo, S. Weber, D. Hayes, and M. Lone. „Aeroelastic Scaling for Flexible High Aspect Ratio Wings“. In: *AIAA SciTech Forum, 7-11 January 2019, San Diego* (2019) (cit. on pp. 101, 104, 123).

[193]Zerweckh, S.H., van Flotow, A.H., and J.E. Murray. „Flight Testing a Highly Flexible Aircraft: Case Study on the MIT Light Eagle“. In: *Journal of Aircraft* 27.4 (1988), pp. 342–349 (cit. on p. 14).

[194]Yonghui Zhao, Chengyu Yue, and Haiyan Hu. „Gust load alleviation on a large transport airplane“. In: *Journal of Aircraft* 53.6 (2016), pp. 1932–1946 (cit. on p. 165).

[195]Zhihua Zhou, Dichen Li, Zhengyu Zhang, and Junhua Zeng. „Design and fabrication of a hybrid surface-pressure airfoil model based on rapid prototyping“. In: *Rapid Prototyping Journal* 14.1 (2008), pp. 57–66 (cit. on p. 33).

[196]Weijun Zhu, Xinglei Zhao, Wei Zhang, et al. „Design and evaluation of fully configured models built by additive manufacturing“. In: *AIAA Journal* 52.7 (2014), pp. 1441–1451 (cit. on p. 33).

Appendix: General Transport Model

A

Scaling coefficient c	natural frequencies 1^{st} [Hz]	2^{nd} [Hz]	3^{rd} [Hz]	4^{th} [Hz]	5^{th} [Hz]
1	2.01	2.24	3.37	3.51	1.5
1.5	1.34	1.49	2.25	2.34	1.00
2	1.01	1.12	1.68	1.75	0.75
2.5	0.81	0.89	1.35	1.43	0.60
3	0.67	0.75	1.12	1.17	0.50
3.5	0.57	0.64	0.96	1.00	0.43

Tab. A.1.: List of the structure natural frequencies adopted for the simulation and corresponding scaling coefficient

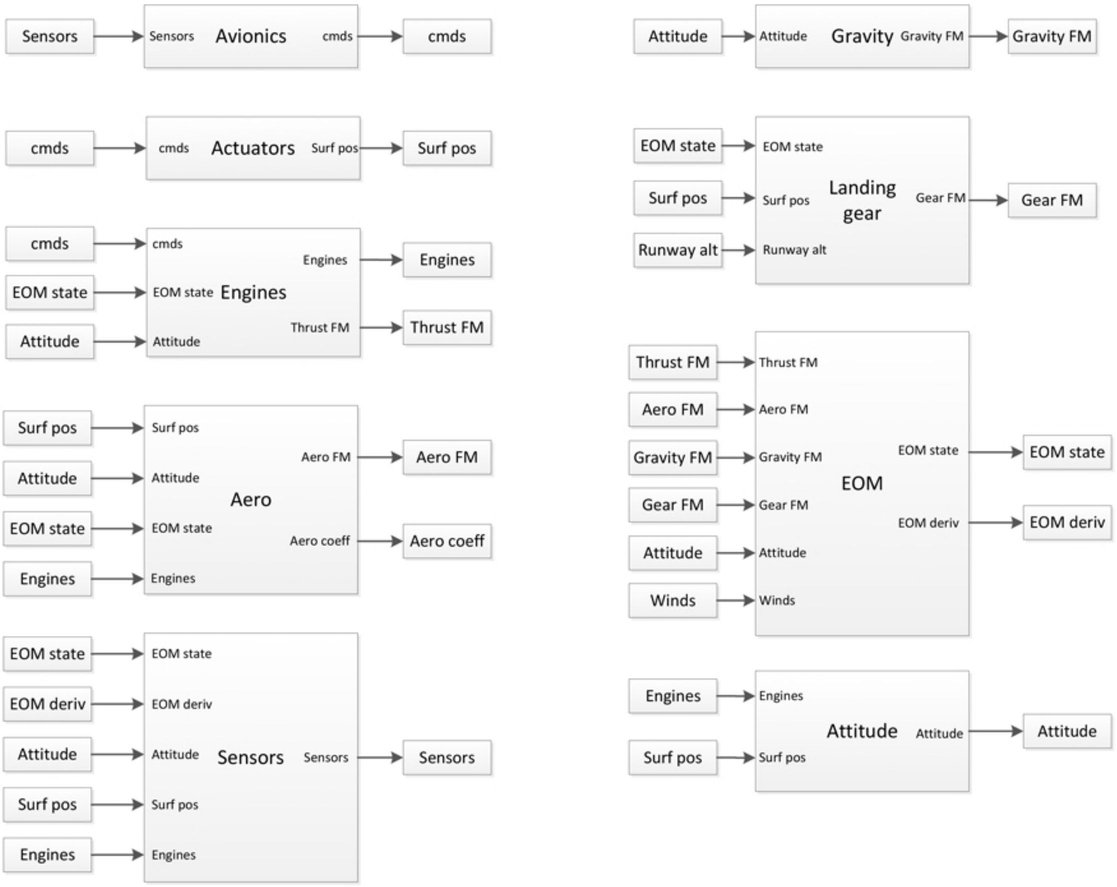

Fig. A.1.: Generic Transport Model Simulink inner loop.

Appendix: XB-2 design

B

Section	EA*10^6 [Pa m^2]	EI_{xx} [Pa m^4]	EI_{zz}*10^3 [Pa m^4]	GJ [Pa m^2]
1	12.5192	175.4235	4.8903	81.0830
2	12.0661	170.8071	4.7133	78.7157
3	11.6171	166.1907	4.5379	76.3483
4	11.1680	161.5743	4.3625	73.9809
5	10.7149	156.9579	4.1855	72.2053
6	10.2659	152.3415	4.0101	69.8379
7	9.8168	147.7251	3.8346	67.4706
8	9.3638	143.1087	3.6577	65.1032
9	8.9147	138.4922	3.4823	62.7358
10	8.4656	133.8758	3.3068	60.3684
11	8.0126	129.2594	3.1299	58.0010
12	7.5635	124.6430	2.9545	55.6336
13	7.1144	121.5654	2.7790	53.2662
14	6.6614	116.9490	2.6021	50.8988
15	6.2123	112.3326	2.4266	48.5314
16	5.7632	107.7162	2.2512	46.7559
17	5.3102	103.0998	2.0743	44.3885
18	4.8611	98.4834	1.8988	42.0211
19	4.4081	93.8670	1.7219	39.6537
20	3.9590	89.2505	1.5464	37.2863
21	3.5099	84.6341	1.3710	34.9189
22	3.0569	80.0177	1.1941	32.5516
23	2.6078	75.4013	1.0186	30.1842
24	2.1587	70.7849	0.8432	27.8168

Tab. B.1.: Spar properties at each node extracted from the numerical stiffness matrix *[K]*.

Section	b	c	a	t
1	0.074	0.003	0.020	0.002
2	0.073	0.003	0.020	0.002
3	0.072	0.003	0.020	0.002
4	0.072	0.003	0.020	0.002
5	0.071	0.003	0.020	0.002
6	0.070	0.003	0.020	0.002
7	0.068	0.003	0.020	0.002
8	0.067	0.003	0.020	0.002
9	0.066	0.002	0.020	0.002
10	0.065	0.002	0.020	0.002
11	0.064	0.002	0.020	0.002
12	0.063	0.002	0.020	0.002
13	0.061	0.002	0.020	0.002
14	0.060	0.002	0.020	0.002
15	0.059	0.002	0.018	0.002
16	0.057	0.003	0.017	0.002
17	0.056	0.003	0.016	0.002
18	0.054	0.004	0.015	0.002
19	0.052	0.005	0.014	0.002
20	0.050	0.006	0.013	0.002
21	0.048	0.007	0.012	0.002
22	0.046	0.009	0.011	0.002
23	0.043	0.012	0.010	0.002
24	0.038	0.015	0.009	0.002

Tab. B.2.: Section properties.

B.1 Control surfaces

Although for this specific test the control surfaces were not used, the XB-2 model was designed to feature two spoilers and one aileron in order to assess the wing response to control surfaces input and to validate GLA strategies developed with any numerical tool. Specifications of the spoiler are given in Table B.3, while ailerons details are provided in Table B.4. The control surfaces are designed to be actuated by servomotors. In order to select the appropriate servo with the right torque, some considerations were made. The servo was chosen based on the torque required by aileron in the case of maximum dynamic pressure. The geometric characteristics of the aileron are listed in Table B.4. The angle of attack provided in Table B.4 represents the target AoA for the XB-2 test. The steps to evaluate the aerodynamic load acting on the surface are provided. As first, the lift distribution over the wing is estimated as shown in Section 6.6.

		Units	**Value**
Spoiler 1	Inboard edge	[%b]	35
	Outboard edge	[%b]	42
	Chord	[m]	0.032
	Area	[m^2]	0.003
Spoiler 2	Inboard edge	[%b]	54
	Outboard edge	[%b]	61
	Chord	[m]	0.037
	Area	[m^2]	0.003

Tab. B.3.: XB-2 spoilers specifications.

	Units	**Value**		**Units**	**Value**
AoA	[deg]	6	ξ^{max}	[deg]	30
MAC	[m]	0.18	**Chord**	[m]	0.03
Inboard edge	[% b]	75	C_{l_α}		2π
Outboard edge	[% b]	95	**S**	[m^2]	0.011

Tab. B.4.: XB-2 aileron characteristics

$$\mu(\alpha_0-\alpha)=\sum_{n=1}^{N}A_n\sin(n\theta_i)\left(1+\frac{\mu n}{\sin\theta_i}\right) \tag{B.1}$$

where

$$\mu=\frac{\bar{C}_i C_{l_\alpha}}{4b}. \tag{B.2}$$

The unknown parameters are the coefficients A_n, while $\bar{C}_i$ is the mean geometric chord, θ is the local lifting-line theory angle and N is the number of nodes along the wing. For XB-2, N=25. The obtained C_l distribution is shown in Figure B.1a. Assuming the lift distribution equally distributed on the surface, the portion of lift acting on the aileron surface is defined as [152]:

$$\bar{L}^a = L\tau_a \tag{B.3}$$

where τ_a is the aileron effectiveness which depends on the aileron-to-wing chord ration and it is shown in Figure B.1b.

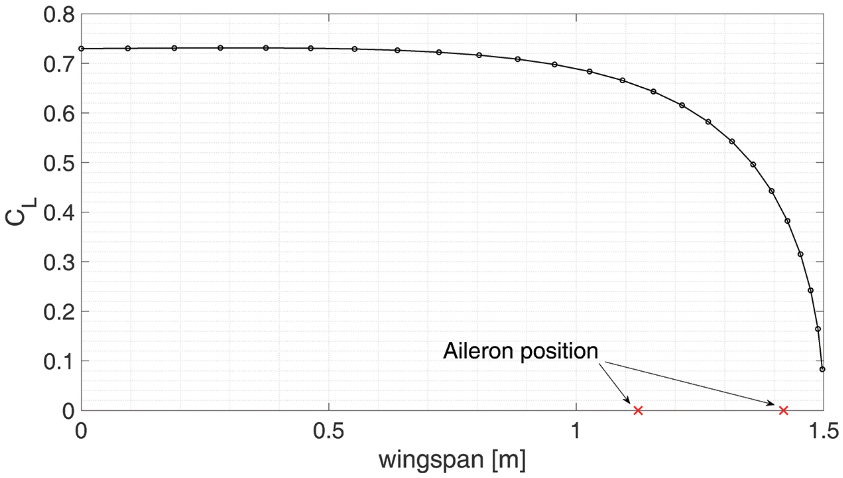

(a) XB-2 lift distribution at 40 m/s and $\alpha = 6°$

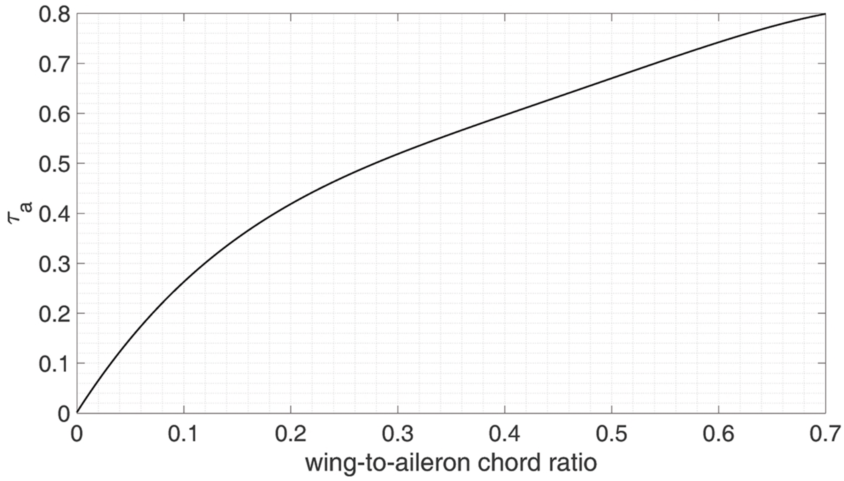

(b) Aileron effectiveness curve (reproduced from [152]).

Fig. B.1.: Lift estimation of the XB-2 aileron section.

The lift just calculated is considered as the lift in *clean* configuration, i.e. with no control surfaces deflected. In addition to this, the extra lift due to the aileron deflection is calculated as:

$$\Delta L = q S^a C_l^a \tag{B.4}$$

where S^a is the aileron area and C_l^a is the lift coefficient of the aileron defined as [152]:

$$C_l^a = C_{l_\xi}^a \tau_a \xi^a. \tag{B.5}$$

where ξ^a is the aileron deflection. The overall lift acting on the aileron is then defined as:

$$L^a = \bar{L}^a + \Delta L \tag{B.6}$$

Assuming the lift acting at the aileron quarter chord (the origin is the leading edge) and the hinge ideally placed on the aileron leading edge line, the moment acting on the aileron is:

$$M = L^a c^a / 4 = 0.3970 \quad \text{Nm} \tag{B.7}$$

	Value
Weight [g]	28.4
Torque @ 4.8 V [N m]	0.7
Torque @ 6 V [N m]	0.86
Speed @ 4.8 V [s/deg]	0.15
Speed @ 6 V [s/deg]	0.12
Dimensions [mm]	30 x 10 x 34.5

Tab. B.5.: TGY-A55H servo motor specifications.

Many assumptions were made in this calculation, such as assuming a constant lift distribution along the chord, while most of the lift is produced at the leading edge; or an elliptic lift distribution along the span, which is clearly a theoretical case. To account for the limitation of the modelling, a *safety* factor of 2 was used. Then, the required torque is:

$$M_r = 2M = 0.7940 \quad \mathrm{Nm} \tag{B.8}$$

Characteristics of the servo must include to have the required torque, to be as small as possible to fit in the tight inner volume of the model and to be as light as possible to not interfere with the wing mass distribution. The chosen servo is the Turnigy^{TM} TGY-A55H. Specifications of the servo are listed in Table B.5.

C

Appendix: XB-2 model manufacturing

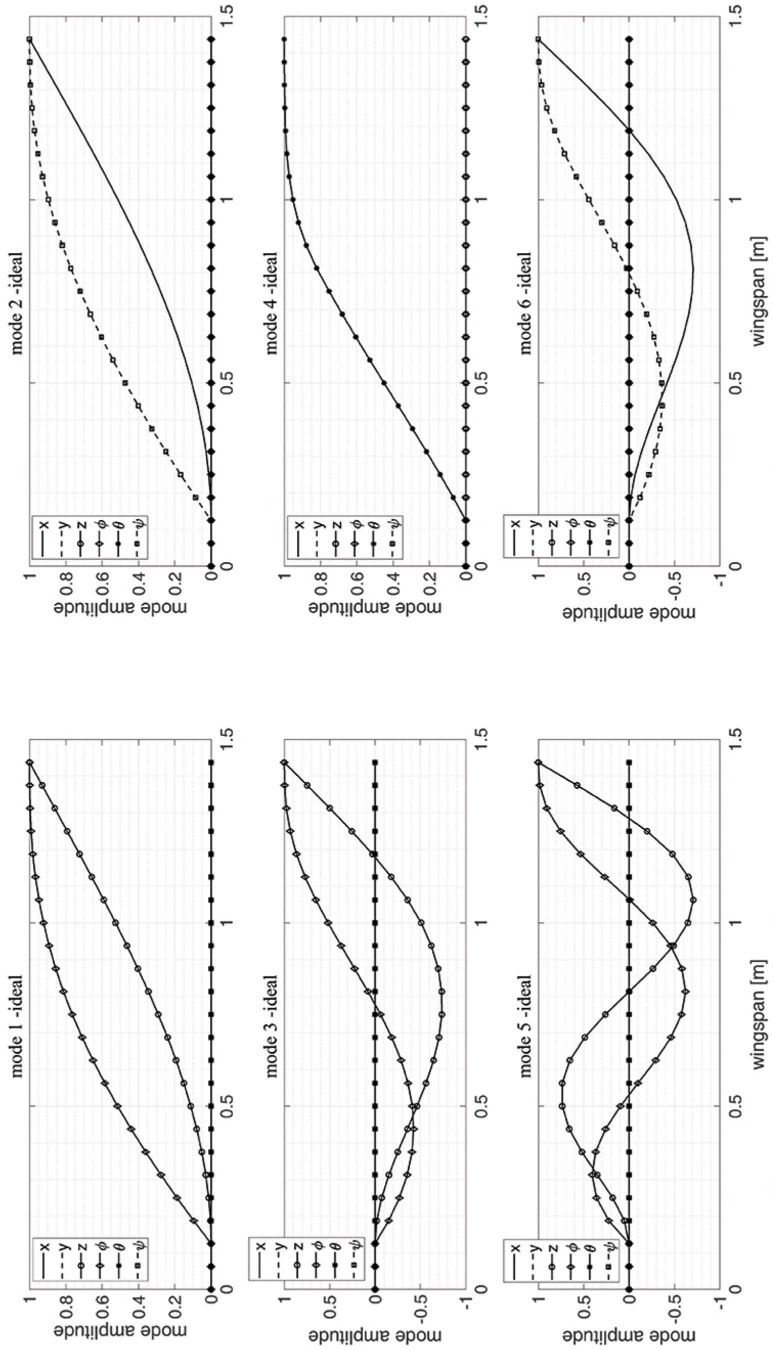

Fig. C.1.: Representation of the 6 degrees of freedom of the ideal spar case for the first six modes. The plot was used to identify the spar modes.

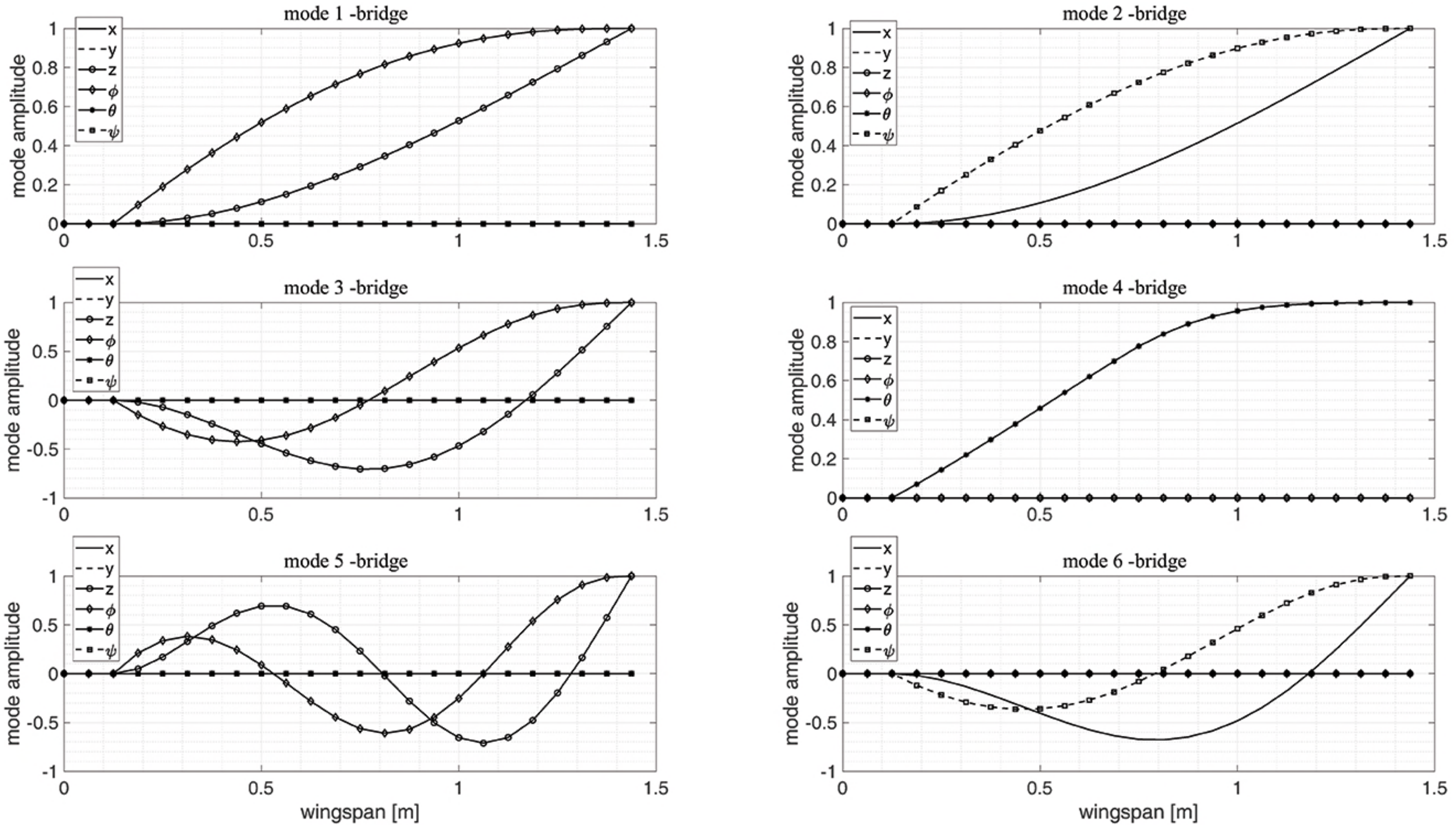

Fig. C.2.: Representation of the 6 degrees of freedom of the manufactured spar case (where the bridge was included) for the first six modes. The plot was used to identify the spar modes.

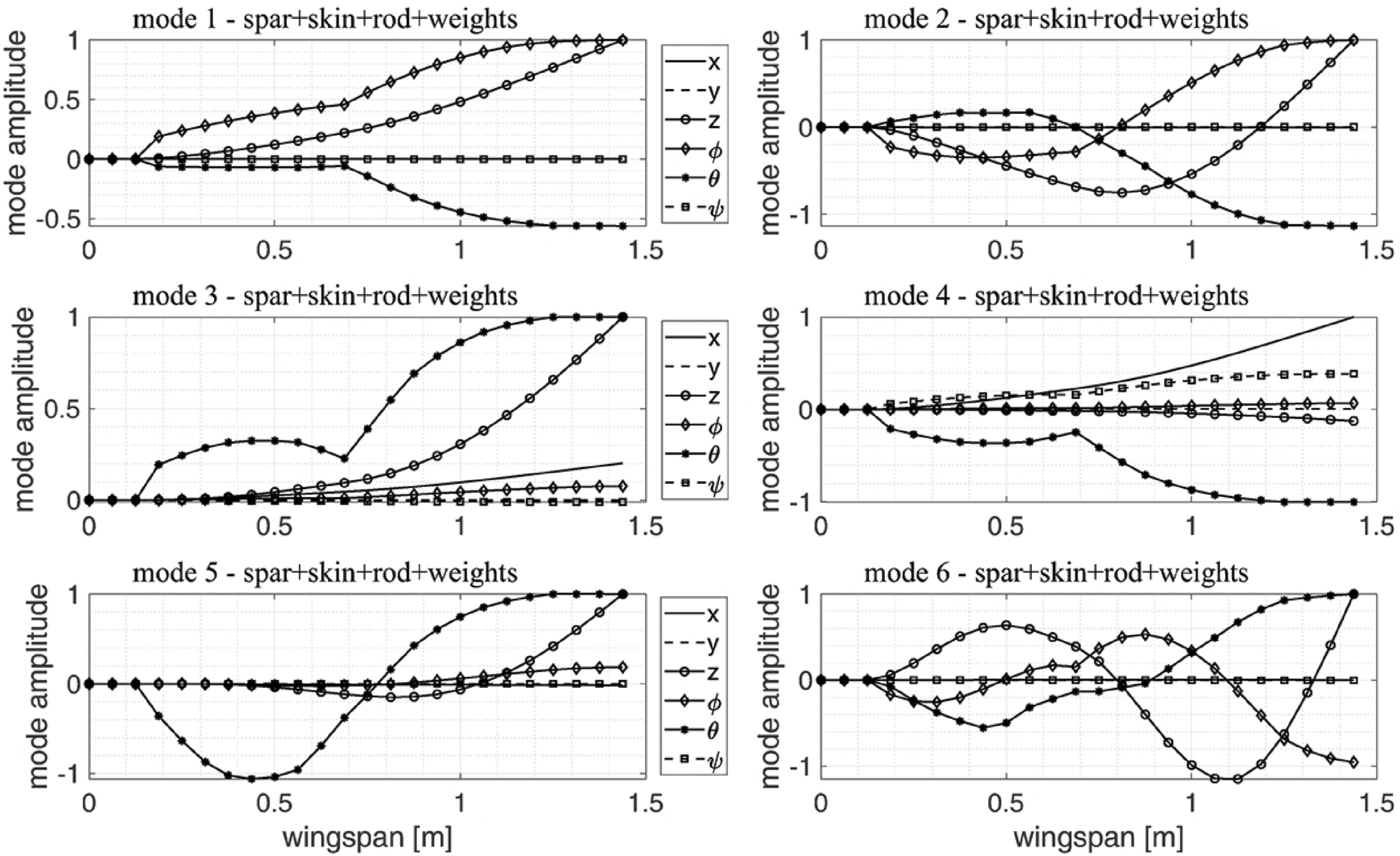

Fig. C.3.: Representation of the 6 degrees of freedom of the manufactured spar, with stiffening rod and weights along the spar.

		20 m/s			25 m/s			30 m/s			35 m/s			40 m/s		
	AoA [deg]	**WTT**	BEaRDS^{TM}	Δ [%]	**WTT**	BEaRDS^{TM}	Δ [%]	**WTT**	BEaRDS^{TM}	Δ [%]	**WTT**	BEaRDS^{TM}	Δ [%]	**WTT**	BEaRDS^{TM}	Δ [%]
lift	-2	-3.65 N	-4.79 N	-31.4	-6.00 N	-7.59 N	-26.5	-9.41 N	-11.12 N	-18.5	-13.64 N	-15.40 N	-12.8	-18.95 N	-20.32 N	-7.2
	0	6.3 N	5.6 N	-11.26	9.5 N	8.50 N	-10.3	13.20 N	11.80 N	-10.6	17.82 N	15.37 N	-13.8	24.45 N	19.03 N	-22.2
	2	17.47 N	15.95 N	-8.7	25.72 N	24.53 N	-4.62	36.25 N	34.59 N	-4.6	49.26 N	45.84 N	-6.9	65.78 N	57.85 N	-12.1
	4	30.33 N	26.28 N	-13.4	43.78 N	40.42 N	-7.7	60.05 N	57.01 N	-5.1	79.84 N	75.56 N	-5.3	102.91 N	95.43 N	-7.3
	6	40.74 N	36.54 N	-10.3	60.29 N	56.10 N	-6.9	82.40 N	78.99 N	-4.1	107.12 N	104.54 N	-2.4	133.71 N	131.93 N	-1.3
	8	47.0 N	46.71 N	-0.7	71.02 N	71.58 N	0.8	98.25 N	100.58 N	2.3	126.12 N	132.94 N	5.4	150.62 N	167.71 N	11.4
drag	-2	0.93 N	0.45 N	-51.5	1.14 N	0.69 N	-51.2	2.03 N	0.98 N	-52.1	2.8 N	1.3 N	-53.4	3.79 N	1.7 N	-55.1
	0	0.80 N	0.45 N	-43.3	1.20 N	0.69 N	-42.2	1.80 N	0.97 N	-45.7	2.60 N	1.31 N	-49.7	3.57 N	1.70 N	-52.4
	2	0.96 N	0.55 N	-43.0	1.39 N	0.84 N	-40.2	2.02 N	1.18 N	-41.6	2.79 N	1.57 N	-43.8	3.89 N	2.03 N	-48.0
	4	1.12 N	0.73 N	-34.6	1.58 N	1.12 N	-29.2	2.21 N	1.57 N	-29.2	3.08 N	2.08 N	-32.3	4.35 N	2.66 N	-38.8
	6	1.38 N	1.00 N	-27.6	1.95 N	1.53 N	-21.6	2.75 N	2.14 N	-22.1	3.73 N	2.83 N	-24.2	5.41 N	3.59 N	-33.6
	8	1.61 N	1.36 N	-15.4	2.31 N	2.07 N	-10.1	3.31 N	2.89 N	-12.4	4.69 N	3.81 N	-18.9	7.53 N	4.81 N	-36.2
side	-2	0.75 N	-	-	1.20 N	-	-	1.70 N	-	-	2.32 N	-	-	3.02 N	-	-
	0	0.75 N	-	-	1.20 N	-	-	1.70 N	-	-	2.32 N	-	-	3.02 N	-	-
	2	0.28 N	-	-	0.28 N	-	-	0.00 N	-	-	-0.73 N	-	-	-2.3 N	-	-
	4	-0.30 N	-	-	-0.96 N	-	-	-2.26 N	-	-	-4.70 N	-	-	-8.68 N	-	-
	6	-0.84 N	-	-	-2.42 N	-	-	-5.12 N	-	-	-9.40 N	-	-	-15.08 N	-	-
	8	-1.80 N	-	-	-4.35 N	-	-	-8.60 N	-	-	-14.35 N	-	-	-19.85 N	-	-

Tab. C.1.: XB-2 static forces test summary

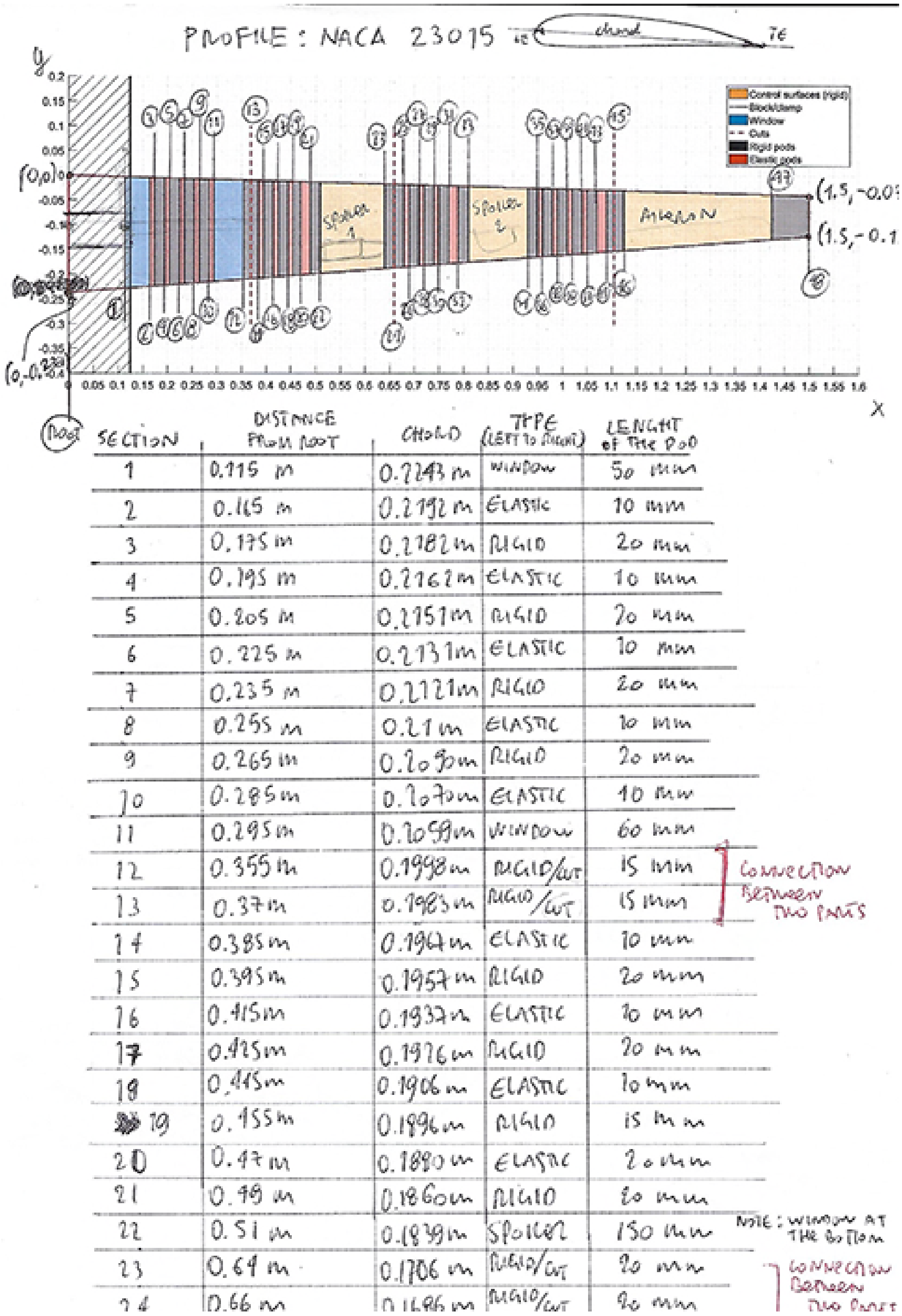

SECTION	DISTANCE FROM ROOT	CHORD	TYPE (LEFT TO RIGHT)	LENGHT OF THE POD
1	0.115 m	0.2243 m	WINDOW	50 mm
2	0.165 m	0.2192 m	ELASTIC	10 mm
3	0.175 m	0.2182 m	RIGID	20 mm
4	0.195 m	0.2162 m	ELASTIC	10 mm
5	0.205 m	0.2151 m	RIGID	20 mm
6	0.225 m	0.2131 m	ELASTIC	10 mm
7	0.235 m	0.2121 m	RIGID	20 mm
8	0.255 m	0.21 m	ELASTIC	10 mm
9	0.265 m	0.2090 m	RIGID	20 mm
10	0.285 m	0.2070 m	ELASTIC	10 mm
11	0.295 m	0.2059 m	WINDOW	60 mm
12	0.355 m	0.1998 m	RIGID/CUT	15 mm
13	0.37 m	0.1983 m	RIGID/CUT	15 mm
14	0.385 m	0.1967 m	ELASTIC	10 mm
15	0.395 m	0.1957 m	RIGID	20 mm
16	0.415 m	0.1937 m	ELASTIC	10 mm
17	0.425 m	0.1976 m	RIGID	20 mm
18	0.445 m	0.1906 m	ELASTIC	10 mm
19	0.455 m	0.1896 m	RIGID	15 mm
20	0.47 m	0.1880 m	ELASTIC	20 mm
21	0.49 m	0.1860 m	RIGID	20 mm
22	0.51 m	0.1839 m	SPOILER	150 mm
23	0.64 m	0.1706 m	RIGID/CUT	20 mm
24	0.66 m	0.1686 m	RIGID/CUT	20 mm

CONNECTION BETWEEN TWO PARTS (sections 12–13)

NOTE: WINDOW AT THE BOTTOM (section 22)

CONNECTION BETWEEN TWO PARTS (sections 23–24)

Fig. C.4.: Sketch of a preliminary idea for XB-2 model (1/6)

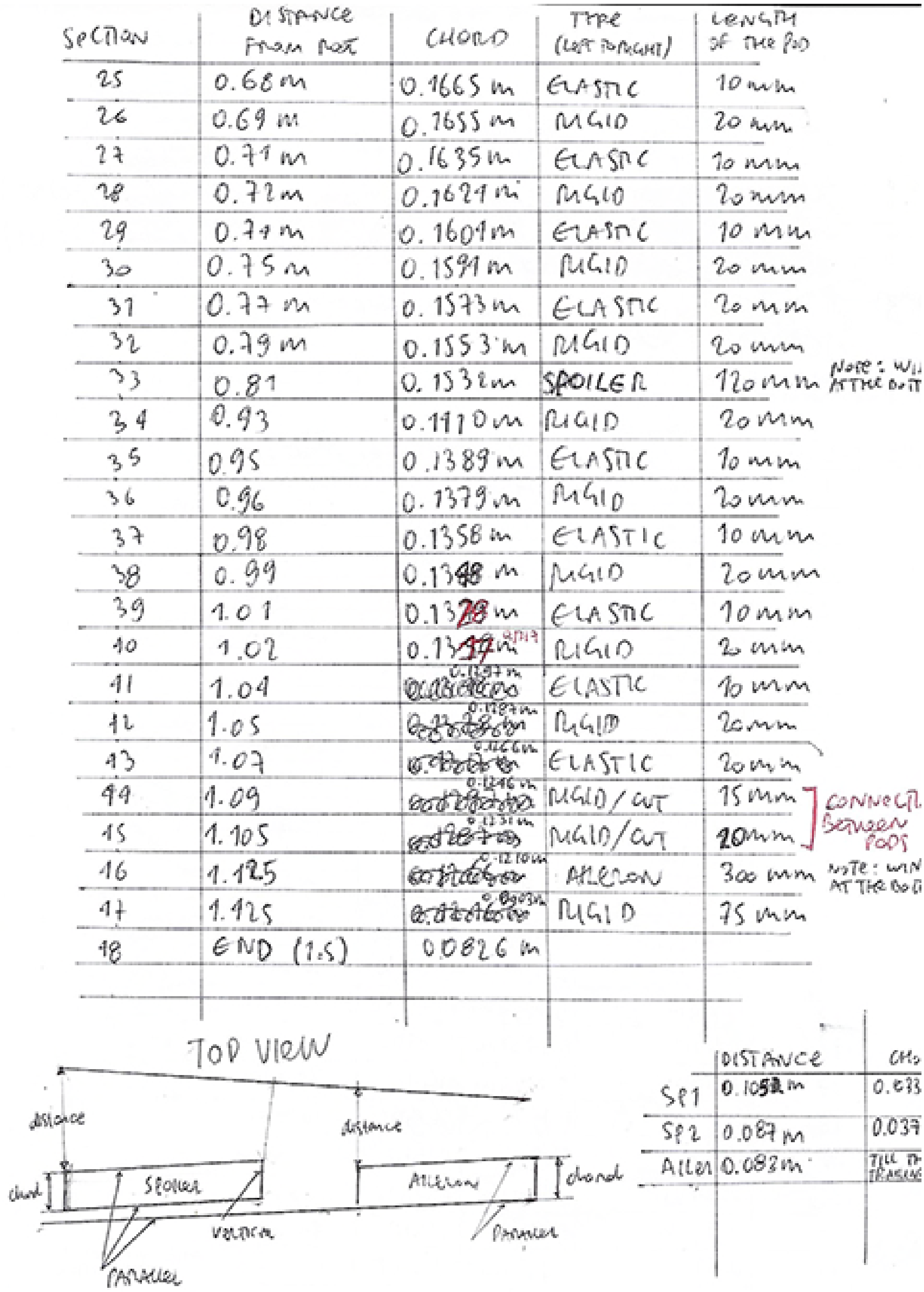

SECTION	DISTANCE FROM ROOT	CHORD	TYPE (LEFT TO RIGHT)	LENGTH OF THE POD	
25	0.68 m	0.1665 m	ELASTIC	10 mm	
26	0.69 m	0.1655 m	RIGID	20 mm	
27	0.71 m	0.1635 m	ELASTIC	10 mm	
28	0.72 m	0.1624 m	RIGID	20 mm	
29	0.74 m	0.1604 m	ELASTIC	10 mm	
30	0.75 m	0.1591 m	RIGID	20 mm	
31	0.77 m	0.1573 m	ELASTIC	20 mm	
32	0.79 m	0.1553 m	RIGID	20 mm	
33	0.81	0.1532 m	SPOILER	120 mm	Note: WI AT THE BOTT
34	0.93	0.1410 m	RIGID	20 mm	
35	0.95	0.1389 m	ELASTIC	10 mm	
36	0.96	0.1379 m	RIGID	20 mm	
37	0.98	0.1358 m	ELASTIC	10 mm	
38	0.99	0.1348 m	RIGID	20 mm	
39	1.01	0.1328 m	ELASTIC	10 mm	
40	1.02	0.1317 m 0.1317	RIGID	20 mm	
41	1.04	0.1297 m	ELASTIC	10 mm	
42	1.05	0.1287 m	RIGID	20 mm	
43	1.07	0.1266 m	ELASTIC	20 mm	
44	1.09	0.1246 m	RIGID / CUT	15 mm	CONNECTI BETWEEN PODS
45	1.105	0.1231 m	RIGID / CUT	20 mm	
46	1.125	0.1210 m	AILERON	300 mm	NOTE: WIN AT THE BO
47	1.125	0.0903 m	RIGID	75 mm	
48	END (1.5)	0.0826 m			

	DISTANCE	CH
SP1	0.1052 m	0.033
SP2	0.087 m	0.037
AILER	0.083 m	TILL TH TRAILIN

Fig. C.5.: Sketch of a preliminary idea for XB-2 model (2/6)

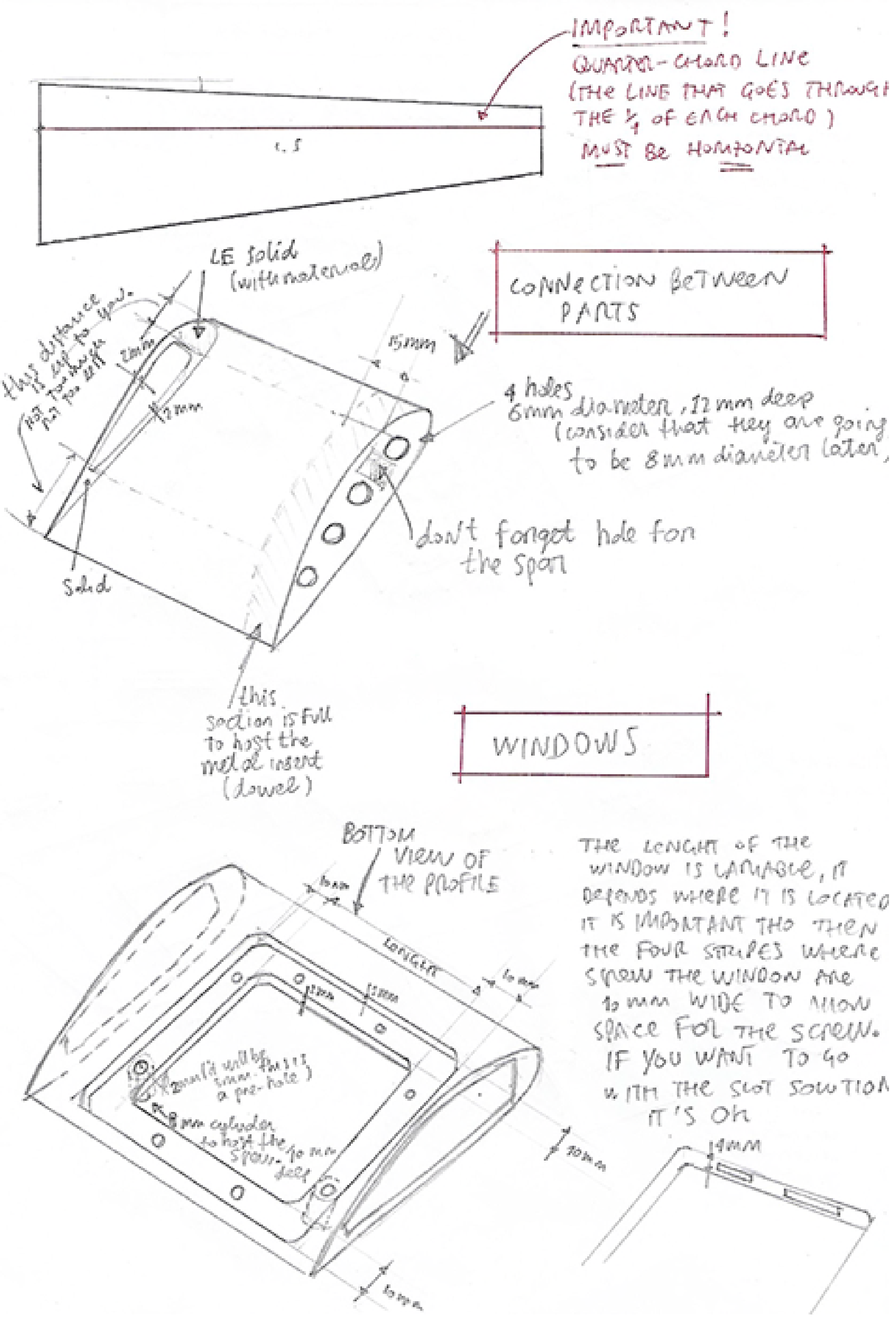

Fig. C.6.: Sketch of a preliminary idea for XB-2 model (3/6)

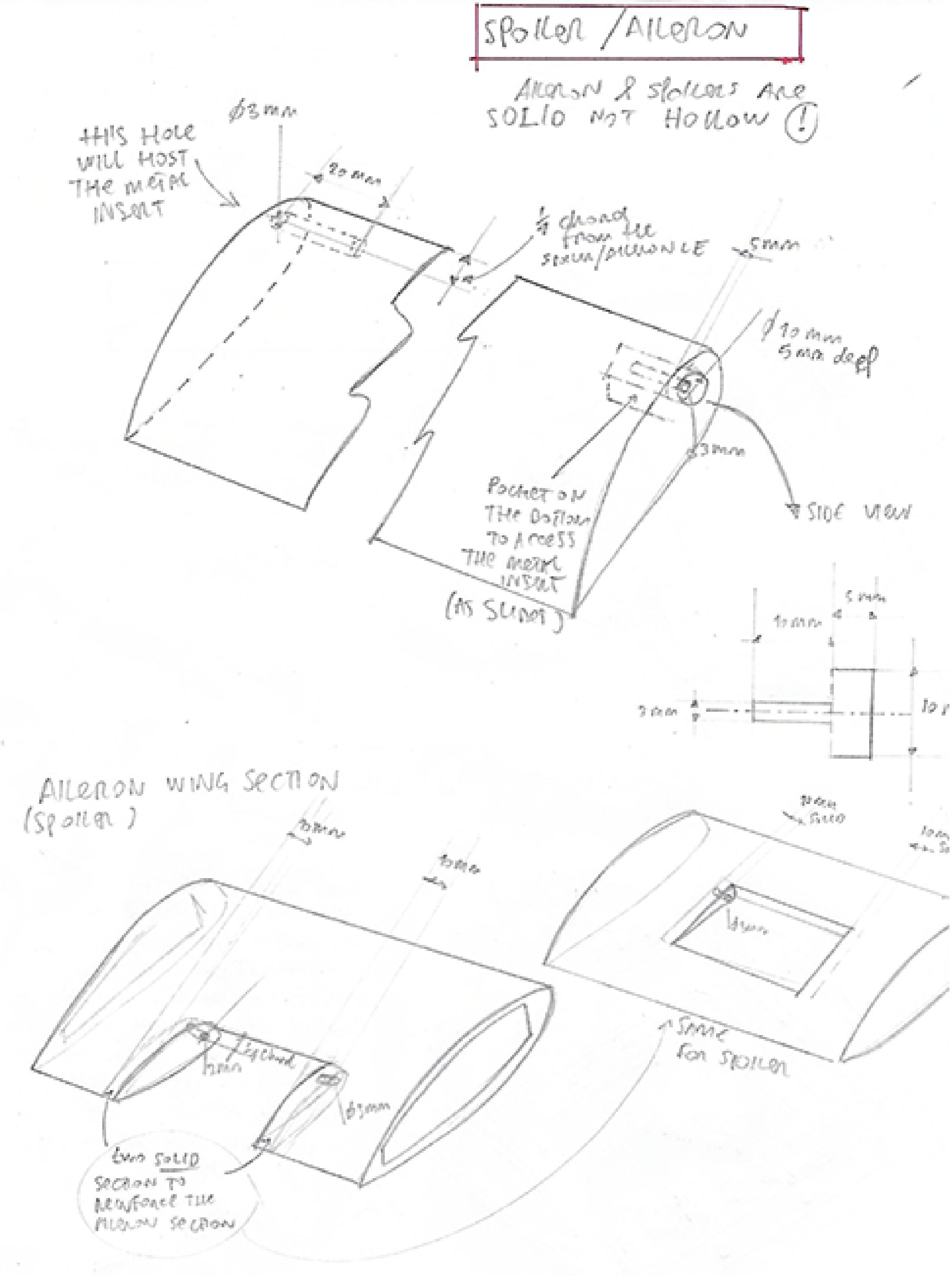

Fig. C.7.: Sketch of a preliminary idea for XB-2 model (4/6)

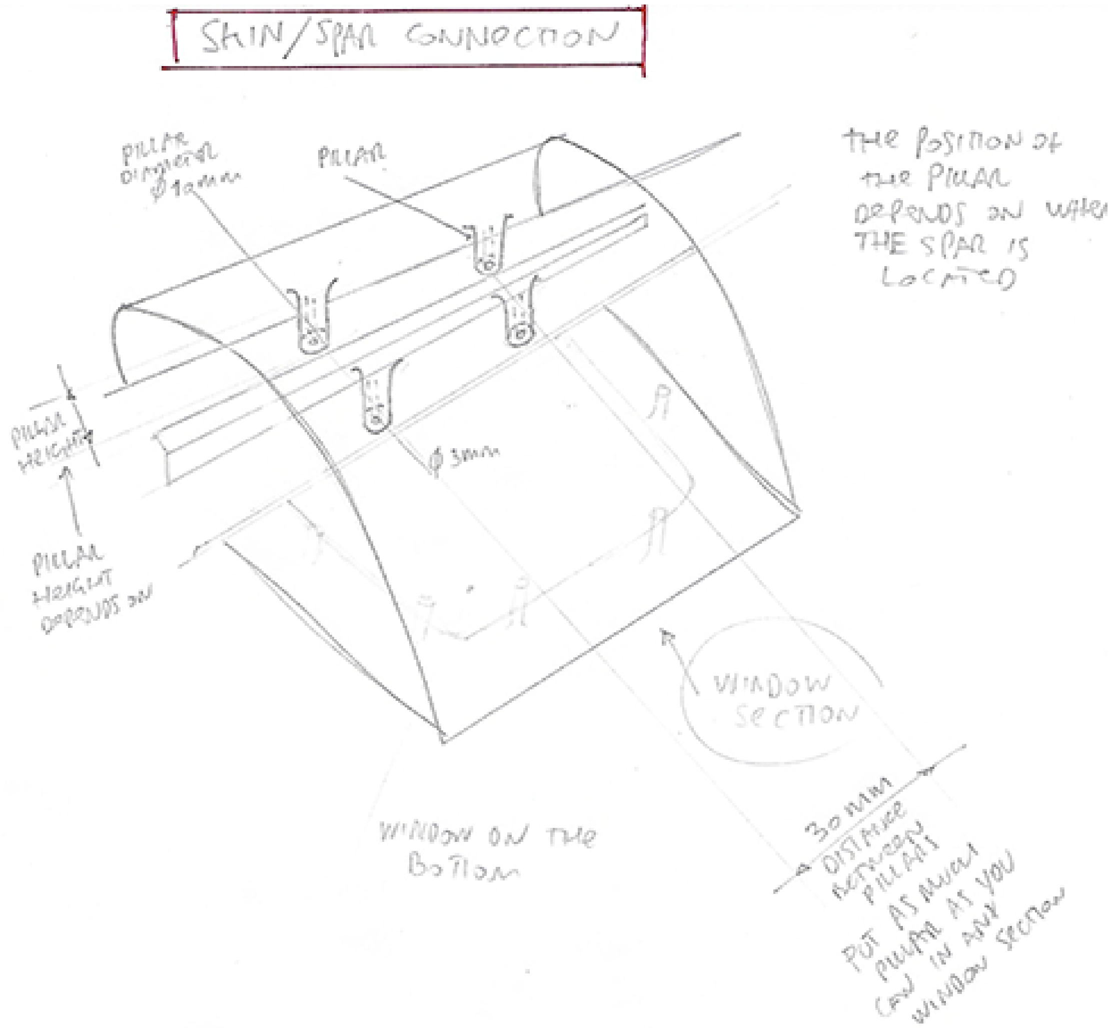

Fig. C.8.: Sketch of a preliminary idea for XB-2 model (5/6)

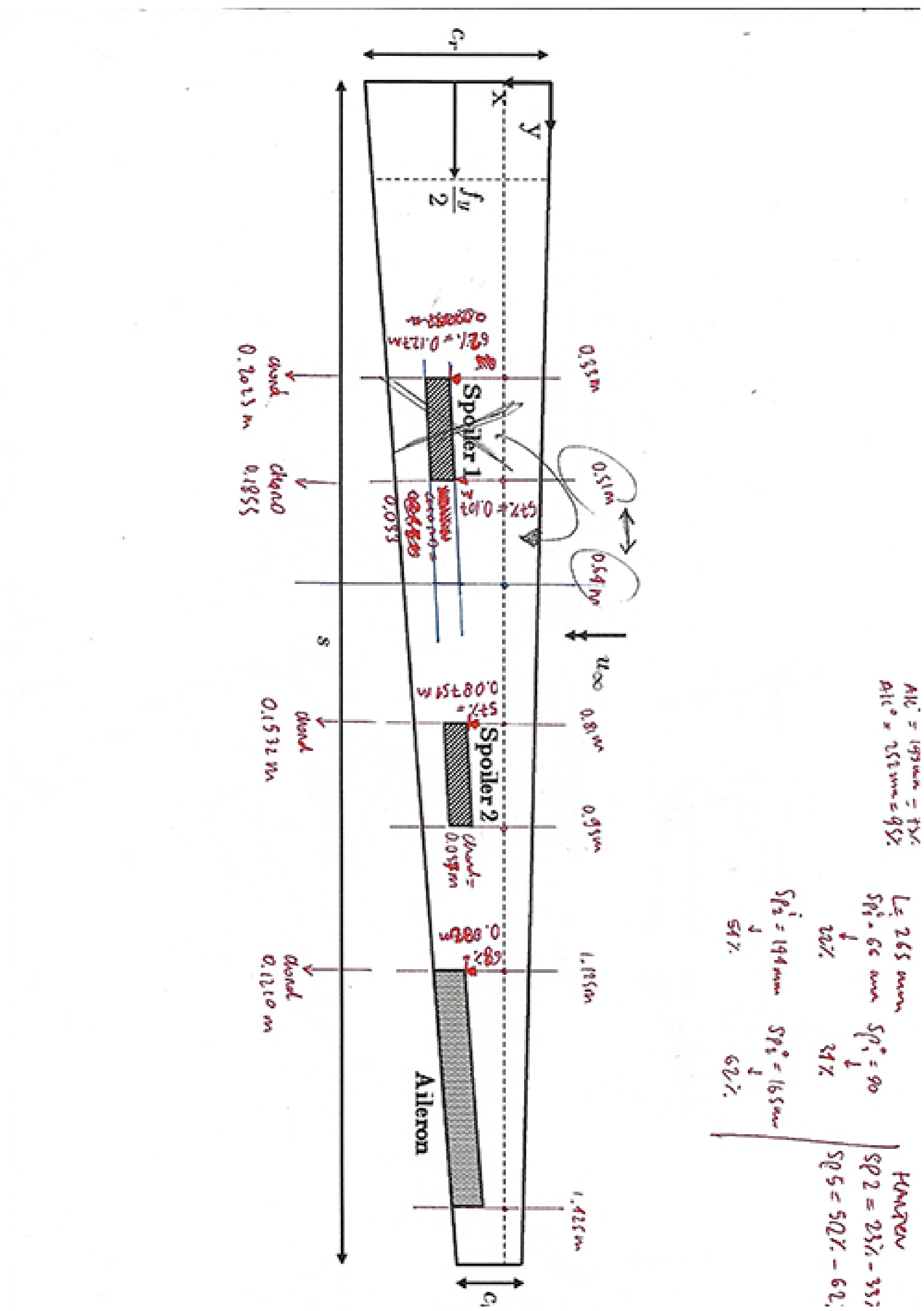

Fig. C.9.: Sketch of a preliminary idea for XB-2 model (6/6)

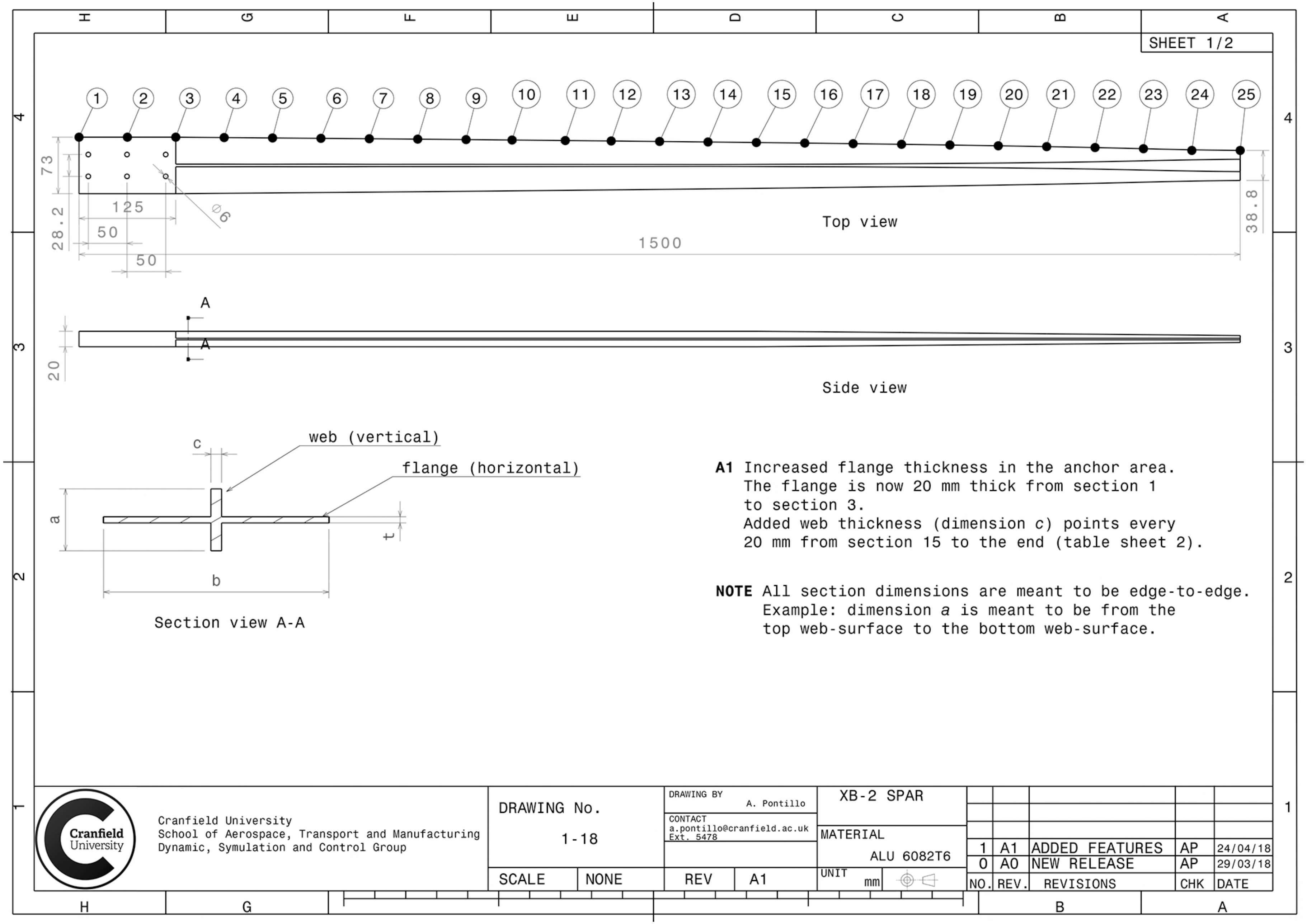

A1 Increased flange thickness in the anchor area.
The flange is now 20 mm thick from section 1
to section 3.
Added web thickness (dimension c) points every
20 mm from section 15 to the end (table sheet 2).

NOTE All section dimensions are meant to be edge-to-edge.
Example: dimension *a* is meant to be from the
top web-surface to the bottom web-surface.

Fig. C.10.: Manufacturing drawing of XB-2 spar. Sheet 1/2.

SHEET 2/2

Section	Dist from root	b	c	c/2	a	t
1	0	73	-	-	20	2
2	62.5	73	-	-	20	2
3	125	73	3.0	1.5	20	2
4	187.5	72	3.0	1.5	20	2
5	250	71	3.0	1.5	20	2
6	312.5	70	3.0	1.5	20	2
7	375	69	3.0	1.5	20	2
8	437.5	67.9	3.0	1.5	20	2
9	500	66.8	3.0	1.5	20	2
10	562.5	65.7	3.0	1.5	20	2
11	625	64.5	3.0	1.5	20	2
12	687.5	63.3	3.0	1.5	20	2
13	750	62	3.0	1.5	20	2
14	812.5	60.6	3.0	1.5	20	2
15	875	59.2	3.0	1.5	19	2
	895		3.0	1.5		2
	915		3.1	1.5		2
	935		3.2	1.6		2
16	937.5	57.8	3.2	1.6	18	2
	955		3.3	1.6		2
	975		3.4	1.7		2
	995		3.6	1.8		2
17	1000	56.2	3.7	1.9	16.8	2
	1015		3.8	1.9		2
	1035		4.0	2.0		2
	1055		4.3	2.1		2
18	1062.5	54.5	4.3	2.2	15.6	2
	1075		4.5	2.3		2
	1095		4.8	2.4		2
	1115		5.0	2.5		2
19	1125	52.7	5.1	2.6	14.6	2
	1135		5.3	2.7		2
	1155		5.7	2.8		2
	1175		6.0	3.0		2
20	1187.5	50.8	6.1	3.1	13.4	2
	1195		6.4	3.2		2
	1215		6.8	3.4		2
	1235		7.2	3.6		2
21	1250	48.7	7.5	3.8	12.4	2
	1255		7.7	3.9		2
	1275		8.2	4.1		2
	1295		8.8	4.4		2
22	1312.5	46.2	9.4	4.7	11.2	2

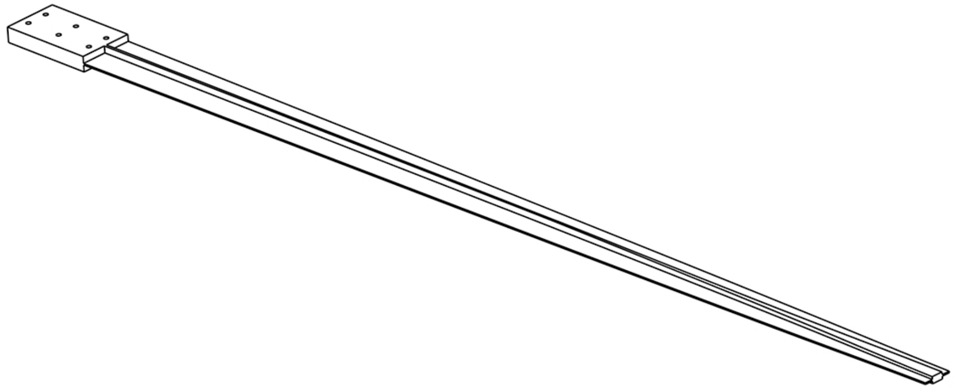

Section	Dist from root	b	c	c/2	a	t
	1315		9.5	4.7		2
	1335		10.2	5.1		2
	1355		11.1	5.5		2
23	1375	43.1	12.0	6.0	10.2	2
	1395		13.1	6.6		2
	1415		14.4	7.2		2
	1435		15.8	7.9		2
24	1437.5	38.7	15.9	8.0	9	2
	1455		16.8	8.4		2
	1475		17.5	8.8		2
	1495		17.9	9.0		2
25	1500	38.8	18	9.0	8	2

Cranfield University
School of Aerospace, Transport and Manufacturing
Dynamic, Symulation and Control Group

DRAWING No.
1-18

SCALE NONE
REV A1

DRAWING BY A. Pontillo
CONTACT
a.pontillo@cranfield.ac.uk
Ext. 5748

XB-2 SPAR

MATERIAL
ALU 6082T6

UNIT mm

NO.	REV.	REVISIONS	CHK	DATE
1	A1	ADDED FEATURES	AP	24/04/18
0	A0	NEW RELEASE	AP	29/03/18

Fig. C.11.: Manufacturing drawing of XB-2 spar. Sheet 2/2.

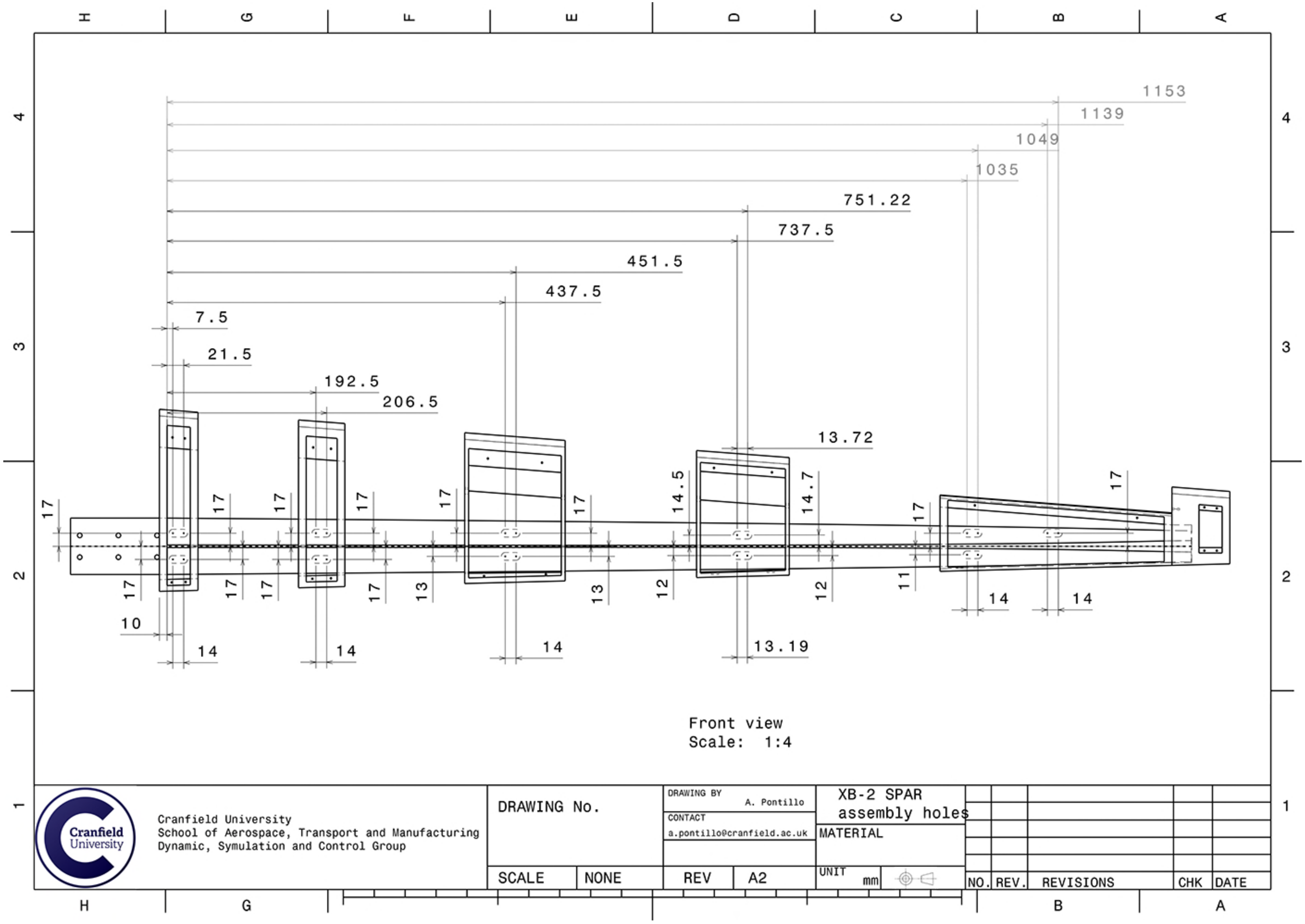

Fig. C.12.: Pillars-spar connection holes.

Appendix: GLA system

D

D.1 Optimization results

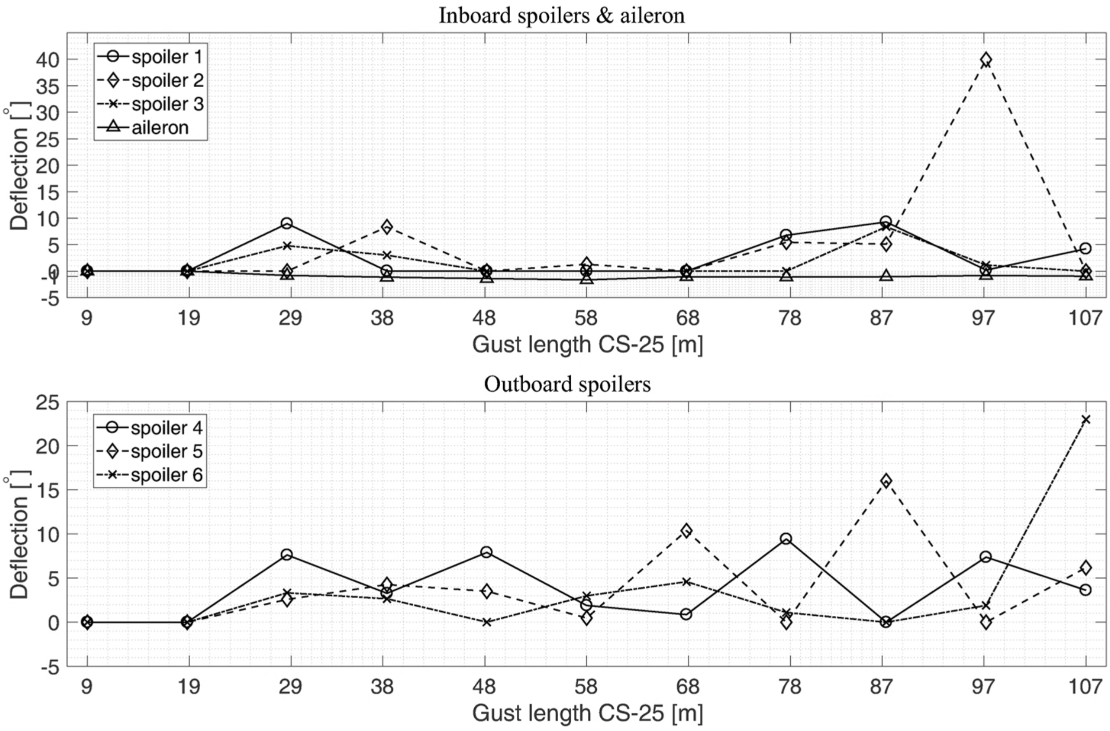

Fig. D.1.: Impact of the flexibility: HARTEN optimized computational control surface deflections.

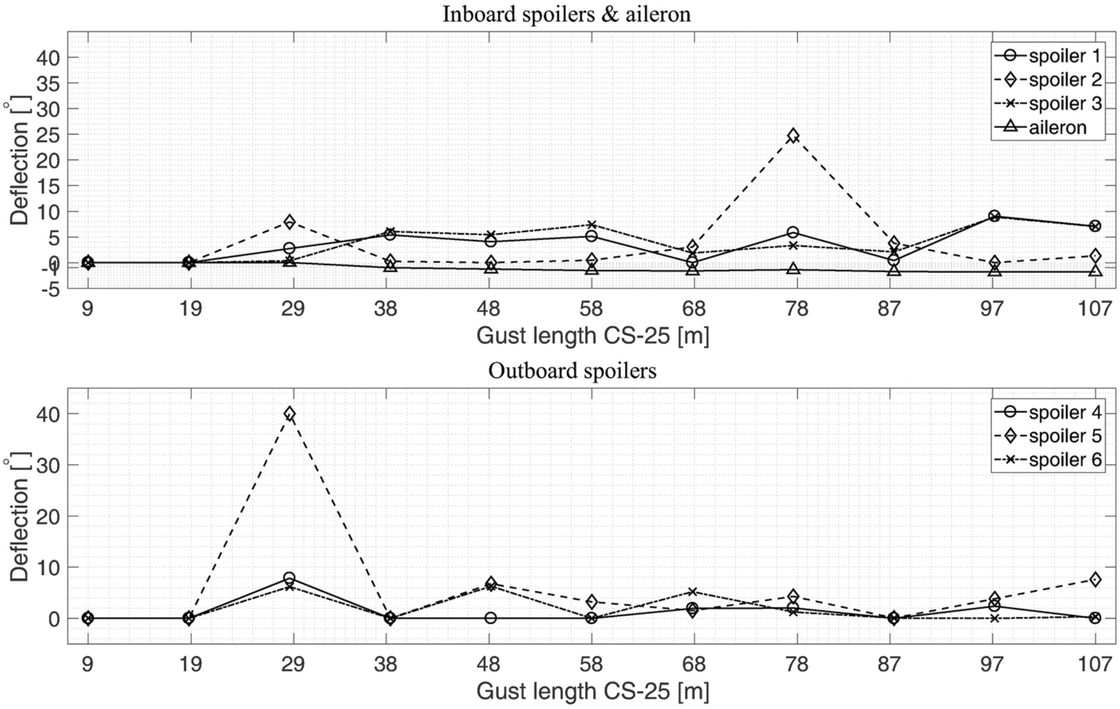

Fig. D.2.: $\tau = 2.5$ s: HARTEN optimized computational control surface deflections.

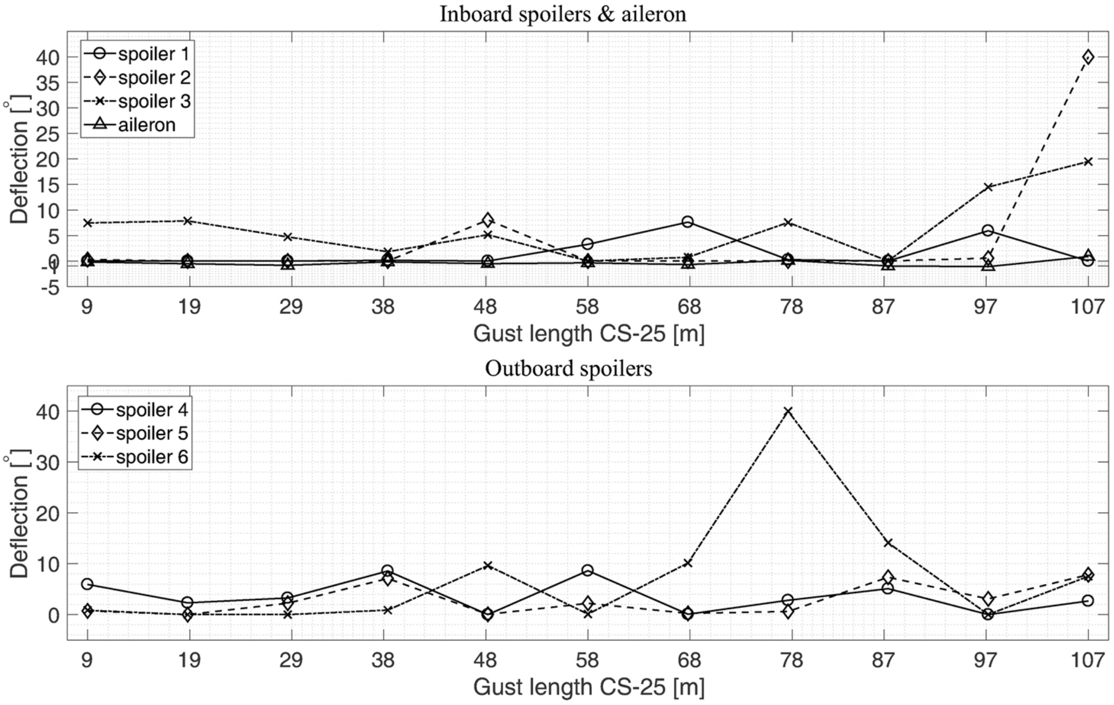

Fig. D.3.: Threshold = 0.2 g: HARTEN optimized computational control surface deflections.

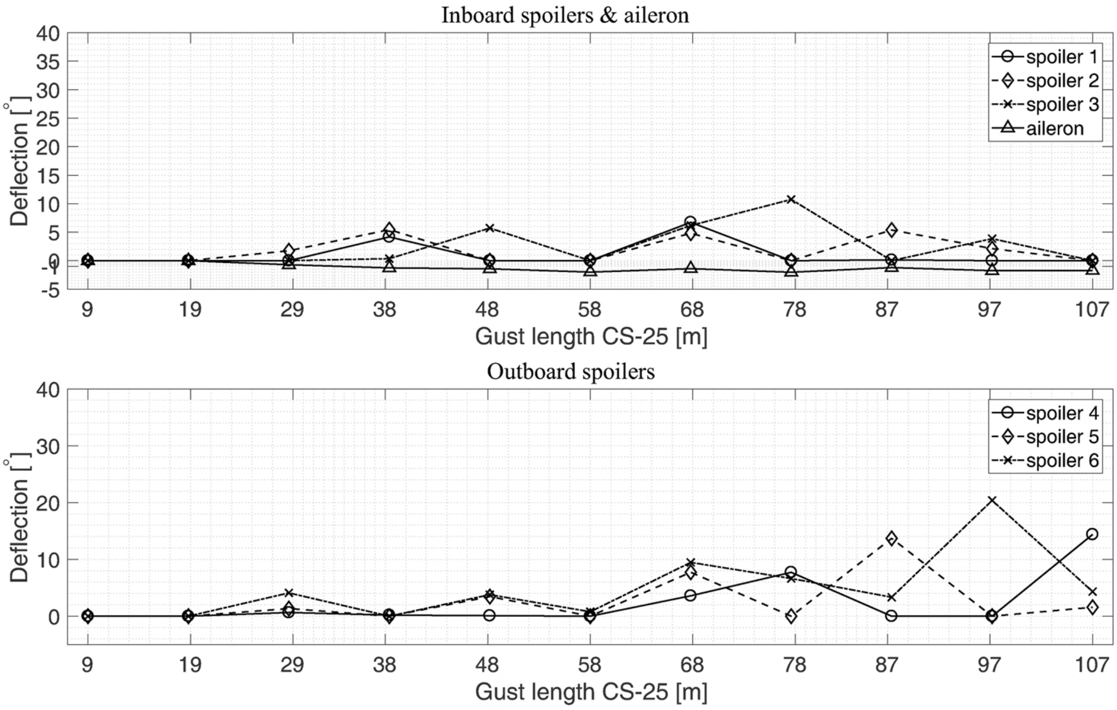

Fig. D.4.: Variable τ and threshold: HARTEN optimized computational control surface deflections.

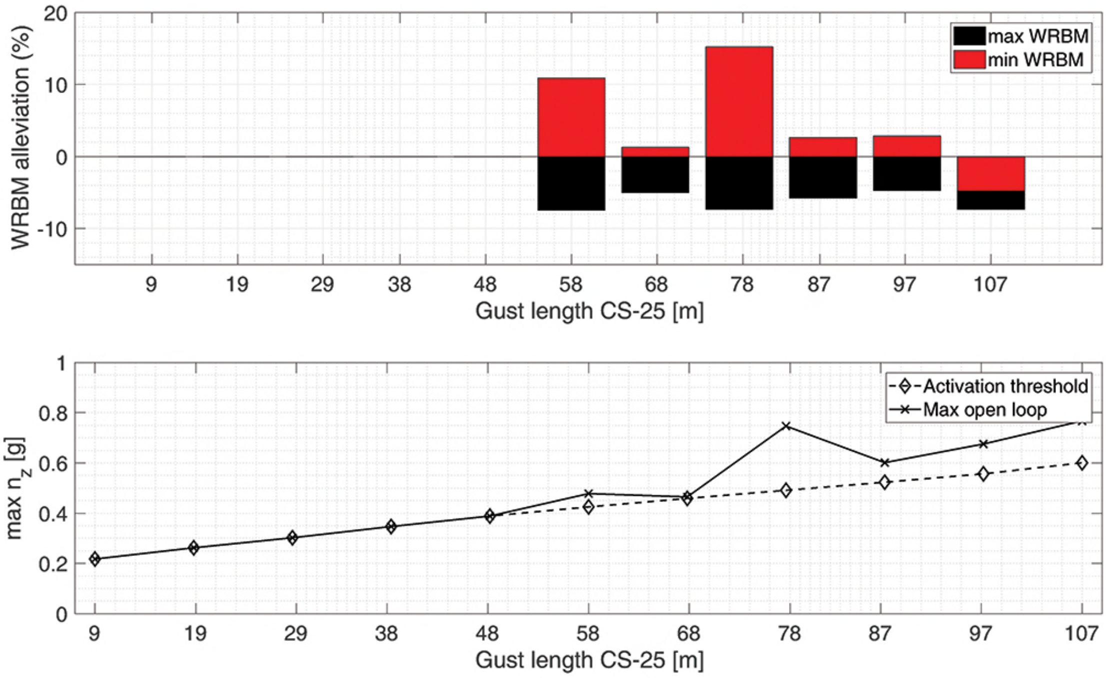

Fig. D.5.: Variable τ and threshold (random initial point): HARTEN optimized computational control surface deflections.

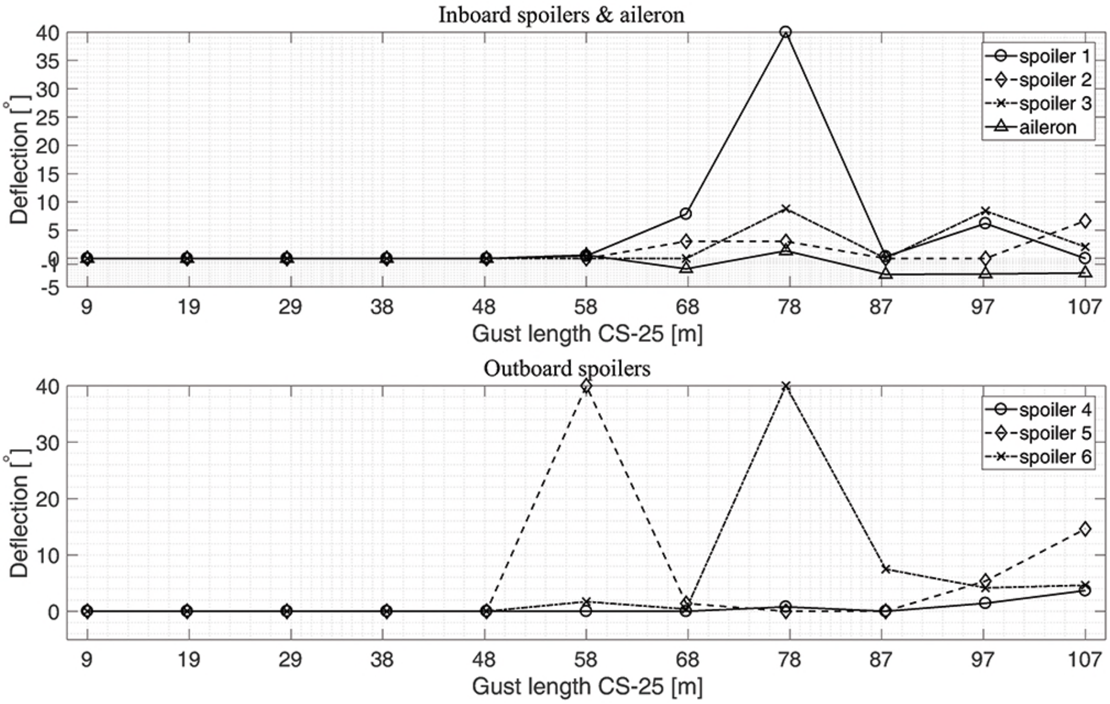

Fig. D.6.: Variable τ and threshold (random initial point): HARTEN optimized computational control surface deflections.

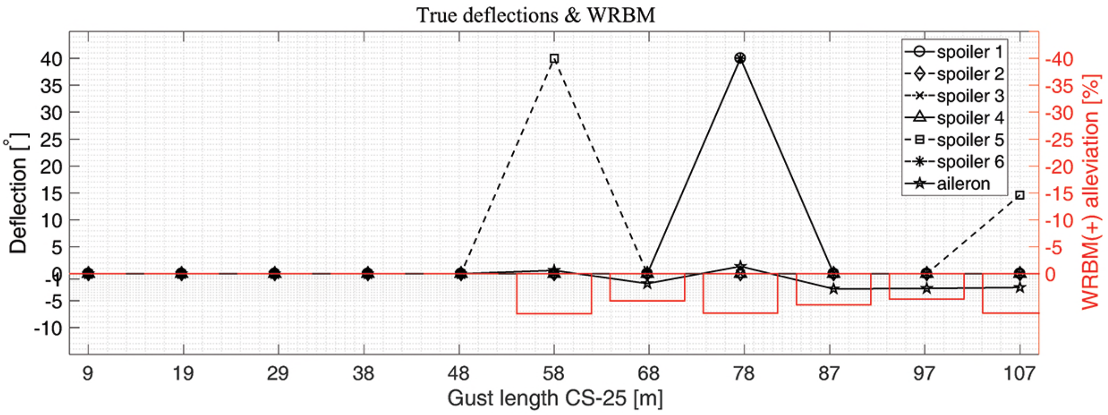

Fig. D.7.: Variable τ and threshold (random initial point): HARTEN optimized *true* control surface deflections.

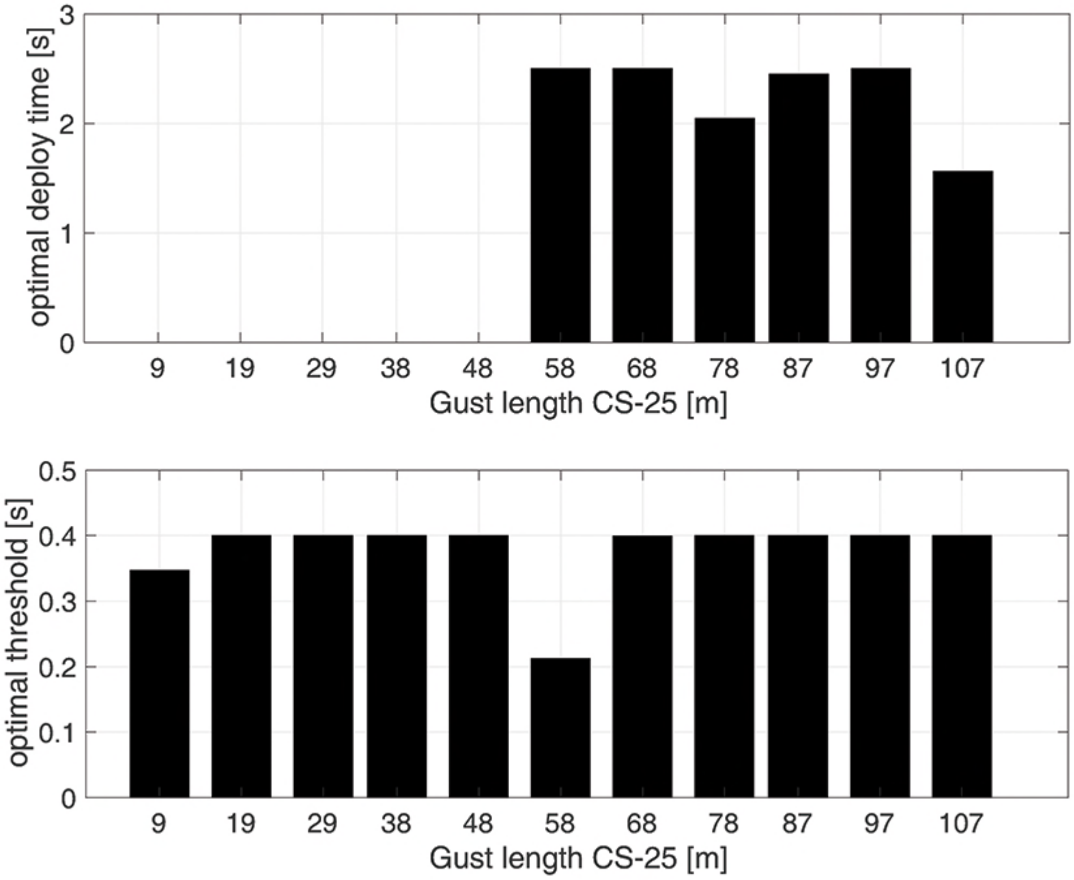

Fig. D.8.: Variable τ and threshold (random initial point): HARTEN optimized hold time and threshold values.

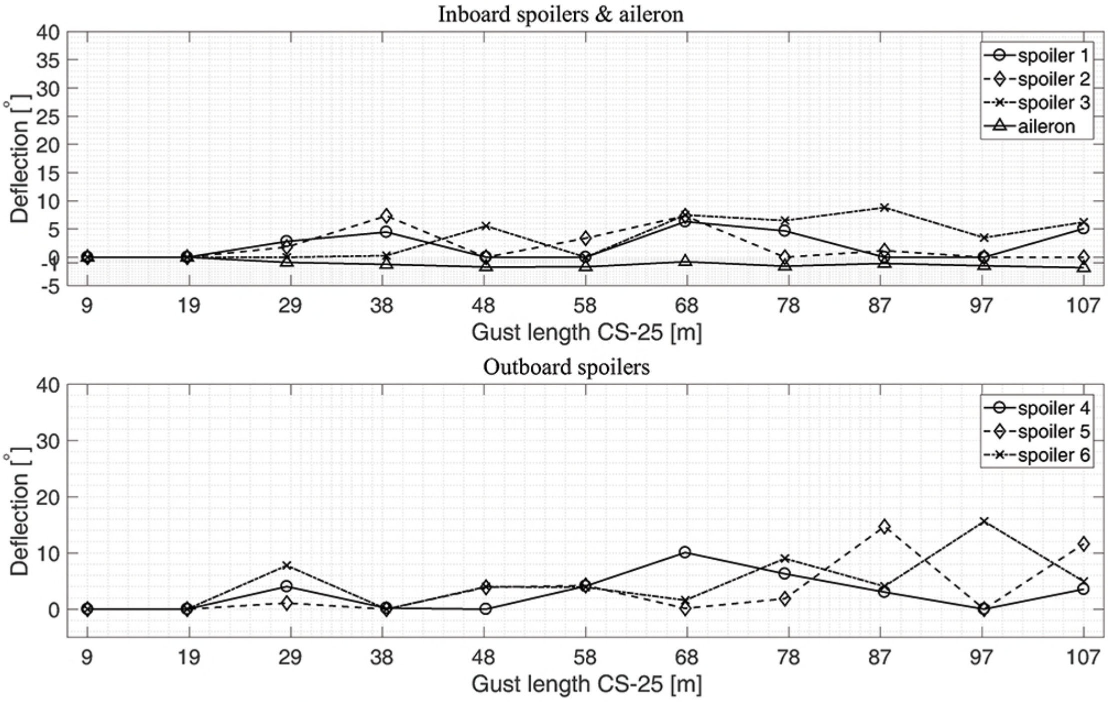

Fig. D.9.: Second threshold: HARTEN optimized computational control surface deflections.

D.2 M_w estimation

In order to estimate the M_w stability derivative, a linear model of the model pitch response was derived as:

$$I_{yy}\dot{q} = M_\alpha \alpha + M_q q + M_\delta \delta \tag{D.1}$$

Assuming:

$$\alpha = \frac{w}{u} \tag{D.2}$$

and thus:

$$\frac{\partial \alpha}{\partial w} = \frac{1}{U} \tag{D.3}$$

The stability derivative M_w can be written as:

$$M_w = \frac{\partial M}{\partial \alpha}\frac{\partial \alpha}{\partial w} \tag{D.4}$$

Substituting Equation D.3 in equation D.4, the desired stability derivative is given as:

$$M_w = \frac{1}{U} M_\alpha \tag{D.5}$$

To acquire the aircraft response in order to estimate M_α, the model was excited with a doublet elevator input of magnitude 3 deg and period $T = 1s$. The response of the aircraft to the elevator input is shown in Figure D.10 and zoomed in Figure D.11. The following and final step was to plot the curve $\dot{q} - \alpha$ (Figure D.12). The dataset acquired was linearly interpolated. The inclination of the line provided the stability derivative M_α and therefore M_w.

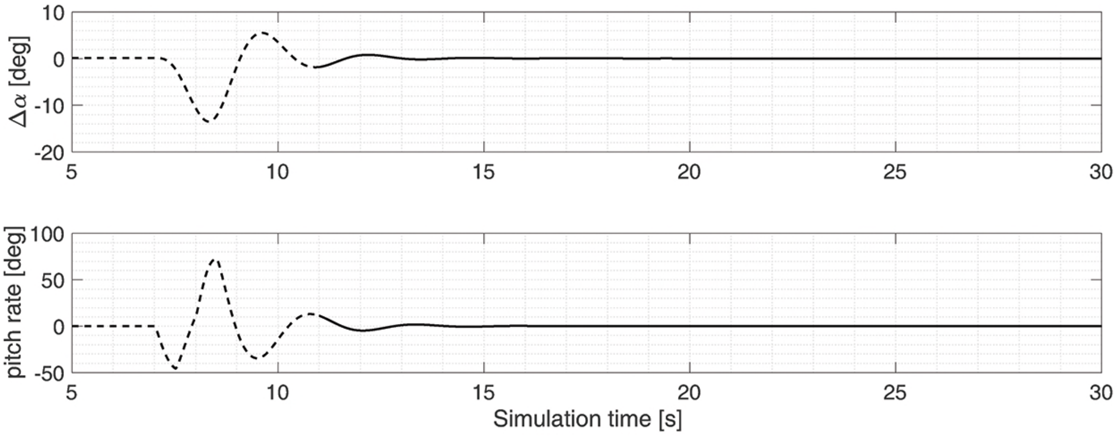

Fig. D.10.: Pitch rate and AoA time history for M_w estimation.

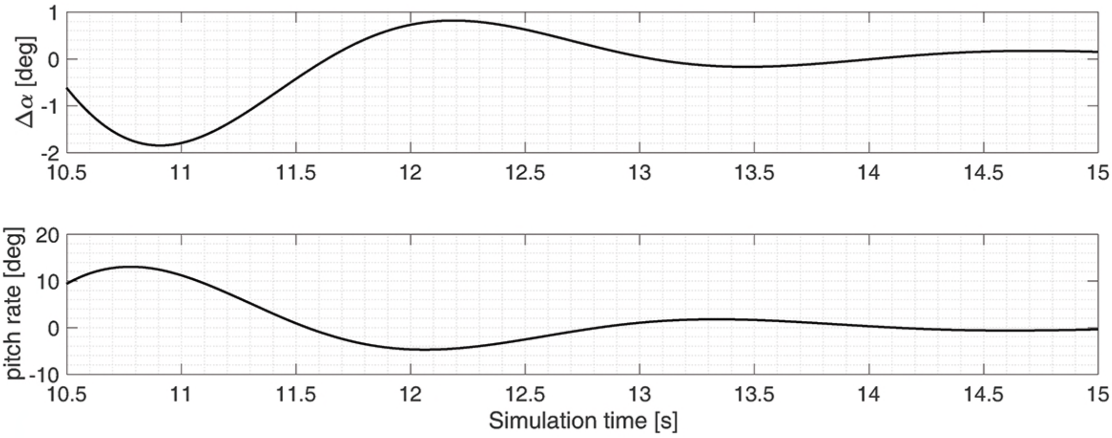

Fig. D.11.: Pitch rate and AoA zoom of time history for M_w estimation.

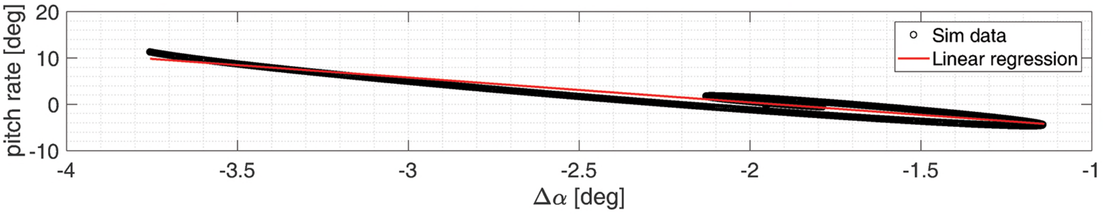

Fig. D.12.: M_w estimation and linear regression.